UNIVERSITY OF CALIFORNIA SANTA BARBARA

V-defect Engineering for Long Wavelength III-N Light Emitting Diodes

A dissertation submitted in partial satisfaction of the requirements for the degree

Doctor of Philosophy

in

Materials

by

Jacob J. Ewing

Dissertation Committee:

Professor Steven P. DenBaars, Chair

Professor James S. Speck

Professor Shuji Nakamura

Dr. Stacia Keller, Principal Development Engineer

September 2024

The dissertation of Jacob J. Ewing is approved:

Stacia Keller

Shuji Nakamura

James S. Speck

Steven P. DenBaars, Committee Chair

July 2024

V-defect Engineering for Long Wavelength III-Nitride Light Emitting Diodes

by

Jacob J. Ewing

Acknowledgements

Although a degree is given to a single person, getting one is by no means a one-person task. This is why I want to start this dissertation with acknowledgements to the people that have been invaluable to this process. Furthermore, in scientific research, no project is done in isolation and much of the work in this dissertation was done in collaboration with researchers at UCSB or at other institutions. In specific sections of chapters, where a majority of the work was done by a collaborator, there's a specific acknowledgement in the text, under the section heading.

First, I thank my PhD committee. My advisor Steve DenBaars for his support, advice, and resources throughout my entire 5 years from start to finish. And for running the business side of the solid-state lighting and energy efficiency center (SSLEEC) at UCSB. To Jim Speck, for being the principal investigator on my project and a second advisor for me. His expertise in LEDs, material science, crystallographic defects, characterization, and much more were instrumental in the work that is presented. The 100 (?) hours that were spent in his office during these years have made me a far better scientist than I was when I started. To Shuji Nakamura, for inspiring a generation of LED scientists, and for your expertise and insights important to this work. To Stacia Keller, for her valuable knowledge on III-N epitaxy and MOCVD.

Dr. Feng Wu, Senior transmission electron microscopy scientist. Her TEM work is a central part of this thesis. All TEM images in Chapters 3-6 were captured by Dr. Feng Wu, including sample preparation, electron microscopy, and much of the analysis. This data was instrumental in guiding the experiments in this thesis. Chapter 3 is a paper authored by Feng

Wu (which I helped write and grow samples for). Her work is also a significant part of Chapter 5 and a very important contribution to Chapters 4 and 6.

Dr. Cheyenne Lynsky. Her expertise and mentorship in MOCVD growth paved the way for me to accomplish what's described in this dissertation. She was also a close collaborator in the work in chapter 4 and helped grow the samples for the TEM work in chapter 3. Alejandro Quevedo worked closely with me for the second half of my PhD and made very significant contributions to the work presented in chapters 5 and 6. Tanay Tak was also a close collaborator for the second half of my PhD and made very significant contributions to the V-defect project as a whole, parts of chapter 6, and the characterization in chapter 5. Dr. Matthew Wong, for his mentorship in device processing and for being an insightful officemate for 2 years. Dr. Ryan White for his mentorship in processing and characterization. Dr. Jordan Smith for his collaboration on building the on-chip testing setup that was used for efficiency measurements in chapter 4. Dr. Pavel Shapturenka for his work on the light extraction efficiency (LEE) simulations that were used in chapter 4. Other important mentors on growth, processing, characterization, and general LED knowledge include Dr. Yi Chao Chow, Dr. Wan Ying Ho, Dr. Panpan Li, Zachary Biegler, Dr. Ryan Ley, Dr. Ryan Anderson, Emily Trageser, Dr. Nate Palmquist, Dr. Clayton Qwah, Vincent Rienzi, Vineeta Muthuraj, Stephen Gee, Camille Pivard, and Michael Wang. Professor Saulius Marcinkevičius and Rinat Yapporov at KTH Royal Institute of Technology, Stockholm, Sweden have had an on-going collaboration on understanding V-defects. Specifically, chapter 6 section 5 was mostly work done at KTH and based off a paper by Saulius where I'm the second author. Professor Mike Gordon was incredibly helpful in building test setups and loaned us some space in his lab. His knowledge of optics and equipment were vital to the work in chapter 4. Distinguished professor Claude

Weisbuch, joint appointment at UCSB and Ecole Polytechnique, France, made significant contributions to the V-defect project. His device physics knowledge and discussions at UCSB and at various conferences were incredibly valuable.

Mike Iza, for his expertise and experience in MOCVD hardware. Without Mike the reactors wouldn't have functioned, and the LEDs grown in this work couldn't have been made. David Whitlach, for the many hours he spent changing ammonia cylinders, doing maintenance and logistics around the lab. Also, the rest of the SSLEEC staff, Yukina Warner, Fukiko Miyazaki, Tara Owens, Emi Sautot, Brenda McGowen, and Brain Carrillo.

Umesh Mishra, Omar Saleh, Jonathan Klamkin, Jim Speck, Steve DenBaars, Chris Palmstorm, John Harter, and Anton Van Der Ven for teaching key classes and helped my general knowledge of physics and semiconductors.

During my PhD I interned at Meta Reality Labs in Redmond, WA in the Optics and Display Research division. Although this dissertation does not contain any work that was done at Meta, my summer there was very insightful in understanding LED research, the display industry, and how my research fits into bigger picture of the scientific industry. Hopefully, this writing was informed by that knowledge. I specifically thank Christophe Hurni, for his mentorship and advising, Jim Bonar, for providing me with the opportunity in this group, and the entire O&DR team for many fun and valuable lunch discussions. Special thanks to Wyatt Moore and Toshi Take for helping me with lab stuff and for the many interesting discussions.

` I also thank my many friends and fellow graduate students with whom I've had wonderful discussions, parties, and adventures. Specifically, my grad school brothers and housemates Elias Sebti and Trevor Steiner. And everyone else. You know who you are. :)

I thank my parents Dean and Mary, for their years of support and wisdom. Thanks for weekly calls from FL. My siblings Ben, Caleb, Sam, Hannah, and Isaac. Thanks for all the support, friendship, and adventures.

And finally, to the great state of California and the Pacific Ocean for being an unforgettable playground for surfing, climbing, backpacking, snowboarding, hiking, and camping. During my time in graduate school, I traveled across California, Oregon, Washington, Idaho, British Columbia, Alberta, Montana, Wyoming, South Dakota, Utah, Nevada, Arizona, Minnesota, Illinois, Iowa, Wisconsin, and North Dakota, as well as many trips to Florida. I surfed from San Diego County to Vancouver Island and made the most of the big storms that hit Santa Barbara, making lifelong memories. I also traveled to Japan for the International Conference on Nitride Semiconductors (ICNS). I'm grateful to the wild places, the call of adventure, and all my friends and family for keeping me (relatively) sane during grad school.

Curriculum Vitae

Dr. Jacob J. Ewing

EDUCATION

UNIVERSITY OF CALIFORNIA SANTA BARBARA (PhD) **Santa Barbara, CA**

Materials Engineering *September 2019 – July 2024*

- National Science Foundation Graduate Research Fellow

UNIVERSITY OF FLORIDA (B.S.) || 3.96 || **Gainesville, FL**

Materials Science and Engineering *January 2017-May 2019*

- Summa Cum Laude

SANTA FE COLLEGE (A.A.) || 4.0 || **Gainesville, FL**

Associate of Arts *August 2014 – December 2016*

- Highest distinction, Honors Certificate

PROFESSIONAL EXPERIENCE

UNIVERSITY OF CALIFORNIA SANTA BARBARA **Santa Barbara, CA**

Graduate Researcher *September 2019 – July 2024*

Solid-state lighting and energy electronics center (SSLEEC), DenBaars and Speck groups.

META REALITY LABS **Redmond, WA**

Research Scientist Intern in Optics and Display Research *June 2023 – September 2023*

SANDIA NATIONAL LABORATORIES **Albuquerque, NM**

MEMS Technologies R&D Student Intern *June 2018 – August 2018*

UNIVERSITY OF FLORIDA **Gainesville, FL**

Undergraduate Researcher *March 2017 – July 2019*

Interdisciplinary Microsystems Group, Magnetic Materials, Arnold Group

SANTA FE COLLEGE MATH DEPARTMENT **Gainesville, FL**

Mathematics Tutor at Santa Fe Math Studio *January 2016 – December 2016*

Teaching Assistant – Trigonometry and Pre-Calculus *August 2016 – December 2016*

PUBLICATIONS

J. Ewing, C. Lynsky, M. S. Wong, F. Wu, Y.C. Chow, P. Shapturenka, M. Iza, S. Nakamura, S.P. Denbaars, J.S. Speck, "High external quantum efficiency (6.5%) InGaN V-defect LEDs at 600 nm on patterned sapphire substrates" *Optics Express*, 31, 25, 41351-41360 (2023).

J. Ewing, F. Wu, A. Quevedo, T. Tak, S. Nakamura, S.P. DenBaars, J.S. Speck, "Pure Edge Dislocation Half-Loops in Low Temperature GaN for V-defect Formation", *Phy. Rev. Applied,* 21 (6), 064042 (2024)

J. Ewing, C. Lynsky, J. Zhang, P. Shapturenka, M. Wong, J. Smith, M. Iza, J.S. Speck, S.P. DenBaars, "Influence of Superlattice Structure on V-Defect Distribution, External Quantum Efficiency and Electroluminescence for Red InGaN Based μLEDs on Silicon", *Crystals*, *12*, 1216 (2022).

J. Ewing, Y. Wang, D.P. Arnold, "High-current-density electrodeposition using pulsed and constant currents to produce thick CoPt magnetic films on silicon substrates," *AIP Adv.* 8 (5) (2018).

F. Wu, **J. Ewing**, C. Lynsky, M. Iza, S. Nakamura, S.P. DenBaars, J.S. Speck, "Structure of V-defects in long wavelength GaN-based light emitting diodes", *Journal of Applied Physics*, 133 (3) (2023)

S. Marcinkevičius, **J. Ewing**, Rinat Yapparov, Feng Wu, Shuji Nakamura, and James S. Speck. "Experimental evidence of hole injection through V-defects in long wavelength GaN-based LEDs." *Applied Physics Letters* 123, no. 20 (2023).

P. Li, **J. Ewing**, M.S. Wong, Y. Yao, H. Li, S. Gandrothula, J.M. Smith, M. Iza, S. Nakamura, S.P. DenBaars, "Advances in InGaN-based RGB micro-light-emitting diodes for AR applications: Status and perspective", *APL Materials*, 12 (8) (2024).

C. Velez, **J. Ewing**, S. Hwangbo, K. Sondhi, T. Schumann, Y.K. Yoon, D.P. Arnold, "Low-temperature micropatterning of thick-film $BaFe_{12}O_{19}$ composites on semiconductor substrates for integrated millimeter wave devices," *2018 IEEE MTT-S Int. Microw. Work. Ser. Adv. Mat. Process. RF THz Appl.*, vol. 3, p. 19–21, (2018).

Y. Wang, **J. Ewing**, and D. P. Arnold, "Ultra-Thick Electroplated CoPt Magnets for MEMS," *Journal of Microelectromechanical Systems*, 28 (2) 311-320 (2019).

R. Yapparov, T. Tak, **J. Ewing**, F. Wu, S. Nakamura, S.P. DenBaars, J.S. Speck, S. Marcinkevičius, "Carrier diffusion in long wavelength InGaN quantum well LEDs after injection through V-defects", *Appl. Phys, Letters*, 125 (3) (2024).

R. Yapparov, T. Tak, **J. Ewing**, S. Nakamura, S.P. DenBaars, J.S. Speck, S. Marcinkevičius, "Properties of V-defect injectors in long wavelength GaN LEDs studied by near-field electro- and photoluminescence", *J. Appl. Phys.* 136, 083103 (2024).

A. Quevedo, F. Wu, T.Y. Tsai, **J. Ewing**, T. Tak, S. Gandrothula, S. Gee, X. Li, S. Nakamura, S.P. DenBaars, J.S. Speck, "Dislocation half-loop control for optimal V-defect density in GaN-based light emitting diodes", *Appl. Phys. Letters*, 125 (4) (2024).

L.K. Heki, Y. Mohtashami, R. Chao, **J. Ewing**, A. Quevedo, S. Nakamura, S.P. DenBaars, J.A. Schuller. "Optimizing Polarization Selective Unidirectional Photoluminescence from Phased-Array Metasurfaces." *Advanced Optical Materials*, 2303186 (2024).

Y.C. Chow, T. Tak, F. Wu, **J. Ewing**, S. Nakamura, S.P. DenBaars, Y.R. Wu, C. Weisbuch, and J.S. Speck. "Origins of the high-energy electroluminescence peaks in long-wavelength (~495–685 nm) InGaN light-emitting diodes." *Applied Physics Letters*, 123, no. 9 (2023).

C. Velez, S. Hwangbo, S. T. Chyczewski, **J. Ewing**, R. Bowrothu, C. S. Smith, Y. K. Yoon, D. P. Arnold, "Investigation of Ferromagnetic Resonance Shift in Screen-Printed Barium Ferrite/Samarium Cobalt Composites", *IEEE Transactions on Microwave Theory and Techniques,* 67, 8, 3230-3236 (2019)

T. Tak, A. Quevedo, F. Wu, S. Gandrothula, **J. Ewing**, S. Gee, S. Nakamura, S.P. DenBaars, J.S. Speck, "Planarization of p-GaN surfaces on MOCVD grown V-defect engineered GaN-based LEDs", *Appl. Phys. Letters*, 124 (17) (2024).

Y. Mohtashami, L.K. Heki, M.S. Wong, J.M. Smith, **J. Ewing**, W.J. Mitchell, S. Nakamura, S.P. DenBaars, and J.A. Schuller. "Metasurface Light-Emitting Diodes with Directional and Focused Emission." *Nano Letters*, 23, no. 22, 10505-10511 (2023).

T. Tak, A. Quevedo, F. Wu, S. Gandrothula, **J. Ewing**, S. Gee, S. Nakamura, S. P. DenBaars, J. S. Speck, "*Planarization of p-GaN surfaces on MOCVD grown V-defect engineered GaN-based LEDs*", Appl. Phys. Letters, 124, 17, (2024).

PRESENTATIONS

Photonics West 2023 San Francisco, CA
6.5% external quantum efficiency in V-defect engineered red InGaN LEDs
J. Ewing, C. Lynsky, F. Wu, M. Wong, M. Iza, J.S. Speck, S.P. DenBaars

Internation Conference in Nitride Semiconductors (ICNS) 2023 Fukuoka, Japan
Pure Edge Dislocation Half-Loops in Low Temperature GaN for V-defect Formation
J. Ewing, F. Wu, A. Quevedo, T. Tak, S. Nakamura, S.P. DenBaars, J.S. Speck

Photonics West 2024 (invited) San Francisco, CA
Recent advances in micron scale III-nitrides based RGB MicroLEDs
J. Ewing, M. Wong, J. Smith, P. Li, S. Nakamura, S.P. DenBaars

AWARDS

National Science Foundation Graduate Research Fellowship Program recipient (2019)

Best Student Award at ICNS, Fukuoka, Japan (2023)

Outstanding Graduate Research Achievement award, SSLEEC (2021 and 2022)

Summa Cum Laude at University of Florida (2019)

Highest distinction, Honors Certificate at Santa Fe College (2017)

Florida Bright Futures Scholarship recipient (2016)

ABSTRACT

V-defect Engineering for Long-Wavelength III-N Light Emitting Diodes

by

Jacob Ewing

The highly efficient blue InGaN-based light emitting diode (LED) has given rise to the solid-state lighting revolution, replacing its inefficient predecessors in home lighting, flashlights, displays, projectors, automotive lighting and much more. However, long-wavelength (green & red) InGaN-based LEDs have lagged in efficiency, often referred to as the 'green gap' in the LED industry. Addressing the green gap has become an increasingly important area of research for color-mixed home lighting and a wide range of display applications including AR and VR displays. Long-wavelength III-N LEDs have more non-radiative recombination and higher internal voltage barriers which hinder LED performance, especially the forward voltage and wall-plug efficiency (WPE).

In the last decade, LED researchers have discovered that strategic use of V-defects (or V-pits) can help address these issues by creating energetically favorable pathways for carrier (electron and hole) transport. This novel approach to LEDs, makes use of the anisotropic electrical properties in III-N crystals by using *c*-plane for epitaxial growth and light emission and the $\{10\bar{1}1\}$ plane (V-defect sidewall) for carrier transport. The lateral injection through the semipolar V-defect sidewalls reduces the polarization barriers and leads to reduced forward voltage and better WPE. In a few short years, V-defect approaches to green and red LEDs have been adopted by most major LED companies.

In this work, we study the structure and formation of V-defects in LEDs grown by metal-organic chemical vapor deposition (MOCVD). Through advanced microscopy we investigate how V-defect structure, formation and density evolve in III-N epitaxial growth on (111) Si and sapphire. We demonstrate novel ways of forming V-defects and generating the threading dislocations that lead to V-defect nucleation. We also studied extended defects in LED active regions, their impact on LED efficiency, and provide experimental evidence of lateral injection through V-defects. We achieved high external quantum efficiencies of 6.5% in red LEDs and 30% in green LEDs grown on PSS with V-defect engineering. Furthermore, we show low voltage operation (2.8 V at 20 A/cm^2) in green LEDs with V-defects. These results help provide a pathway to solving the green gap through V-defect engineering and advance the scientific understanding of V-defect formation and structure in III-N epitaxy.

TABLE OF CONTENTS

1

Introduction

The story of LEDs could go as far back as we want it too, from the early humans use of fire as an artificial light source, to the discovery of the periodic table of elements and all their unique properties, to Edison and the incandescent light bulb, to early work on semiconductors, doping, heterostructures, chemical vapor deposition, reactor design, electromagnetism, and all the complex physics, material science, chemistry, and systems engineering that have made the modern field of optoelectronics possible. But we must take some things for granted. And so, let's start with the discovery of Electroluminescence in 1907 by H. J. Round, an English engineer at Marconi Labs. In "A Note on Carborundum", Round observed "On applying a potential of 10 volts between two points on a crystal of carborundum, the crystal gave out a yellowish light" [1]. In 1927, Oleg Losev, a Russian inventor, created the first LED using SiC but it would be decades before LEDs found any practical use [2].

Here we can pause to explain a few of the most basic concepts of LEDs. Electroluminescence is a fancy word that describes the phenomenon of light being emitted (luminescence) in response to a flow of current or the application of voltage. Nowadays, we care tremendously about how efficiently that happens, but in the early days, scientists were just amazed that light could be generated from the application of electric current across a material: Electroluminescence. So that's the 'light emitting' part, but what about diodes? Diodes are (mostly) one-way channels for current. More specifically, diodes have high

electrical resistance in one direction and low electrical resistance in the other. The semiconductor diode is the most common diode in use today. Typically, semiconducting diodes consist of a crystalline piece of semiconducting material where one side of the material is p-doped (having excess holes) and the other n-doped (having excess electrons). When placed next to each other in a crystal the p-and n- type materials form a p-n junction, one of the key building blocks of all modern electronics. Unsurprisingly, a light emitting diode is a diode that's designed to be electroluminescent.

The key feature of a semiconductor is having a 'bandgap', a region within the electronic band structure where there aren't any available states for electrons. In an LED, the goal is to create a special p-n junction that localizes positive and negative charge carriers and encourages them to 'recombine' across the bandgap. The process of recombination is where an electron in the conduction band (higher energy states) will drop down to the valence band (lower energy states) filling an existing hole (the absence of an electron in the crystalline lattice). Since holes are quasi particles, physicists would simply say that the electron and hole are combining and annihilating one another. But because this process involves an electron moving from high energy to low energy it results in the release of energy. Where that energy goes is dependent on the exact process of recombination. It could be released as lattice vibrations (heat generation). It could also excite a different electron to jump up from the valence band to the conduction band (the Auger process), or it can be released as a photon (a light particle) with the same energy as the bandgap (the energy lost by the 'hot' electron during recombination). Obviously in the case of an LED we want photons to be generated, but inevitably the other processes will occur as well, generating some amount of inefficiency. In many LEDs the inefficiencies dominate, resulting in a poor LED. It's only through very careful engineering

that we can cause the radiative (light generating) recombination to dominate the device's behavior.

Because the emitted photon will be the same energy as the bandgap of the semiconductor, we can predict the wavelength (which is inversely proportional to the energy) based on the bandgap of the semiconductor. The lower the bandgap, the longer the emission wavelength will be. The wavelength determines if the photon will be an X-ray, ultraviolet, blue, green, yellow, red, infrared, microwave, a radio wave, etc. Furthermore, we can tune the emission of the LED simply by changing the bandgap. In binary compounds such as GaAs, InP, GaN, ZnSe, and InN, the bandgap is fixed by the material and electrical properties of the compound and the emission wavelength will also be fixed. But in ternary compounds such as $Al_xGa_{1-x}P$ or $In_xGa_{1-x}N$ the bandgap will be directly dependent on the relative fraction of the group III species. We'll return to this in a bit.

It's the mid-50's and the telecom boom is well underway. Semiconductors are drawing tons of interest from government and private research labs with a lot of work on compound semiconductors. Rubin Braunstein at the Radio Corporation of America (RCA) in Princeton, NJ, found that he could measure a spectrum of electromagnetic radiation from a variety of compound semiconductors including GaSb, GaAs, and InP. In his 1955 paper, Braunstein noticed that the spectral emission matched the predicted bandgap of the materials and concluded this must be direct recombination across the bandgap [3]. Early work on LEDs and related III-V and II-VI compound semiconductor work was happening at all the major telecom research labs including G.E. labs, RCA, IBM, Bell Labs, and Lincoln Labs at MIT, but it was Texas Instruments and the work of James Biard and Gary Pittman that claimed the first practical LED patent on the GaAs infrared LED [4]. By the 60's there was increasing interest

in an LED that could emit visible light. Nick Holonyak of G.E. demonstrated the first visible LED in GaAsP which emitted a dim red light [5]. GaAsP LEDs were the first commercial visible LEDs and found uses as indicator lights in calculators, lab equipment, TVs, radios, and watches [6].

Gallium Nitride (GaN) burst onto the scene in the early 70's with the first blue/violet LED demonstration at Stanford University in Palo, Alto. H. Maruska published a paper in 1973 where they grew GaN on sapphire followed by Mg-doped GaN [7]. Since unintentionally doped (UID) GaN is always slightly n-type, this structure formed a GaN p-n junction. Violet luminescence was observed at 10-20 V. But these devices were far too dim for any practical use and not much happened in the world of GaN LEDs until the early 90's. The big issues were bad epitaxial growth, very ineffective p-doping of GaN, and high n-type conductivity due to parasitic oxygen contamination. Shuji Nakamura was a young scientist working on metal-organic chemical vapor deposition (MOCVD) at Nichia Corporation. Nakamura made a couple of key discoveries that led to him to publishing the brightest blue LED at the time [8]. One of his key inventions was thermal annealing of p-type GaN which allowed H_2, a gas that's commonly used during growth, to diffuse out of the p-GaN [9]. It turns out that H_2 passivates the Mg making it ineffective as a dopant. This was a key breakthrough for early GaN LEDs. Nakamura was so pivotal to the development of the blue LED that it won him the 2014 Nobel Prize in Physics alongside Hiroshi Amano and Isamu Akasaki of Nagoya University who developed methods for growing high quality GaN on sapphire. Special thanks to Shuji Nakamura for his contributions to the solid-state lighting revolution and for serving on my PhD Committee.

At the same time that the early LEDs were being developed, Herbert Kroemer, who would later become a Nobel Prize winner and UCSB faculty, was developing the theoretical and experimental work behind the heterostructure and was the first to propose using double heterostructures in semiconducting lasers in 1963 [10]. A heterostructure is formed when two materials with different bandgaps are placed next to each other in a crystal. Typically done through growing epitaxially compliant materials in a molecular beam epitaxy (MBE), metal organic chemical vapor deposition (MOCVD), or a similar crystal growth technique. A double heterostructure is formed when one material (typically higher bandgap) is grown on either side of another material (typically lower bandgap) to form a 'sandwich'. If the middle material has a lower bandgap, the double heterostructure forms a quantum well in both the conduction band and valance band. Technically, an LED doesn't need quantum wells, it just needs carriers recombining across the bandgap and a supply of electrons and holes from n- and p-type layers. But all high-performance LEDs and laser diodes (LDs) use quantum wells in the p-n junction to better localize the carriers and promote radiative recombination. A well-designed quantum well can trap electrons and holes spatially in the crystal and dramatically increase the radiative recombination.

In visible III-N LEDs, this is accomplished by growing coherent $In_xGa_{1-x}N$ between layers of GaN or $Al_xGa_{1-x}N$ to form $In_xGa_{1-x}N$ quantum wells (QWs). The use of InGaN QWs was key to Shuji Nakamura's early blue LEDs and were a big improvement from the initial violet LED demonstration with was simply a p-n junction in GaN [11]. GaN has a bandgap of 3.4 eV which corresponds to 365 nm emission, the bottom of the visible spectrum. InN has a bandgap of 0.7 eV at room temperature which corresponds to 1.77 μm emission, near infrared (IR). $In_xGa_{1-x}N$ has a bandgap that ranges from 0.7 eV to 3.4 eV depending on the composition of In.

Theoretically, an InGaN QW in GaN could emit from the high end of the ultraviolet, through the entire visible range, and into near IR. Practically, there's a limit of what can be grown coherently (strained) to GaN. InN has a much larger in-plane lattice constant (a = 3.545 Å) compared to GaN's in-plane lattice constant (a = 3.189 Å) in the Wurzite hexagonal structure. This arises because In sits one row lower on the periodic table and thus has a much larger atomic radii. Practically speaking, there's a limit to how much In can be incorporated into an $In_xGa_{1-x}N$ film grown coherently to GaN. At some point if there's too much In, the crystal will become defective, or cease to grow epitaxially. The problem of lattice mismatch with InGaN compared to GaN turns out to be one of the key challenges of long-wavelength (500-700 nm III-N LEDs) and it plays a big role in the rest of this dissertation.

But why was the blue LED such a big deal? Why did it win a Nobel Prize whereas the red LED invented decades before, didn't? The truth is Nakamura, Amano, and Akasaki didn't just win the Nobel Prize because they were good LED growers but because their inventions enabled a revolution in how humans generated artificial lighting. This was the solid-state lighting revolution. As any decent physics student knows, white light doesn't have a specific wavelength. Blue is ~450 nm, green is ~520-540 nm, yellow ~570-590 nm, and red ~600-660 nm, depending on if you're talking about what is visibly red to the human eye vs what will get your journal article more visibility for your not-quite-red LED. But white light is a combination of all of them. One way to make white is to combine red, green, and blue LEDs. This is called a color-mixing approach. But the more common method is to use a blue LED and 'down-convert' some of the light to a lower energy (longer wavelength). This is typically done by adding a yellow phosphor coating to the blue LED. The blue light from the LED combined with the yellow light, which is caused from photoluminescence of the phosphor being optically

pumped by the blue LED, produces the white light that is now ubiquitous in solid-state lighting products across the globe. But the key point is that this only works if you start from the higher energy (blue) light. This can't go the other way. You can't take a red LED and convert some of the light to blue, because that would violate conservation of energy. And that's why the blue LED wins a Nobel Prize, and the red LED doesn't.

Unlike the late 20th century, the LED world of today is an incredibly mature field. Most of the important theoretical work has been done many times over. Blue LEDs operate with remarkable efficiencies often in excess of 80% [12], [13]. Blue LEDs are produced on a massive scale through multinational corporations, yellow phosphors are very effective, and the price of lighting has never been cheaper. In addition, the work on phosphide-based red LEDs has greatly matured since the early days. AlInGaP red LEDs grown lattice matched on GaAs substrates have reached very high efficiencies as well. However, phosphide LED efficiency falls off rapidly lower than 630 nm. Nitride LED efficiency falls off steadily as the wavelength increases for a variety of reasons including crystal quality, lattice strain, increased defect generation, piezoelectric polarization in the quantum wells, longer radiative lifetimes, and much more. Long-wavelength InGaN LEDs will be discussed in much more detail in Chapter 2. In short, green LEDs have always been much less efficient compared to blue III-N LEDs and red AlInGaP LEDs. This has been called the 'green gap' in the LED literature. For the purpose of most solid-state white LEDs the green gap isn't really a problem since blue LED/yellow phosphor-based approaches work just fine with WPE's dramatically higher than any incandescent or fluorescent light bulb could even dream of. Theoretically a color-mixed approach would be the most efficient way of creating a white LED if the red, green, and blue where all highly efficient. Although phosphor-based approaches are effective, they have some

inherent inefficiencies since some of the energy of the photons coming from the blue LED is inevitably lost in the process of converting blue light to yellow. But for most applications this is good enough. There is some renewed interest in color-mixed approaches due to increased awareness of the effects of the optical spectrum on human well-being. For instance, more blue light is better in the early parts of the day and a redder spectrum is optimal for later parts of the day. One advantage of the color-mixed approach is that the light bulbs can be easily color-tuned simply by adjusting the relative current going through the red, green, and blue pixels. The U.S. Department of Energy has set out initiatives to investigate and realize color-mixed lighting which has been a driving force for research into green III-N LEDs. In fact, DOE grant money aimed at color-mixed light was a significant funding source to the research that was carried out in this dissertation.

However, the biggest driving force for III-N LED efficiency at all wavelengths has always been the display industry. Displays have undergone many revolutions, just like home and industrial lighting. But because displays are increasingly mobile and run on batteries that can only store so much power, there's been incredible pressure from display manufacturers to make ever more efficient light sources to reduce the overall energy consumption of the display. In most consumer electronics the display ranks 2nd behind the CPU in overall power consumption. Displays have evolved from the early days of cathode ray tubes (CRTs) to liquid crystal displays (LCDs), to a wide variety of advanced technologies employed today. LCDs are a filtering method where white light is shown behind the screen and the liquid crystals selectively filter the light into blue, green, or red. The backlight for LCDs screens used to be a fluorescent bulb but quickly switched to LEDs once they became sufficiently cheap and efficient. But filtering processes are inherently inefficient and it's incredibly difficult to

produce true black. Enter self-emissive displays. The concept of a self-emissive display is that rather than using a red, green, and blue filter for white light, you have a red, green, and blue pixel which are controlled separately and can be modulated separately to produce any desired color. The big benefits are cutting out the inefficiencies inherent in filtering methods and the realization of true black which makes the screen look so much better to the eye. The biggest success in the world of self-emissive displays has been the organic LED (OLED) display. OLED displays have taken over the world of TVs, smartphone displays, laptop displays, and much more. They've had their issues such as poor efficiency, low brightness, and poor lifetimes but these keep getting better year over year. OLED is here to stay and it's and success often makes me consider switching fields. Quantum dot LED (QLED) displays are also a relative newcomer and combine some of the self-emissive processes with a filtering process. QD light conversion is similar in concept to the LCD, but most QLED architectures also allow for pixels to turned on and off individually which gives them many of the same advantages of OLED.

In the world of III-N LEDs the big driver of efficiency research has been interest in using inorganic LEDs, either just nitride or nitride + phosphide LEDs combined, to create a self-emissive display. To get high resolution one would need small pixels so the LED size would have to decrease substantially compared to 'standard size' LEDs which typically have an area of 0.1 mm^2. And thus, the microLED (µLED) is born. Theoretically, from the standpoint of efficiency, brightness, lifetime, and color gamut, the inorganic µLED is the best option available to the display industry. However, as of 2024 you won't find a single µLED TV on the shelves of Costco whereas you'll see plenty of OLED and QLED TVs. So far, the Achillies heal of µLED has been assembly, although things like size-dependent efficiency and

the green gap have also been significant barriers. Because compound semiconductor LEDs are grown on single crystal wafers in massive reactors and blue, green, and red must be grown and processed separately, the cost-effective manufacturing of μLED displays has yet to be realized. But that hasn't stopped hundreds of millions of dollars of research funding from being poured into the μLEDs and long-wavelength III-N LEDs. That's where the other half of the funding for this PhD came from. From a manufacturing perspective, it would be a lot simpler for all μLEDs to be made from the same material system, which would have to be III-N's. Thus, a tremendous amount of effort has also been poured into researching red III-N as well as green. Chapter 4 will focus on red μLED development.

But regardless of whether red and green III-N LEDs will ever see large scale adoption in any meaningful technology, there's a lot of very interesting engineering, physics, and material science involved in addressing the green gap, growing better LEDs with MOCVD, and in making LEDs on the micron scale. It's these challenges and the promise of scientific and engineering solutions that motivate a PhD researcher to do his work everyday and make advancements and discoveries in the lab. The field of V-defect (or V-pit) engineered LEDs is a prime example. GaN, for all its marvelous materials properties, has some strange properties to boot. For instance, it has a highly anisotropic polarization in the crystal. Each plane of GaN sees very different built-in polarization and that has major implications for building electronic devices in GaN. Essentially, a polarization field will be reflected in the electronic band structure as a sloped band and results in a net electric field inside the quantum wells. Furthermore, because the InGaN QWs grow strained to the GaN, a piezoelectric field (polarization in response to strain) is also created. This can have some positive effects on the emission properties. For instance, it will allow longer wavelength emission at relatively less In

which can make the growth a bit easier. But it has other negative externalities such as increased barriers to electron and hole injection, electron and hole wavefunction separation, and in a laser structure the gain will be reduced.

Because of the many polarization-related problems, the last few decades of GaN research have seen a lot of interest in growth on semipolar planes. This requires bulk GaN substrates because sapphire is only useful to grow *c*-plane GaN which adds cost. In laser diodes the semipolar work has been somewhat successful with a variety of companies opting for semipolar-based designs due to the increased gain. But in the world of LEDs, the semipolar revolution mostly hasn't happened and slowly everyone has returned to *c*-plane. The big problems with semipolar turned out to be cost of substrates, generation of complex extended defects, and high impurity uptake. In short, semipolar LEDs were less bright and more expensive and so industry and research institutions have returned to developing LEDs on *c*-plane. But there's an interesting twist in the semipolar story and that's the V-defect or V-pit. V-defects are naturally occurring defects (or pits) that occur in *c*-plane LEDs. They look like inverted hexagonal pyramids and typically will nucleate off existing defects in the material. But in theory, they can nucleate off any perturbations in the step-flow crystal growth. For years, V-defects were thought to be unwanted defects and were systematically removed from LED structures as much as possible. But the story doesn't end there.

The interesting thing about V-pits is they have semipolar sidewalls and once opened, the semipolar sidewalls grow their own epi structure but with very different properties compared to *c*-plane. First of all, the semipolar planes already have much lower polarization which has benefits in enabling carrier transport. In addition, the semipolar planes uptake significantly less In and Ga leading to thinner QWs, thinner quantum barriers (QBs), and less

piezoelectric polarization [14]. These factors also lead to less discontinuities at the heterointerfaces. In short, the V-pits become the path of least resistance for holes coming from the p-GaN and electrons coming from the n-GaN [15]. And because the V-defects extend down into the multi-quantum well (MQW) structure, they also provide spatially shorter pathways into the QWs. This makes the V-pits superhighways for carriers and importantly it allows the carriers to reach the QWs at much lower forward voltage (V_F) than they otherwise would, especially in green and red III-N LEDs. In theory, a red or green LED should operate at a lower voltage than a blue LED. The photon being emitted is less energetic and it should take less energy to make them. In fact, a marker of a good LED is how close it operates to the photon voltage (essentially the bandgap divided by the elemental charge). For blue at 450 nm the photon voltage is 2.75 V, for green at 520 nm its 2.4 V and for red at 620 nm it's 2 V. But for years, LEDs didn't follow these voltage trends because the long wavelengths had all these other issues with high piezoelectric effects and significant voltage barriers at the heterointerfaces. Only in the last 5 years, with the careful inclusion of V-pits in LEDs, have the voltages started to reflect the theoretical trends where blue operates at the highest voltage followed by green and red [16], [17].

This dissertation is a study of V-defects. It's an attempt to understand their structure, formation, and properties at a depth that most researchers and commercial manufacturers have yet to reach. It uses MOCVD, device processing, advanced characterization, transmission electron microscopy (TEM), and a bit of theory to better understand V-defects. It also has an engineering component. We're not just concerned about what V-defects are and what they look like but how can we manipulate the structure to realize better LED performance. And

importantly, how can we use our understanding of V-pits to design LEDs with better lateral carrier injection.

This concludes the semi-technical introduction. Hopefully this gives a broad overview of the research, its setting in the bigger field of LEDs and optoelectronics, as well as some of the motivations for doing this research in the first place. Chapter 2 is the technical background. Here I'll dive into the math and science of LEDs, defects, growth and processing. Laying the foundation for Chapters 3-6 which will present the findings of my PhD.

References:

[1] H. J. ROUND, “A Note on Carborundum,” in *Semiconductor Devices: Pioneering Papers*, WORLD SCIENTIFIC, 1991, pp. 879–879.

[2] O. V. Losev, “Luminous carborundum [silicon carbide] detector and detection with crystals,” *Telegr. i Telef. bez Provodov*, vol. 44, pp. 485–494, 1927.

[3] R. Braunstein, “Radiative Transitions in Semiconductors,” *Phys. Rev.*, vol. 99, no. 6, pp. 1892–1893, Sep. 1955, doi: 10.1103/PhysRev.99.1892.

[4] W. T. Matzen, “Semiconductor Single-Crystal Circuit Development,” Mar. 1963. doi: 10.21236/AD0411614.

[5] N. Holonyak and S. F. Bevacqua, “COHERENT (VISIBLE) LIGHT EMISSION FROM Ga(As1− x P x) JUNCTIONS,” *Appl. Phys. Lett.*, vol. 1, no. 4, pp. 82–83, Dec. 1962, doi: 10.1063/1.1753706.

[6] F. E. Schubert, *Light Emitting Diodes*. Cambridge University Press, 2003.

[7] H. P. Maruska, D. A. Stevenson, and J. I. Pankove, “Violet luminescence of Mg-doped GaN,” *Appl. Phys. Lett.*, vol. 22, no. 6, pp. 303–305, 1973, doi: 10.1063/1.1654648.

[8] S. Nakamura, T. M. Takashi Mukai, and M. S. Masayuki Senoh, “High-Power GaN P-N Junction Blue-Light-Emitting Diodes,” *Jpn. J. Appl. Phys.*, vol. 30, no. 12A, p. L1998, Dec. 1991, doi: 10.1143/JJAP.30.L1998.

[9] S. Nakamura, T. Mukai, M. Senoh, and N. Iwasa, “Thermal annealing effects on P-type Mg-doped GaN films,” *Jpn. J. Appl. Phys.*, vol. 31, no. 2, pp. 139–142, 1992, doi: 10.1143/JJAP.31.L139.

[10] H. Kroemer, “A Proposed Class of Heterojunction Injection Lasers,” *Proc. IEEE*, 1963.

[11] S. Nakamura, T. Mukai, and M. Senoh, “Candela - class high - brightness InGaN / AlGaN double - heterostructure blue - light - emitting diodes Candela-class high-brightness InGaN / AIGaN,” vol. 1687, no. 1994, pp. 7–10, 1996.

[12] C. A. Hurni *et al.*, “Bulk GaN flip-chip violet light-emitting diodes with optimized efficiency for high-power operation,” *Appl. Phys. Lett.*, vol. 106, no. 3, 2015, doi: 10.1063/1.4905873.

[13] L. Y. Kuritzky *et al.*, “High wall-plug efficiency blue III-nitride LEDs designed for low current density operation,” *Opt. Express*, vol. 25, no. 24, p. 30696, Nov. 2017, doi: 10.1364/oe.25.030696.

[14] F. Wu *et al.*, “Structure of V-defects in long wavelength GaN-based light emitting diodes,” *J. Appl. Phys.*, vol. 035703, no. 133, 2023, doi: 10.1063/5.0135278.

[15] Z. Quan, L. Wang, C. Zheng, J. Liu, and F. Jiang, “Roles of V-shaped pits on the improvement of quantum efficiency in InGaN/GaN multiple quantum well light-emitting diodes,” *J. Appl. Phys.*, vol. 116, no. 18, Nov. 2014, doi: 10.1063/1.4901828.

[16] F. Jiang *et al.*, “Efficient InGaN-based yellow-light-emitting diodes,” *Photonics Res.*, vol. 7, no. 2, pp. 144–148, 2019.

[17] S. Zhang *et al.*, “Efficient emission of InGaN-based light-emitting diodes: toward orange and red,” *Photonics Res.*, vol. 8, no. 11, p. 1671, 2020, doi: 10.1364/prj.402555.

2

Background

2.1 Material Science of Hexagonal Crystals

Material science is the study of the structure, properties, processing, and performance of materials and using advanced characterization techniques to understand their interrelations. This is a dissertation in Materials, specifically III-N compound semiconductor materials. Therefore, we'll start with material science. Materials are composed of atoms. One of the fundamental aspects of material science is understanding how atoms arrange themselves to form crystals. In crystallography we typically simplify atoms as balls that can have a variety of different stacking sequences. Based on how tightly they atoms are packed we can define the atomic packing factor.

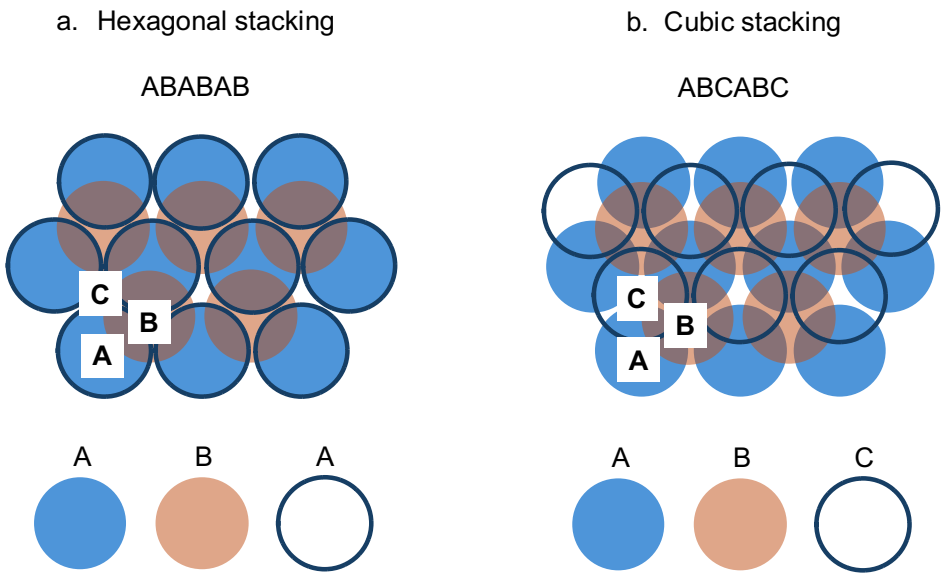

Figure 2.1: a) Hexagonal close-packed stacting (HCP) b) Cubic close-packed stacking (FCC)

It turns out that the face centered cubic and hexagonal crystal structures have the same atomic packing factor of 0.74 and are collectively called close-packed crystal structures. The differences between the two close-packed structures are illustrated in Figure 2.1. After the first stacking layer A, there are two equivalent sites where the next layer can stack while remaining close-packed. These are represented with white boxes B and C in the figure. In HCP stacking the next layer goes on B and then reverts to A in the next layer. In FCC stacking the second layer goes on the B site and the third layer stacks on the C site before reverting to A and starting the stacking sequence over again.

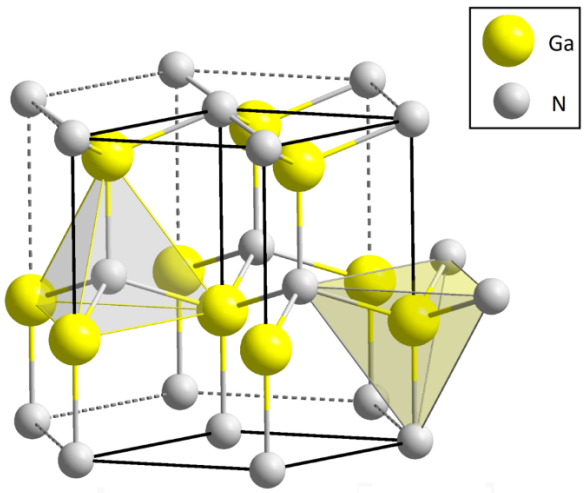

Figure 2.2: Wurzite crystal structure for GaN. Gallium is shown in yellow, nitrogen in grey. In the case of AlGaN and InGaN some fraction of the yellow atoms would be substitued for the Al or In.

GaN, and the rest of the III-N material system, can form either cubic or hexagonal crystal structures. But in almost all growth of (AlInGa)N for LEDs it will take a hexagonal wurzite structure which is pictured in Figure 2.2. Cubic (AlInGa)N forms a zinc blende structure, but this is less thermodynamically stable and is very rarely used. Pure AlN or InN also will take the wurzite structure as well as all the respective III-N alloys. Each group III atom in the wurzite structure is tetrahedrally coordinated. Both the group III and group V elements in the wurzite form sublattices which are HCP-type. The space group for all wurzite structures is $P6_3mc$ in Hermann-Mauguin notation. The 6_3 means it has a six-fold screw rotation about the c-axis. Since the c-axis (normal to *c*-plane) is the typical growth direction this is very relevant for GaN LEDs. It means that when grown on *c*-plane the properties in the lateral directions are equivalent with six-fold symmetry. The m in $P6_3mc$ means there's a mirror plane which is normal to {100} what we call the *a*-directions. The c means there's a

glide plane in the c-directions with normal {120}. In other words, glide can occur along m-planes in the c-direction.

Importantly, wurtzite lacks inversion symmetry making it non-centrosymmetric. This results in wurzite crystals having piezoelectricity which does not occur in centrosymmetric crystals. The polarization in GaN can be subdivided into the spontaneous electrical polarization $\mathbf{P}^{sp}$ and the strain-induced piezoelectric polarization $\mathbf{P}^{pz}$. In an unstrained homoepitaxial layer the only polarization present is the $\mathbf{P}^{sp}$ component, but as we'll see in the section on III-N epitaxy, in most LED structures, InGaN or AlGaN layers grow strained to GaN layers and thus the piezoelectric component $\mathbf{P}^{pz}$ is also highly relevant. The total polarization in a III-N layer can be found by combining the two polarizations as is shown in Equation 2.1.

$$\boldsymbol{P}^{total} = \boldsymbol{P}^{sp} + \boldsymbol{P}^{pz} \qquad \text{(Eq. 2.1)}$$

$\mathbf{P}^{sp}$ and $\mathbf{P}^{pz}$ can be further defined for the different materials (GaN, InN, AlN) and their respective alloys. This is described in detail in Refs [1]–[3]. For the purposes of this dissertation the important points are that the spontaneous polarization is different for each crystallographic planes with some symmetries (e.g. 6-fold symmetry around the c-axis) and the piezoelectric polarization is dependent on crystallographic strain. In epitaxy that arises when epitaxial layers are grown strained to the substrate beneath. This occurs when their relative lattice constants are slightly different but not so different to disrupt the epitaxy. This will be discussed in detail in the next section. Importantly, the spontaneous polarization of the planes in GaN is different depending on which plane we measure. *c*-plane is the most polar, *m*-plane and *a*-plane are non-polar. All other planes are semipolar (having a polarization somewhere between *m*- and *c*-plane.

Although epitaxially grown materials are considered to be single crystals, no crystal is ever 100% perfect. They always contain defects, whose type and structure are very important in understanding the properties and performance of optoelectronic crystals. Crystallographic defects can be divided into point defects, linear defects (called dislocations), and planar defects such as grain boundaries, antiphase boundaries, or stacking faults. In III-N epitaxy point defects, dislocations, and stacking faults all occur readily and can have a big impact on LED performance. There are also three-dimensional defects such as pores, cracks, voids, and precipitates. The V-defect would fall into the category of a 3D defect but for now we'll focus on the simpler defects in GaN.

Point defects are the simplest defects. They occur at only one lattice point and have no extended dimensions in space. Typically, point defects are considered to be no more than a few extra or missing atoms in the lattice. Vacancy defects (or Schottky defects) are where a single atom or sometimes an ionic pair is missing from the lattice. Ga vacancies or N vacancies are both observed in GaN growth and can add energy states inside the bandgap, deep levels or traps [4]–[6]. Most defects or dislocations can add parasitic energy levels which is generally not good for LED performance since it adds recombination pathways other than direct electron-hole recombination across the bandgap at the desired wavelength. For instance, under photoluminescence GaN is known to give off a yellowish light which has been attributed to the existence of Ga vacancies or C interstitials [7], [8]. Impurities can incorporate as interstitials or substituting on a Ga or N site. They can become donors or acceptors but in either case tend to have a negative effect on radiative recombination and should be eliminated in the growth processes as much as possible [9], [10].

When a defect is extended linearly through a crystal it becomes a dislocation. Dislocations are abrupt irregularities in the crystal where the atomic arrangement is displaced. The Burgers vector is often used to indicate the direction of displacement that the atoms undergo at the dislocation. If we know the Burgers vector of a dislocation, we know its character and something about how it will move. In a primary dislocation, the atomic order is displaced by a full lattice translation and the crystalline order is restored on the other side. In a partial dislocation the displacement is less than a full lattice translation and the crystalline order isn't restored. Primary dislocations can be further divided based on their mobility. A sessile dislocation is immobile whereas a glissile dislocation can glide along the glide planes in a crystal structure. A stair-rod dislocation is an example of sessile dislocation. Edge and screw dislocations (pictured in Figure 2.3) are examples of glissile dislocations.

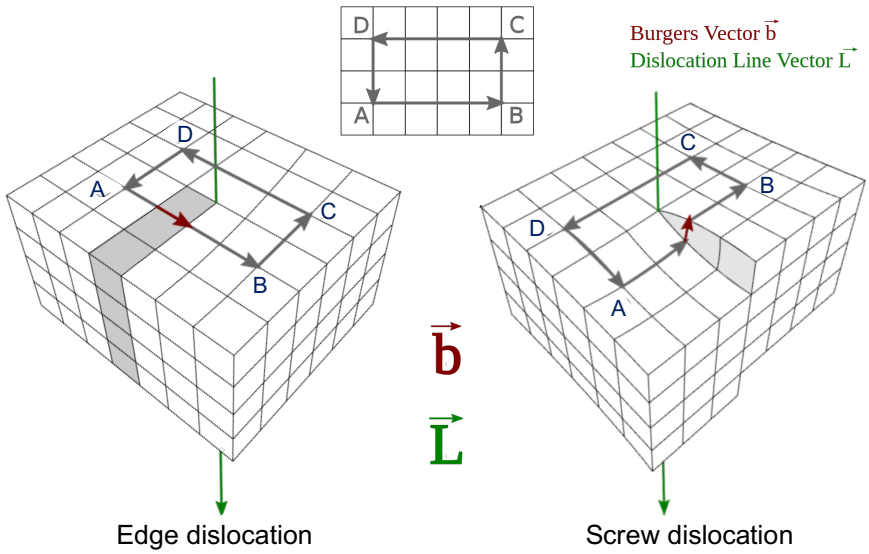

Figure 2.3: An edge dislocation (left) and screw dislocation (left) and their respective Burgers vectors. The Burgers vector can be determined by drawing a loop around the dislocation as illustrated in the figure. The extra vector needed to complete the loop is the Burgers vector and indicates the displacement associated with the dislocation. A mixed dislocation is a combination of the two. In GaN, when the dislocation line vector **L** is along the c-direction these are called edge threading dislocations (TDs), screw TDs, and mixed TDs.

A key feature of dislocations is that they can never terminate inside a crystal. They have to end either in another dislocation or at the edge of a crystal. In III-N epitaxial growth, most dislocations will bend such that their dislocation line becomes approximately normal with the growth surface. In the case of GaN epitaxy that means the dislocation line is parallel to the *c*-axis. As the crystal grows epitaxially the dislocation also continues to grow such that it always terminates at the surface. These extended line defects that grow normal to the growth surface are called threading dislocations. GaN has a very high density of threading dislocations compared to other III-V optoelectronic materials. Threading dislocations can be edge-type, screw-type, or mixed (a combination of edge and screw). In GaN, edge type TDs will have a Burgers vector parallel to the growth surface in the a-direction, screw type TDs have a Burgers vector in the c-direction, and mixed TDs have (a+c) Burgers vectors. When a threading dislocation meets the surface, it will create a small surface depression associated with the line tension of the dislocation [11]. This can be observed in epitaxial growth and can also nucleate larger 3D defects under specific growth conditions. It's also possible for threading dislocations to form loops that are fully enclosed in the crystal or half-loops where both ends terminate at the edge of the crystal.

Stacking faults are planar defects that often occur during epitaxy. In ideal step-flow growth each layer stacks perfectly on top of the previous one but if the step terrace width becomes too large or growth conditions don't allow sufficient surface mobility, the growth mode can switch locally to layer-by-layer or island growth. Under these conditions it's easy for the stacking sequence to be disrupted, forming a stacking fault. As discussed earlier in this section, GaN is hexagonal which means the stacking sequence is ABABAB in the [0001]

direction. There are two main categories of stacking faults (SFs), basal plane stacking faults (BPSFs) and prismatic SFs. There are 4 types of BPSFs that can occur in GaN, typically called I_1, I_2, I_3 and extrinsic and they all have different energies associated with them [12]. I_1 is the simplest stacking fault and the most common because it's the lowest energy. I_1 occurs due to growth errors and are the result of the removal of a single basal plane in the crystal. To avoid AA or BB stacking, which is very unfavorable energetically, I_1's are accompanied by a shear of $\frac{1}{3}\langle 1\bar{1}00\rangle$ to form …ABABCBCB. From the earlier discussion we know that ABC is cubic close packed stacking. So an I_1 can also be thought of as a layer of cubic included in an HCP lattice. Because the shear is less than a lattice translation, I_1 BPSFs are bounded by sessile Frank-Shockley partial dislocations. I_1 only have one stacking violation which makes them the lowest energy BPSFs [13].

Type-II BPSFs (I_2) have two stacking violations and follow the stacking sequence ABABCACAC. They also have a cubic inclusion and have a different stacking sequence on the other side of the fault. I_2's can also form due to growth errors or from the dissociation of a perfect dislocation into partials. I_3 occurs if the A or B layer occupies the C position such as ABACAB. These have the second lowest formation energy but aren't generally observed in GaN. Finally, extrinsic (E-type) BPSFs have an additional C layer inserted to form ABCABAB stacking. E-type has 3 stacking violations and is thus the highest energy BPSF. It is rarely observed.

Dislocation generation and evolution is a vast topic in III-N epitaxy and has many implications for LED performance. In the next section we'll take a closer look at III-N epitaxy and how growth processes affect material quality and device performance.

2.2 Epitaxy of III-N Materials

Epitaxy is the process of single crystal material growth where new layers are formed on a crystalline seed layer. The new layers have a well-defined orientation with respect to the seed crystal. Optoelectronic crystals generally need to be single crystalline with many distinct layers serving different purposes in the device. Epitaxy is generally the method of choice. Epitaxy can be subdivided into homoepitaxy and heteroepitaxy. In homoepitaxy the substrate and the film are that same material whereas in heteroepitaxy refers to growing one material on a different seed material. Even in the case of heteroepitaxy the two materials generally need to be similar in terms of crystal structure and lattice constant. Otherwise, achieving epitaxial growth is difficult although there are some tricks that can be played to widen the possibilities for epitaxial growth.

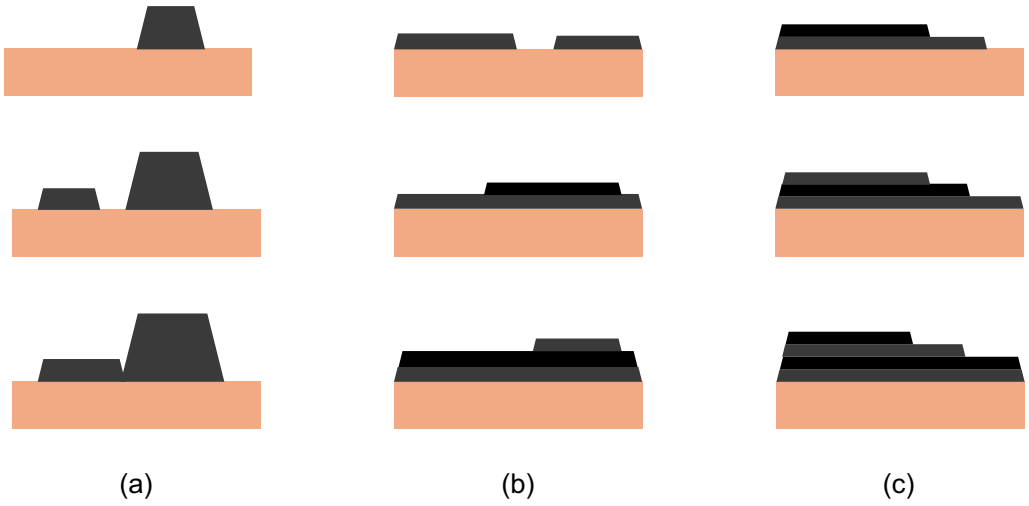

Figure 2.4: (a) Volmer-Weber (island) growth (b) Frank-van der Merve (layer-by-layer) growth (c) step-flow growth

Figure 2.4 shows several different growth modes that are possible during epitaxy. Vomer-Weber or island growth occurs when the material being grown forms small nucleates

that turn into islands and then grow and coalesce (merge). This is shown in Figure 2.4c. Island growth is common for heteroepitaxy of dissimilar materials. When GaN is grown on sapphire, the early growth is typically island growth and coalescence. The coalescence boundaries often form dislocations. When lines of mostly pure edge threading dislocations occur in GaN, this is usually indicative of island coalescence boundaries from Volmer-Weber growth. Frank-van der Merwe growth is layer-by-layer growth (Figure 2.4b). Here a single atomic layer will form until it completely covers the surface, followed by another layer and then another. Stranski-Krastanov growth is the combination of island and layer-by-layer growth.

A special kind of Frank-van der Merwe growth is called step-flow growth which is pictured in Figure 2.5. This occurs when the layers are arranged in steps. As the epitaxial layers are deposited the steps grow and 'flow' over each other. Step-flow growth is generally the most desired type of growth in epitaxy since it produces the fewest defects and maintains the best crystal quality. To encourage step-flow growth, the bulk seed crystals are typically 'miscut' at some angle such that the seed already has a step-terrace structure. Sapphire (the most common substrate for GaN epitaxy) is usually miscut 0.2° along a-direction (which corresponds to m-direction of GaN). While it's most common to have a very slight miscut, there are examples of heteroepitaxy where the miscut can be very large. For instance, AlInGaP red LEDs are grown on GaAs substrates with a 14° miscut. The miscut is determined by the lattice constants and growth planes of the substrate and material being grown. The terrace width is determined by the miscut and is important to promote good step-flow growth. If the terrace width gets too wide, local layer-by-layer (non-step-flow) or island growth may occur. Generally, any disruption in step-flow growth will favor defect formation.

Figure 2.5 shows a detailed schematic of step-flow growth. Adatoms are free atoms on the surface of the crystal that haven't yet been incorporated at a step. Adatoms can deposit and desorb or diffuse across the surface. In effective step-flow growth the terrace widths are short enough that adatoms can deposit and quickly diffuse to the step, be incorporated, and the process continues. If the terrace width becomes too large, the adatoms may not diffuse to the step edges and local island growth can occur.

Where threading dislocations meet the crystal surface there may be some disruption to the terrace structure. As illustrated in Figure 2.5, step edge pinning can occur causing the terrace width to be larger or smaller than in the rest of the step-terrace structure. Because of step edge pinning and the fact that threads can be accompanied by local surface depressions, threading dislocations often become nucleation sites for larger, 3-dimensional defect formation. If the terrace width shrinks to zero, the result is a larger step that's two monolayers rather than one.

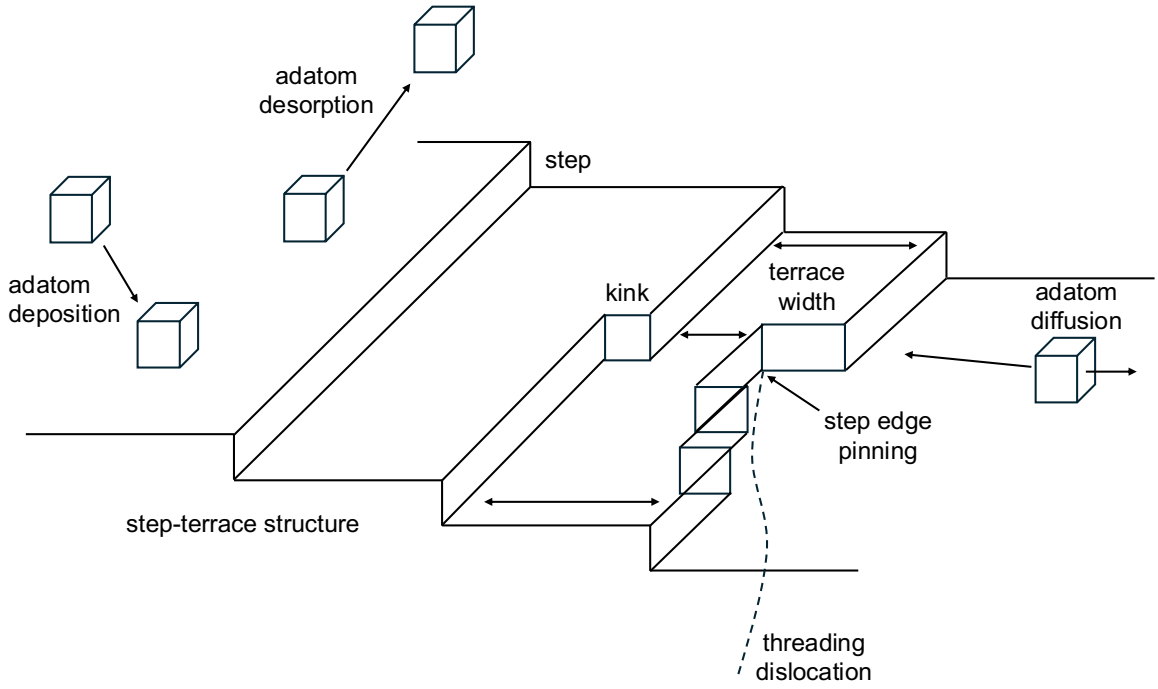

Figure 2.5: Step-flow growth on a miscut substrate. This figure illustrates how adatoms move on terraces, how terrace width may vary across the sample, and how a threading dislocation may cause step edge pinning.

Every crystalline solid has a preferred lattice constant that allows the electronic attractions and repulsions to balance. The larger the atoms in the crystal, the larger the lattice constant. Lattice constants also change with temperature. In the III-N material system AlN, GaN, and InN all have different lattice constants since the group III elements all have different atomic weights and sizes. In wurzite, there's a c-lattice constant (the height of the unit cell) and the a-lattice constant, which is in the growth plane. For the purposes of epitaxy, the in-plane lattice constant is the most important since that's where atoms must align to the sites beneath it in the crystal. The *a* lattice constants for AlN, GaN, and InN are 3.112 Å, 3.189 Å, and 3.545 Å, respectively. The lattice parameters of $In_xGa_{1-x}N$ and $Al_yGa_{1-y}N$ alloys are weighted averages of the lattice constants of their constituent binary compounds, following Vegard's law [14].

$$a_{InGaN} = x \cdot a_{InN} + (1 - x) \cdot a_{GaN} \quad \text{(Eq. 2.2)}$$

$$a_{AlGaN} = y \cdot a_{AlN} + (1 - y) \cdot a_{GaN} \quad \text{(Eq. 2.3)}$$

When a material is grown epitaxially on a substrate with the same lattice constant the atoms have no issue aligning themselves with the layer below it. If every atom in an epitaxial layer aligns to the layer below it, we say the growth is coherent. When some amount of lattice mismatch is present during heteroepitaxy the epitaxial layer has to strain to grow coherently.

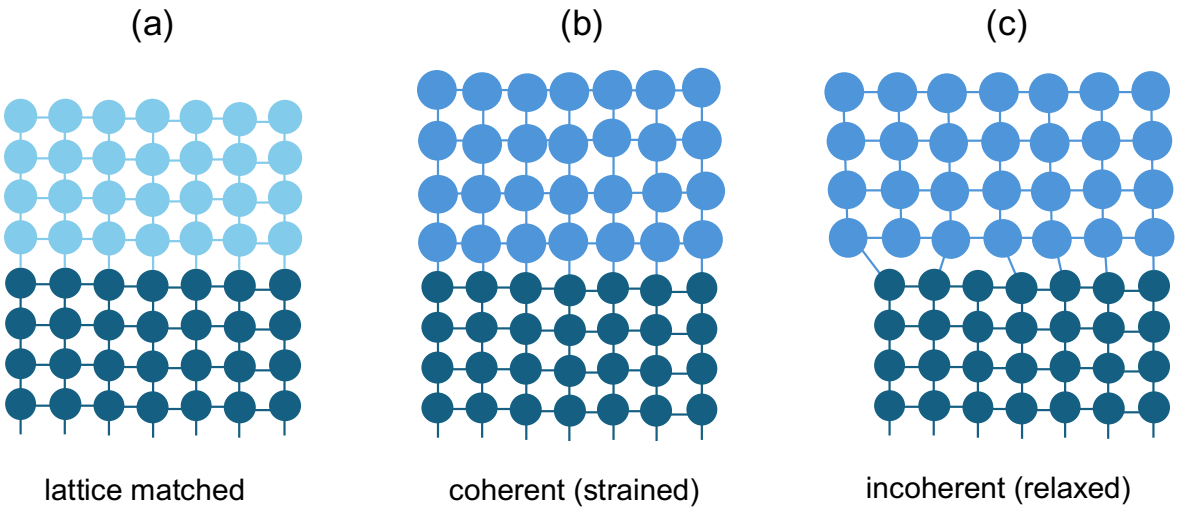

Figure 2.6: Different types of epitaxial crystal growth. (a) Lattice matched growth where the lattice constants of the two materials are equal. This will grow unstrained. (b) Coherent growth with a lattice mismatch. The top material will be strained. (c) incoherent growth, both materials will be relaxed but defects are generated at the interface.

Figure 2.6 illustrates the different ways that heteroepitaxy can occur. If there's no lattice mismatch between the two materials, then they grow coherently and without strain (Fig 2.6a). If there is a lattice mismatch the materials may still grow coherently but the top material will be strained (Fig 2.6b). This means that the in-plane lattice constant stays the same and the top material will stretch in the z-direction to compensate. If the lattice mismatch is too large incoherent growth can occur and the top material will relax (Fig 2.6c). Incoherent growth will

result in the generation of defects at the interface. If two materials with a lattice mismatch grow strained to one another there's a certain critical thickness below which they can maintain a perfect crystal. Above the critical thickness the strain will become so large that it will cause the top material to crack (if it's under tension). As mentioned previously, III-N materials are piezoelectric so when an InGaN layer grows strained to GaN there's an electric field in the crystal that is generated. This causes the conduction and valence bands to slope in the strained material and has major implications on the electrical properties and emission wavelength of an LED structure.

GaN can be grown on both bulk GaN and foreign substrates. Bulk GaN growth provides the lowest dislocation density and it's possible to grow on non-polar and semipolar planes with bulk GaN substrates. However, bulk GaN crystal growth is difficult and low volume so the substrates are incredibly expensive. For this reason, the majority of LEDs are grown on either sapphire or (111) Si. When choosing a foreign substrate for growth, it's important to find a material that has a similar lattice parameter and crystal structure. For commercial purposes it's also important that the substrate material is inexpensive and easily available. Sapphire has a hexagonal crystal structure as is shown in Figure 2.7a. Sapphire has an a-plane lattice of 4.758 Å which is a 33% lattice mismatch. This would seem to be impossibly large for achieving epitaxy, but the trick is that when GaN grows on sapphire, the crystal rotates 30° compared to the substrate such that a-plane GaN aligns with m-plane sapphire.

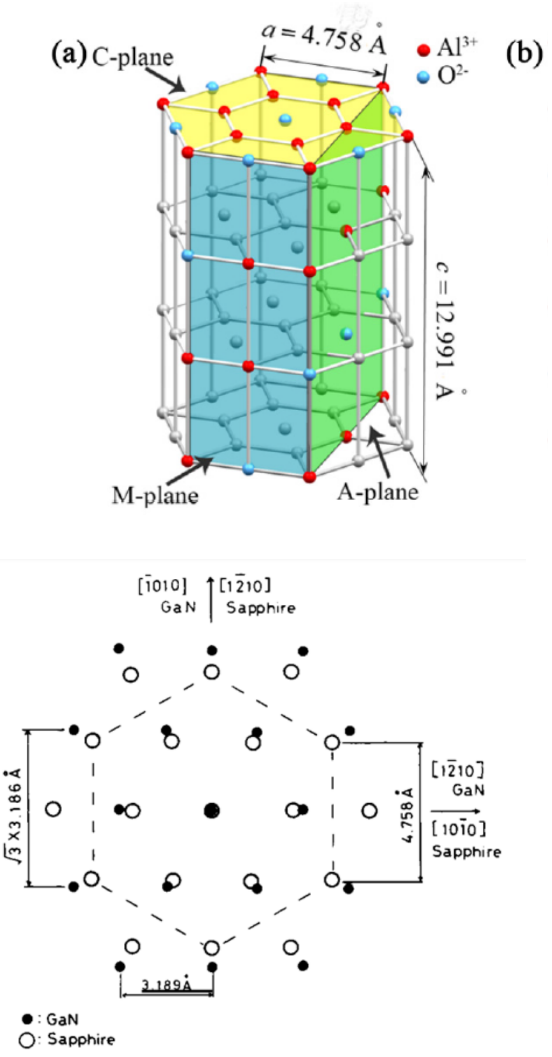

Figure 2.7: (a) The hexagonal crystal structure of sapphire (b) diagram of a GaN crystal (black dots) aligned to a sapphire crystal (open circles) showing how the two crystals align themselves during heteroepitaxial growth. Images from Refs [15] and [16].

Figure 2.7b shows a schematic of a GaN crystal aligned to a sapphire substrate crystal. The distance between two lattice points along an a-plane in GaN is $\sqrt{3} \cdot 3.186\ \text{Å} = 5.524\ \text{Å}$. This aligns with the m-planes of sapphire which have the same length as the a-lattice constant of sapphire, 4.758 Å. With this configuration the lattice mismatch is reduced to 13.8% which is much easier for compliant growth. Still, with this large of a mismatch, the early GaN growth

on sapphire is a fairly defect-ridden process involving both cubic and hexagonal GaN, GaN islands, and island coalescence [17].

Getting GaN to form at all on sapphire is a difficult process. The standard method is to use a very low temperature growth conditions (~ 500 – 600 °C) to generate small GaN nucleates which may be (111) oriented cubic or (0001) oriented hexagonal GaN. Once there is some initial GaN on the sapphire the temperature is ramped to above 1000 °C and the growth rate is increased to 50-100 nm/min. The high temperature favors hexagonal GaN, which is more thermodyanically stable compared to cubic GaN. The hexagonal GaN islands undergo rapid island growth and coalescence. It's common to grow several microns of GaN to improve the crystal quality as much as possible. But GaN on sapphire always has a high density of threading dislocations (TDs). Typical TD densities (TDDs) are 10^7 cm^{-2} - 10^9 cm^{-2} depending on if the sapphire is patterned or flat. Typically patterned sapphire will have a lower TDD. TD formation may occur during the HT island growth where predominantly mixed TDs will form. But most of the TD formation occurs at island coalescence boundaries where mostly pure edge TDs are formed along with a few mixed TDs [17]. This is illustrated in Figure 2.8.

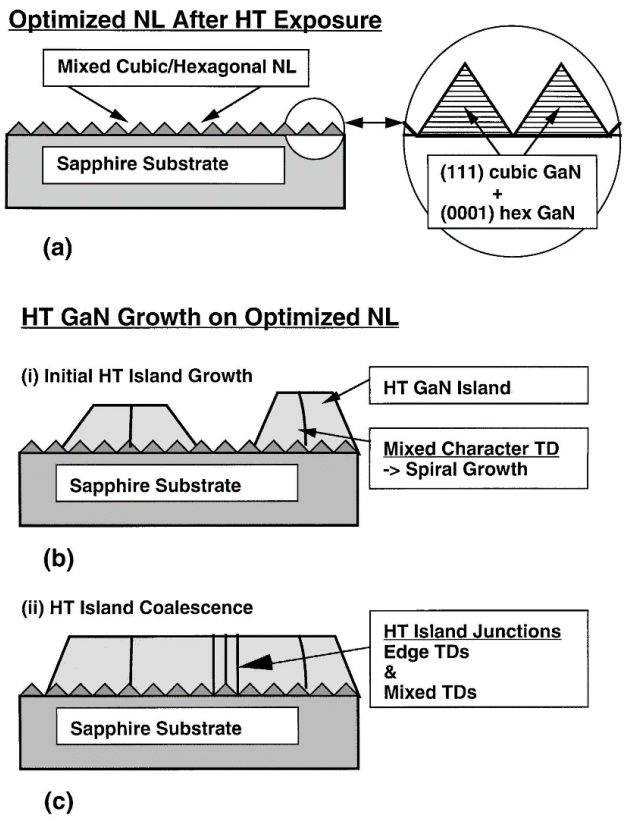

Figure 2.8: (a) Early nucleation on sapphire is a mix of (111) oriented cubic GaN and (0001) oriented hexagonal GaN. This is usually done at very low temperatures ~ 500 – 600 °C. (b) After island formation high temperature (HT) GaN is grown. Hexagonal GaN is more stable at high temperatures so HT island growth favors hexagonal GaN. Some mixed character TDs can be generated here. (c) The islands coalesce and edge and mixed TDs are generated at the coalescence boundaries. Fig reproduced from Ref [17].

GaN growth on (111) Si is a bit more complicated. GaN and Si have very different thermal expansion coefficients which can easily cause cracking. It's common to use AlN buffer layers which can be deposited through a chemical vapor deposition (CVD) or physical deposition process like sputtering or puled laser deposition followed by annealing to crystallize the buffer layer before epitaxy. The AlN buffer layers force the GaN to grow under compression which help compensate for the differences in thermal expansion coefficients. The

TDD is generally much higher in GaN on Si (>10^9 cm^{-2}) with a relatively high density of mixed TDs (>50% mixed) which is quite different from GaN on sapphire were 80-90% are pure edge.

2.3 MOCVD and LED Growth

Metal-organic chemical vapor deposition (MOCVD) is the primary method for epitaxial growth of III-N LEDs in both commercial production and research labs. MOCVD reactors are essentially large airtight ovens where vapor phase chemicals are deposited. The sources for the group III metals are metal-organic compounds, which is where MOCVD gets its name. The substrate crystal is heated to very high temperatures (often > 1000 °C) which enables the source molecules (especially the NH_3) to decompose. During MOCVD, metal-organic precursors are introduced into the deposition chamber. These precursors undergo pyrolysis, which is the thermal decomposition of the chemical compounds at high temperatures. As the precursors decompose, metal atoms and other elements are released. These atoms react with each other and the substrate to form a thin film. The pyrolysis process enables the controlled deposition of materials onto the substrate, forming layers with desired thickness and properties. MOCVD is a cold wall process, meaning the reactor walls are not heated and the non-reactant species and byproducts are quickly collected at the walls of the reactor. Unlike MBE, MOCVD is conducted at or near atmospheric pressure.

In MOCVD growth of III-N materials, the metal-organic precursors are trimethylgallium (TMG) and triethylgallium (TEG), trimethylaluminum (TMA), and trimethylindium (TMI). TMG is used for rapid GaN growth (because of its higher vapor pressure) and TEG is used for slower, higher purity GaN growth (because its decomposition method results in less carbon incorporation). An important process in MO decomposition is β-elimination. MO precursors contain β-hydrogens and are removed as part of the decomposition

process and affect the quality of the film being deposited. If the process is not well-controlled, it can lead to unwanted side reactions, which may produce defects in the film or alter the desired film composition and properties. The group V source is ammonia (NH_3). The Si source (n-type dopant) is silane (SiH_4) or disilane (Si_2H_6) and the Mg source (p-type dopant) is bis(cyclopentyl)magnesium (Cp2Mg). Most MO precursors are solid or liquid at room temperature. Bubblers are used to get a vapor phase of the precursor. H_2 and N_2 are used as carrier gases with all the MO sources to deliver them to the reactor at the correct partial pressure. The flow of gases is precisely controlled by mass flow controllers (MFCs). When gases are flowed across a surface with high velocity, a boundary layer forms at the surface of the substrate. In MOCVD the boundary layer has a huge impact on the growth rates and incorporation of species. MOCVD reactors often have additional flows of inert gases (H_2 and/or N_2) to modify the boundary layer for better growth.

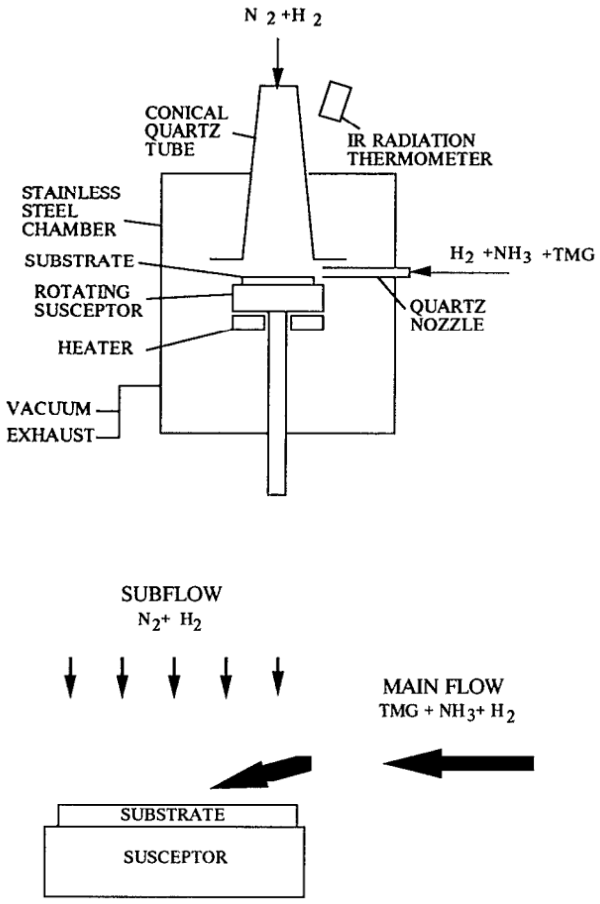

Figure 2.9: Two-flow reactor design from Shuji Nakamura's first paper [18]. This reactor design was used for all MOCVD growth in this dissertation. Right: Schematic of the entire reactor. Left: Diagram showing how the subflow applies a downward force to the main flow, modifying the boundary layer.

Figure 2.9 shows the two-flow reactor design that Shuji Nakamura published in his first paper at Nichia [18], shown in Figure 2.9. This reactor design was instrumental in his creation of the first bright blue LEDs in the 1990's. A modified version of design was used in all the MOCVD growth in this dissertation. The two-flow reactor has a main flow where all the reactant precursors are injected along with N_2 and/or H_2 carrier gases. The subflow contains

H_2 and N_2 is designed to apply a downward force on the main flow and modifying the boundary layer at the surface of the substrate. The flow rates are optimized to maintain laminar flow.

With no intentional doping, GaN will have a slight n-type doping due to oxygen incorporation around 10^{15} - 10^{17} cm^{-3}. Although, in very high purity GaN it's possible to get insulating behavior due to [C] being higher than [O]. With disilane doping levels of 10^{18} - 10^{19} cm^{-3} can easily be achieved. Disilane acts as a slight anti-surfacant in GaN, meaning it has a negative affect on adatom mobility and surface morphology. p-doping in GaN is generally more challenging since the presence of H_2 can passivate the Mg. An activation anneal is required after all p-GaN growth which is a ~625 °C bake for 15-20 min. This can be done either in-situ or ex-situ in an oven. The activation step removes H_2 from the material, but even after activation only ~2% of the Mg in the crystal will act as acceptors. This is because Mg acts as a deep acceptor in GaN and only a small fraction of the states will be thermally active due to Maxwell-Boltzmann statistics. Thus, the [Mg] concentration will often be 10^{19} – 10^{20} cm^{-3} with the understanding that the actual acceptor levels are much lower.

Most III-N LEDs structures use an n-doped InGaN/GaN superlattice (SL) prior to active region growth. The role of the superlattice has not been fully understood, although there's good experimental evidence that shows SLs can increase light output power in all GaN LEDs. The leading theory is that superlattices play an important role in impurity capture and the reduction of point defects higher in the structure [19], [20]. Point defects are understood to be Shockley Read Hall (SRH) centers so reducing them in the QWs would reasonably have a positive impact on power. Furthermore, in V-defect engineered LEDs the superlattice is understood to play an important role in V-defect formation and structural evolution [21], [22].

The epitaxial design of the LED active region is a big topic which will be discussed at length throughout this dissertation. From a high level, III-N active regions consist of usually 3-7 InGaN QWs with GaN or AlGaN quantum barriers. Growth of InGaN is difficult because In desorbs very easily, making it difficult to get high incorporation rates. To compensate for this InGaN QWs must be grown under very high In flows and relatively low temperatures compared to the rest of the LED stack. For red LEDs it's often necessary to quickly grow an AlGaN capping layer after each InGaN QW to prevent In from desorbing in future steps [23]. However, growth at low temperatures is generally bad for morphology and defect formation which causes significant challenges for long wavelength LED growth. This can be mitigated to some extent by growing hotter quantum barriers in H_2 at reduced growth rates. Therefore, a typical GaN active region will consist of several different temperature steps, with different growth rates, and different V/III ratios. Active region design is discussed at length in Chapter 6.

2.4 The *p-n* Junction

As discussed in Chapter 1, the fundamental building block of an LED is a *p-n* junction which forms a semiconducting diode. *p-n* junctions are one of the most important components in a variety of electronic devices including LEDs, solar cells, laser diodes and transistors (the building blocks of computers). Understanding *p-n* junctions and their electrical properties is important for understanding all forms of electronics and electronic material fabrication. In its simplest form a p-n junction is just a piece of *p*-type material that is directly adjacent to a piece of *n*-type material. In semiconductor fabrication, this is usually accomplished through ion implantation or through epitaxy.

p-type material is characterized by having excess holes and n-type is characterized by having excess electrons. When placed next to each other in a junction, there will be a concentration gradient of positive and negative charge carriers which will result in diffusion of both electrons and holes. With this concentration gradient, electrons will start flowing from the n-side to the p-side leaving behind uncompensated donor ions (N_D^+) on the n-side. Holes will move in the opposite direction, from p- to n- leaving behind uncompensated acceptors (N_A^-). This net movement of charge creates a region at the junction which has no mobile charge carries, known as the depletion region. The depletion region width (W_D) depends on the doping levels of the *n*- and *p*-type materials. But once the depletion region is formed, n-side will be depleted in electrons (slight positive charge), and the p-side will have accepted excess electrons (slight negative charge). This sets up an electric field which will cause a drift current in the opposite direction from the diffusion current. In equilibrium, a p-n junction has a drift current which is equal and opposite to the diffusion current and zero net flow of charge. Diffusion current obeys Fick's law (Eq. 2.4) and drift current obeys Ohms Law (Eq. 2.5).

$$J = -qD\frac{d\rho}{dx} \text{ (Fick's Law)} \qquad \text{(Eq. 2.4)}$$

$$J = q\rho\mu E \text{ (Ohm's Law)} \qquad \text{(Eq. 2.5)}$$

From the equations above we see that the diffusion current depends on the slope of the carrier concentration and the drift current always moves in the direction of the electric field. For a p-n junction in equilibrium we can find the electric field in relation to the carrier concentration from setting the equations equal to one another. A diagram of a p-n junction in equilibrium is shown in Figure 2.10.

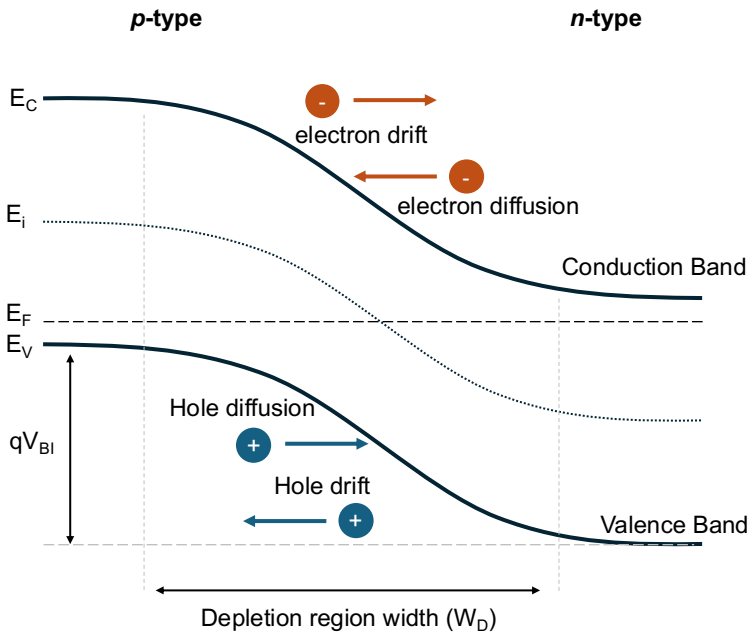

Figure: 2.10: Energy band diagram of a p-n junction in equilibrium, showing the drift and diffuison currents for holes and electrons, the depletion region width, and relevant energy levels.

From Figure 2.10 we can begin to understand how a semiconducting diode works. When a reverse bias is applied, the electric field opposing the diffusion current will increase, this causes an increase in the drift current, but is compensated by an increase in the diffusion current. The depletion region will widen, and no current will flow. Therefore, in reverse bias the diode is off. Under forward bias, the applied electric field opposes the built-in electric field. When the forward bias is high enough the drift current will switch directions causing the diffusion and drift current to add together. This causes a net flow of current under sufficient forward voltage. In this configuration the diode is on. If the depletion region is large compared to the minority carrier diffusion length, we can say the diode is "long" and if there is no recombination in the depletion region, the current is described by the Shockley Diode equation (Eq. 2.6) where J_S is the reverse saturation current, and the forward current is dependent on V

and the thermal energy kT. The thermal energy in a diode often allows it to turn on slightly before the expected turn-on based on electric fields alone.

$$J_T = J_S\left(e^{\frac{qV}{k_BT}} - 1\right) \quad \text{(Eq. 2.6)}$$

In a real diode (especially and light emitting diode), there is deviation from this ideal behavior because of generation and recombination that occurs. In this case we add an ideality factor η to capture this behavior (Eq. 2.7).

$$J_T = J_S\left(e^{\frac{qV}{\eta k_BT}} - 1\right) \quad \text{(Eq. 2.7)}$$

2.5 Light Emitting Diodes

Technically, a simple GaN *p-n* junction can behave as a weak violet LED as long as some amount of recombination is occurring in the junction under forward bias conditions. However, all modern III-N visible LEDs make use of double heterostructures consisting of GaN/InGaN/GaN or sometimes low In% InGaN as the barrier. Because GaN has a larger bandgap compared to InGaN, and the GaN/InGaN heterostructure is Type I (meaning the conduction and valance bands of InGaN sit at a lower energy than GaN), the double heterostructure of GaN/InGaN/GaN forms a quantum well in both the conduction and valence bands. In quantum physics, quantum wells are often discussed as a method for confining a particle inside a particular area. From here we can discuss the possible states it can occupy with different energies associated with each one. In real materials, the quantum well is a bit more complicated, but the general principle still applies. Quantum wells are used for carrier confinement. When placed between a p-n junction, quantum wells create regions with a narrower bandgap and encourage electrons and holes to localize spatially in the LED.

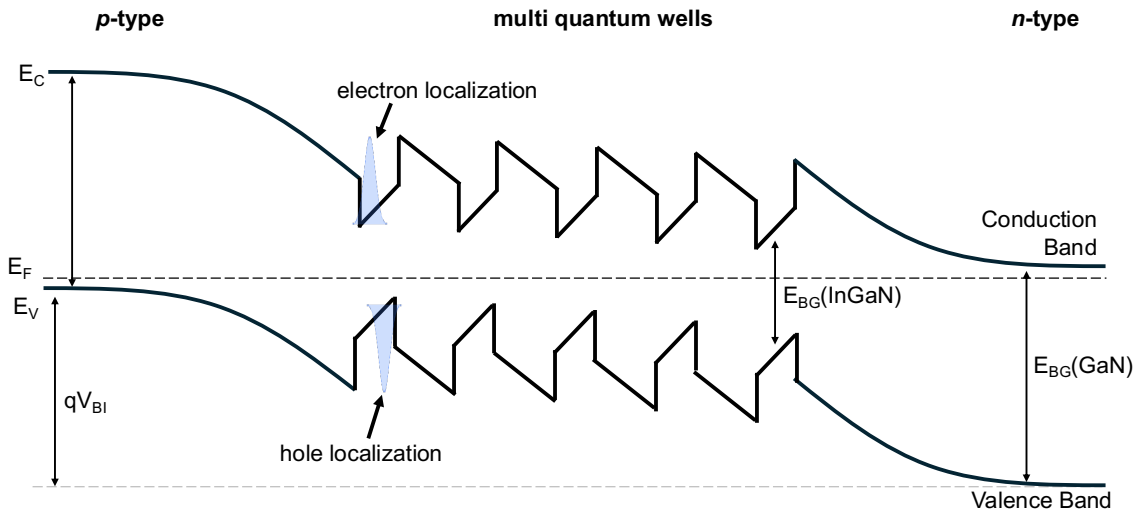

Figure 2.11: Schematic of an LED with 5 QWs in equilibrium (zero bias). The smaller bandgap of InGaN combined with the double heterojunction of GaN, allow for electron and hole localization in quantum wells.

Figure 2.11 illustrates a GaN p-n junction with 5 InGaN quantum wells in equilibrium. Because InGaN has a smaller bandgap, carriers get localized in the quantum wells. Under forward bias, when current is flowing through the quantum wells the carrier populations in the wells can get high enough to achieve appreciable radiative recombination. This total voltage across the diode in equilibrium is called the built-in voltage of the diode (V_{BI}). However, the total voltage of an LED is not necessarily the same as the diode voltage. The best circuit model for an LED is a diode and resistor in series. We can further subdivide the series resistance into the resistances of each element. This is shown in Figure 2.12. As long as the contacts are ohmic and the n- and p-doping are sufficiently high. The total series resistance (and the corresponding voltage drop) is small compared to the diode voltage. In that case the V_F is similar to V_{diode}.

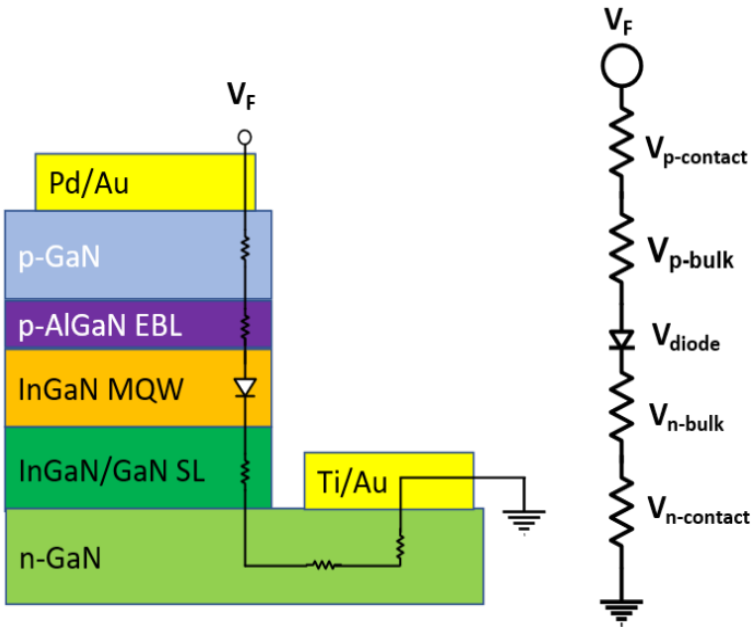

Figure 2.12: Schematic of the equivalent circuit model of an LED with a simplified diagram of a epitaxial stack and the circuit elements that correspond to each layer of the structure.

In 2024, the LED world is very mature with most of the on-going research aimed at design optimizations that give slightly improved efficiency. Much of the work of this dissertation is in line with this, aimed at voltage improvements and quantum efficiency improvements. But there are many different ways of defining LED efficiency so it's worth going through each in detail. In their simplest form, LEDs convert current (the flow of electrons) into photons. The most basic efficiency is the internal quantum efficiency (IQE) which is a measure of how many photons are generated per number of electrons that flow through the diode under forward voltage operation. If one photon is generated for every two electrons that flow through the diode the IQE is 50%. However, just because a photon is generated doesn't necessarily mean that it escapes the device. Things like internal reflection and reabsorption of the photons can cause light that is generated to never escape the device.

Therefore, when we measure the light output from an LED, we aren't measuring the IQE directly. Instead, we're measuring the combination of the IQE and the light extraction efficiency (LEE). LEE is the fraction of the photons generated in the active region of the LED that exit the material. The product of the light extraction and the IQE is called the external quantum efficiency (EQE) as shown in Eq. 2.8. EQE is typically the efficiency that is measured experimentally and one of the most common efficiencies that is reported in the literature.

$$EQE = IQE \times LEE = \frac{L/h\nu}{I/q} \quad \text{(Eq. 2.8)}$$

The L in Eq 2.8 is the optical power emitted into free space, $h\nu$ is the energy of a photon, q is the elemental charge, and I is the injected current. It's notable that L is the power measured, so when measuring EQE it's important to collect *all* the light emitted by the LED. This is usually achieved by using an integrating sphere. If the LED is packaged, it can easily be placed inside an integrating sphere where ~100% of the light is collected. If the LED is measured on-chip, it's difficult to measure all the light but there's a variety of tricks that can be played. This will be discussed further in Chapter 4 on red μLEDs grown on Si and measured on-chip. Optimizing light extraction is also important for maximizing EQE. In μLEDs, there's a light extraction affect with mesa diameter. Smaller mesas tend to have higher LEE. When LEDs are packaged, there's also a LEE boost due to the epoxy that's chosen to better match the index of refraction of air and reduce internal reflection.

$$EE = \frac{V_{ph}}{V_F} \quad where \quad V_{ph} = \frac{h\nu}{q} \quad \text{(Eq. 2.9)}$$

The electrical efficiency (EE) is another important efficiency to understand. The EE is the ratio of the photon voltage and the forward voltage (Eq. 2.9). The photon voltage depends on the frequency of the light emitted, which means that higher frequency (shorter wavelength)

will have a higher photon voltage. In theory, the longer wavelength LEDs should operate at lower voltages, all else being equal, because they have lower photon voltages. In practice, this isn't always the case which will be described at the end of this chapter on the challenges with long wavelength III-N LEDs. Getting green and red LEDs to operate near their photon voltages is one of the key aims of the V-pit work presented in this dissertation (much more on that to come). Combining the EE and the EQE we get the wall plug efficiency (WPE) or the power conversion efficiency (PCE) given in equation 2.10.

$$WPE = EQE \times EE = \frac{L/h\nu}{I/q} \times \frac{h\nu}{q} \times \frac{1}{V_F} = \frac{L}{I \times V_F} \qquad \text{(Eq. 2.10)}$$

The WPE is best understood as the ratio of optical power out over electrical power in. Ultimately, in most applications, WPE is what matters. It's inversely related to forward voltage and directly related to light output power. So, optimizing WPE (and LED performance in general) is all about maximizing the photons generated at the lowest current and voltage achievable. This is the task of V-defect engineering and active region growth optimization which are the central themes of this dissertation.

Beyond the basic equations for efficiency and light output measurements, there's a lot more that can and has been done to understand LED efficiencies and inefficiencies. As mentioned already, LEDs aren't just diodes where current flows in the forward direction, they're diodes with (a) recombination plane(s) between the p- and n- regions. Recombination can broadly be separated into radiative recombination and non-radiative recombination. Radiative recombination is band-to-band recombination of a single electron with a single hole to create a single photon at the energy of the bandgap. This is what we want in an LED. This contributes to efficiency. Non-radiative recombination can be separated into two primary

types. Shockley Read Hall (SRH) and the Auger process. Figure 2.13 shows an LED with 5 QWs under forward operation. The three types of recombination process are illustrated in the diagram SRH (a), radiative recombination (b) and Auger (c).

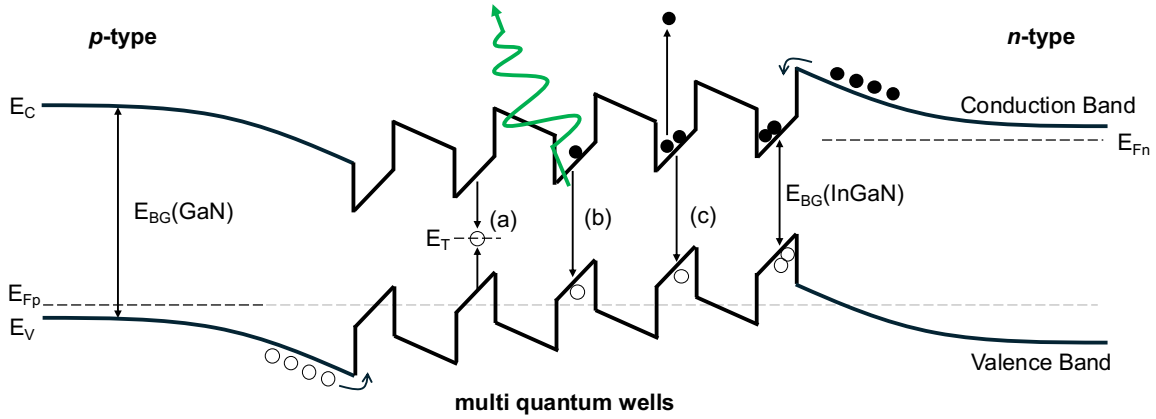

Figure 2.13: Schematic of an LED in forward operation with 5 QWs. Quasi fermi levels, and GaN and InGaN bandgaps are labeled. The 3 primary recombination process are shown, SRH (a), band-to-band radiative recombination (b), and the Auger process (c).

SRH involves a free carrier relaxing into a trap state within the bandgap. In Figure 2.13 that trap (labeled E_T) is at mid-gap although it's possible for that trap to be at other energies. The rate of SRH is determined by either the speed of hole or electron capture (whichever is slower) and is linear with that carrier concentration. This means that SRH recombination in an LED is directly proportional to carrier concentration. SRH = An, where A is the SRH coefficient and n is the carrier concentration. Radiative recombination has quadratic dependence on carrier concentration because it requires the simultaneous recombination of both an electron and a hole. Therefore, rad rec = Bn^2, where B is the radiative coefficient and n is the carrier concentration. Auger occurs when an electron and hole recombine but rather than that energy going into the production of a photon, the energy is transferred to a new 'hot' carrier. If a hot electron is produced, we call it *eeh* Auger and if a hot hole is produced we call

it *ehh* Auger. In either case, Auger depends on 3 carriers and thus the Auger recombination = Cn^3, where C is the Auger coefficient and n is the carrier concentration. Using these dependences, we can write an equation for the total current under steady state conditions (Eq. 2.11)

$$J = qd \times (An + Bn^2 + Cn^3) \quad \text{(Eq. 2.11)}$$

Here we've combined the two Auger processes into just a single coefficient C. J is the current density, q is the elemental charge, and d is the total thickness of the emitting regions. From here we can define IQE as a ratio of the different recombination processes (Eq. 2.12).

$$IQE = \frac{Bn^2}{An + Bn^2 + Cn^3} \quad \text{(Eq. 2.12)}$$

This is called the ABC model of recombination and is a very useful approximation for how recombination behaves in an LED. Optimizing IQE is really a process of maximizing the B coefficient relative to the A and C coefficients. In highly, inefficient LEDs the A and C coefficients are large, and the B is small. Furthermore, it's understood that the A coefficient (SRH) tends to dominate the inefficiencies at low current densities and C coefficients (Auger) dominates the inefficiencies at high current densities. This understanding helped solve a major dispute in the LED world for years, which was what was the source of droop in LEDs. Droop is the consistent fall off in efficiency at high current densities which is observed for all high-performance LEDs. Generally, the field has agreed that droop occurs because of Auger recombination in highly efficient, well designed LEDs [24], [25]. Carrier overshoot has also been proposed as a potential source of droop [26]. Although for high performance LEDs, Auger is now understood to be the primary droop mechanism. If Auger is indeed the primary explanation for droop, then reducing pathways for Auger can reduce droop. Trap assisted

Auger recombination (TAAR) is a dominate mechanism for Auger. Reducing trap states would reduce both TAAR and SRH. Practically, in LED growth this means less point defects, less dislocations, and better crystal quality which can be a challenge in long wavelength III-N where the QWs are highly strained and grown a low temperatures to incorporate sufficient Indium.

2.6 Electron Microscopy

Advanced characterization of epitaxial materials is an important part of understanding the structure and evolution of defects in III-N LEDs and is a central part of this dissertation. This section overviews some of the theories and experimental techniques used to image epitaxial materials. Standard optical microscopy is generally insufficient to learn about the atomic structure of a material since the resolution in optical microscopy is fundamentally limited by the wavelength of the light used for imaging. Since optical light has a wavelength of ~400-700 nm it's impossible to measure features on the atomic scale ~ 1 nm or smaller. As a result, electron microscopy is the standard method for imaging atoms and defects since the wavelength of an electron can be ~100,000 times smaller than visible light, depending on the electrons' momentum. Electron microscopy uses electron optics, typically an electromagnet, to focus and defocus the beam. This is analogous to how an optical lens can focus and defocus visible light in an optical microscope.

The electron microscopy techniques that are relevant to this dissertation are transmission electron microscopy (TEM), scanning transmission electron microscopy (STEM), and scanning electron microscopy (SEM). TEM and STEM are methods used for ultra-high-resolution imaging of very thin samples that have to be specially prepared with a

focused ion beam (FIB) prior to measurement. As their names imply, TEM and STEM involve electrons being transmitted (passing through) the sample, which is why it must be very thin. SEM, on the other hand, is for slightly lower resolution and involves electrons scattering off the material being imaged and detected on a series of detectors located above the sample.

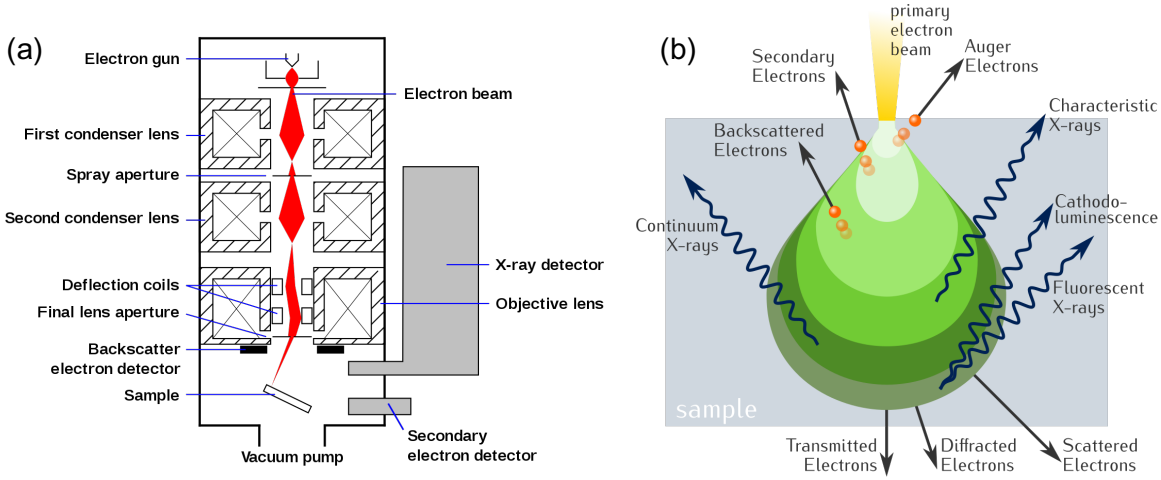

Figure 2.14: (a) Schematic of a scanning electron microscopy (SEM) chamber with lenses and detectors labeled. (b) Schematic of the 'tear drop' shape of electrons interacting with the sample being imaged.

Figure 2.14a shows a schematic of an SEM chamber. The electrons are generated at an electron gun and focused and redirected by a series of lenses. The focused electron beam interacts with the sample in what's known as a 'tear drop' shape, shown in Figure 2.14b. If the sample is thin enough some electrons are transmitted, diffracted, and scattered through the sample. This is the case for TEM and STEM. In most SEM imaging, the sample is too thick for any appreciable amount of transmission. Therefore, in SEM the detectors are designed for the other signals. Almost all SEMs have a secondary electron detector. Secondary electrons have very low energies (~50 eV) and thus don't travel far in the material. Secondary electrons occur when an atom in the sample is ionized by ejecting one of the outer shell electrons. In

SEM, secondary electrons produce the highest signal and because they don't travel far in the material (typically a few nanometers), they are good for getting high resolution images. Secondary electron detection is useful for determining the topography of a sample surface, which is typically the first thing one wants to measure in SEM.

In physics, backscattering refers to a signal, wave, or particle being reflected back towards its source. Electron backscattering was famously used by Ernest Rutherford in the gold foil experiment to postulate that atoms had a tightly packed, positively charged nucleus. This was the only reasonable explanation for how an electron could be reflected towards its source with such a high momentum. Backscatter SEM uses precisely this technique to understand something about the topology and atomic weight (Z) of the sample being imaged. A backscatter detector in an SEM is placed directly above the sample. Backscatter electrons reflect off atomic nuclei in the sample and are detected at the backscatter detector. Backscatter electrons have higher energies compared to secondary electrons and therefore travel a little further in the sample. Backscatter electron microscopy can be effective at showing morphology and also gives information about the atomic weight of the elements in the sample. Higher Z will show up as brighter since electrons reflected off a large nucleus will have more energy. Far fewer backscatter electrons are emitted during SEM compared to secondary electrons so the signal in backscatter SEM is significantly weaker.

Besides electrons, electron microscopy can also generate photons (either visible or x-rays). Many SEMs have additional detectors for photons which can help further characterize the sample. When atoms are excited, electrons can jump to higher energy levels and subsequently fall back to the lower energy levels. When electrons fall back to lower energy levels, they can emit x-rays that have the same energy as the energy difference between

electron states in the particular atoms. The energy of the x-ray will then be directly dependent on the type of atom since each atom will have slightly different spacing between energy levels. These x-rays are called Characteristic X-rays. Counting characteristic x-rays can tell us what kind of atoms are in the sample. This technique is called energy dispersive X-ray spectroscopy (EDS or EDX) or X-ray fluorescence. This technique can be used in TEM and STEM as well to get relative atomic fractions at very high resolutions.

For materials with an optical bandgap, the excitation by electrons can also cause recombination across the bandgap (similar to photoluminescence but with electron excitation). This causes light to be emitted at the bandgap energy. In the case of III-N materials, that's visible light. This technique is called cathodoluminescence (CL). Some SEMs are also equipped with cathodoluminescence detectors which are good for determining where luminescence is coming from with very high resolution. Cathodoluminescence is especially useful in optical materials to image defects. Because defects generally don't emit much light, they appear as dark spots in a CL image. CL is a good way for determining threading dislocation density in LED epitaxy.

Transmission electron microscopy (TEM) shares many features with SEM but is used for thinner samples (~100 nm) and higher resolution. A key difference in TEM is that the detector is under the sample and the electrons measured are those that pass through. Generally, TEMs have much more complicated electron sources and focusing systems since they need to get electrons focused down to atomic length scales and then amplify them to make an image. The focusing system uses lenses, which are typically solenoid coils which cause magnetic fields. Electrons, of course, respond to magnetic fields by spiraling around the curved magnetic field lines. The current passing through a magnetic lens changes it's focusing power.

Additionally, TEM systems have apertures, which are circular holes in strips of metal. Some apertures are adjustable and can be adjusted to achieve different scattering angles to achieve certain diffraction patterns. Diffraction is key to understanding TEM and the results it generates. We know from quantum mechanics that electrons behave as waves and waves undergo diffraction when they interact with a crystalline sample. When electrons pass through a crystalline material, they interact with the regularly spaced atoms within the crystal lattice. This interaction causes the electrons to scatter in different directions, much like how light waves diffract when passing through a narrow slit or around an obstacle. The diffraction pattern obtained in TEM is a result of the interference of these scattered electron waves. The crystal lattice acts as a diffraction grating, causing the electrons to be diffracted into specific angles according to Bragg's law. Bragg's law (Eq. 2.13) states that for constructive interference to occur, the path difference between waves scattered from adjacent crystal planes (distance d) must be an integer multiple (n) of the wavelength (λ) of the electron beam, where θ is the angle of incidence.

$$n\lambda = 2d\sin(\theta) \qquad \text{(Eq. 2.13)}$$

By measuring the angles and intensities of the diffracted electron beams, we can obtain valuable information about the crystal structure of the sample, including lattice spacing, orientation, and the presence of defects or imperfections. In III-N epitaxy the identification and characterization of defects is one of the most useful features. In a diffraction pattern, dislocations can produce streaking or broadening of diffraction spots. The intensity and direction of the streaks provide information about the type and density of dislocations present in the crystal. Stacking faults occur when there is a deviation from the regular stacking sequence of atomic layers within the crystal lattice. These faults can result from errors in crystal

growth. In the diffraction pattern, stacking faults can manifest as additional diffraction spots or streaks that are displaced from the main diffraction spots corresponding to the perfect crystal structure, indicating a deviation from perfect crystallographic stacking. Furthermore, vacancies and interstitials can cause slight changes in the spacing between crystal planes, leading to subtle shifts or splitting of diffraction spots in the diffraction pattern.

Scanning Transmission Electron Microscopy (STEM) is a powerful imaging technique that combines the capabilities of transmission electron microscopy (TEM) with scanning capabilities similar to those used in scanning electron microscopy (SEM). STEM offers several features and advantages over conventional TEM, making it a valuable tool for nanoscale imaging and analysis. STEM was used extensively in chapters 3, 5, and 6 in this dissertation thanks to the work of Dr. Feng Wu. Some of the key features of STEM and applications are detailed below.

- High Spatial Resolution: STEM can achieve sub-angstrom resolution, allowing researchers to visualize individual atoms and atomic structures within materials. This high spatial resolution is essential for studying the exact structure of epitaxial layers in an LED.
- Simultaneous Imaging and Analysis: Unlike TEM, where images are formed by directly detecting transmitted electrons, STEM employs a focused electron beam that scans across the sample. This scanning beam interacts with the sample, producing signals such as transmitted electrons, scattered electrons, and secondary electrons. By detecting these signals simultaneously, STEM can provide both imaging and analytical capabilities in real-time.

- Z-Contrast Imaging: STEM offers a unique imaging mode known as Z-contrast imaging, which relies on the detection of electrons scattered at high angles (large-angle scattering). In Z-contrast imaging, heavy elements appear brighter than lighter elements in the image, making it particularly useful for studying materials with complex compositions, such as catalysts and biological samples.
- Chemical Mapping and Elemental Analysis: STEM can perform energy-dispersive X-ray spectroscopy (EDS) or electron energy-loss spectroscopy (EELS) in conjunction with imaging. This allows for chemical mapping and elemental analysis of the sample, providing valuable information about the distribution of elements and their chemical bonding environment at the nanoscale.

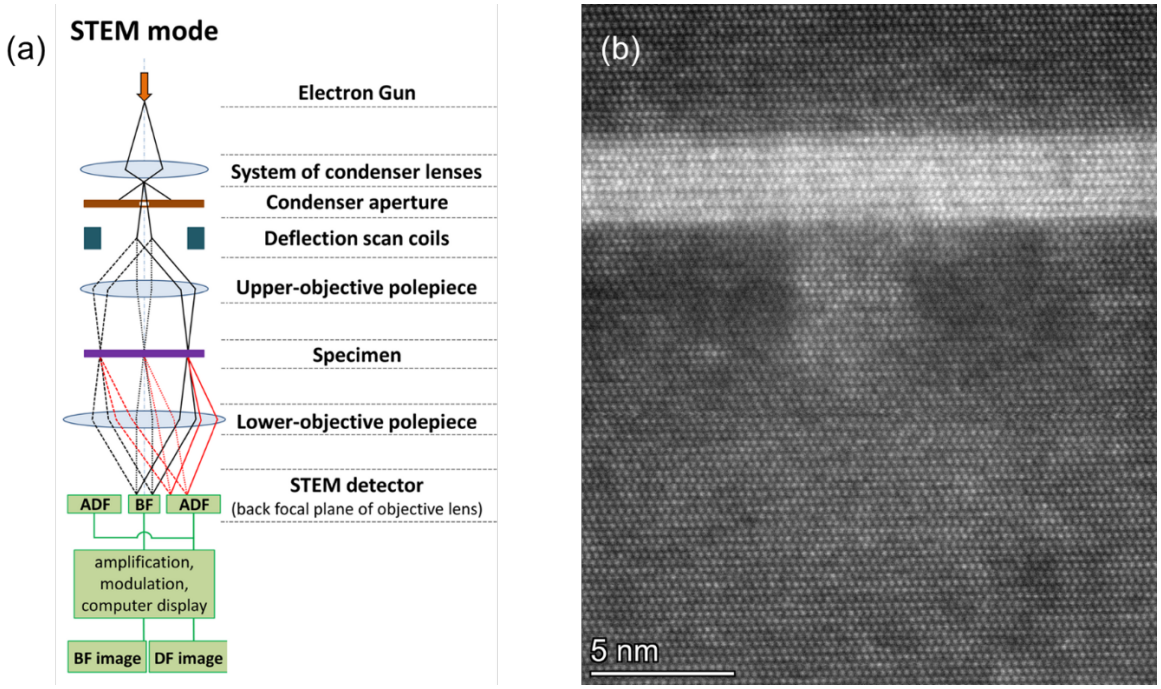

Figure 2.15: (a) Schematic of scanning transmission electron microscopy (b) a STEM image of an InGaN QW in GaN. Dot arrays are columns of atoms. The brighter regions (e.g. the QW) indicate higher Z.

STEM employs various detectors and imaging modes to provide detailed information about the sample's structure, composition, and properties at the nanoscale. Some of the commonly used detectors and imaging modes in STEM are detailed below:

- Annular Dark-Field (ADF) Imaging: ADF imaging is a high-angle scattering technique where electrons scattered at large angles are detected by an annular detector placed around the beam. In ADF imaging, heavy atoms appear brighter than lighter atoms due to the strong dependence of scattering intensity on atomic number. This imaging mode is sensitive to variations in atomic number and is particularly useful for visualizing heavy elements and interfaces in materials.
- Annular Bright-Field (ABF) Imaging: ABF imaging is a low-angle scattering technique where electrons scattered at small angles are detected by an annular detector. ABF imaging is sensitive to atomic column positions within the crystal lattice, allowing for the direct visualization of light atoms, such as carbon, oxygen, and nitrogen, in materials with heavy elements. ABF imaging is especially useful for studying complex oxides, catalysts, and biological samples.
- High-Angle Annular Dark-Field (HAADF) Imaging: HAADF imaging is a variation of ADF imaging that uses a high-angle annular detector to collect electrons scattered at even larger angles. HAADF imaging provides enhanced sensitivity to heavy elements and atomic columns, making it ideal for imaging materials with high atomic number contrast. HAADF imaging is widely used for characterizing nanomaterials, catalysts, and semiconductor devices.
- Bright-Field (BF) Imaging: BF imaging is a conventional imaging mode where transmitted electrons that pass through the sample without scattering are detected. BF

imaging provides a bright image of the sample, with contrast depending on variations in thickness and density. BF imaging is useful for visualizing overall sample morphology and defects, but it lacks atomic resolution compared to ADF and ABF imaging.

- Energy-Dispersive X-ray Spectroscopy (EDS): EDS (or EDX) is an analytical technique used in conjunction with STEM for chemical mapping and elemental analysis. EDS detectors detect characteristic X-rays emitted by the sample when it is bombarded with the electron beam. By analyzing the energy and intensity of these X-rays, EDS can determine the elemental composition and distribution within the sample.

As mentioned earlier, diffraction patterns and deviations from regular diffraction patterns are important in characterizing defects. One specific method which is important for this dissertation is g·B analysis, a technique used to extract quantitative information about strain and deformation in crystalline materials at the nanoscale. This technique relies on the analysis of changes in the diffraction pattern obtained from the sample under various conditions, such as different orientations of the electron beam or sample rotation. The process of g·B analysis is as follows:

- Diffraction Pattern Collection: Initially, a diffraction pattern is collected from the sample using a STEM instrument. This diffraction pattern contains information about the arrangement of atoms in the crystal lattice and any distortions or strains present in the material.
- Beam or Sample Tilt: The electron beam or the sample itself is tilted to a different orientation relative to the crystal lattice. This change in orientation alters the diffraction pattern, causing shifts or changes in the position and intensity of diffraction spots.

- Analysis of Spot Shifts: By comparing diffraction patterns obtained at different beam or sample orientations, the shifts in the positions of diffraction spots can be analyzed. These shifts are related to the local strain and deformation within the crystal lattice.
- g·B Analysis: The shifts in diffraction spot positions are quantitatively analyzed using the g·B method. This method involves multiplying the reciprocal lattice vector (g) associated with each diffraction spot by the strain tensor (B) to obtain the strain-induced displacement of the spot. If $g \cdot B = 0$, no contrast will be seen in the STEM image. In the case of a threading dislocation, this means that the diffraction beam is normal to the dislocation line (the dot product is zero). We use this technique to determine whether TDs are edge, mixed, or screw.

Overall, electron microscopy is a very powerful set of techniques to better understand the science and structure of LEDs. Detailed STEM was a very important part of this dissertation which seeks to better understand the crystallographic and epitaxial details of V-pit engineering in LEDs. In the final section of this chapter, we'll take a close look at the literature on long-wavelength InGaN LEDs, the challenges, the approaches to solving such challenges and the emergence of V-pit engineering as one of the most important methods for addressing the low WPE in green and red III-N LEDs.

2.7 Long-wavelength III-N LEDs

Growing highly efficient LEDs is a combination of electrical engineering, device physics, material science, chemistry, and systems engineering. Just because a structure is theoretically possible or mathematically advantageous doesn't mean it can be actually be realized within the constraints of the epitaxial growth techniques and electrical and optical

properties of the materials being grown. GaN growth has a variety of cheap and effective substrates. There isn't any practical way to grow bulk InGaN on a reasonable substrate. And so visible LEDs are based around GaN. GaN emits in violet/UVA range. Blue LEDs work very well because they require just a little bit of Indium ~13-15% in the QWs to achieve blue emission. That's not much of a lattice mismatch so the QWs are only a little strained as grown. Only a little strain means only a little piezoelectric polarization, and a relatively small electric field in the QWs. Also critically important is MOCVD growth temperature needed grow the LED since this has a direct effect on crystal quality and the number of defects in the material. Blue LEDs are pretty good here as well, we don't have to go to very low temperatures to get 13% In in a blue QW. Furthermore, when you have piezoelectric strain that induces a barrier to carrier injection at the edge of the QW. In blue, the heterojunction discontinuities are small, and carriers (electrons and holes) have a relatively easy time moving through the MQW structure.

As we go to longer wavelength III-Ns such as green and red LEDs, lower growth temperatures are required which increase the number of defects and degrade QW morphology through less effective step-flow growth. This increases SRH and TAAR centers and reduces IQE. Furthermore, the lattice mismatch increases, causing more piezoelectric strain, more internal electric fields leading to separation of electron and hole wavefunctions, which reduces radiative recombination (B in the ABC model), and it increases the barriers to electron and hole injection. The higher barriers to injection have the effect of increasing the forward voltage needed to drive the LED. Effectively, if you have voltage barriers in your LED the carriers need to have more energy (greater electric field to encourage drift) in order for the LED to operate. Since V_F is inversely proportional to WPE, the WPE in green and red LEDs grown on

c-plane will suffer even more than the EQE. These are the primary reasons for the drastic fall-off in efficiency that's observed in InGaN-based LEDs as the In% increases. Figure 2.16 shows a simplified schematic of single quantum well (SQW) structures that illustrate how increasing the indium content in the wells increases the piezoelectric polarization inside the QWs, the band offsets, the barriers to carrier injection, and the presence of SRH and TAAR centers in the wells. This has the net effect of significant reduction in EQE and WPE by increasing forward voltage and A and C coefficients in the ABC model of recombination.

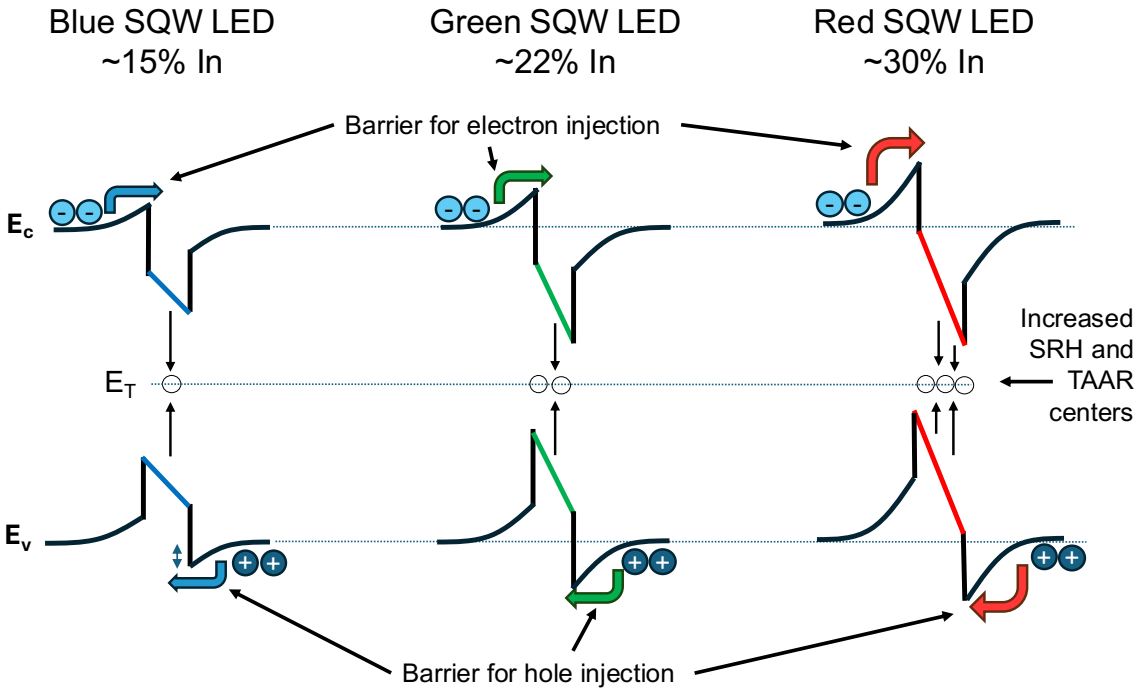

Figure 2.16: Simplified schematics of blue, green and red single quantum well (SQW) structures illustrating the increase barriers for carrier injection and increased Shockley-Read-Hall (SRH) and trap-assisted Auger recombination (TAAR) centers that exist at longer wavelength InGaN-based LEDs. This leads to reduced EQE and WPE.

The combination of the factors shown in Figure 2.16 is the origin of the so-called "green gap" in LEDs. If we consider only nitrides, there's no gap, just a steady fall-off in efficiency

as the emission wavelength (and In content in the QWs) increases. The term “green gap” arose because AlInGaP-based phosphide LEDs grown on gallium arsenide are highly efficient red emitters [27]. These issues have long been understood and discussed in III-N LED research with a wide variety of potential solutions. 10 years ago the big push in the LED industry was to develop non *c*-plane approaches to LED growth that could have mitigated some of these issues by starting on planes with lower polarization [28]. Semipolar LEDs saw significant R&D efforts but in the last 5 years they’ve mostly been abandoned in LED growth, although in lasers the higher gain has kept semipolar approaches alive. The big problems were defect formation and impurity uptake leading to poor brightness. In short, the MOCVD growth just never worked as well as *c*-plane, combined with the fact that the substrates were prohibitively expensive for large-scale production.

With the industry stuck on *c*-plane, LED researchers had to come up with methods to mitigate issues with high In content QW growth. On a quick pass, it might seem as though all the issues arise from lattice mismatch, if you didn’t have lattice mismatch, you wouldn’t have the polarization fields from the piezoelectric effect (although you would still have the band offsets). Furthermore, part of the reason that InGaN with high In% has to be grown at such a low temperature is because it has a high lattice mismatch. The In atom doesn’t ‘fit’ well in a GaN lattice and so In easily desorbs during growth which becomes worse at higher temperatures and so crystal growers just grow cold, but that introduces a host of other problems due to low adatom mobility causing degraded step-flow growth. If some about of lattice relaxation can be achieved, the In incorporation will increase allowing for higher growth temperatures. This is called compositional pulling. And so, a slew of different strain relaxation approaches where created to allegedly fix the lattice mismatch issue, many of them developed

at UCSB. These included InGaNOS pseudo-substrates which used InGaN-based buffer layers to increase the lattice constant and grow more relaxed InGaN active layers [29]. Porous GaN has also drawn research interest because, in theory, if you can create a mechanically weak layer beneath the epitaxial structure, you can create pathways for relaxation to occur. This was demonstrated at UCSB showing a red-shift in samples with porous underlayers compared to samples without [30]–[32]. While these results were promising, subsequent internal attempts to replicate the work proved unsuccessful, drawing questions as to whether these methods were actually viable for long wavelength LEDs. The porous GaN project at UCSB has essentially been abandoned as of 2024.

In addition, there was an idea to grow a very high In composition (as high as 50%) layer at the beginning of the structure [33]. Because of the thermodynamic properties of $In_{0.5}Ga_{0.5}N$, which isn't stable at high temperatures, subsequent high temperature growth would cause the $In_{0.5}Ga_{0.5}N$ to decompose creating pores in the material, not unlike the porous GaN approach. These pseudo-substrates showed incredible compositional pulling effects allowing red InGaN QWs to be grown at nearly 100 °C hotter than other approaches [34], [35]. These LEDs also showed remarkably low voltage for red LEDs. But more detailed characterization showed that the decomposition layer was actually just a massive defect generation mechanism which increased TDD to 10^{10} cm^{-2} and generated a surface covered in V-defects (thus the low voltage) and compositional pulling from defect mediated relaxation [36]. So far strain-relaxation approaches have not been effective in demonstrating high EQE or WPE. First of all, it turns out that most 'strain relaxation' approaches are really just fancy ways of making a bunch of new defects, which of course, will relax the strain. But defect generation *is* one of the primary reasons that the strain is detrimental to long wavelength III-N LEDs. So, if strain relaxation is

achieved through the creation of defects, the problem hasn't been solved, it's just been moved to a different part of the epitaxial structure. Furthermore, good LEDs are based on double heterostructures (a.k.a. QWs), the real problem has to do with the fact that the two materials that compose double heterostructure have a lattice mismatch and piezoelectric polarization, which creates discontinuities in the band structure at the heterointerface, and in a GaN/InGaN/GaN QW these discontinuities increase with In%. Even if you could grow on bulk InGaN, you don't fundamentally solve this. In that case you'd just be straining the GaN (in tensile) to bulk InGaN rather than straining InGaN (in compression) to GaN. Straining GaN might even be worse since there's far more GaN grown in an LED than InGaN. Of course, one approach would be to use a mostly InGaN structure but this also poses a problem since InGaN has to be grown at relatively low temperatures due to its phase diagram and thermodynamic properties. The reality it's highly unlikely that there will ever be a complete solution to the green gap because it's based on fundamental material science and device physics problems. But there are a variety of things we can do to mitigate each of the challenges at long wavelengths. Combined, these approaches have been shown to significantly move the needle on green and red InGaN-based LED efficiency.

V-defects (or V-pits) have been known to exist in III-N epitaxial materials for decades [37]. V-pits are inverted hexagonal pyramidal 3D defects with six $\{10\bar{1}1\}$ sidewalls and most commonly form around threading dislocations. Historically, they were believed to be detrimental to device performance especially when formed inside the active region. However, there has been an understanding that they play a role in affecting carrier transport around threading dislocations, effectively 'screening' the threads from being SRH centers [38]. In the industry, V-pits have long been understood to play an important role in electrostatic discharge

(ESD) [39]. But in the mid 2010's a series of papers emerged from Nanchang University in China showing that V-shaped pits where useful for something else, bypassing the high polarization barriers on *c*-plane by providing semipolar pathways for holes to reach the quantum wells [39]–[43]. A V-defect schematic is shown in Figure 2.17a with the relevant crystal planes. Furthermore, simulations showed that the theory was lining up with experiment [44] (Figure 2.17b). V-defects could help bridge the gap between the polarization benefits of semipolar plans with the better MOCVD growth and defect reduction that was achievable on *c*-plane growth. And all on cheap substrates!

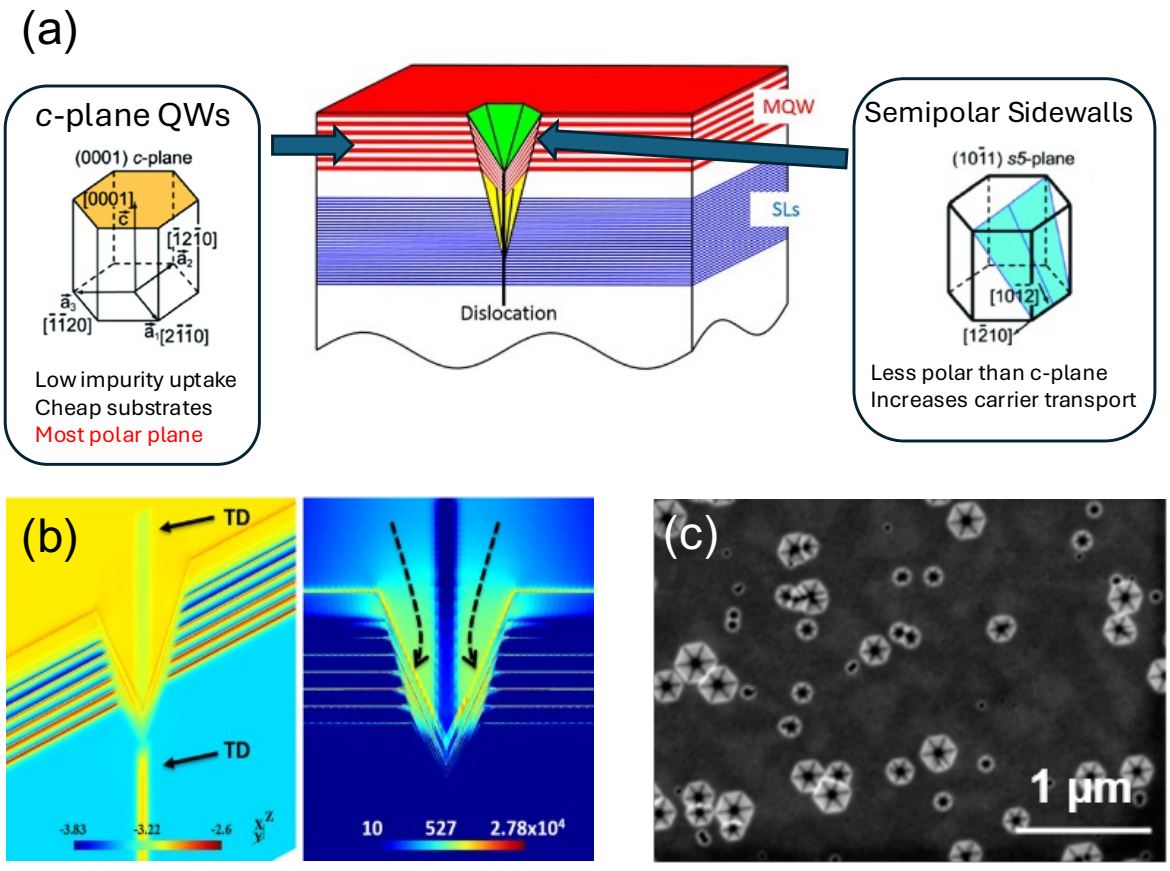

Figure 2.17: (a) Schematic of a V-defect formed in the SL (blue horizontal lines) on a TD (black verticle line) and extending through the MQWs (red and white horizontal lines). The relevant growth plane and sidewall planes are shown with their advantages/disadvantages. Images from Refs [45], [46]. (b) Simulation result showing the effects of V-defects on strain

and carrier transport (from Ref [44]). (c) Planview SEM image showing V-pits in an LED structure (from Ref [47]).

Interestingly, the work from Nanchang wasn't done on sapphire, these engineers, many of whom came out of Lattice Power (a GaN-on-Si power electronics company), were making their LEDs in GaN-on-Si. For reasons which were only understood later, GaN-on-Si is uniquely suited for V-pit LEDs. This will be discussed in much more detail in Chapters 3-5, but in essence it has to do with a favorable threading dislocation density and a high percent of mixed TDs compared to pure edge. In the subsequent years, Nanchang published a series of papers boasting the best numbers anyone had ever seen for green and red III-N LEDs [48], [49]. These LEDs were sent to UCSB and tested for verification, and they were even better than originally claimed. It's only in the last year that Lumileds has published data for LEDs on sapphire that compares and, in some cases, surpasses the Nanchang results [50]. The effect of V-defects on voltage in green LEDs is shown in Figure 2.18.

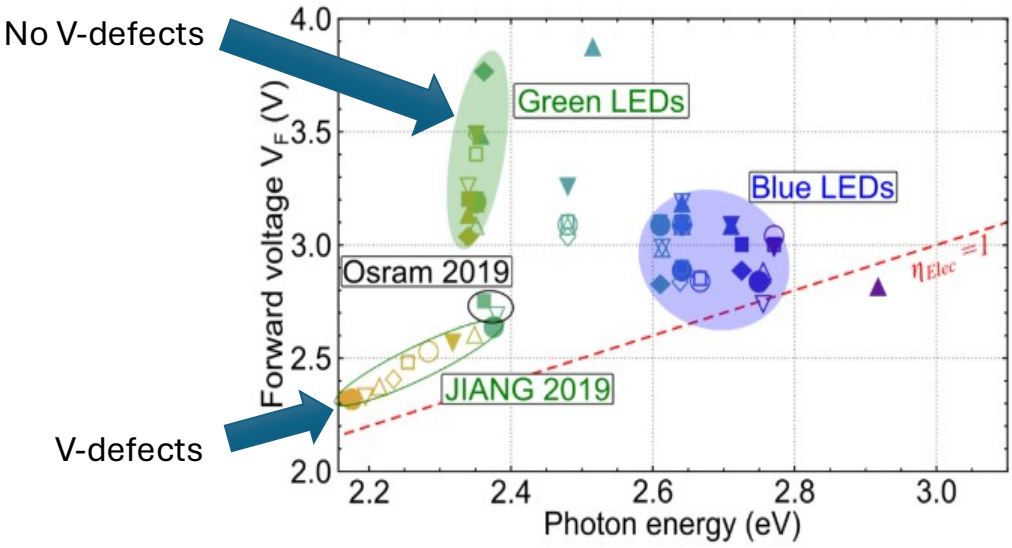

Figure 2.18: The effect of V-defects on voltage in green LEDs. The dotted line shows electrical efficiency = 1 and represents near ideal LED performance. Figure from Ref [51].

The dotted line in Figure 2.18 shows the electrical efficiency = 1. Since the photon voltage scales with wavelength, near ideal LED performance would show voltage steadily decreasing as the wavelength increased. However, until the use of V-pit engineering, this trend went in the other direction because of the injection barriers. What V-pits did was bypass the higher injection barriers in high In% active regions on *c*-plane allowing LEDs operate with a forward voltage comparable to the photon voltage for green and red [52]. The effect of V-defect engineering on the peak WPE efficiency is plotted in Figure 2.19.

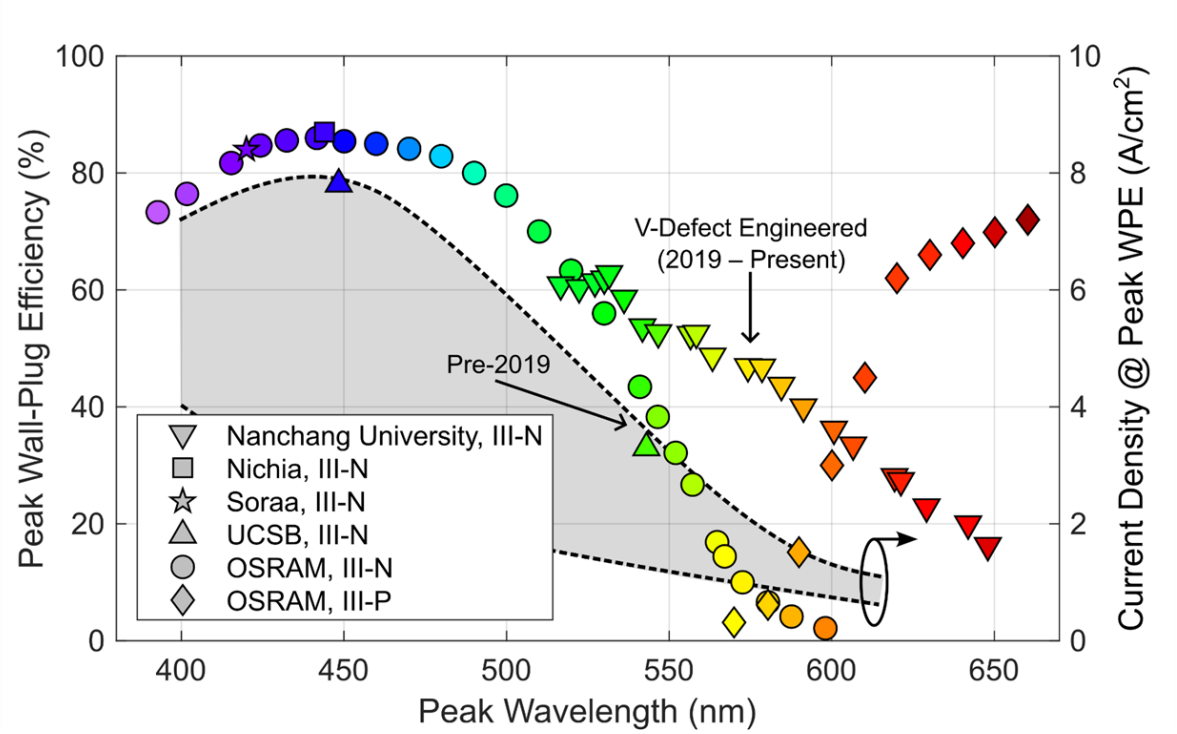

Figure 2.19: Peak wall-plug efficiency for III-N LEDs without V-defects (squares, stars, upward triangle, and circles), III-P LEDs (diamonds), and III-N with V-defects from Nanchang (downward trianges). Each is color-coded to the emission wavelength. This plot illustrates the dramatic effect of V-defect engineering on the green gap. Figure credit to T. Tak.

The green gap still exists, but as Figure 2.19 illustrates, V-defects have already proven themselves to be the most viable solution to the green gap (especially in WPE) by significantly improving performance at the longer wavelengths as shown by the Nanchang results. It's important to note that these results were also achievable through advancements in active region growth for green and red LEDs such as the use of very high TMI flows, AlGaN capping layers, pre-well layers and much more [23]. This will be discussed in detail in Chapter 6. There's also a lot more background on V-defects that could be covered but since V-defect engineering is the subject of the rest of this dissertation, we'll discuss it in future chapters.

This concludes the introduction and background. Now on to the findings of this PhD!

References:

[1] O. Ambacher *et al.*, "Pyroelectric properties of Al(In)GaN/GaN hetero- and quantum well structures," *J. Phys. Condens. Matter*, vol. 14, no. 13, pp. 3399–3434, 2002, doi: 10.1088/0953-8984/14/13/302.

[2] F. Bernardini and V. Fiorentini, "First-principles calculation of the piezoelectric tensor d of III-V nitrides," *Appl. Phys. Lett.*, vol. 80, no. 22, pp. 4145–4147, 2002, doi: 10.1063/1.1482796.

[3] V. Fiorentini, F. Bernardini, and O. Ambacher, "Evidence for nonlinear macroscopic polarization in III-V nitride alloy heterostructures," *Appl. Phys. Lett.*, vol. 80, no. 7, pp. 1204–1206, 2002, doi: 10.1063/1.1448668.

[4] W. Götz, N. M. Johnson, H. Amano, and I. Akasaki, "Deep level defects in n -type GaN," *Appl. Phys. Lett.*, vol. 65, no. 4, pp. 463–465, Jul. 1994, doi: 10.1063/1.112337.

[5] L. Cai and C. Feng, "Effect of Vacancy Defects on the Electronic Structure and Optical Properties of GaN," *J. Nanotechnol.*, vol. 2017, no. 7, pp. 1–6, 2017, doi: 10.1155/2017/6987430.

[6] D. C. Look, G. C. Farlow, P. J. Drevinsky, D. F. Bliss, and J. R. Sizelove, "On the nitrogen vacancy in GaN," *Appl. Phys. Lett.*, vol. 83, no. 17, pp. 3525–3527, 2003, doi: 10.1063/1.1623009.

[7] J. Neugebauer and C. G. Van de Walle, "Gallium vacancies and the yellow luminescence in GaN," *Appl. Phys. Lett.*, vol. 69, no. 4, pp. 503–505, 1996, doi: 10.1063/1.117767.

[8] C. B. Soh, S. J. Chua, H. F. Lim, D. Z. Chi, W. Liu, and S. Tripathy, "Identification of deep levels in GaN associated with dislocations," *J. Phys. Condens. Matter*, vol. 16, no. 34, pp. 6305–6315, 2004, doi: 10.1088/0953-8984/16/34/027.

[9] J. Neugebauer and C. G. Van de Walle, "Native defects and impurities in GaN," 1996, pp. 25–44.

[10] M. A. Reshchikov and H. Morkǫ, "Luminescence properties of defects in GaN," *J. Appl. Phys.*, vol. 97, no. 6, 2005, doi: 10.1063/1.1868059.

[11] F. . Frank, "The influence of dislocations on crystal growth," *Discuss. Faraday Soc.*, vol. 5, pp. 48–54, 1949.

[12] F. Wu *et al.*, "Stacking fault formation in the long wavelength InGaN/GaN multiple quantum wells grown on m -plane GaN," *Appl. Phys. Lett.*, vol. 96, no. 23, 2010, doi: 10.1063/1.3447940.

[13] C. Stampfl and C. G. Van de Walle, "Energetics and electronic structure of stacking faults in AlN, GaN, and InN," *Phys. Rev. B - Condens. Matter Mater. Phys.*, vol. 57, no. 24, pp. R15052–R15055, 1998, doi: 10.1103/PhysRevB.57.R15052.

[14] A. R. Denton and N. W. Ashcroft, "Vegard's law," *Phys. Rev. A*, vol. 43, no. 6, p. 3161, 1991.

[15] Q. Wen, X. Wei, F. Jiang, J. Lu, and X. Xu, "Focused Ion Beam Milling of Single-Crystal Sapphire," *Materials (Basel).*, vol. 12, no. 13, p. 2871, 2020, doi: https://doi.org/10.3390/ma13122871.

[16] A. S. Bakri, N. Nayan, A. Shuhaimi, A. Bakar, M. Tahan, and N. Amaliyana, "A

Review on the Different Techniques of GaN Heteroepitaxial Growth : Current Scenario and Future Outlook," *Int. J. Nanoelectron. Mater.*, vol. 13, no. 1, pp. 199–220, 2020.

[17] X. H. Wu *et al.*, "Dislocation generation in GaN heteroepitaxy," vol. 190, pp. 231–243, 1998.

[18] S. Nakamura, Y. Harada, and M. Seno, "Novel metalorganic chemical vapor deposition system for GaN growth," *Appl. Phys. Lett.*, vol. 58, no. 18, pp. 2021–2023, 1991, doi: 10.1063/1.105239.

[19] C. Haller *et al.*, "GaN surface as the source of non-radiative defects in InGaN/GaN quantum wells," *Appl. Phys. Lett.*, vol. 113, no. 11, Sep. 2018, doi: 10.1063/1.5048010.

[20] W. Y. Ho *et al.*, "Detection of hot electrons originating from an upper valley at ∼1.7 eV above the Γ valley in wurtzite GaN using electron emission spectroscopy," *Phys. Rev. B*, vol. 107, no. 3, p. 35303, 2023, doi: 10.1103/PhysRevB.107.035303.

[21] C. Lynsky *et al.*, "Role of V-defect density on the performance of III-nitride green LEDs on sapphire substrates," *J. Cryst. Growth*, vol. 560–561, no. November 2020, p. 126048, 2021, doi: 10.1016/j.jcrysgro.2021.126048.

[22] J. Ewing *et al.*, "Influence of Superlattice Structure on V-Defect Distribution, External Quantum Efficiency and Electroluminescence for Red InGaN Based μLEDs on Silicon," *Crystals*, vol. 12, no. 9, Sep. 2022, doi: 10.3390/cryst12091216.

[23] J. Il Hwang, R. Hashimoto, S. Saito, and S. Nunoue, "Development of InGaN-based

red LED grown on (0001) polar surface," *Appl. Phys. Express*, vol. 7, no. 7, 2014, doi: 10.7567/APEX.7.071003.

[24] E. Kioupakis, P. Rinke, K. T. Delaney, and C. G. Van De Walle, "Indirect Auger recombination as a cause of efficiency droop in nitride light-emitting diodes," *Appl. Phys. Lett.*, vol. 98, no. 16, pp. 1–4, 2011, doi: 10.1063/1.3570656.

[25] J. Iveland, L. Martinelli, J. Peretti, J. S. Speck, and C. Weisbuch, "Direct measurement of auger electrons emitted from a semiconductor light-emitting diode under electrical injection: Identification of the dominant mechanism for efficiency droop," *Phys. Rev. Lett.*, vol. 110, no. 17, pp. 1–5, 2013, doi: 10.1103/PhysRevLett.110.177406.

[26] M. H. Kim *et al.*, "Origin of efficiency droop in GaN-based light-emitting diodes," *Appl. Phys. Lett.*, vol. 91, no. 18, pp. 1–4, 2007, doi: 10.1063/1.2800290.

[27] T. Langer *et al.*, "Origin of the 'green gap': Increasing nonradiative recombination in indium-rich GaInN/GaN quantum well structures," *Phys. Status Solidi Curr. Top. Solid State Phys.*, vol. 8, no. 7–8, pp. 2170–2172, Jul. 2011, doi: 10.1002/pssc.201001051.

[28] S. Pleasants, "Overcoming the 'green gap,'" *Nat. Photonics*, vol. 7, no. 8, pp. 585–585, 2013, doi: 10.1038/nphoton.2013.202.

[29] R. C. White *et al.*, "Ingan-based microled devices approaching 1% eqe with red 609 nm electroluminescence on semi-relaxed substrates," *Crystals*, vol. 11, no. 11, pp. 1–9, 2021, doi: 10.3390/cryst11111364.

[30] S. S. Pasayat *et al.*, "Compliant micron-sized patterned ingan pseudo-substrates

utilizing porous GaN," *Materials (Basel).*, vol. 13, no. 1, pp. 6–15, 2020, doi: 10.3390/ma13010213.

[31] S. S. Pasayat *et al.*, "Growth of strain-relaxed InGaN on micrometer-sized patterned compliant GaN pseudo-substrates," *Appl. Phys. Lett.*, vol. 116, no. 11, 2020, doi: 10.1063/5.0001480.

[32] S. S. Pasayat *et al.*, "Color-tunable < 10 μ m square InGaN micro-LEDs on compliant GaN-on-porous-GaN pseudo-substrates," *Appl. Phys. Lett.*, vol. 117, no. 6, 2020, doi: 10.1063/5.0011203.

[33] P. Chan, S. P. DenBaars, and S. Nakamura, "Growth of highly relaxed InGaN pseudo-substrates over full 2-in. wafers," *Appl. Phys. Lett.*, vol. 119, no. 13, 2021, doi: 10.1063/5.0064755.

[34] P. Chan *et al.*, "Demonstration of relaxed InGaN-based red LEDs grown with high active region temperature," *Appl. Phys. Express*, vol. 14, no. 10, 2021, doi: 10.35848/1882-0786/ac251d.

[35] V. Rienzi *et al.*, "Demonstration of III-Nitride Red LEDs on Si Substrates via Strain-Relaxed Template by InGaN Decomposition Layer," *Crystals*, vol. 12, no. 8, Aug. 2022, doi: 10.3390/cryst12081144.

[36] N. Lim, P. Chan, H. Chang, V. Rienzi, M. J. Gordon, and S. Nakamura, "Structural, Optical, and Electrical Characterization of 643 nm Red InGaN Multiquantum Wells Grown on Strain-Relaxed InGaN Templates," *Adv. Photonics Res.*, vol. 4, no. 3, pp. 1–8, 2023, doi: 10.1002/adpr.202200286.

[37] X. H. Wu *et al.*, “Structural origin of V-defects and correlation with localized excitonic centers in InGaN/GaN multiple quantum wells,” *Appl. Phys. Lett.*, vol. 72, no. 6, pp. 692–694, 1998, doi: 10.1063/1.120844.

[38] A. Hangleiter *et al.*, “Suppression of nonradiative recombination by V-shaped pits in GaInN/GaN quantum wells produces a large increase in the light emission efficiency,” *Phys. Rev. Lett.*, vol. 95, no. 12, Sep. 2005, doi: 10.1103/PhysRevLett.95.127402.

[39] Z. J. Quan, J. L. Liu, F. Fang, G. X. Wang, and F. Y. Jiang, “Effect of V-shaped Pit area ratio on quantum efficiency of blue InGaN/GaN multiple-quantum well light-emitting diodes,” *Opt. Quantum Electron.*, vol. 48, no. 3, pp. 1–8, Mar. 2016, doi: 10.1007/s11082-016-0464-7.

[40] Z. Quan, L. Wang, C. Zheng, J. Liu, and F. Jiang, “Roles of V-shaped pits on the improvement of quantum efficiency in InGaN/GaN multiple quantum well light-emitting diodes,” *J. Appl. Phys.*, vol. 116, no. 18, 2014, doi: 10.1063/1.4901828.

[41] X. Wu *et al.*, “Electroluminescence from the sidewall quantum wells in the V-shaped pits of InGaN light emitting diodes,” *Appl. Phys. Lett.*, vol. 104, no. 22, Jun. 2014, doi: 10.1063/1.4880731.

[42] X. Wu, J. Liu, and F. Jiang, “Hole injection from the sidewall of V-shaped pits into c -plane multiple quantum wells in InGaN light emitting diodes,” *J. Appl. Phys.*, vol. 118, no. 16, Oct. 2015, doi: 10.1063/1.4934503.

[43] J. L. Liu *et al.*, “Status of GaN-based green light-emitting diodes,” *Chinese Phys. B*, vol. 24, no. 6, 2015, doi: 10.1088/1674-1056/24/6/067804.

[44] C. K. Li *et al.*, “3D numerical modeling of the carrier transport and radiative efficiency for InGaN/GaN light emitting diodes with V-shaped pits,” *AIP Adv.*, vol. 6, no. 5, May 2016, doi: 10.1063/1.4950771.

[45] F. Wu *et al.*, “Structure of V-defects in long wavelength GaN-based light emitting diodes,” *J. Appl. Phys.*, vol. 035703, no. 133, 2023, doi: 10.1063/5.0135278.

[46] A. E. Romanov, T. J. Baker, S. Nakamura, and J. S. Speck, “Strain-induced polarization in wurtzite III-nitride semipolar layers,” *J. Appl. Phys.*, vol. 100, no. 2, 2006, doi: 10.1063/1.2218385.

[47] J. J. Ewing *et al.*, “High External Quantum Efficiency (6.5%) InGaN V-defect LEDs at 600 nm on Patterned Sapphire Substrates,” *Opt. Express (accepted Publ.*, 2023.

[48] F. Jiang *et al.*, “Efficient InGaN-based yellow-light-emitting diodes,” *Photonics Res.*, vol. 7, no. 2, pp. 144–148, 2019.

[49] S. Zhang *et al.*, “Efficient emission of InGaN-based light-emitting diodes: toward orange and red,” *Photonics Res.*, vol. 8, no. 11, p. 1671, 2020, doi: 10.1364/prj.402555.

[50] R. Armitage, Z. Ren, M. Holmes, and J. Flemish, “True-Red InGaN Light-Emitting Diodes for Display Applications,” *Phys. status solidi – Rapid Res. Lett.*, Mar. 2024, doi: 10.1002/pssr.202400012.

[51] G. Lheureux, C. Lynsky, Y.-R. Wu, J. S. Speck, and C. Weisbuch, “A 3D simulation comparison of carrier transport in green and blue c-plane multi-quantum well nitride light emitting diodes,” *J. Appl. Phys.*, vol. 128, no. 23, 2020, doi: 10.1063/1.5143276.

[52] C. Lynsky *et al.*, “Barriers to carrier transport in multiple quantum well nitride-based c -plane green light emitting diodes,” *Phys. Rev. Mater.*, vol. 4, no. 5, pp. 1–6, 2020, doi: 10.1103/PhysRevMaterials.4.054604.

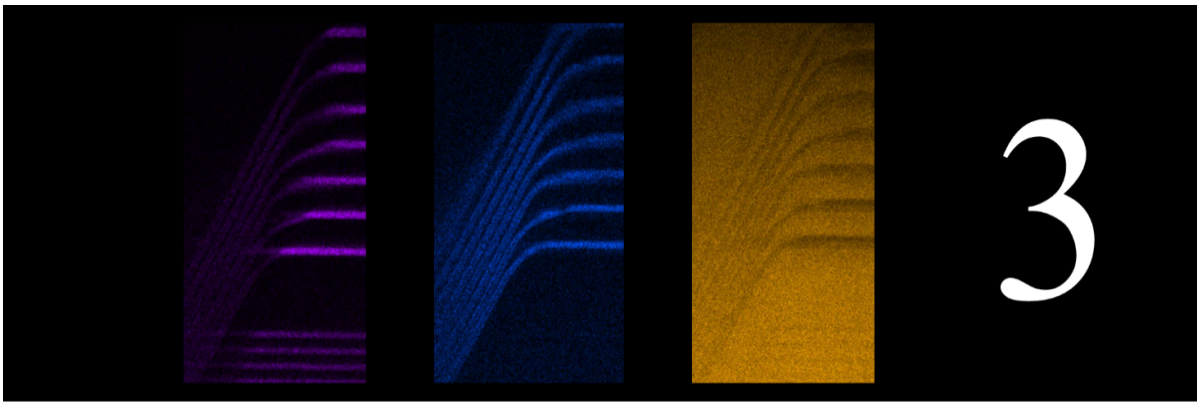

Structure and Properties of V-defects in LEDs

3.1 GaN growth and V-defect formation

The heteroepitaxial growth of GaN leads to a defective microstructure due to either the dissimilar bonding between the wurtzite structure nitrides and the foreign substrate or the large lattice mismatch [1], [2]. (0001) sapphire is the most widely used substrate for the growth of GaN for light emitting diodes. For [0001] oriented growth on sapphire the typical microstructure consists of a high density of threading dislocations (TDs) with ~[0001] line direction and either a Burgers vector $\mathbf{b} = \mathbf{a}_i = \frac{1}{3}\langle 11\bar{2}0\rangle$ or $\mathbf{b} = \mathbf{a}_i \pm \mathbf{c} = \frac{1}{3}\langle 11\bar{2}3\rangle$ Burgers vector. The TDs with $\mathbf{b} = \mathbf{a}_i$ usually have pure edge character and the $\mathbf{b} = \mathbf{a}_i \pm \mathbf{c}$ have mixed edge and screw character and are commonly referred to as "mixed" TDs. Growth on (0001) oriented sapphire or SiC typically results in a total TD density of 1×10^8 cm^{-2} – 1×10^9 cm^{-2} with ~80-90% of the TDs having pure edge character and 10-20% having mixed character. The density of pure screw TDs with $\mathbf{b} = \pm\mathbf{c}$ is typically on the order of 1×10^6 cm^{-2} [3], [4]. Despite the dislocation densities in typical GaN layers, the spacing between dislocations is sufficiently large compared to carrier diffusion lengths, such that today's blue LEDs can have peak internal quantum efficiencies (IQE) in excess of 90% [5], [6].

Circa 1950, F.C. Frank published a series of papers that theoretically described the structure of surface structure of crystal surfaces with dislocations [7], [8]. These papers predicted that the existence of dislocations would cause a local surface depression, such that the surface stress (often referred to as surface tension) would balance the line tension of the dislocation at the intersection of the dislocation and the free surface [9]. Figure 3.1a shows a surface depression resulting from a TD terminating at the surface of a crystal. In the mid-to-late 1990s, several research groups identified a morphological defect that forms at TDs in (0001) oriented growth of GaN [10]–[12]. The "V-defect" is an open hexagonal inverted pyramid with six $\{10\bar{1}1\}$ planes. The V-defects are also referred to as "V-pits" or "V-shaped" defects. The V-defects form at surface perturbations, such as the slight surface depression at the intersection of a TD with the (0001) surface, under conditions of kinetically limited growth [4]. Once nucleated, the growth velocity in the [0001] direction is faster for the (0001) plane than the $\{10\bar{1}1\}$ planes, as shown in Figure 3.1b and 3.1c. Reduced growth temperature and conditions with limited surface diffusion, or mass transport by sublimation/condensation, favor V-defect formation.

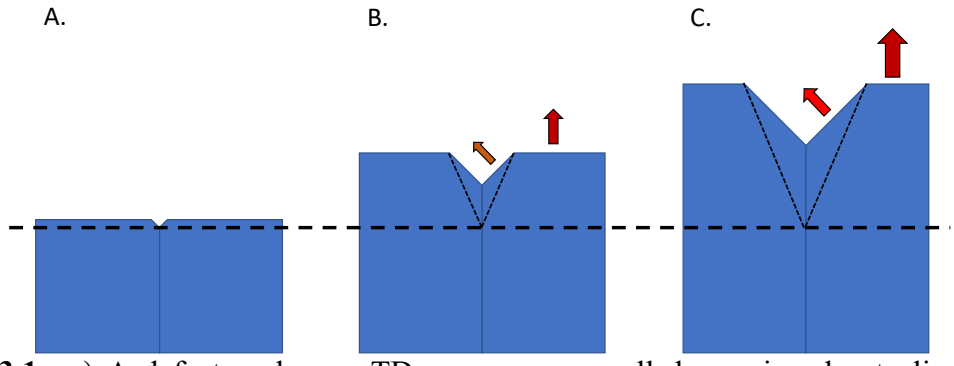

Figure 3.1: a.) A defect such as a TD can open a small depression due to line tension (described by F. C. Frank [8]) b.) Under select growth conditions that depression can open up into a V-defect with $\{10\bar{1}1\}$ sidewalls c.) Once the V-defect is sufficiently opened it will continue to enlarge as long as the c-plane growth rate exceeds the $(10\bar{1}1)$ growth rate. The horizontal dashed line provides a guide to the layer thickness at the onset of V-defect formation.

V-defects can also form at other perturbations of the growth surface, such as particulates, other contaminants, or intentional masking. Once formed, V-defects can easily be healed by subsequent high temperature growth or growth under conditions that allow sufficient mass transport to planarize the growth surface. It is common in nitride heterostructures, particularly those used for LEDs, to have either intentionally or unintentionally formed V-defects and yet have no morphological feature on the final growth surface.

In the last 10 years, LED researchers have begun to understand the importance of V-defects for realizing high IQE in long-wavelength LEDs. Most GaN LEDs are grown in the (0001) c-plane orientation, which has numerous epitaxial advantages over other planes but suffers from high polarization-related electrical fields that create significant barriers to vertical carrier injection through the InGaN/GaN quantum well/quantum barrier interface in the multi-quantum well (MQW) structures [13]–[15]. LED researchers realized through both experimental work and simulations that V-defects provided a unique opportunity to inject holes through the semi-polar $\{10\bar{1}1\}$ planes, which have slower growth rate leading to thinner quantum wells (QWs) and quantum barriers (QB) and, more importantly, lower polarization fields [16], [17]. In a 3D numerical modeling paper, Li *et al*. showed via a stress-strain solver and Poisson-drift-diffusion solver that semi-polar sidewalls provide pathways for current to flow and inject into the MQWs [18]. In a subsequent paper, Ho *et al*. showed that in green LEDs, due to the high polarization field, the V-defects provide an energetically preferred pathway for injection [19]. Furthermore, at high current densities the carriers injected through the sidewalls can screen some of the polarization field and thus enhance vertical transport. It has also been shown both in simulations and experimentally that higher V-defect densities lead

to lower forward voltage in green LEDs although extremely high V-defect densities cause a reduction in active region area which may reduce total efficiency [20].

The National Institute of LED on Silicon Substrate at Nanchang University pioneered much of the early experimental work on V-defect engineered long-wavelength LEDs as well as some key simulation results. Quan *et al*. showed via simulations that 'V-shaped pits' can decrease the barriers for injection for holes and therefore enable deeper hole injection in the MQWs [16]. Higher hole concentrations in the lower wells were shown to decrease the efficiency droop in simulated IQE plots. The following year (2015), Wu *et al*. showed experimental evidence of hole injection through the V-defect sidewalls [21]. In 2016, Quan *et al*. published a numerical investigation into the ideal size and density of V-defects for optimal IQE in blue LEDs [22]. They determined that 2-3 x 10^9 cm^{-2}, 110-140 nm, and 50% were the ideal density, size, and area ratio, respectively.

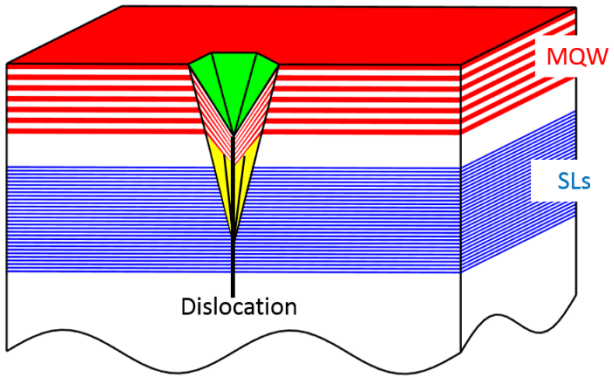

Figure 3.2: Schematic of a V-defect forming on a dislocation in the superlattice of an LED with red MQWs.

Realizing the ideal V-defect size distribution required further investigation into the formation of V-defects during growth. Qi *et al*. investigated the use of InGaN/GaN superlattices (SL) at varying thickness ratios [23]. They identified that V-defects were

consistently forming both in the InGaN/GaN superlattice, these they called “large V-pits”, and in the MQW region, which they referred to as “small V-pits”. Figure 3.2 shows a schematic of a large V-defect forming in the SL and opening into the MQW region. After showing that the InGaN/GaN superlattice could effectively nucleate the proper type of V-defects, the Nanchang LED group published a series of ground breaking papers on yellow LEDs and red/orange LEDs grown on (111) Si [24], [25]. The first paper showed 41.3% wall-plug efficiency (WPE) for green and 24.6% WPE for yellow at 20 A/cm^2. Their second paper showed 16.8% WPE for red (620 nm) and 30.1 WPE for orange (~595 nm) at 0.8 A/cm^2. These results far exceeded other WPEs in the literature at the respective wavelengths and greatly increased commercial and academic interest in V-defects as a method for increasing IQE in long-wavelength LEDs. Part of the success of the Nanchang group emerged from their expertise in GaN-on-Si technology and the higher threading dislocation density (TDD) (especially higher mixed-component TDD) that exists in GaN grown on (111) Si. Realizing a high TDD on patterned sapphire substrates (PSS) is challenging and much epitaxial research will be required to match these results on PSS or flat sapphire substrates (FSS).

In addition to V-defect engineering, there have been a number of other important innovations that have been important for the realization of high IQE green and red InGaN LEDs. Researchers at Toshiba pioneered the exceptionally high temperature growth of InGaN QWs, realized using very high indium precursor flows, followed by immediate capping of the InGaN QW with a thin (1 - 2 nm) AlGaN capping layer followed by higher temperature GaN quantum barrier layers to reduce impurity incorporation [26]. The UCSB group built on this work and developed improved quantum barriers that resulted in record efficiency green LEDs [27]. This innovation significantly increased the efficiency of green, yellow, and red LEDs by

using growth conditions that improved the material quality and likely reduced the density of Shockley-Reed-Hall (SRH) nonradiative recombination centers [28], [29].

This chapter gives a detailed structural analysis of the active region in high performance III-nitride green and red LEDs grown on either GaN on patterned sapphire substrates (PSS) or GaN on (111) silicon templates. We use scattering contrast transmission electron microscopy (TEM), high angle annular dark field (HAADF) scanning transmission electron microscopy (STEM), x-ray fluorescence maps from STEM, and atom probe tomography (APT). We show excellent agreement between chemical analysis from x-ray fluorescence and APT for the QW and QB composition and structure. The InGaN/GaN SL is effective at creating favorable large V-defects, nucleated below the active region, which initiate at mixed character TDs. Within the active device region (QWs and QBs) small V-defects may form – these V-defects are likely associated with stacking faults and three-dimensional stacking fault boxes. Scattering contrast TEM studies show that the mixed TD associated with V-defects is inclined on one of the six $\{10\bar{1}1\}$ V-defect sidewalls as opposed to sustaining a straight [0001] line direction – this is consequential for nonradiative recombination.

3.2 Experimental methodology

All samples described in this article were grown by atmospheric pressure metalorganic chemical vapor deposition (MOCVD) at UCSB. The samples are all long wavelength LEDs grown on either PSS or (111) GaN-on-silicon templates from Enkris Semiconductor. The general growth approach follows our recent work on long wavelength LEDs where the pre-QW short period InGaN/GaN superlattice (SL) forms the desirable larger 200-300 nm diameter V-defects with well-defined $\{10\bar{1}1\}$ sidewalls that promote hole injection [21]. The active region uses high trimethyl indium (TMI) flows during quantum well growth to enable higher growth

temperatures for the active region. To suppress decomposition of the InGaN QW, a thin AlGaN capping layer was grown at the same temperature as the QW followed by a multistep quantum barrier growth at higher temperatures [27], [30].

For all samples high resolution x-ray diffraction (HRXRD) ω-2θ measurements of thick InGaN and AlGaN calibration samples were performed on a Panalytical MRD PRO using Cu $K_{\alpha 1}$ radiation (λ = 1.5405 Å) to calibrate the alloy compositions and growth rates. Secondary ion mass spectroscopy (SIMS) using a Cameca IMS 7f Auto SIMS was used to calibrate the Mg- and Si-doping concentrations.

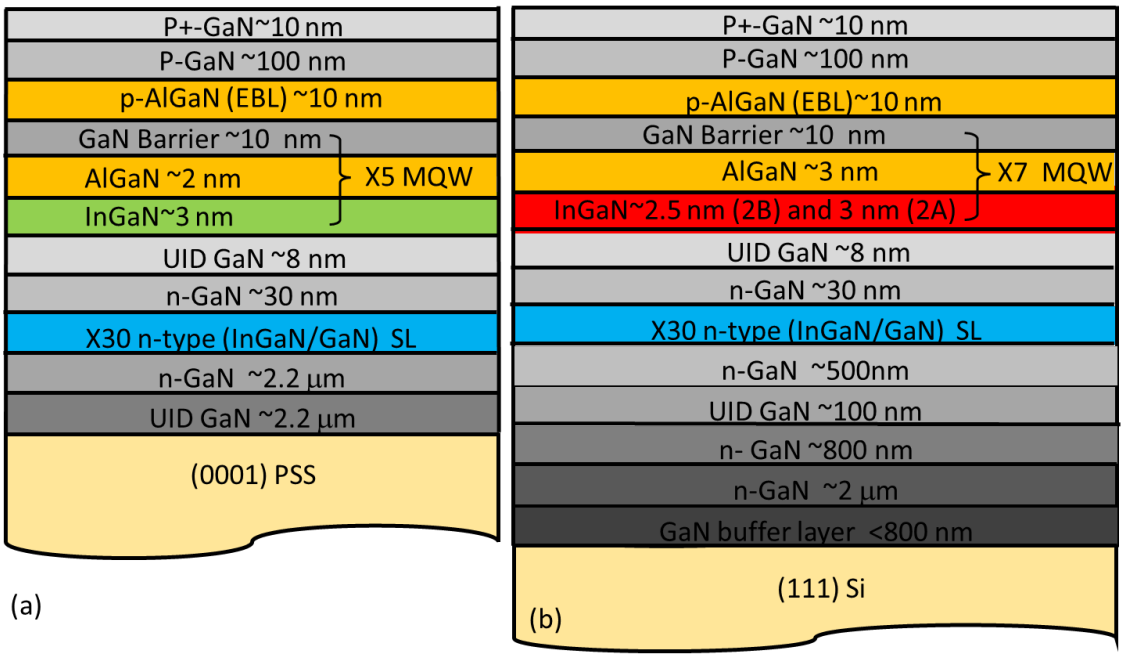

Figure 3.3: Epitaxial structures for (a) samples 1 (green LED, In ~22%) and (b) samples 2A and 2B (red LEDs, In ~ 27-30%)

Sample 1 was a green LED (peak wavelength ~515 nm) grown on PSS. A low temperature GaN nucleation layer was followed by 2.2 µm of unintentionally doped (UID) GaN, 2.2 µm of *n*-GaN ([Si] = 5×10^{18} cm^{-3}), a 30-period *n*-type InGaN (2.5 nm)/GaN (5 nm) superlattice, a 30 nm *n*-GaN layer, and an 8 nm UID GaN spacer. The five QW period active

region was undoped and consisted of 3 nm InGaN QWs, 2 nm $Al_{0.1}Ga_{0.90}N$ capping layers, and 10-nm GaN QBs. The *p*-side of the LED contained a 10 nm *p*-AlGaN electron blocking layer ([Mg] = 9×10^{19} cm^{-3}), 100 nm of *p*-GaN ([Mg] = 5×10^{19} cm^{-3}), and a 10 nm *p*+-GaN contact layer. The schematic is shown on the left side of Figure 3.3.

Samples 2A and 2B were red LEDs (peak wavelength ~600 nm and ~620 nm, respectively) grown on commercial GaN-on-Si templates purchased from Enkris Semiconductor. The Enkris template consists of a (111)-oriented Si substrate, a <800 nm buffer layer, 2 μm of *n*-GaN ([Si] < 1×10^{17} cm^{-3}), 800 nm of *n*-GaN ([Si] = 5×10^{18} cm^{-3}), and 100 nm of UID GaN. The 6-inch GaN-on-Si templates were diced into 13x13 mm^2 pieces and cleaned using heated n-Methylpyrrolidone (NMP), acetone, isopropanol, and water before re-growth. The re-growth began with 500 nm of *n*-GaN ([Si] = 5×10^{18} cm^{-3}) followed by a 30-period *n*-type ([Si] = 5×10^{18} cm^{-3}) InGaN (2.5 nm)/GaN (5 nm) superlattice, a 30 nm *n*-GaN layer, and a 2 nm UID GaN spacer. The seven QW period active region was undoped and consisted of low temperature InGaN QWs (3 nm for Sample 2A and 2.5 nm for Sample 2B), 3 nm $Al_{0.35}Ga_{0.65}N$ capping layers, and 10 nm GaN QBs. Thinner QWs were used for the longer wavelength sample because it provided more consistent control of the emission wavelength. The *p*-side of the LED contained a 10 nm *p*-AlGaN electron blocking layer ([Mg] = 1×10^{20} cm^{-3}), 100 nm of *p*-GaN ([Mg] = 5×10^{19} cm^{-3}), and a 10 nm *p*+-GaN contact layer. The schematic on the right side of Figure 3.3 shows the epitaxial structure on Si.

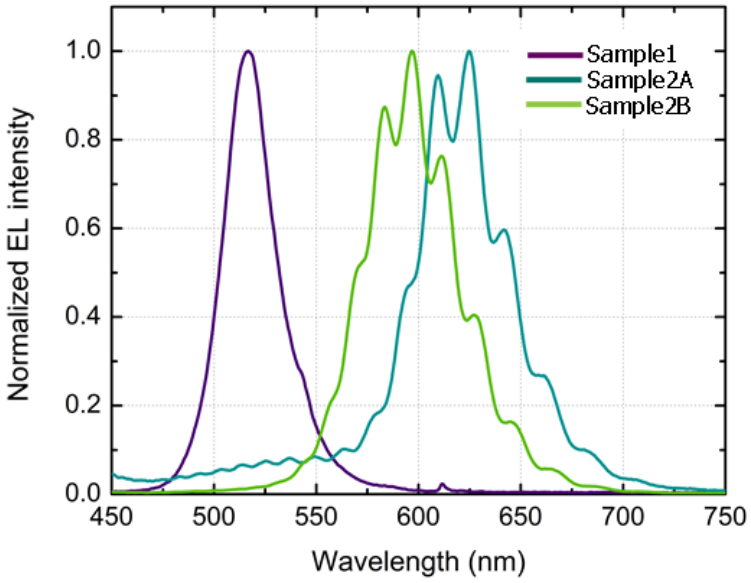

Figure 3.4: Electroluminescence spectra of the three samples studied in this paper. The data is taken from quick test at 20 mA. The peak wavelength/FWHM (as determined by Gaussian fitting) are: Sample 1-517/33 nm, Sample 2A-620 nm/53 nm, Sample 2B 596 nm/55 nm.

Figure 3.4 shows the electroluminescence spectra for the three samples. The green LED (Sample 1) had a peak emission wavelength of ~517 nm and a full width at half maximum (FWHM) of 33 nm. Samples 2A and 2B had peak emission wavelength of 620 and 596 nm and FWHMs of 53 and 55 nm respectively.

Conventional TEM (CTEM), HAADF STEM, and x-ray fluorescence as measured in an energy dispersive x-ray spectroscopy (EDS) mapping were performed with a ThermoFisher Talos G2 200X TEM/STEM system equipped with EDS, operated at 200 kV. Velox STEM/TEM software including an EDS analysis package was used for supporting imaging and analysis. APT analysis was performed using a Cameca 3000XHR LEAP Microscope, in pulsed laser mode with a 532 nm green laser. The specimen base temperature was approximately 45 K, the laser pulse energy was 0.25 nJ, and pulse frequency was 200 kHz.

Data reconstruction and analysis were done using IVAS 3.8 software. The cross-sectional and plan-view TEM samples, as well as the needle-shape APT sample, were prepared by focused ion beam (FIB) using an FEI Helios Dualbeam Nanolab 600 instrument.

3.3 Transmission Electron Microscopy of V-defects in LEDs

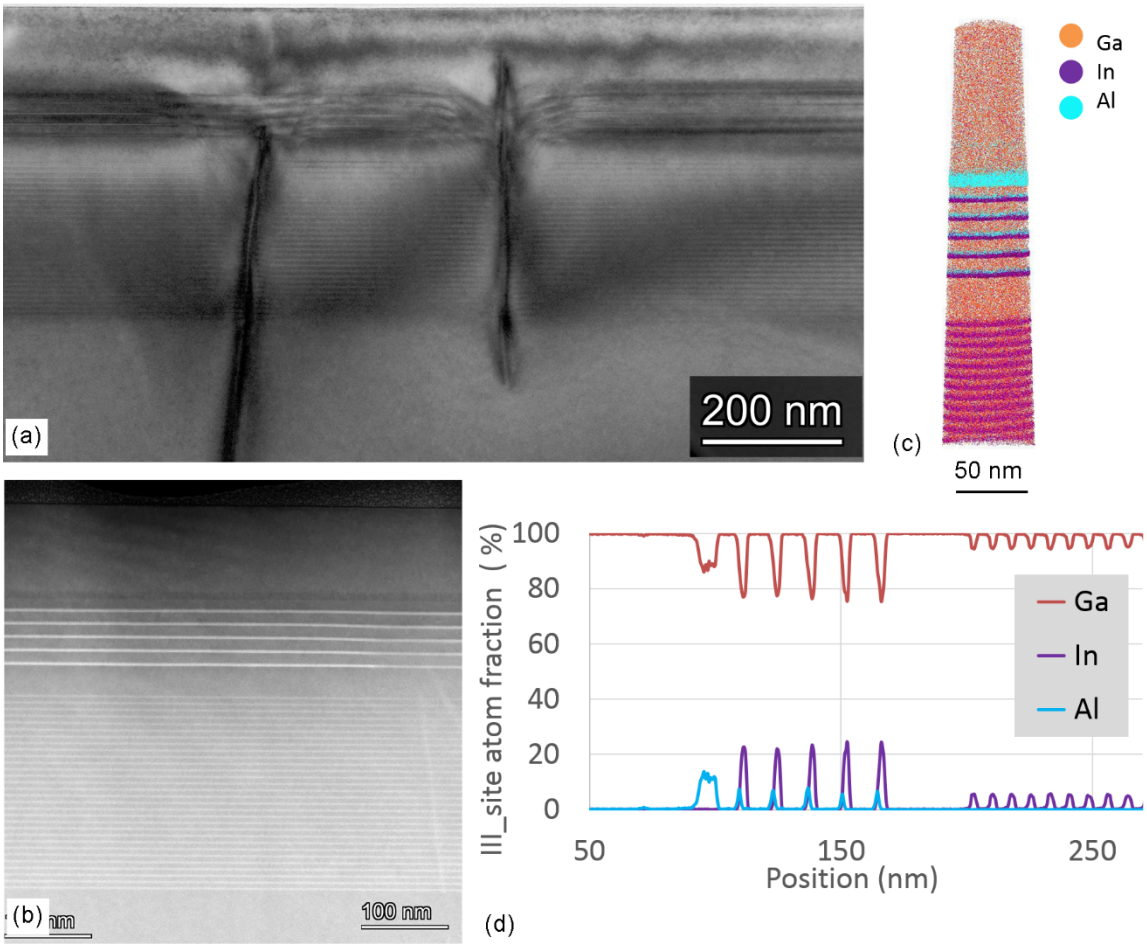

Figure 3.5: Sample 1 green LED TEM/STEM and APT (a) cross-section electron scattering contrast TEM: planar and V-defect region taken in a $[11\bar{2}0]$ zone axis. (b) HAADF showing planar QW and QB (to show epi approach). (c) APT showing planar QW and QB APT composition line profile. The aluminum composition in EBL layer is about 10% and in the MQW capping layer is about 8%. The indium composition in the QW is about 23% and in SL is about 6%. (d) APT composition line profile showing Ga, In, and Al site fractions.

Figure 3.5 shows TEM and APT result from the green LED sample. Figure 3.5a is a multiple beam electron beam scattering contrast image taken in a $[11\bar{2}0]$ zone axis. Two

threading dislocations show contrast in the image, where both cause V-defect generation in the InGaN/GaN SL. The V-defects in SLs were partially filled by the following GaN layer. In the MQW growth stage, the MQW grew on the sidewalls of the open hexagonal inverted pyramids. The sidewalls are comprised of well-defined $\{10\bar{1}1\}$ planes. The open V-defects were subsequently filled by the following GaN:Mg layer to realize the final smooth surface. Figure 3.5b is an HAADF image from a region only showing the planar QWs (away from any V-defects). The layer structure is in close agreement with the expected MOCVD growth structure as it shows all layers at their expected thicknesses. Figure 3.5c and 3.5d are APT results. Figure 3.5c is a three dimensional (3D) APT element map which shows the pre-well SL, InGaN QWs with the AlGaN caps, the AlGaN EBL, and the top GaN:Mg layer. Figure 3.5d is one dimensional (1D) chemical composition profile. The indium group III site atom concentration in QWs and SLs was about 23% and 6%, respectively – these compositions are consistent with our earlier work on green LEDs [27], [30]. The HAADF STEM image shows that away from the V-defects both the QWs and pre-well SLs are planar and laterally uniform. The green LED results shown here were grown on PSS substrates with growth procedures that have not been optimized for the intentional formation of large V-defects – namely because the density of mixed character TDs is too low [20].

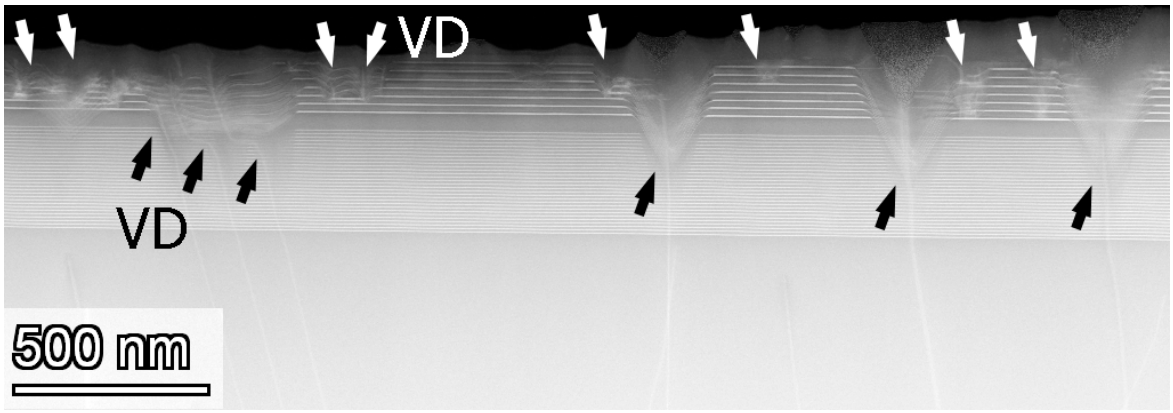

Figure 3.6: Low magnification cross-section HAADF image of Sample 2 showing two types of V-defects (VD in the figure). Large V-defects, indicated by black arrows, from SL and small V-defects, indicated by white arrows, from the QW caused by stacking faults (SFs) or SF boxes.

Long wavelength LEDs can also be successfully developed on silicon substrates, as pioneered by the Nanchang University group. GaN-on-Si templates typically have higher total TD density than GaN on PSS and a higher density of mixed character TDs, ~ 1×10^{9} cm^{-2}, which initiate the formation of the favorable large V-defects in the pre-well SL. As an example, Fig. 3.6 is an HAADF cross-section STEM images taken from a red LED on Si (Sample 2A). Large V-defects, indicated with black arrows, form at TDs in the pre-well SL. Within the active region of the device, unfavorable V-defects form and are usually associated with basal plane stacking faults (BPSFs) or three-dimensional stacking fault boxes (SFB) – we will provide full details of the structure of the SFB in a separate paper. The large V-defects should be similar to the favorable V-defects for lateral carrier injection. The formation of smaller V-defects in the active region and associated BPSFs, which are terminated by partial dislocations, and the SFBs are all likely associated with locally high nonradiative recombination and thus reduced device efficiency. Through improved epilayer design and growth procedures the unfavorable small V-defects and other extended defects within the active region can be eliminated. The roughness on top of the sample is due to p-GaN conditions that were not optimized for planarization; however, this has no effect on the underlying V-defect formation.

For V-defects to act as preferential sites for hole injection, they must have relatively uniform $\{10\bar{1}1\}$ semi-polar sidewalls where the holes can be laterally injected into the planar QWs. A close inspection of the V-defects shown in Figure 3.6 reveals that only 'large' V-defects (black arrows) have these well-defined semi-polar sidewalls. The 'small' V-defects (white arrows) that form in the MQW region show non-uniform growth of the QWs, AlGaN caps, and GaN barriers. In addition, it is likely that crystallographic defects are introduced into the QWs locally around small V-defects. These would become SRH and Trap-Assisted Auger Recombination (TAAR) centers and further degrade performance. Furthermore, small V-defects often form in conjunction with stacking fault boxes or other complex defects which provide additional sites for non-radiative recombination.

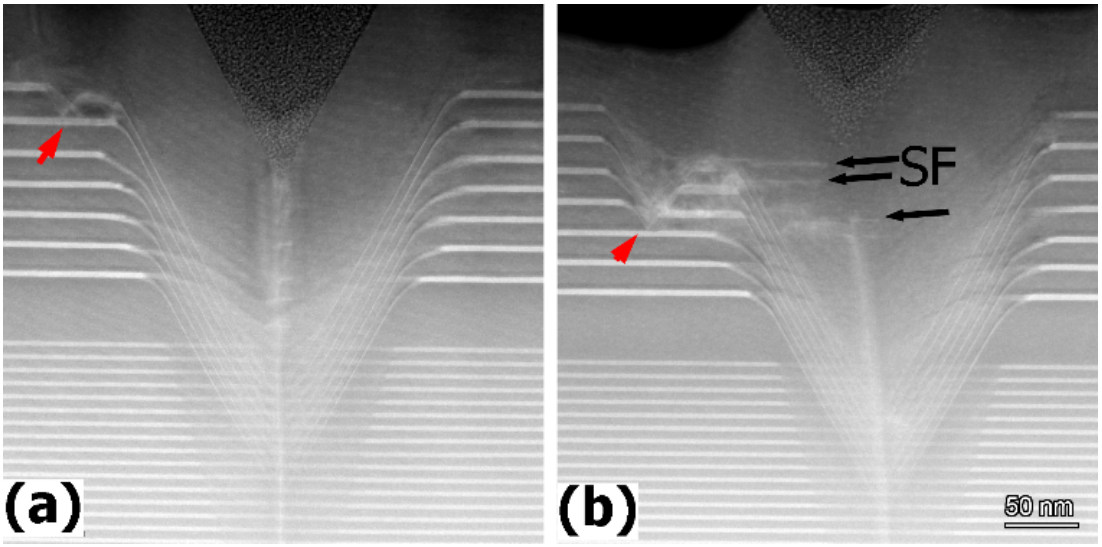

Figure 3.7: HAADF of large V-defects in Sample 2A (a) shows a large V-defect forming in the superlattice with well-defined semi-polar sidewalls that merge into the planar QWs, and the central TD. (b) is a similar image but showing a smaller V-defect that formed in the QW. The red arrows for images (a) and (b) show the formation of small V-defects. Additionally, in image (b), BPSFs are observed as indicated by the black arrows.

Figure 3.7 is an enlarged HAADF image of Figure 3.6 (Sample 2A). The MQW grown on the $\{10\bar{1}1\}$ sidewall of V-defect are thinner compare to those on planar area. As described in the Introduction, the $\{10\bar{1}1\}$ sidewalls have lower growth rate in comparison with the [0001]

growth rate of the planar (0001) regions, thus the QWs are thinner on the sidewalls than the planar regions. The new V-defects ("small V-defects") generated in different layers of MQW are denoted by the red arrows in Figure 3.7a and 3.7b. The large V-defect shown in Figure 3.7b exhibits more obvious V-defect feature. Compared to the large V-defects generated from the SL, the inclined MQW layers of the small V-defect are not parallel; however, the shape is still an inverted hexagonal pyramid with $\{10\bar{1}1\}$ sidewalls. The lateral line contrast corresponds to BPSFs, suggesting that stacking faults were induced by the large V-defect, which in turn caused new V-defect formation. As a result, the planar MQW layer quality is further reduced.

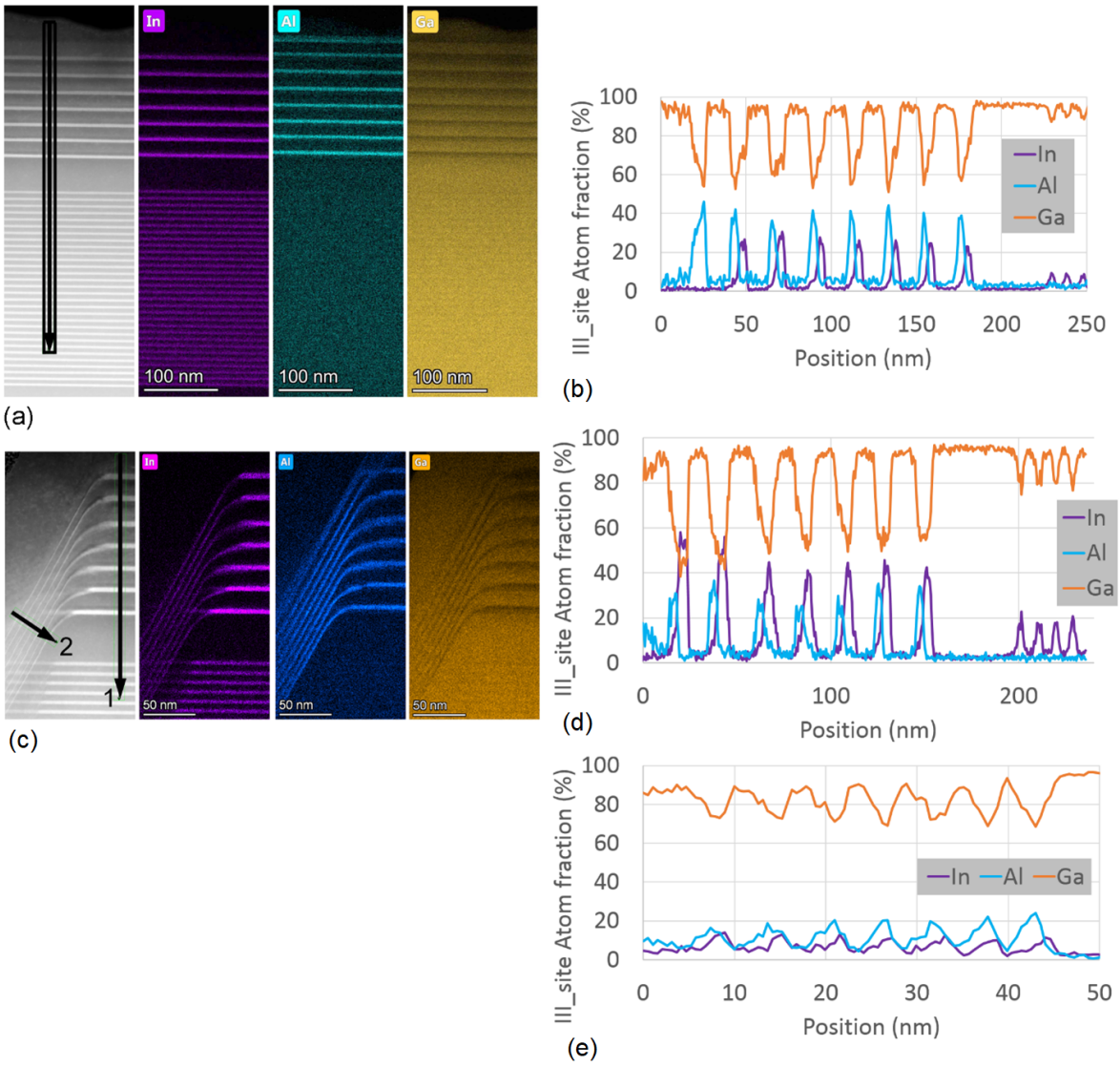

Figure 3.8: HAADF imaging and x-ray fluorescence-based composition maps for In, Al, and Ga (a) Image, compositions, and (b) 1D concentration profile in a planar region (away from V-defects) for Sample 2A (red LED). The x-ray fluorescence shows that that peak In content in the QWs is ~27% and the peak Al content in the AlGaN capping layer is ~43%. (c) Image, compositions, and (d) 1D concentration profile in a planar region near the V-defects – the composition profile (right panel) is from line 1 indicated in the figure. Note that the planar QWs adjacent to the V-defect have higher peak In content of nearly ~40% and the top (p-side) QW has a composition as high as ~55%. The Al content in the planar regions adjacent to the V-defect is lower at ~30%. (e) X-ray fluorescence line scan normal to the $\{10\bar{1}1\}$ sidewall QWs. The thin sidewall QWs have a peak In content of ~12% and the AlGaN capping layers on the sidewalls have a peak Al content of ~20%. The In and Al peaks appear wider and less abrupt due to the smaller scale for the line scan and the lower signal to noise ratio in EDS.

Figure 3.8 shows the STEM EDS results of the Sample 2A. Figure 3.8a show the In, Al, and Ga element maps and corresponding 1D group III site concentration profile, taken from the planar region away from the V-defect. The indium concentration in the MQW is ~27%, in very reasonable agreement of the results from APT on sample 2B. The Al content of the capping layer is 43%. Figure 3.8b shows image, composition, and 1D concentration profiles in the planar region near a V-defect – the composition profile (right panel) is from line 1 indicated in the figure. Note that the planar QWs adjacent to the V-defect have higher peak In content of nearly~40% and the top QW has a composition as high as ~55%. The higher In fraction proximal to the V-defects was not observed in all V-defects. The planar In content near V-defects remains an topic of ongoing study. The Al content in the planar regions adjacent to the V-defect is lower at ~30%. Figure 3.8c shows the X-ray fluorescence line scan normal to the $\{10\bar{1}1\}$ sidewall QWs, indicated by line 2 in Figure 3.8b. The thin sidewall QWs have a peak In content of ~12% and the AlGaN capping layers on the sidewalls have a peak Al content of ~20%. The lower Al content of the capping layers on the V-defect sidewall is a surprise as Al normally has a high sticking or incorporation coefficient in MOCVD growth and thus we may expect higher Al content in the sidewall capping layers.

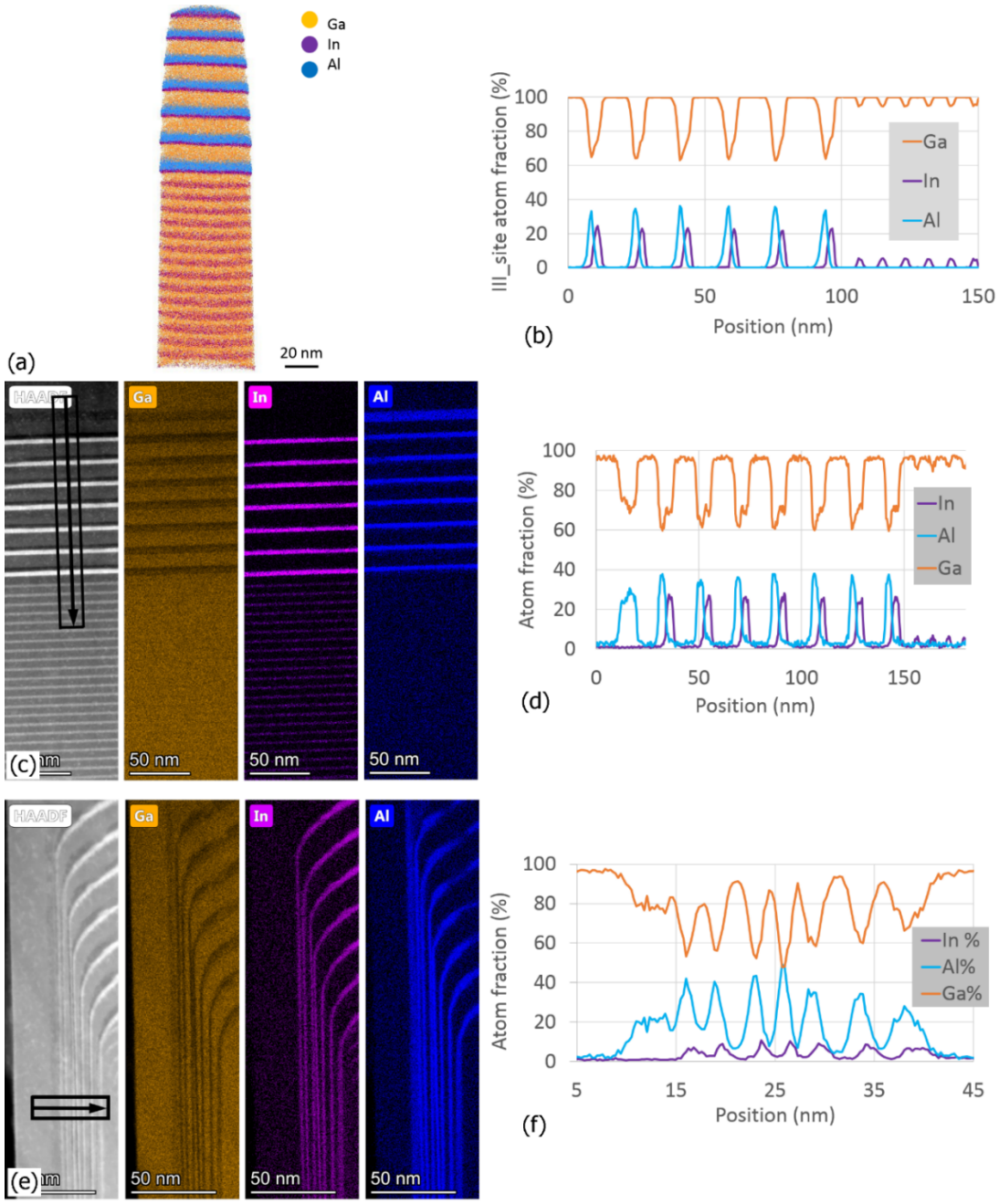

Figure 3.9: APT, HAADF, and x-ray fluorescence from Sample 2B. (a) APT showing planar QW and QB APT composition line profile. (b) The composition line profile shows that that peak indium content in the QWS is ~27% and the peak Al content in the AlGaN capping layer is ~38%. (c) X-ray fluorescence element maps measured by EDS. The arrow indicates the direction of the line scan and the box around the arrow indicates the width of the line scan. (d) atomic fractions from the line profile in a planar region (away from V-defects). The composition measured by EDS is close to APT result. (e) X-ray fluorescence element maps via EDS, and (f) line profile line scan normal to the $\{10\bar{1}1\}$ sidewall QWs. The thin sidewall QWs have peak indium content of ~8% and the AlGaN capping layer on the sidewalls has a peak Al content of ~40%.

Figure 3.9 shows APT, HAADF, and x-ray fluorescence from Sample 2B. Figure 3.9a is the III-site chemical composition result measured via APT showing planar QW and QB composition line profile. The composition line profile (Figure 3.9b) shows that that peak indium content in the QWS is ~23% and the peak Al content in the AlGaN capping layer is ~38%. Figure 3.9c is EDS element maps from flat area far from the V-defects. The indium concentration measure by EDS is about 25% as shown in Figure 3.9d, close to APT result. Figure 3.9e is EDS element maps from the line scan taken from sidewall of a V-defect, and Figure 3.9f is 1D concentration profile cross the MQW. The indium concentration is below 10%. Unlike the results from Sample 2A, for Sample 2B, the Al capping layers have similar Al content for the planar (0001) QW regions and for the $\{10\bar{1}1\}$ sidewall QWs.

The STEM x-ray fluorescence and APT studies provide close agreement in the QW, AlGaN capping layer, and AlGaN electron blocking layer composition – both for the planar (0001) active region and for the V-defect region. Combined with layer thicknesses determined from HAADF imaging, these studies provide excellent quantitative inputs for 3D transport simulations for V-defect LEDs. Scattering contrast TEM studies (sometimes referred to as conventional TEM (CTEM)) provide excellent quantification of the nature of extended defects.

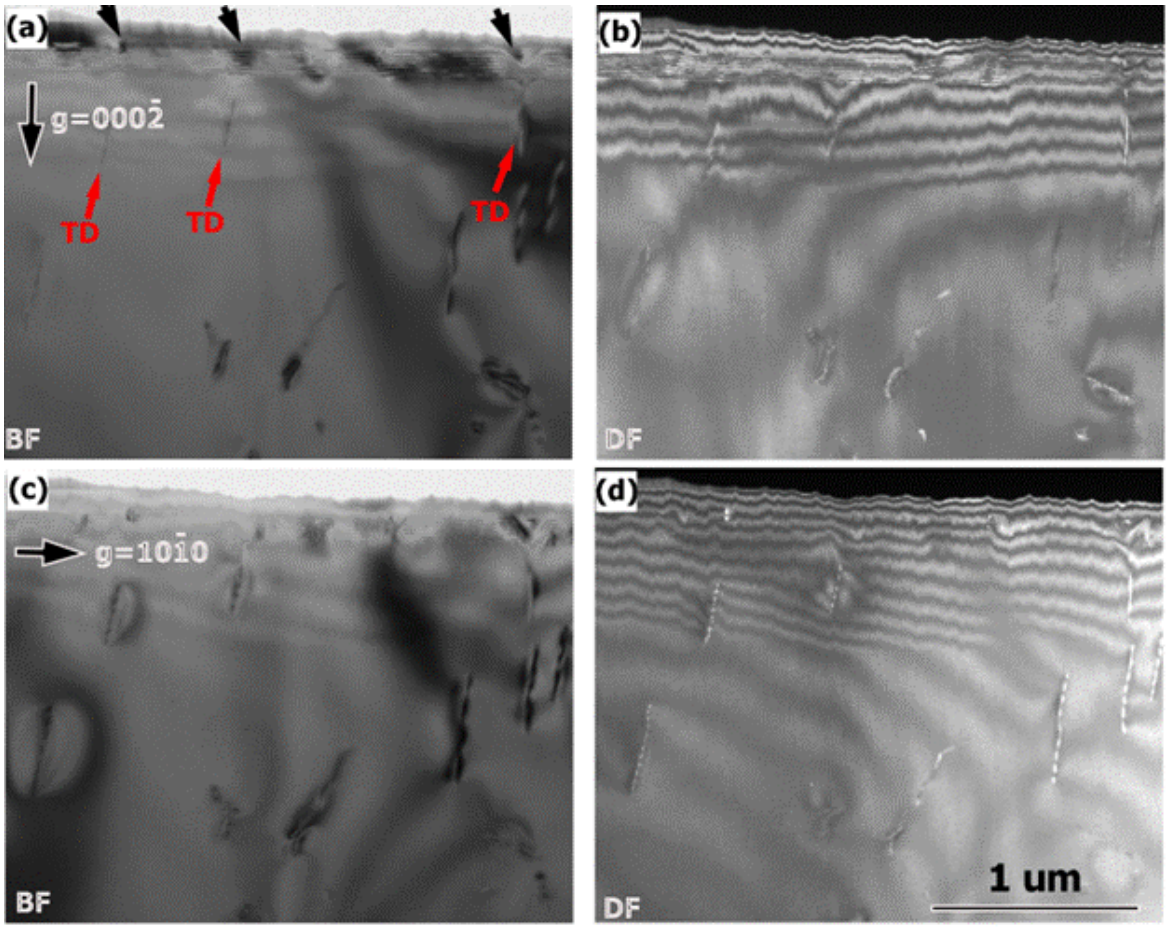

Figure 3.10. Cross-section two-beam imaging from Sample 2B to determine the Burgers vector and thus nature of the TDs in the GaN on Si template. (a) $\boldsymbol{g} = 000\bar{2}$ bright field (BF) and (b) dark field (DF) images. (c) $\boldsymbol{g} = 10\bar{1}0$ BF and (d) DF images. About 60% dislocations are a+c type, which are visible in both diffraction conditions, and about 40 % are pure a-type dislocations which are only visible in g=10$\bar{1}$0.

Figure 3.10 is $[11\bar{2}0]$ cross-sectional CTEM image taken from Sample 2B. Figure 3.10a and 3.10b are two beam bright field (BF) and weak beam dark field (WBDF) in g = $000\bar{2}$, respectively. Figure 3.10c and 3.10d are BF and dark field (DF) images taken in g=10$\bar{1}$0, respectively. About 60% dislocations are a+c type, which are visible in both diffraction conditions, and about 40 % are pure a-type dislocations which are only visible in g=10$\bar{1}$0. Among the dislocations, there are three a+c type dislocations extending through the SL (red arrows in Figure 3.10a). One dislocation leads to a V-defect generated in the SL as marked

with the rightmost black arrow in Figure 3.10a. Another two dislocations are inclined out of the TEM foil, and the V-defects related with them are also out of foil. The effects of these two V-defects on MQW roughness are still observed as marked with leftmost and center black arrows in Figure 3.10a.

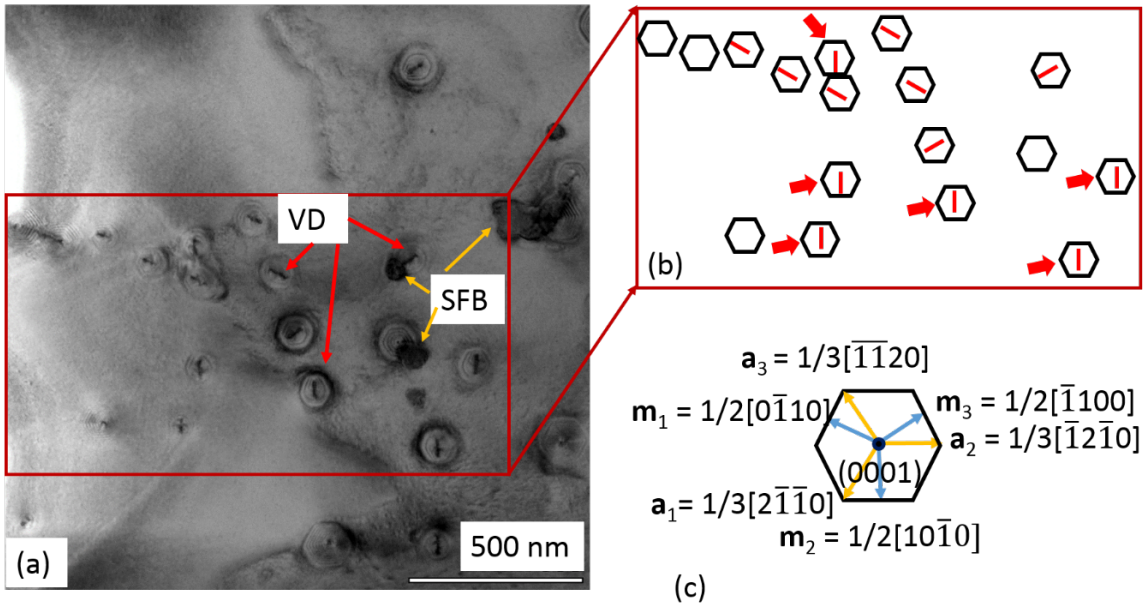

Figure 3.11: (a) Scattering contrast zone-axis plan-view image of Sample 2B. The V-defects (VD) are indicated by red arrows. They show a central inclined TD and fringe contrast due to the projection through the $\{10\bar{1}1\}$ sidewall QWs. Many of the V-defects are decorated with BSFs or SF boxes (denoted as SFB in the image) at the edge of the V-defect. The SFs or SFBs give dark contrast in these images. (b) Shows a diagram of the distribution of V-defects (hexagons) and TDs (red lines) inside the V-defects. (c) A diagram of a V-defect showing relevant crystallographic planes and directions.

Figure 3.11a is plan-view TEM image taken in zone axis [0001]. The faint hexagonal features are the scattering contrast contours of V-defects, and some are labeled with VD in Figure 3.11a. Each V-defect has a dislocation inside that project as a line in one of the $\boldsymbol{m_i} = \frac{1}{2}\langle 10\bar{1}0\rangle$ directions. The projection of V-defect sidewalls in [0001] direction is parallel to six $\{10\bar{1}0\}$ m-planes. The projected segment of dislocations is parallel to one of the six m-directions. Six dislocations inclined to $\pm\mathbf{m_2}$, i.e. $\frac{1}{2}[10\bar{1}0]$ direction in Fig. 3.11, were selected for Burgers vector determination as marked with red arrows in Figure 3.11b. Note that, there

are some dark areas whose contrast is from SFs. Our other work revealed that the stacking fault is an enclosed 3D defect including lower and upper basal stacking faults and a series of a-plane prismatic stacking fault (F. Wu, J. Ewing, C. Lynsky, A. Alhassan, S. Nakamura, S.P. DenBaars, J.S. Speck, unpublished). We called it as a stacking fault box (SFB). Some SFBs are labeled in Figure 3.11a. The SFB and V-defects affect to each other, the details will be published in a separate paper. Figure 3.11b shows the outline of large V-defects and dislocations in the area of the red box shown in Figure 3.11a. Figure 3.11c shows a- and m-directions in the (0001) plane.

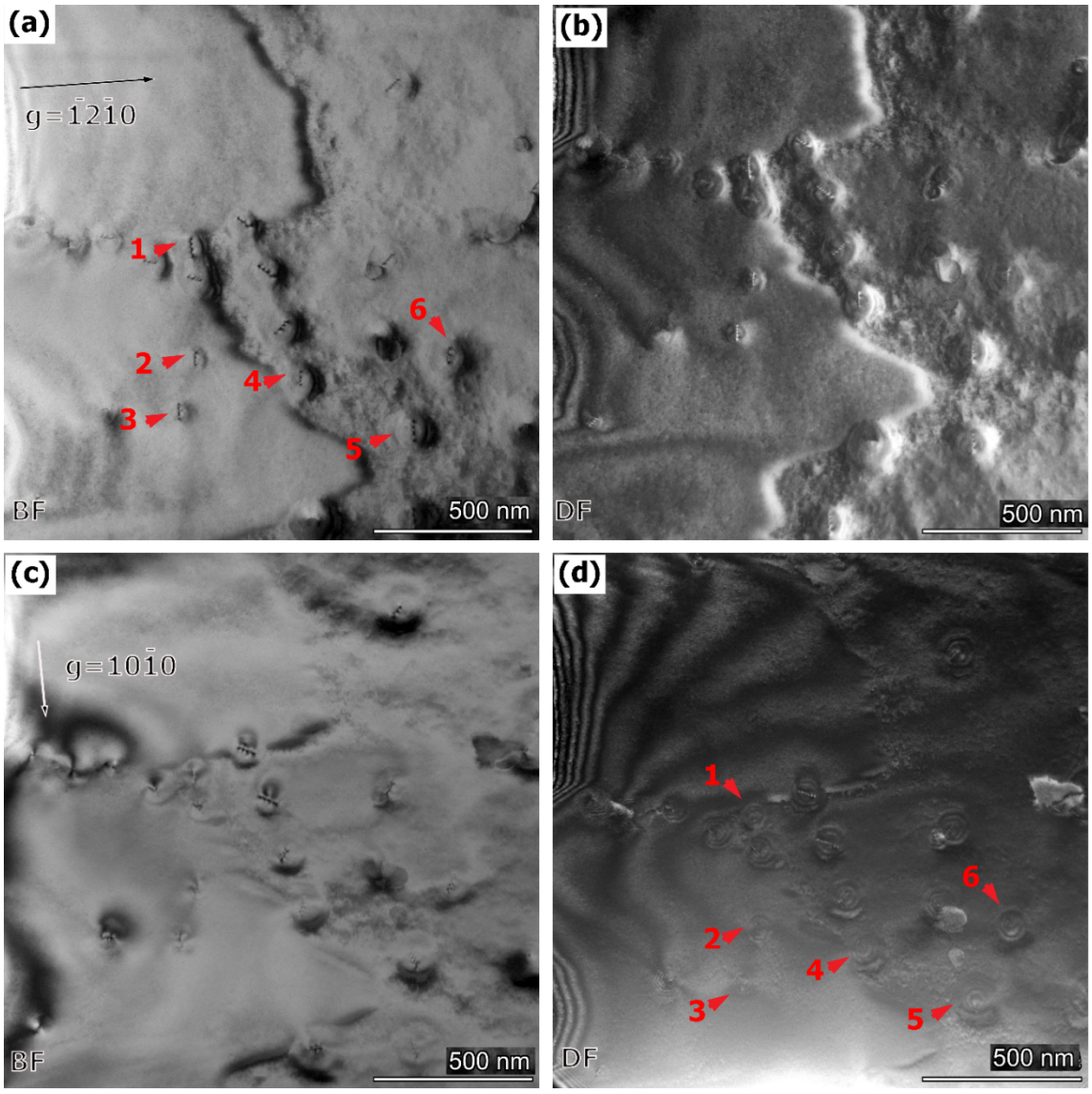

Figure 3.12: Plan-view two-beam scattering contrast imaging (same sample and area as Figure 11). (a) $\boldsymbol{g} = 1\bar{2}10$ bright field (BF) and (b) dark field (DF) images. (c) $\boldsymbol{g} = 10\bar{1}0$ BF and (d) DF images. The red arrows indicated specially identified V-defects and TDs.

Figure 3.12a and 3.12b are BF and DF images in $\mathbf{g} = \bar{1}2\bar{1}0$, respectively. Figure 3.12c and 3.12d are BF and DF images taken in $\mathbf{g} = 10\bar{1}0$, respectively. The six dislocations (indicated by the red arrows) show strong contrast in $g = \bar{1}2\bar{1}0$ (Fig. 3.12a) and show weak contrast in $\mathbf{g} = 10\bar{1}0$ (Figure 3.12d). Based on the visibility criterion of dislocations, we

conclude that the Burgers vector of the dislocations is vertical to $[10\bar{1}0]$. It could be either $\boldsymbol{b} = \pm\frac{1}{3}[\bar{1}2\bar{1}0] = \pm\boldsymbol{a}_2$ (a-type TDs) or $= \pm\frac{1}{3}[\bar{1}2\bar{1}3] = \pm\boldsymbol{a}_2 \pm \boldsymbol{c}$ (a+c type TDs).

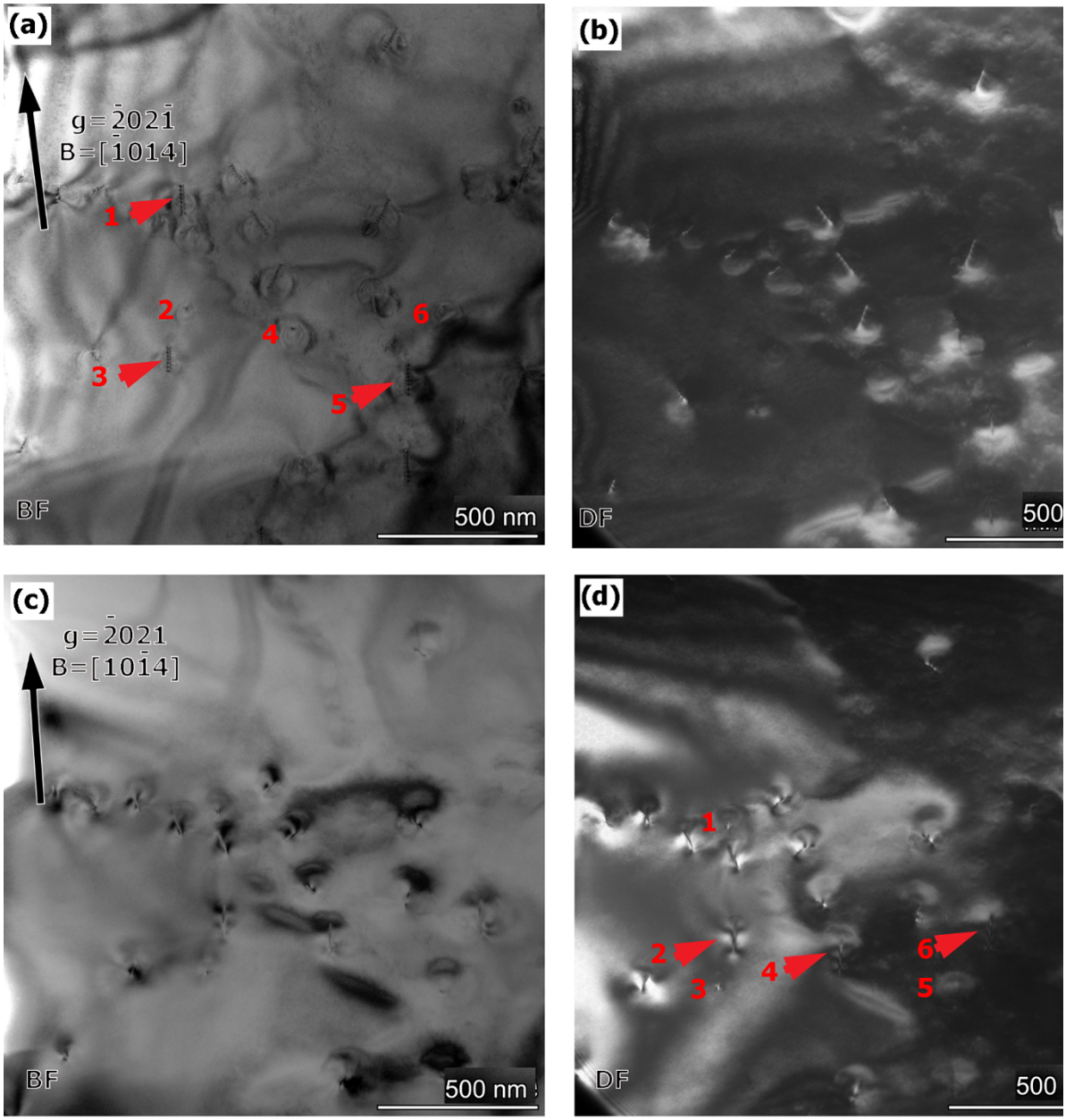

Figure 3.13: Plan-view, highly inclined two beam scattering contrast images of the same region as Fig. 12. (a) BF and (b) DF images are recorded near the $[\bar{1}014]$ zone axis with $\boldsymbol{g} = \bar{2}02\bar{1}$. (c) BF and (d) DF images are recorded near the $[10\bar{1}4]$ zone axis with $\boldsymbol{g} = \bar{2}021$. These scattering contrast images are used to determine if V-defect TDs have a c-component to their Burgers vector.

To clarify if there is c-component to the TDs shown in Fig. 3.12, the sample was tilted from the [0001] axis to the $[\bar{1}014]$ and $[10\bar{1}4]$ zones axes, respectively. Figure 3.13a and 3.13b are BF and DF images taken in $\mathbf{g} = \bar{2}02\bar{1}$, respectively, close to the $[\bar{1}014]$ zone axis. Figure 3.13c and 3.13d are BF and DF image taken in $\mathbf{g} = \bar{2}021$, respectively, close zone axis $[10\bar{1}4]$. The three dislocations (arrows 1, 3, and 5) show strong and longer segment contrast in $[\bar{1}014]$ zone axis as marked with the arrows in Figure 3.13a indicating that at least the three dislocations contain c-component. They show end contrast in $[10\bar{1}4]$ zone axis, indicating that their line direction is close to $[10\bar{1}4]$, i.e., the dislocations inclined towards $\mathbf{m_2}$-direction. In contrast, another three dislocations (marked as 2, 4, and 6) show short segment contrast in the $[\bar{1}014]$ zone axis, and long segment contrast in $[10\bar{1}4]$ zone axis as marked with the arrows in Figure 3.13d, indicating that they also contain a c-component, but the line direction is inclined towards the $-\mathbf{m_2}$-direction.

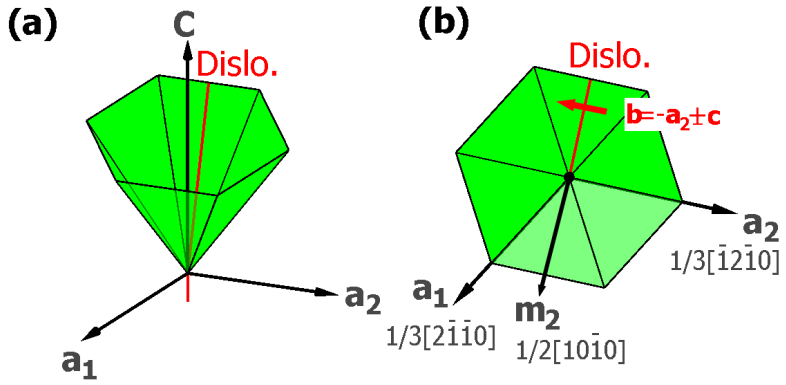

Figure 3.14: Schematic with inclined TDs in a V-defect with $\mathbf{b} = -\mathbf{a_2} \pm \mathbf{c}$

From the analysis above, dislocations with inclined directions parallel to $\pm\mathbf{m_2}$ have Burgers vectors of $\pm\mathbf{a_2} \pm\mathbf{c}$; note that $\mathbf{m_2}$ is perpendicular to $\mathbf{a_2}$ and $\mathbf{c}$. In other words, the dislocations causing V-defect generation in the SL are a+c type dislocations – i.e, mixed character TDs. The inclination direction of the dislocation is not random; it is perpendicular to

its Burgers vector. Our previous and on-going work reveal that all the dislocation inclination happening in AlGaN/GaN and InGaN/GaN layers have the same behavior. Figure 3.14a shows a schematic prospective of the TD line, in red, within the V-defect (which is often filled with p-GaN in the final LED structure). Figure 3.14b shows a plan-view schematic of the V-defect with the mixed character TD inclined on the $\{\bar{1}011\}$ facet.

The inclination of the TD onto the V-defect sidewall is similar to our previous work on the generation of stress gradients due to TD inclination in c-axis GaN growth [31]–[33]. In the case of GaN growth, inclination of pure edge TDs into a climb-like geometry results in compression to tension (toward the growth surface) stress gradients. In the case of the V-defects we suspect a similar situation. However, this may not be a major issue in tensile stress generation as the TD inclination is likely over just the active region of the device.

More significantly the TD within the large, lateral injection promoting V-defect is on one of the six sidewalls and thus in a geometry that would lead to significant non-radiative recombination. While lateral injection could still occur on the other five faces, the face with the TD inclined would see a significant increase in non-radiative processes. The new detailed observation of the TD line on the V-defect sidewall is in contrast to prior work from Hangleiter et al. [34] that predicted that the TD line would be on the axis ([0001] direction) of the V-defect and thus the V-defect would geometrically screen the TDs from nonradiative recombination.

References:

[1] B. Heying *et al.*, "Role of threading dislocation structure on the x-ray diffraction peak widths in epitaxial GaN films," *Appl. Phys. Lett.*, vol. 643, no. August 1995, p. 643, 1995, doi: 10.1063/1.116495.

[2] B. Heying, E. J. Tarsa, C. R. Elsass, P. Fini, S. P. DenBaars, and J. S. Speck, "Dislocation mediated surface morphology of GaN," *J. Appl. Phys.*, vol. 85, no. 9, pp. 6470–6476, 1999, doi: 10.1063/1.370150.

[3] X. H. Wu *et al.*, "Defect structure of metal-organic chemical vapor deposition-grown epitaxial (0001) GaN/Al2O3," *J. Appl. Phys.*, vol. 80, no. 6, pp. 3228–3237, Sep. 1996, doi: 10.1063/1.363264.

[4] X. H. Wu *et al.*, "Structural origin of V-defects and correlation with localized excitonic centers in InGaN/GaN multiple quantum wells," *Appl. Phys. Lett.*, vol. 72, no. 6, pp. 692–694, 1998, doi: 10.1063/1.120844.

[5] C. A. Hurni *et al.*, "Bulk GaN flip-chip violet light-emitting diodes with optimized efficiency for high-power operation," *Appl. Phys. Lett.*, vol. 106, no. 3, 2015, doi: 10.1063/1.4905873.

[6] L. Y. Kuritzky *et al.*, "High wall-plug efficiency blue III-nitride LEDs designed for low current density operation," *Opt. Express*, vol. 25, no. 24, p. 30696, Nov. 2017, doi: 10.1364/oe.25.030696.

[7] W. K. Burton, N. Cabrera, and F. C. Frank, "The growth of crystals and the equilibrium structure of their surfaces," *Philos. Trans. R. Soc. London. Ser. A, Math.*

Phys. Sci., vol. 243, no. 866, pp. 299–358, Jun. 1951, doi: 10.1098/rsta.1951.0006.

[8] F. . Frank, "The influence of dislocations on crystal growth," *Discuss. Faraday Soc.*, vol. 5, pp. 48–54, 1949.

[9] F. C. Frank, "Capillary equilibria of dislocated crystals," *Acta Crystallogr.*, vol. 4, no. 6, pp. 497–501, 1951, doi: 10.1107/s0365110x51001690.

[10] Y. Chen *et al.*, "Pit formation in GaInN quantum wells," *Appl. Phys. Lett.*, vol. 72, no. 6, pp. 710–712, 1998, doi: 10.1063/1.120853.

[11] C. J. Sun *et al.*, "Quantum shift of band-edge stimulated emission in InGaN-GaN multiple quantum well light-emitting diodes," *Appl. Phys. Lett.*, vol. 70, no. 22, pp. 2978–2980, Jun. 1997, doi: 10.1063/1.118762.

[12] F. Scholz *et al.*, "In incorporation efficiency and composition fluctuations in MOVPE grown GaInN/GaN hetero structures and quantum wells," *Mater. Sci. Eng.*, vol. 50, pp. 238–244, 1997.

[13] D. A. Browne, B. Mazumder, Y. R. Wu, and J. S. Speck, "Electron transport in unipolar InGaN/GaN multiple quantum well structures grown by NH3 molecular beam epitaxy," *J. Appl. Phys.*, vol. 117, no. 18, May 2015, doi: 10.1063/1.4919750.

[14] D. A. Browne, M. N. Fireman, B. Mazumder, L. Y. Kuritzky, Y. R. Wu, and J. S. Speck, "Vertical transport through AlGaN barriers in heterostructures grown by ammonia molecular beam epitaxy and metalorganic chemical vapor deposition," *Semicond. Sci. Technol.*, vol. 32, no. 2, Jan. 2017, doi: 10.1088/1361-6641/32/2/025010.

[15] C. Lynsky *et al.*, “Barriers to carrier transport in multiple quantum well nitride-based c -plane green light emitting diodes,” *Phys. Rev. Mater.*, vol. 4, no. 5, pp. 1–6, 2020, doi: 10.1103/PhysRevMaterials.4.054604.

[16] Z. Quan, L. Wang, C. Zheng, J. Liu, and F. Jiang, “Roles of V-shaped pits on the improvement of quantum efficiency in InGaN/GaN multiple quantum well light-emitting diodes,” *J. Appl. Phys.*, vol. 116, no. 18, 2014, doi: 10.1063/1.4901828.

[17] C. C. Hsu, C. K. Wu, C. K. Li, T. C. Lu, and Y. R. Wu, “3D finite element strain analysis of V-shaped pits in light emitting diodes,” in *Proceedings of the International Conference on Numerical Simulation of Optoelectronic Devices, NUSOD*, May 2015, vol. 2015-May, pp. 7–8, doi: 10.1109/NUSOD.2015.7292795.

[18] C. K. Li *et al.*, “3D numerical modeling of the carrier transport and radiative efficiency for InGaN/GaN light emitting diodes with V-shaped pits,” *AIP Adv.*, vol. 6, no. 5, May 2016, doi: 10.1063/1.4950771.

[19] C. H. Ho, J. S. Speck, C. Weisbuch, and Y. R. Wu, “Efficiency and Forward Voltage of Blue and Green Lateral LEDs with v -shaped Defects and Random Alloy Fluctuation in Quantum Wells,” *Phys. Rev. Appl.*, vol. 17, no. 1, Jan. 2022, doi: 10.1103/PhysRevApplied.17.014033.

[20] C. Lynsky *et al.*, “Role of V-defect density on the performance of III-nitride green LEDs on sapphire substrates,” *J. Cryst. Growth*, vol. 560–561, no. December 2020, 2021, doi: 10.1016/j.jcrysgro.2021.126048.

[21] X. Wu, J. Liu, and F. Jiang, “Hole injection from the sidewall of V-shaped pits into c -plane multiple quantum wells in InGaN light emitting diodes,” *J. Appl. Phys.*, vol.

118, no. 16, Oct. 2015, doi: 10.1063/1.4934503.

[22] Z. J. Quan, J. L. Liu, F. Fang, G. X. Wang, and F. Y. Jiang, "Effect of V-shaped Pit area ratio on quantum efficiency of blue InGaN/GaN multiple-quantum well light-emitting diodes," *Opt. Quantum Electron.*, vol. 48, no. 3, pp. 1–8, Mar. 2016, doi: 10.1007/s11082-016-0464-7.

[23] W. Qi *et al.*, "Effects of thickness ratio of InGaN to GaN in superlattice strain relief layer on the optoelectrical properties of InGaN-based green LEDs grown on Si substrates," *J. Appl. Phys.*, vol. 122, no. 8, Aug. 2017, doi: 10.1063/1.5000134.

[24] F. Jiang *et al.*, "Efficient InGaN-based yellow-light-emitting diodes," *Photonics Res.*, vol. 7, no. 2, pp. 144–148, 2019.

[25] S. Zhang *et al.*, "Efficient emission of InGaN-based light-emitting diodes: toward orange and red," *Photonics Res.*, vol. 8, no. 11, p. 1671, 2020, doi: 10.1364/prj.402555.

[26] T. Shioda, H. Yoshida, K. Tachibana, N. Sugiyama, and S. Nunoue, "Enhanced light output power of green LEDs employing AlGaN interlayer in InGaN/GaN MQW structure on sapphire (0001) substrate," *Phys. Status Solidi Appl. Mater. Sci.*, vol. 209, no. 3, pp. 473–476, 2012, doi: 10.1002/pssa.201100356.

[27] A. I. Alhassan *et al.*, "Development of high performance green c-plane III-nitride light-emitting diodes," *Opt. Express*, vol. 26, no. 5, p. 5591, Mar. 2018, doi: 10.1364/oe.26.005591.

[28] A. I. Alhassan *et al.*, "High luminous efficacy green light-emitting diodes with AlGaN

cap layer," *Opt. Express*, vol. 24, no. 16, p. 17868, 2016, doi: 10.1364/oe.24.017868.

[29] J. Ewing *et al.*, "Influence of Superlattice Structure on V-Defect Distribution, External Quantum Efficiency and Electroluminescence for Red InGaN Based μLEDs on Silicon," *Crystals*, vol. 12, no. 9, Sep. 2022, doi: 10.3390/cryst12091216.

[30] C. Lynsky *et al.*, "Improved Vertical Carrier Transport for Green III-Nitride LEDs Using (In,Ga) N Alloy Quantum Barriers," *Phys. Rev. Appl.*, vol. 17, no. 5, May 2022, doi: 10.1103/PhysRevApplied.17.054048.

[31] P. Cantu *et al.*, "Role of inclined threading dislocations in stress relaxation in mismatched layers," *J. Appl. Phys.*, vol. 97, no. 10, May 2005, doi: 10.1063/1.1897486.

[32] S. K. Mathis, A. E. Romanov, L. F. Chen, G. E. Beltz, W. Pompe, and J. S. Speck, "Modeling of Threading Dislocation Reduction in Growing GaN Layers," *Phys. Stat. Sol.*, vol. 179, 2000.

[33] H. M. Foronda, A. E. Romanov, E. C. Young, C. A. Robertson, G. E. Beltz, and J. S. Speck, "Curvature of HVPE c-plane grown GaN wafers in the relation to stress gradients caused by inclined threading dislocations," Aug. 2016, pp. 1–1, doi: 10.1109/iciprm.2016.7528773.

[34] A. Hangleiter *et al.*, "Suppression of nonradiative recombination by V-shaped pits in GaInN/GaN quantum wells produces a large increase in the light emission efficiency," *Phys. Rev. Lett.*, vol. 95, no. 12, Sep. 2005, doi: 10.1103/PhysRevLett.95.127402.

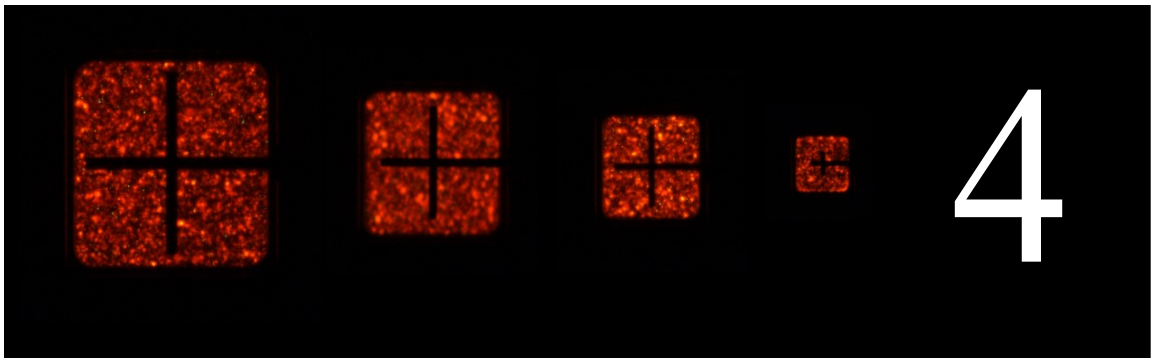

4 Red μLED Growth, Processing, and Performance

4.1 Overview of red LED MOCVD growth

The red LED epi reported in this chapter were grown with MOCVD, primarily on GaN on (111) Si templates from Enkris Semiconductor shown in Table 1. The (111) Si substrates were 6 inches in diameter and 1 mm thick. The substates were diced into 13 mm x 13 mm squares before growth. The substrate thickness is to prevent bowing which can be a big problem for larger substrates and lead to non-uniformity across the wafer. The 800 nm buffer layer used by Enkris semiconductor was proprietary but typically GaN on Si buffers are AlN, possibly some AlGaN. The buffer forces the GaN to grow compressively which helps compensate the large thermal expansion coefficient differences between GaN and Si. Due to the thermal expansion differences, it's not uncommon for the GaN to crack, especially at the edges of the 6 in. substrate.

n-GaN [Si] = 5e18 (1000 nm)
uid-GaN [Si] = 2e17 cm-3 (2000 nm)
Buffer < 800 nm
1 mm Si Substrate

Table 4.1: GaN on (111) Si template structure from Enkris Semiconductor

Some of these red LEDs in this chapter were grown straight from patterned sapphire (PSS), with a 3 μm pitch and a 0.2° miscut along *a*-plane sapphire. This leads to a step terrace structure along *m*-plane GaN. The initial GaN nucleation step is ~560 °C (thermocouple temperature) followed by high temperature (1220 °C) unintentionally doped (UID) GaN island growth and coalescence step and then a few microns of n-GaN. GaN on PSS growth will be discussed in much more detail in chapter 5. It's important to note that the growth temperatures reported in this chapter and throughout this dissertation are thermocouple temperatures, not substrate temperatures, since we don't have a method for directly measuring the substrate temperature during growth. In the GaN on Si growth, the regrowth process always starts with 1220 °C bake and 500 nm of n-GaN at 1220 °C to bury the interface of the template.

The LED structure starts with an InGaN/GaN SL which helps with impurity capture and also is used to generate nucleate V-defects on existing threading dislocations. The superlattice growth rate is a big factor on how effective it is at nucleating V-defects. In these LEDs the growth rate was ~1 Å/s. A slower growth rate was less effective at forming V-defects. The role of the superlattice in forming V-defects is discussed in detail in the next section. There were 5-7 QWs for these LEDs, all grown at the same temperature (~760 °C) with an $Al_xGa_{1-x}N$ cap immediately following. The growth rate of the QWs was ~0.5 Å/s and the capping layer was ~1 Å/s. The QWs are grown with very high TMI flow (2-4X the TEG flow), since TMI incorporation is quite low. The capping layer is grown faster and immediately after the QWs and helps keep TMI from desorbing. The Al% in the cap was 25-40% for the samples grown in this chapter. There was a 10 nm $Al_xGa_{1-x}N$ EBL with 1×10^{20} cm^{-3} [Mg] and ~15-20% Al for all samples followed by 50-100 nm of p-GaN ([Mg] = 5×10^{19} cm^{-3}) and a 10 nm p++ GaN for

all samples. Exact details and epi stacks for the samples that were processed and characterized are reported later in the chapter.

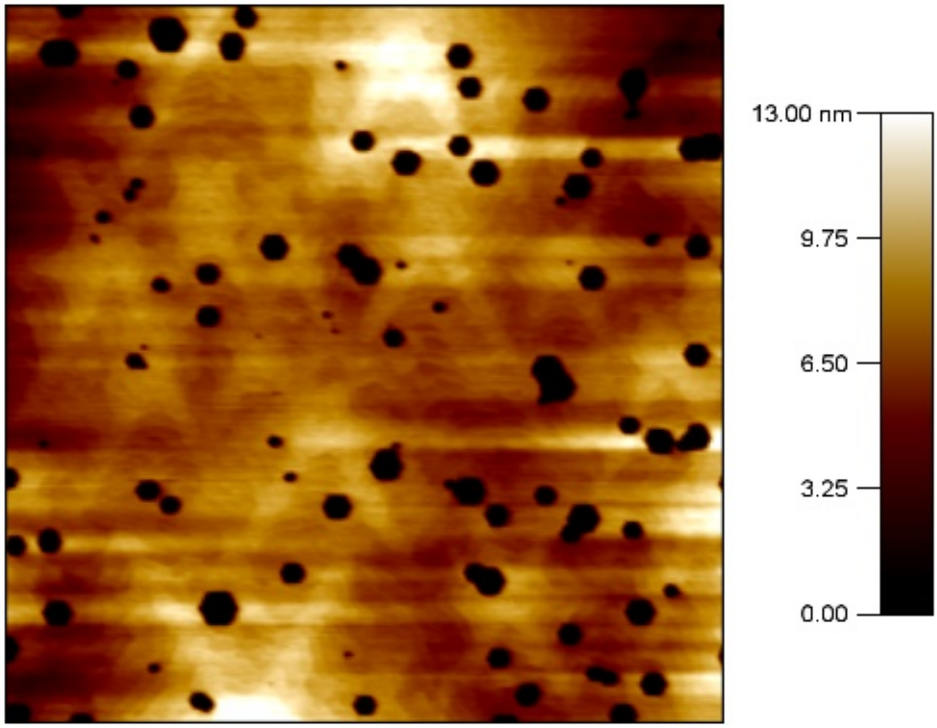

Figure 4.1: Atomic force microscopy (AFM) image of a red LED grown on (111) Si. There was no intentional filling of the V-defects so the pits remain open. This was the case for all LEDs in this chapter, making V-pit characterization very easy through AFM or SEM. V-pit filling is discussed in chapter 6.

Figure 4.1 shows the surface of a red LED grown on (111) Si as characterized by atomic force microscopy (AFM). There was no intentional filling of V-pits during p-GaN growth for the samples reported in this chapter. Although this may have some minor performance drawbacks, it made characterizing V-defect density very easy for these samples through planview AFM or SEM. The step terrace structure can also be observed in Figure 4.1 indicating that the step-flow growth mode was maintained throughout the epi growth.

4.2 Processing and characterization

The LEDs described in this chapter were mostly processed as μLEDs and followed a standard μLED process developed at UCSB with μLED sizes ranging from 5 μm – 100 μm [1], [2]. This process also has a few standard size LEDs (0.1 mm^2) which were used to get packaged LED results. 110 nm of indium-tin-oxide (ITO) was deposited directly on the p-GaN to help with current spreading. Mesas were etched using a $CH_3/H_2/Ar$ reactive ion etch (RIE) for ITO and a $SiCl_4$ RIE for GaN. The etch depth of the GaN was ~700 nm. A $SiO_2/Ta_2O_5/Al_2O_3$ omnidirectional reflector (ODR) was deposited via ion beam deposition (IBD) under the contacts. Atomic layer deposition (ALD) was used to deposit a 25 nm SiO_2 layer for sidewall passivation. ALD passivation is important for suppressing sidewall non-radiative recombination. Devices with passivation typically show less forward and reverse leakage. The contacts are 500/100/500 nm Al/Ni/Au and were deposited via electron beam deposition. This creates ohmic contacts between ITO (on the p-side) and n-GaN.

Electroluminescence (EL) characteristics were measured using an on-chip topside collecting 6-inch diameter integrating sphere (pictured in Figure 4.2). The integrating sphere setup uses a single open port to collect light at an angle of ~180 degrees. The sphere was calibrated using a standard light source from Ocean Insight. The light collected from the integrating sphere was sent through an optical fiber to a monochromator and the light was analyzed with a CCD detector. EQE measurements were taken on-chip with an absorbing Si substrate so the expected light extraction for these LEDs is significantly lower than comparable LEDs on sapphire or another transparent substrate. The CCD detector has a limited wavelength range so to study the entire spectra from 400-700 nm an Ocean Optics spectrometer was used to measure the EL at selected current densities.

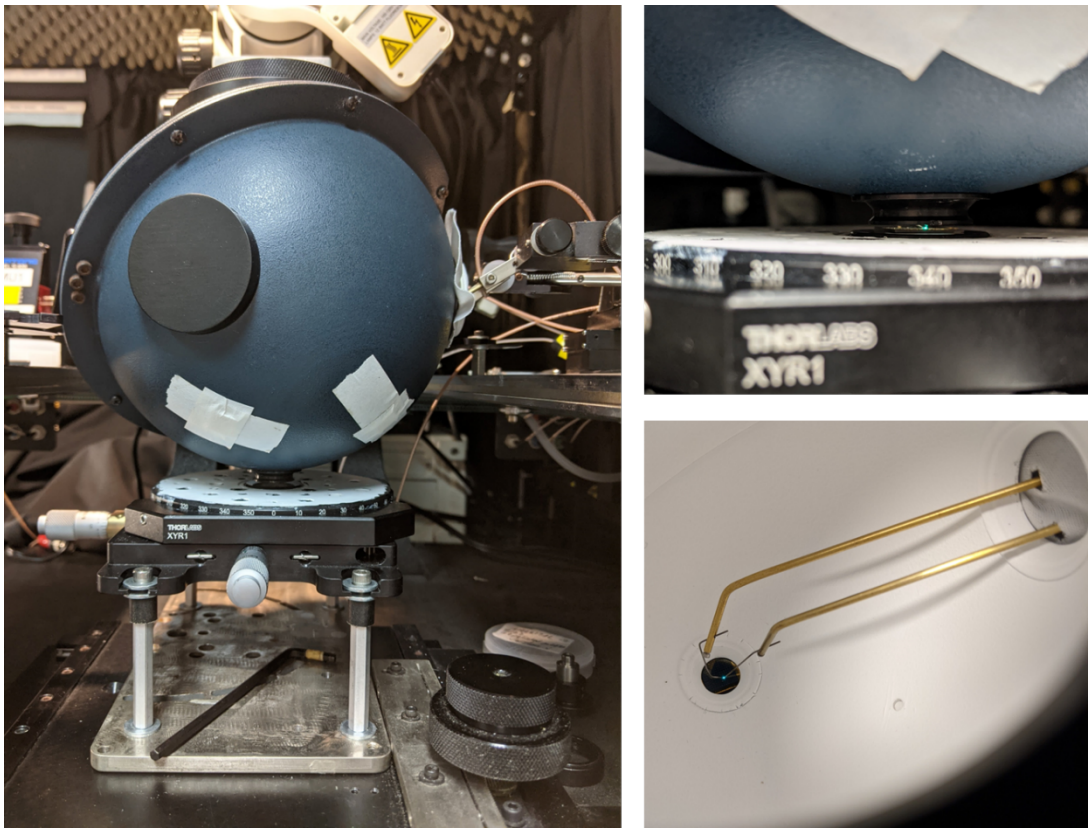

Figure 4.2: (left) Topside collection integrating sphere that was built and calibrated for on-chip relative EQE measurements. This allowed characterization of very small µLEDs with no flip-cihp processing or packaging. (top right) sample stage under the sphere. (bottom right) probe setup inside the sphere. A camera above the sphere was used for probing.

To estimate an accurate IQE and project a flip-chip EQE without an absorbing substrate, Monte Carlo ray tracing simulations were performed using Synopsys LightTools. The simulated structure replicates an LED mesa with ITO contacts, and an ODR with a uniform emission box in the active region of the LightTools LED. This structure was placed on an absorbing Si substrate and the Monte Carlo simulation generated 1,000,000 rays from a 100-nm volume source at 620 nm and 35 nm FWHM. Further calculations simulated the flip-chip configuration with an inverted mesa, a 3 µm 90% reflective silver layer, and a Lambertian-scattering surface with 50/50 first-pass transmission probability on the top side of the mesa.

The mesa size was 20 µm but it was demonstrated that the light extraction efficiency (LEE) didn't vary significantly for different mesa sizes. The calculated LEE for a red µLED on Si was 4.97%. This compared with 85% LEE from an expected flip-chip structure, means that the measured on-chip EQE is substantially lower than the projected flip-chip EQE. Both the measured on-chip EQE and the projected flip-chip EQEs have been plotted in the Results section.

Another important characterization for these LEDs was the V-defect density and distribution on the surface. As mentioned, the V-pits were not filled and so the pits could easily be characterized through topside SEM images. Figure 4.3 shows V-defects with a variety of sizes for a red LED on (111) Si. The hexagonal structure and six semipolar sidewalls can be clearly seen.

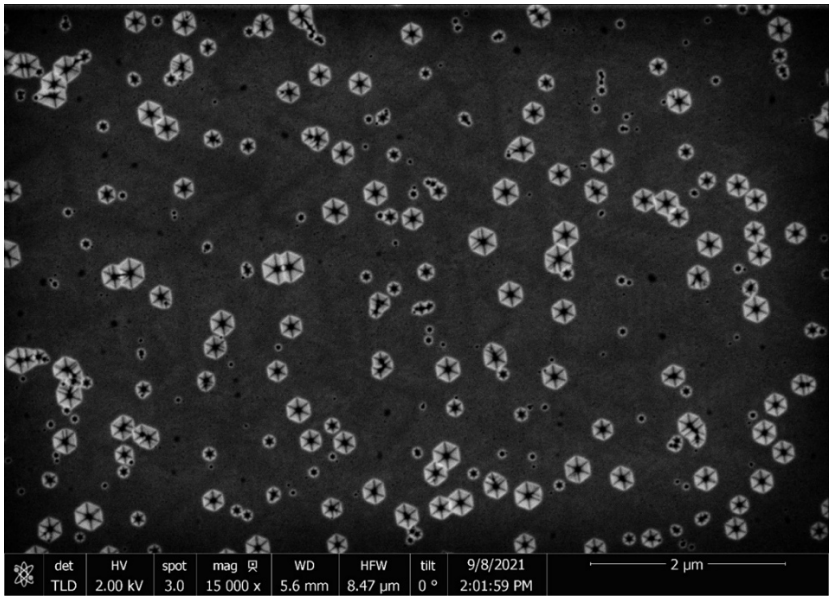

Figure 4.3: Planview SEM image using a secondary electron detector showing V-defects with a variety of sizes for a red LED on (111) Si. The hexagonal structure and six semipolar sidewalls can be clearly seen. The parameters for the SEM image are shown in the bottom of the figure.

The V-defect distribution was characterized by backscatter scanning electron microscope (BS-SEM) images on as-grown epi. Backscatter images were used because they

provide simpler contrast than secondary electron SEM which made image processing easier. SEM images were taken at 15,000X magnification with a spot size of 4 nm and a beam voltage of 4 keV. Image processing was done with Python 3, utilizing the Numpy and Scikit-image libraries and matplotlib for plotting. The images were thresholded to isolate V-defects, then polygons were drawn around the edges of each v-pit. The polygon dimensions were used to estimate average v-pit sizes. The results of 4 images taken near the center of each sample were plotted in histograms to estimate v-pit size distribution. Figure 4.4 shows an example of a backscatter SEM image showing V-defects and a thresholded image with polygons drawn around each V-defect. From this, histograms can be generated giving the V-defect distribution.

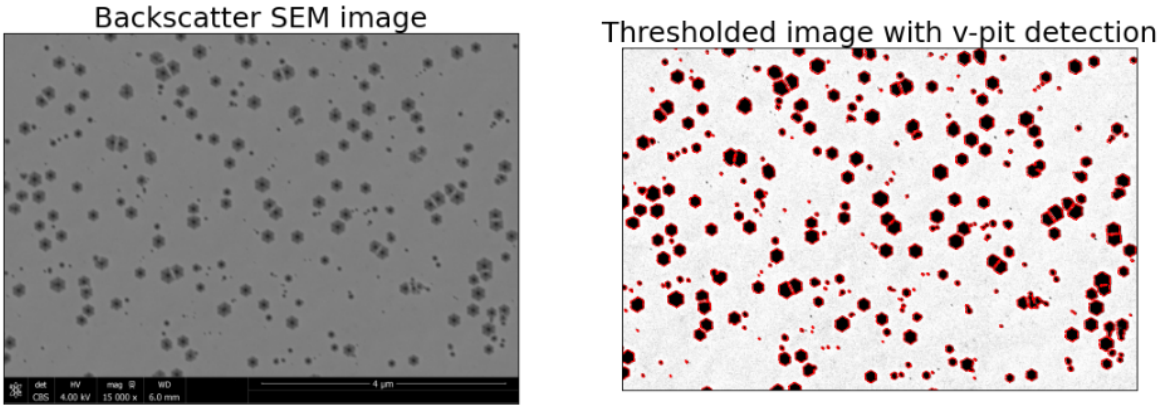

Figure 4.4: Backscatter SEM image showing V-defects before and after image processing.

Figure 4.5 shows the secondary ion mass spectroscopy (SIMS) for a red LED on Si. SIMS uses ion milling to move through a sample. The ions are sent through a mass spectrometer to determine their molecular weight. SIMS is incredibly useful for doping and impurity characterization. The Mg tail is due to the extended structure of V-pits.

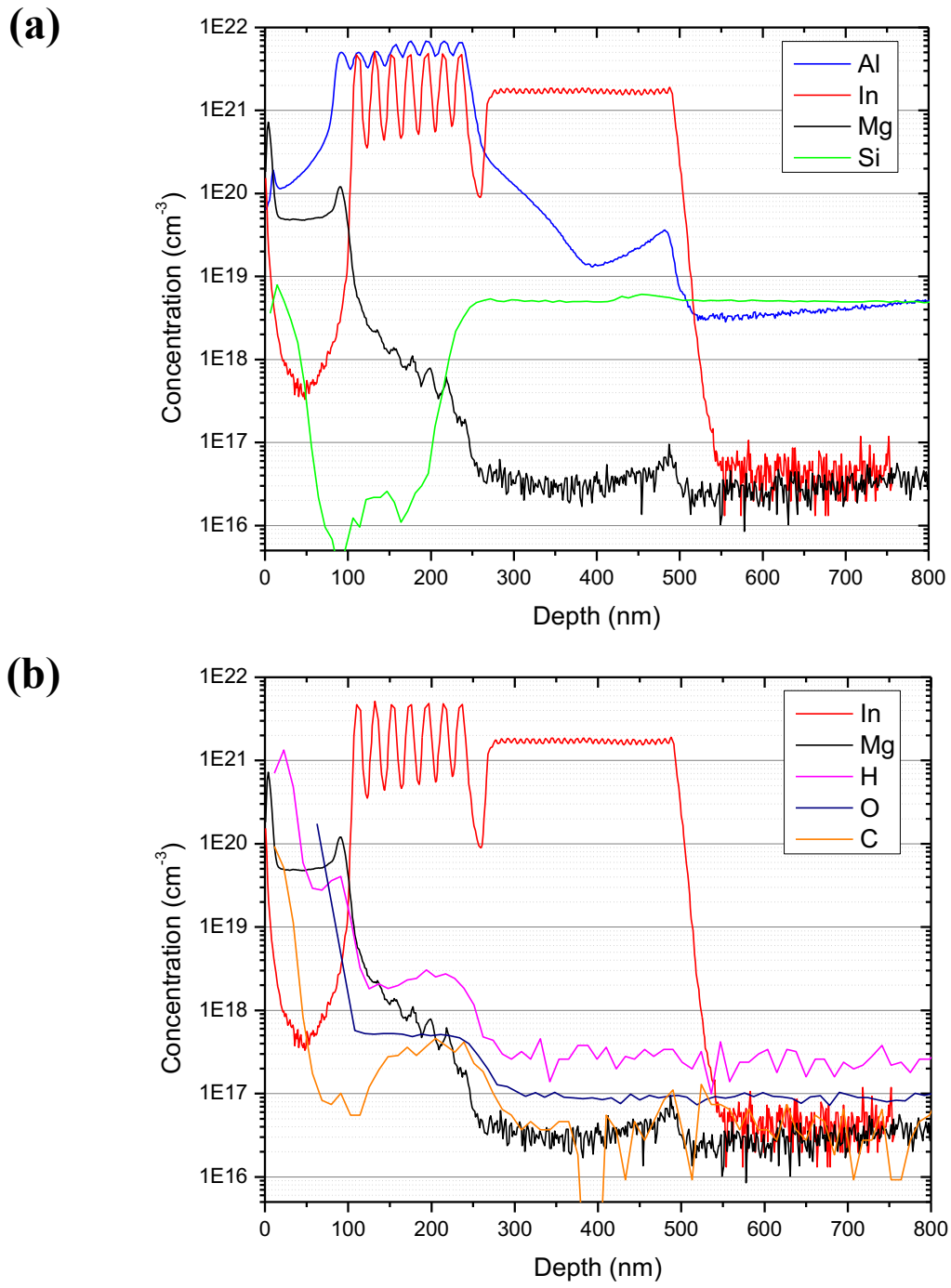

Figure 4.5: Secondary ion mass spectroscopy (SIMS) for a red LED on Si. (a) shows the primary elements and doping. (b) shows impurity levels. The Mg and Al tails are due to the extended structure of V-defects.

4.3 Effect of the superlattice on V-defect distribution and performance

The exact epitaxial structure of the red LEDs for the superlattice structures are shown Figure 4.6. These LEDs had 7 red 2.5 nm QWs. The only difference between samples A, B and C was the thickness of the InGaN layer in the superlattice. The p-GaN thickness was 85 nm with 10 nm of that as a p+ layer for the ohmic contact.

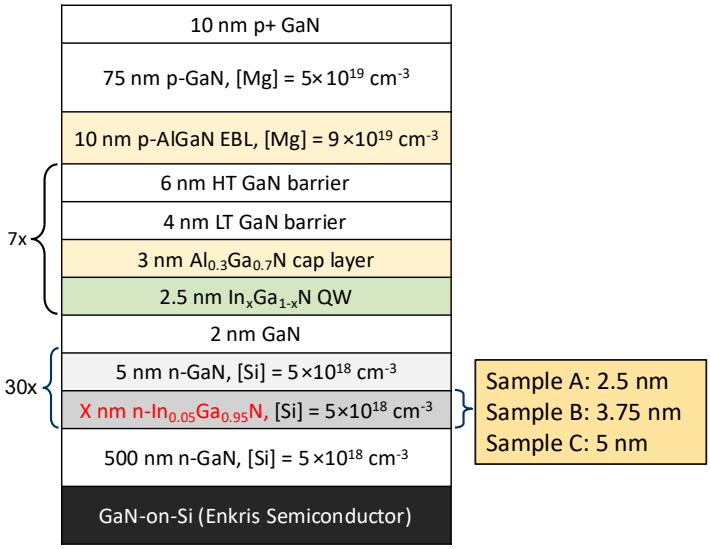

Figure 4.6: Epitaxial structure for GaN-on-Si red LEDs for the superlattice study.

Figure 4.7 shows the V-defect distribution for samples A, B, and C. The GaN-on-Si substrates are diced from the same 6 in wafer so the TDD should be equivalent for all samples. Then we expect that the differences in distribution arise from nucleation conditions in the superlattice where V-defects form around threading dislocations as well as the growth conditions in the active region, which affect the formation of small, generally unwanted V-defects. There is a clear bimodal distribution of V-defects for all samples. This likely represents some fraction of the v-defects that nucleate in the superlattice and a fraction that nucleate higher in the structure, probably in the latter part of the MQW region.

From Figure 4.7 we see that sample C with thicker InGaN has a higher fraction of large V-defects to smaller V-defects compared to Sample B and especially to Sample A. Qi et al. have argued that larger V-defects, namely those that form in the superlattice, are more beneficial to device performance and do not promote leakage like smaller V-pits that form in the MQWs [21]. While it's generally agreed that large V-defects form around threading dislocations generated deep in the 3D-GaN and nucleate when growth conditions such as temperature, growth rate, and V/III ratio are favorable for nucleation, it's less obvious where and why these smaller V-defects form. While it's likely that many still form around threading dislocations from the 3D-GaN some researchers have argued that they may also form around basal plane stacking faults [22]. These basal plane stacking faults might be generated in the InGaN QWs or the AlGaN caping layers. The formation of basal plane stacking faults and small V-defects is an area that requires much more research but it's not unreasonable to assume that preparation layers such as GaN/InGaN superlattices could affect the strain in the QWs and the formation of a variety of defects higher in the structure.

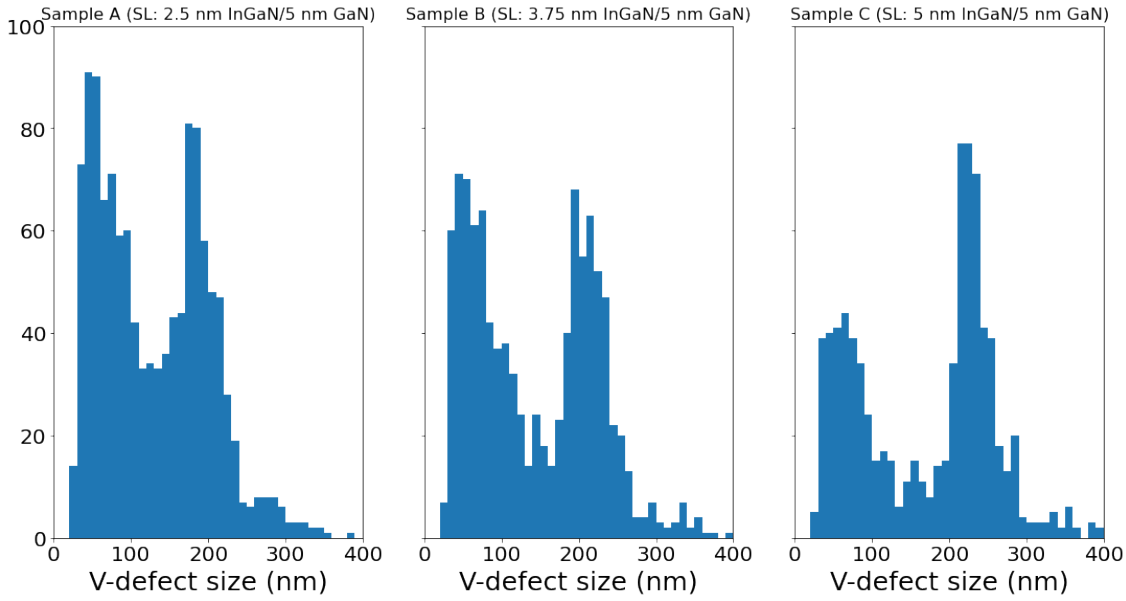

Figure 4.7. V-pit distribution for samples A, B, and C.

Table 4.2 shows some basic statistics regarding distribution of V-defects from the BS-SEM image analysis. The V-defect density is calculated directly from the SEM images. The percent of V-defects formed in the superlattice is estimated based off the geometry of the crystallographic defects and the depth of the structure. Interestingly, despite the different nucleation conditions in the superlattice samples A, B, and C all have very similar densities of large V-defects (V-defects that form in the SL). It's the small V-defects that likely form in the active region that are affected by the superlattice growth conditions. The difference in average diameter is partly a reflection of fewer small V-defects in samples B and C but is also reflective of the total superlattice thickness being greater for Samples B and C. This effect can also be seen in the histograms in Figure 4.7.

Sample	Density of V-defects	% formed in SL	Density of V-defects formed in SL	Average diameter (nm)
A	6.38×10^8	47.4%	3.02×10^8	129.1
B	5.39×10^8	48.5%	2.61×10^8	142.9
C	4.35×10^8	58.2%	2.53×10^8	171.6

Table 4.2: Statistics on v-pit distribution for 3 LEDs with different SL structures

Figure 4.8 shows high angle annular dark field (HAADF) transmission electron microscopy (TEM) images of a small and large V-pit. These illustrate the bimodal distribution of V-defects that was observed in Figure 4.7. The important takeway from the TEM images is that only the large V-pit formed in the superlattice is useful for lateral injection. Thus, the formation of the smaller pits should be suppressed as much as possible.

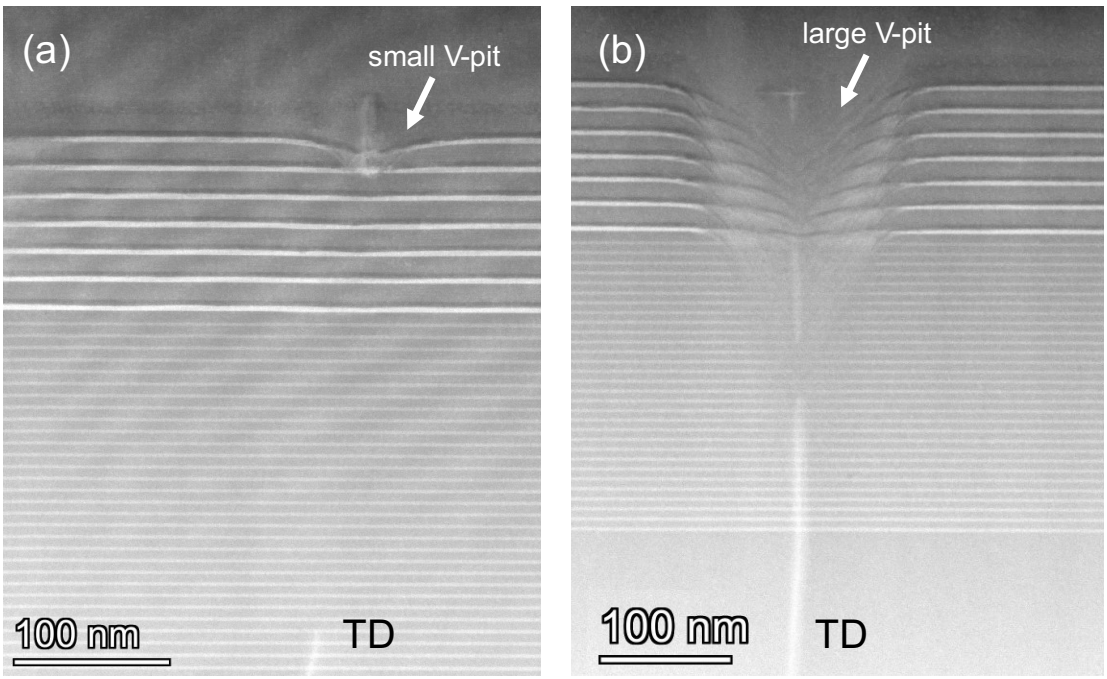

Figure 4.8: HAADF TEM images showing a small v-pit forming in the active region and a large V-pit forming in the superlattice. As illustrated by the image, only the large V-pit is useful for lateral injection of the LED and the small V-pit is likely to only be an SRH and TAAR center.

Another key observation from Figure 4.8a is that a TD can be observed deep in the epitaxial structure indicating that, at least in this case, the small pit is forming on an unused TD from the early GaN growth. If the superlattice was more effective at opening pits, this would have already formed a large V-pit. Getting ALL existing threads to form V-pits is an important component to achieving high performance V-defect engineered LEDs. This is an important topic in chapter 5.

A common problem discussed by researchers looking at red InGaN is the existence of parasitic emission at undesired wavelengths. Generally, this is blue emission, and much research has surrounded its origin and mitigation [3]–[5]. The LEDs fabricated in this paper did display blue emission but only at reasonably high current densities, which is not always the trend observed. Figure 4.9a shows the emission spectra taken on-chip with a spectrometer

at 20, 50, 100, and 300 A/cm^2 from an 80 µm LED on Sample C. At 20 A/cm^2 there is essentially no blue emission and there is still very little at 50 A/cm^2. By 100 A/cm^2 there is appreciable blue emission and the LED looks visually pink. By 300 A/cm^2 the blue emission is so strong that it's almost equal in intensity to the main red emission peak. For some devices, especially on sample A which has the most intense blue emission, the intensity of the blue peak exceeded that of the red peak at 300 A/cm^2. Whatever, the source of the blue emission, it seems to be a diode acting in parallel with a higher turn-on voltage.

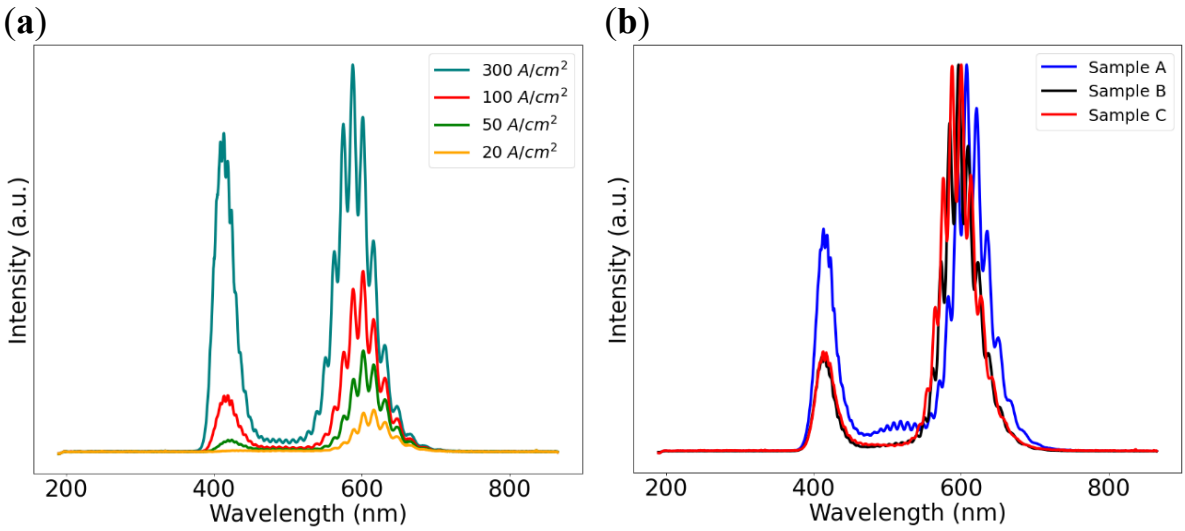

Figure 4.9: (a) Blue emission as a function of current density for an 80 µm LED from Sample C. The Fabry Perot fringes are due to the EL spectra being measured on-chip with a Si substrate which creates an interference pattern. **(b)** EL spectra at 100 A/cm^2 showing parasitic blue emission with red emission for samples A, B, and C.

Figure 4.9b shows a comparison between the 3 samples at 100 A/cm^2. Sample A, which has the highest number of small V-defects, also displays the most intense blue emission. Samples B and C showed very similar blue emission although there was a bit of variability device to device on the same chip.

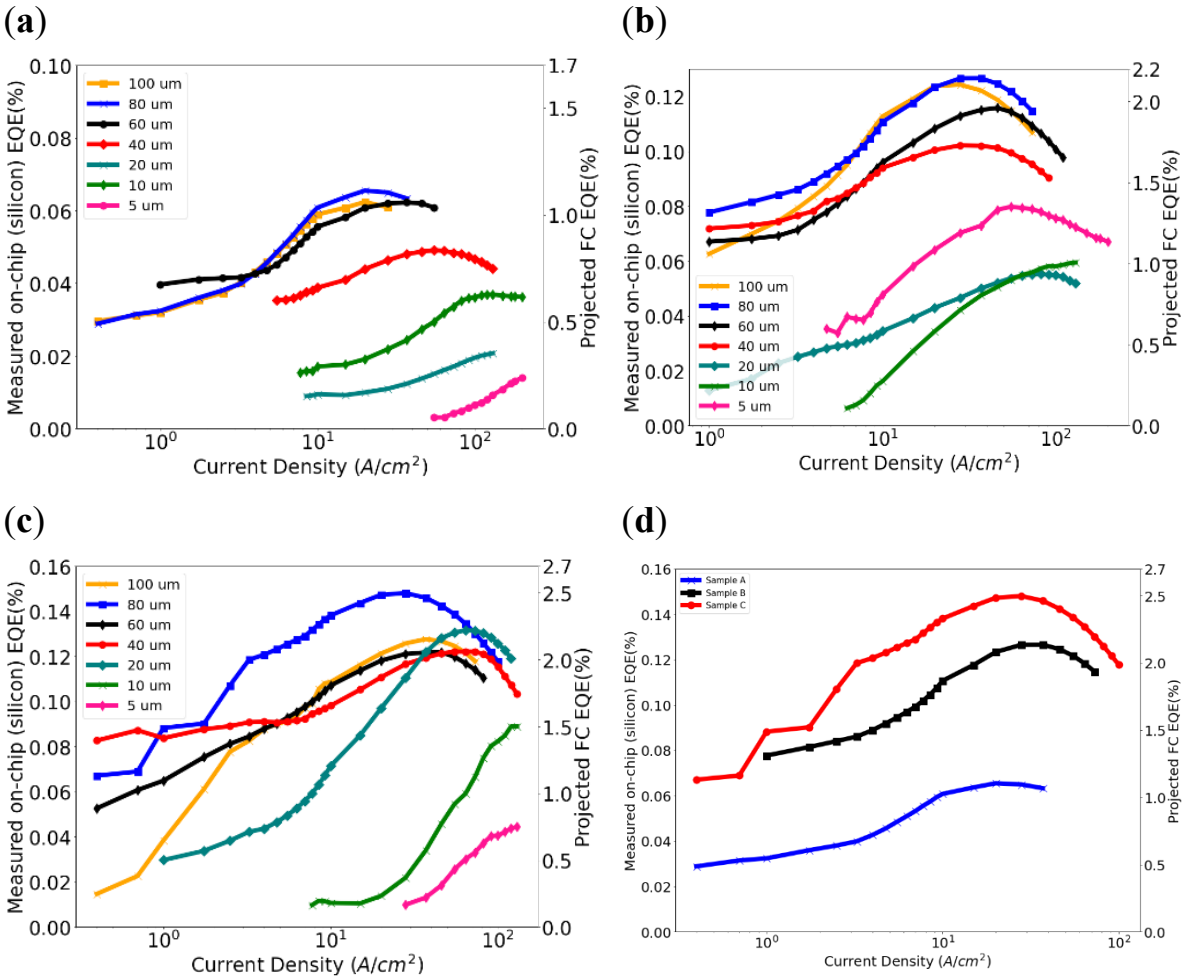

Figure 4.10: EQE plots for 5-100 µm microLEDs for samples a, b, & c respectively (d.) EQE comparison for highest EQE device from each chip (80 µm).

Figure 4.10 shows the EQE measurements for each sample with devices ranging from 100 µm down to 5 µm. On the left-hand axis is the measured on-chip EQE collected from the topside integrating sphere. The right-hand axis is the 'Projected Flip-Chip (FC) EQE' based on the Monte-Carlo LightTools simulations discussed earlier. This accounts for the 5% LEE on silicon and projects an efficiency if the substrate was removed and the flip-chip architecture had a LEE of 85% (also based on Monte-Carlo LightTools simulations). The assumption then is that if these LEDs went through flip-chip processing and substrate removal the efficiency would be similar to the EQE on the right-hand axis of the plots in Figure 4.10. It should be

noted that the CCD detector used to collect this data only collects light in a limited window ~540-680 nm so any blue emission does not factor into the total efficiency. Therefore, EQEs presented are the EQEs of *red emission* only. Additionally, the blue emission is relatively low in the current density range being measured.

The peak EQE is the lowest for sample A and increases for sample B still further for sample C. The projected efficiency for the best device on sample C is ~2.5%. There are also trends in size-dependence. Sample A shows size-independence only for 100-60 μm devices and the efficiency steadily falls off for 40 – 5 μm LEDs. Sample B displays nearly twice the peak efficiency for the 80 & 100 μm LEDs compared to sample A. 40 & 60 μm LEDs still display relatively high efficiency. For μLEDs ≤ 20 μm, the peak efficiency shifts to higher current densities and the efficiency is only ½ to 1/3 of the peak EQE for the larger devices. Finally Sample C, which has the most favorable V-defect distribution, showed the highest peak efficiency and nearly size independent EQE from 100 – 20 μm. Only for 5 & 10 μm was the efficiency reduced and the peak EQE shifted to >100 A/cm^2. Figure 4.10D shows a direct comparison between the three samples for 80 μm LEDs on each chip.

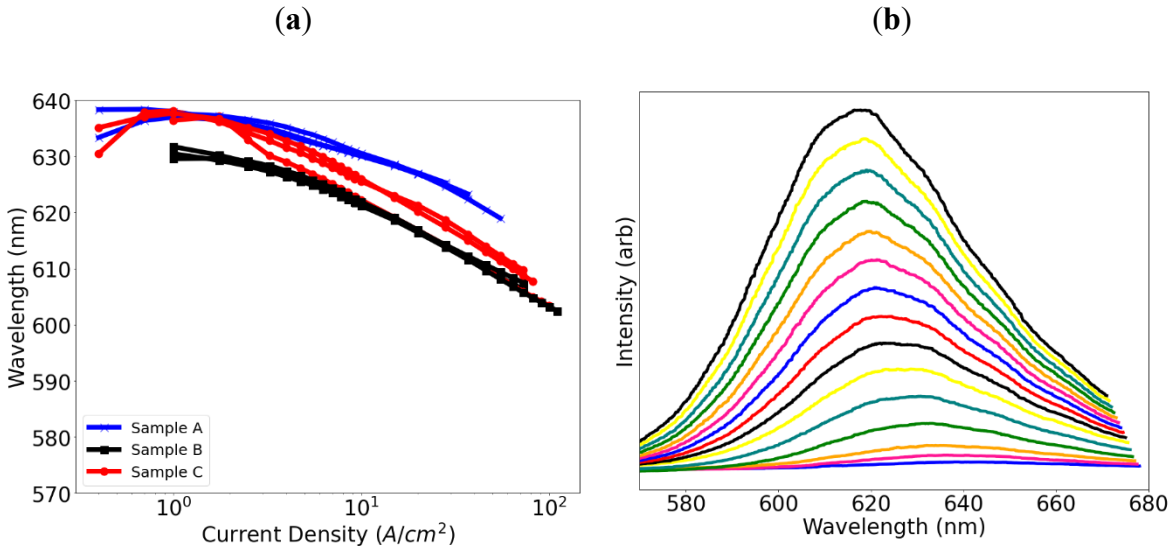

Figure 4.11: Emission profile of red µLEDs on Si (**a**) Wavelength vs current density plots for two µLEDs from each sample. (**b**) Spectra at various current densities (0.4 – 10 A/cm^2) for an 80 µm LED from sample C. Peak emission shifts from 640 nm to 620 nm.

Figure 4.11a shows the wavelength dependence as a function of current density for a couple devices from each sample. For each sample the low current density wavelength was 630-640 nm and dropped to ~600-610 nm at 100 A/cm^2. Figure 4.11**Error! Reference source not found.**b shows the electroluminescence spectra at low current densities for the 80 µm LED on sample C which had a projected EQE of ~2.5%. The shift in emission wavelength is an indication that these LEDs are realizing a sufficiently high carrier density to screen some of the piezoelectric field. The absence of the Fabry-Perot fringes is due to these spectra being taken using an integration sphere which randomizes the direction of the light being emitted.

Superlattices in InGaN LEDs serve many different purposes, from improving carrier dynamics, to incorporating extrinsic impurities, to nucleating v-defects. For yellow and red InGaN there are still many open questions about exactly what role the superlattice plays in increasing performance. Some researchers have argued that SLs, especially those with thick InGaN and high In content, can increase In incorporation in the QWs making it easier to

achieve long-wavelength emission [6]. In this section, we see clear evidence that the superlattices affect V-defect formation and size but didn't see a noticeable wavelength shift indicating higher In content with thicker InGaN [7].

It's difficult to pin down the exact mechanisms by which higher EQEs are achieved but it seems clear that Shockley-Read-Hall (SRH) centers play a big role. In this study we saw improved EQE when we reduced the small V-defects forming in the active region which very likely were centers for SRH. In general, achieving high crystal quality in the MQW region remains one of the key challenges for red InGaN and future work needs to focus on strategic use of V-defects to achieve the highest crystal quality possible in the QWs.

Another key challenge is the mitigation of parasitic blue emission which has been shown to occur from a variety of different sources including superlattice emission, In depletion and/or clustering around defects, and QWs grown on the semi-polar sidewalls of v-pits. More work is required to identify the exact mechanism in the LEDs described here but we do see a possible trend with blue emission being correlated with active region defects. The origin of the parasitic blue emission in red InGaN LEDs remains a topic of on-going study in our group.

A plausible explanation for the EQE trends that relates to the v-pit distributions starts with the idea that small V-defects, forming on threads or around stacking faults, are centers for SRH recombination. A significant part of the 'green gap' and the difficulties in attaining high EQE in long-wavelength InGaN, stems from SRH. If the small V-defects are centers for SRH, then finding preparation layers that help minimize those defects would result in higher EQEs which is what we observed in Samples A, B, and C in this section.

Another very interesting trend was that the samples with fewer small V-defects, especially sample C, appear to also display more size independent properties for μLEDs. Size

trends in μLEDs are also known to, at least in part, be the result of SRH occurring through sidewall defects which become a larger fraction of the total recombination due to the increased perimeter to volume ratio of small μLEDs. This is further supported by the EQE behavior of the small LEDs which have very low efficiency and don't droop, typical behavior of SRH or trap-assisted Auger recombination (TAAR) dominated LEDs [8]. Per-haps the existence of V-defects (especially those initiated in the QWs) on the mesa sidewalls become 'super SRH centers' and further degrade efficiency. If sample C had less of these 'super SRH centers', then it might display more size-independent properties than the other samples as borne out by the data.

4.4 High external quantum efficiency red LEDs

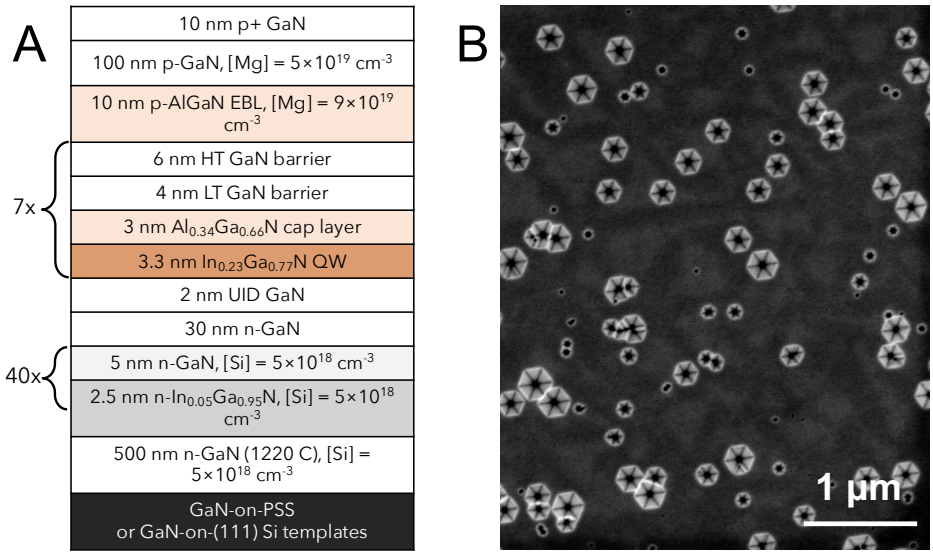

Figure 4.12: a) Epitaxial structure for red InGaN LEDs b) SEM image of growth surface showing unfilled V-defects.

The precise epitaxial structure for the red LEDs in this section is shown in Figure 4.12. LEDs on PSS and GaN-on-Si were identical from the superlattice to the p+ GaN contact layer. The (111) Si LED was grown on a GaN-on-Si template (Enkris Semiconductor Inc.). The (002)

and (102) skew symmetric x-ray rocking curve widths of the GaN on Si templates were 355 and 546 arcseconds respectively. The rocking curve widths for the (002) and (201) reflections on PSS were 228 and 470 arcseconds respectively. The on axis (0002) rocking curve width on (111) Si is large compared to the typical ~200 arcsec rocking curve width for GaN on flat sapphire or pattern sapphire substrates and is indicative of a high density of mixed-component (mostly mixed character with Burgers vector $\mathbf{b} = \pm\mathbf{a}\pm\mathbf{c}$) threading dislocations. Our recent work showed that ~60% of the TDs in the Enkris GaN on (111) Si are a+c mixed component [9].

Regrowth on both the GaN-on-PSS and GaN-on-Si templates started with 500 nm of high temperature GaN to bury any impurities at the regrowth interfaces. A 40-period 2.5 nm n- $In_{0.05}Ga_{0.95}N$/5 nm n-GaN superlattice (SL) ([Si] ~ 5×10^{18} cm^{-3}) was used to nucleate large V-defects (shown in Fig. 1b) and capture impurities before the active region growth [10]. For the SL growth, the thermocouple temperature was 920 ºC, and the growth rate was 0.93 Å/s. V-defects nucleation is enhanced during kinetically limited growth and low adatom mobility. The 40-period SL growth conditions include reduced growth temperature and faster growth rates compared to the rest of the LED structure. V-defect nucleation is discussed in more detail in Reference 25. A 30 nm n-GaN spacer ([Si] ~ $5x10^{18}$ cm^{-3}) was used between the superlattice and active region to increase the size of nucleated V- defects followed by a 2 nm UID GaN spacer. The active region consisted of seven 3.3 nm InGaN QWs grown at a thermocouple temperature of 775 ºC. (thickness measured by transmission electron microscopy (TEM)). Thicker wells allow for longer wavelength emission at lower In composition but have the disadvantage of a larger quantum confined stark effect (QCSE) which decreases electron and hole wavefunction overlap. Each QW was capped with a 3 nm $Al_{0.34}Ga_{0.66}N$ layer, grown at the same temperature as the QW, followed by a 4 nm low

temperature and a 6 nm high temperature GaN barrier. The AlGaN cap was used to suppress In desorption from the QWs which were grown colder than the quantum barriers [11]. The barriers were deposited at a reduced growth rate compared to the rest of the active region and elevated temperature in H_2 to improve the active region morphology during growth and reduce impurities. A 10 nm p-doped $Al_{0.1}Ga_{0.9}N$ electron blocking layer (EBL) with a Mg concentration of 9×10^{19} cm^{-3} was used to prevent electron overflow followed by 100 nm p-GaN ([Mg]=5×10^{19} cm^{-3}) and 10 nm of p+ GaN. Doping concentrations were determined by secondary ion mass spectroscopy (SIMS).

Room temperature photoluminescence (PL) was measured on both the PSS and Si samples with 375 nm wavelength continuous wave (CW) excitation. The wafer was processed into μLEDs (10-100 μm^2) and standard LEDs (0.1 mm^2) using an LED fabrication method described previously [12]. 110 nm of indium tin oxide (ITO) was deposited on the p-GaN with heated electron beam deposition. The mesas were etched with sequential reactive ion etches (RIE). $CH_3/H_2/Ar$ RIE was used to etch the ITO and $SiCl_4$ RIE was used to etch ~700 nm GaN mesas. A $SiO_2/Ta_2O_5/Al_2O_3$ omnidirectional reflector (ODR) was deposited under the contact pad via ion beam deposition (IBD) to improve the light extraction. A 25 nm SiO_2 sidewall passivation layer was deposited via atomic layer deposition (ALD) and 500/100/500 nm Al/Ni/Au contacts were deposited via electron beam deposition. The EQE for the GaN on Si and PSS μLEDs was measured using an on-chip testing setup with topside collection in a calibrated integration sphere. The collected light was sent to a monochromator, collected via CCD and analyzed with in-house LabView programming. The 0.1 mm^2 PSS LEDs were diced, packaged, and encapsulated in epoxy, and tested using a calibrated integrating sphere.

Conventional transmission electron microscopy (TEM) and High Angle Annular Dark Field (HAADF) Scanning TEM (STEM) were performed in both cross-section and plane-view configurations with a Thermo Scientific Spectra 200 TEM/STEM system with energy dispersive x-ray spectroscopy (EDS).

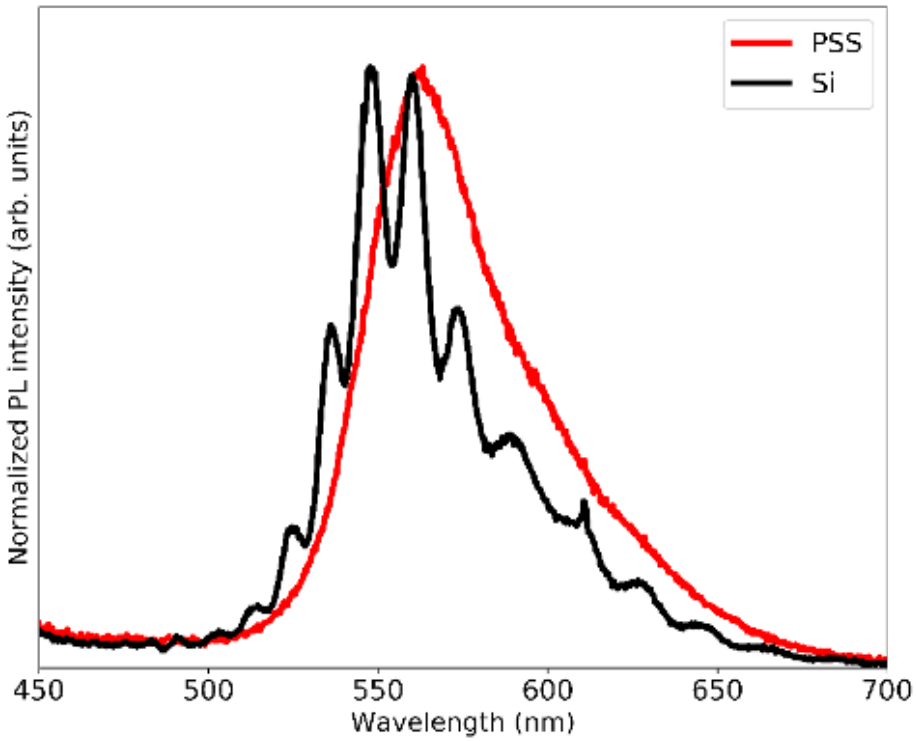

Figure 4.13: Room temperature PL measurements of LEDs on both PSS and Si (PL: 375 nm CW excitation).

Figure 4.13 shows the room temperature PL emission spectra for both PSS and Si LEDs at an excitation wavelength of 375 nm. It is expected that PL will be blue-shifted relative to electroluminescence (EL) because forward biasing a *c*-plane InGaN LED increases the electric field in the QW so that under low current densities the QCSE is enhanced compared to an unbiased LED. This accounts for the peak emission wavelength in PL being <600 nm for these LEDs. Additionally, PL peaks will occur from the V-defect sidewall QWs which are not shown in this data because the spectra is only from 450-700 nm. The sidewall emission is ~420 nm

due to thinner sidewall QWs with much less In [13]. The V-defect sidewall emission is discussed in detail in Ref [13]. The Fabry-Perot fringes occur due to substrate related reflections on flat Si/GaN interface but aren't visible on PSS because the patterning on the PSS/GaN interface scatters the light and thus suppresses the Fabry-Perot fringes.

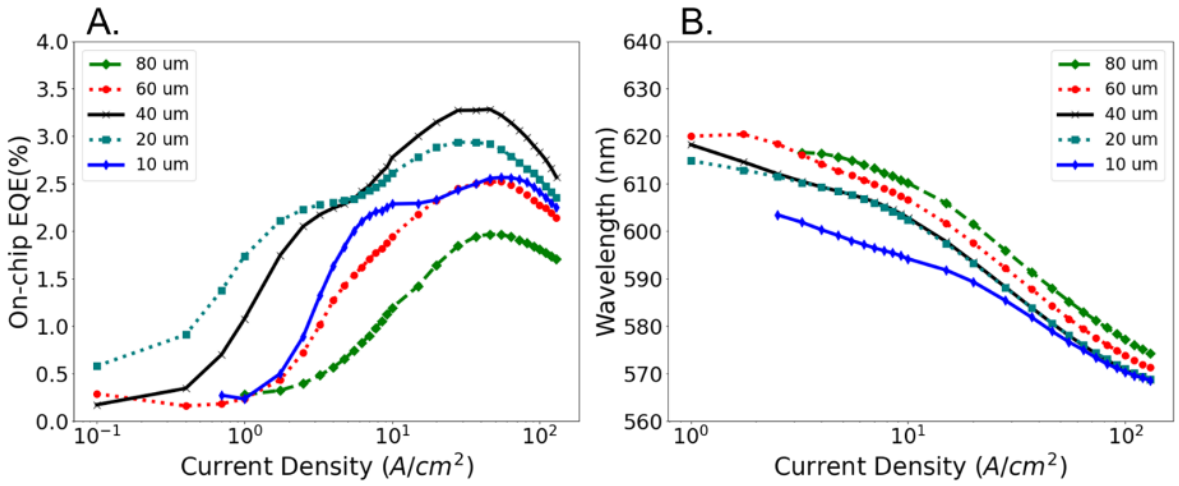

Figure 4.14: Dependence of the on-chip (a) EQE and (b) dominant wavelength on current density for square µLEDs on PSS from 10×10 µm^2 - 80×80 µm^2. The EQE is relatively size independent.

Figure 4.14a shows the EQE curves (measured DC) and wavelength dependence on current density for µLEDs on PSS. The EQE was measured on-chip with an integrating sphere with topside light collection. On-chip measurements do not capture absolute device efficiencies due to collection and absorption losses but allow high device throughput for effective comparison of relative efficiencies. The EQE of the red µLEDs did not show any clear size dependence down to 10×10 µm^2 although there was some variation in EQE. Some of this variation is likely due to wavelength variation across the substrate as shown in Figure 4.14b. The lowest EQE values were for the 60 and 80 µm mesas, which is most likely attributable to lower light extraction. The light extraction effects of InGaN µLED mesas sizes

have been studied in previous work [14], [15]. While the trend isn't quite as clear in this data it is probably the explanation for the lowest EQEs. It's notable that these LEDs show double peak behavior in their EQE plots which is more exaggerated at the smaller μLED sizes. The source of this behavior is an open question that will require further investigation. In V-defect LEDs we suspect that the c-plane injection and semipolar injection act as two parallel diodes with slightly different turn-on voltages. It's plausible that this could be a cause of double peak EQE behavior although this doesn't seem to fully explain why the behavior is more pronounced for smaller size LEDs.

Figure 4.15 shows microscope images of red μLEDs from 100 – 10 μm at 1 A/cm^2 and 10 A/cm^2. At 1 A/cm^2 the emission is much redder, but the smallest sized LEDs aren't visible.

Figure 4.15: Microscope images of electroluminesce of red microLEDs at 1 and 10 A/cm^2

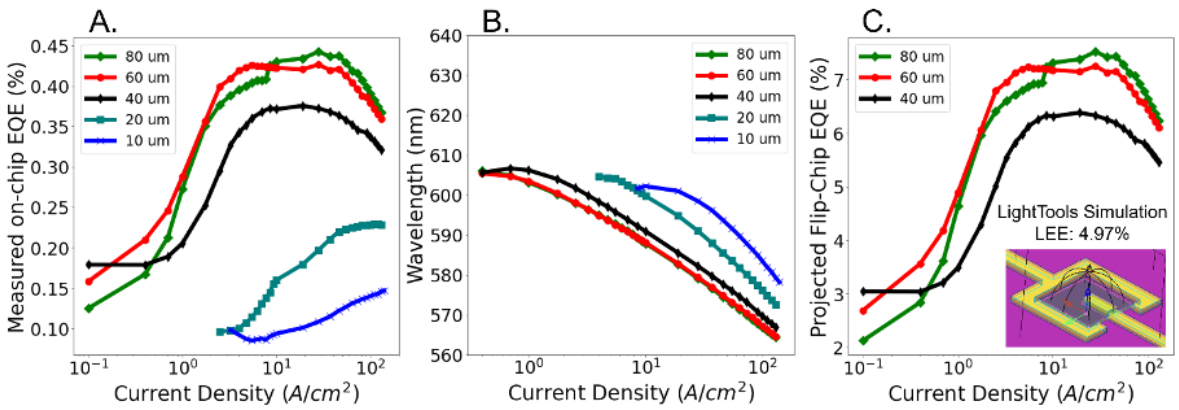

Figure 4.16: Dependence of the (a) on-chip EQE and (b) wavelength for µLEDs on GaN on Si templates (c) Estimated flip-chip EQE for µLEDs after Si substrate removal and N-face roughening. Inset shows LightTools Simulation structure used to determine the LEE of the LED on the GaN on Si template before removal of the Si substrate. The projected efficiency assumes 85% LEE for flip-chipped structure based on ray tracing simulations.

Figure 4.16a and 4.16b show the on-chip EQE and wavelength of LEDs on Si with peak efficiencies of 0.44% on the absorbing substrate. To avoid the complicated flip-chip processing and substrate removal, the Si LEDs were not packaged. To estimate the flip-chip light extraction efficiency (LEE), Monte Carlo ray tracing simulations were performed using Synopsys LightTools. Simulations estimated LEE by replicating a 20x20 μm^2 LED mesa with ITO and metal contacts on an omnidirectional reflector (ODR), atop an absorbing Si substrate. A uniform emission box in the active region area generated 1,000,000 distinct ray trajectories with a Gaussian source emitting at 620 nm with a 35 nm FWHM. Additional simulations examined a flip-chip configuration with an inverted mesa, 3 µm 90% reflective silver layer, and a Lambertian-scattering top-side extraction surface with 50% first-pass transmission probability. It was demonstrated that the LEE didn't vary significantly for different mesa sizes. The simulated structure is shown in inset of Figure 4.16c. The calculated LEE for a red µLED on Si was 4.97% which is significantly lower than ~85% LEE for GaN on PSS. The projected

flip- chip EQE shown in Figure 4.16c estimates the flip-chip EQE using the simulation results. The highest projected efficiency was 7.5% EQE for the 80 µm device but this value was not measured experimentally. Notably, the µLEDs on Si have clear size dependent EQE trends which weren't observed on sapphire. At 10 µm and 20 µm there is clear evidence of a larger A coefficient as seen by the smaller slope in the EQE plot, the peak EQE occurring at higher current density, and the longer emission wavelength which is an indication of less screening in the wells due to lower carrier populations.

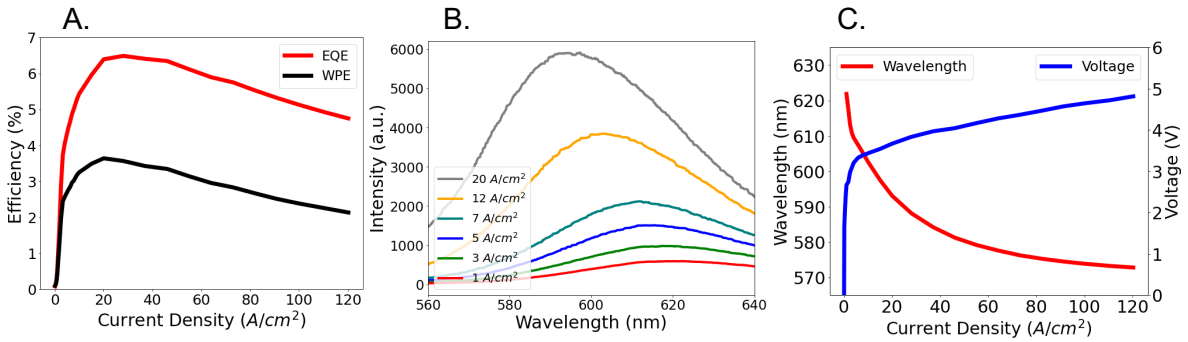

Figure 4.17: Dependence of (a) EQE and WPE (b) EL spectra and (c) emission wavelength and voltage vs. current density for a 0.1 mm2 red/orange LED on PSS.

Figure 4.17a shows the dependence of EQE and WPE on current density for a standard size (0.1 mm^2) LED on PSS that were packaged and fully encapsulated. This LED had a peak EQE of 6.5% at 28 A/cm^2 and 590 nm. The EL spectra at different current densities is shown in Figure 4.17b. The peak WPE was 3.5% and occurred at 20 A/cm^2 and 595 nm. The wavelength decreased from >600 nm at low current densities to ~575 nm at 100 A/cm^2 (Figure 4.17c). The blue shift is a result of screening of the large electric field in the QWs by injected carriers. The high efficiency is attributed to lateral injection through the semipolar sidewalls of V-defects as well as the enhanced light extraction from PSS. It's also plausible that the V-

defects could enhance light extraction by roughening the top surface. However, if the p-GaN growth conditions are optimized to fill the V-defects completely this effect would be mostly eliminated. These semipolar sidewalls provide a pathway that is more energetically favorable for holes from the p-GaN to inject into the 7 MQWs in these LEDs. The forward voltage of this LED is higher than the V-defect LEDs on (111) Si reported by Nanchang[16]. The source of the extra voltage on PSS is a topic of on-going study in our group. Previous work from our group reported 6% EQE for red InGaN μLEDs[17]. While this work does not study V-defects in detail it's likely that these LEDs also contained V-defects due to using a similar SL with similar growth conditions. In this work, we specifically aim to understand the V-defect structure in red μLEDs to determine how future improvements to V-defect structure, density and distribution will be able to further enhance long wavelength InGaN performance.

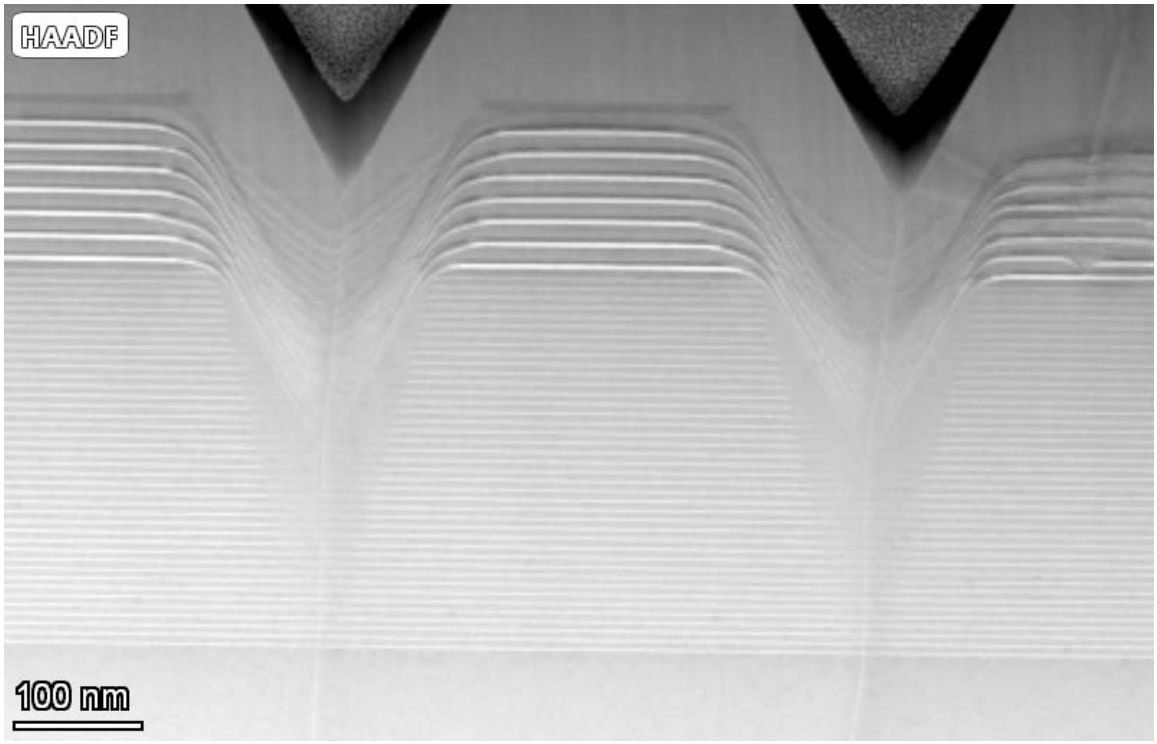

Figure 4.18: High Angle Annular Dark Field (HAADF) image of a pair of V-defects forming in a red LED.

Figure 4.18 shows a High Angle Annular Dark Field (HAADF) TEM image of a pair of V- defects that nucleate towards the bottom of the 40 period superlattice and opening through the active region to provide lateral injection of the quantum wells through the semi-polar $\{10\bar{1}1\}$ sidewalls of the V-defects. The TEM images were taken on unprocessed red LEDs with the same epitaxial structure as shown in Figure 4.12.

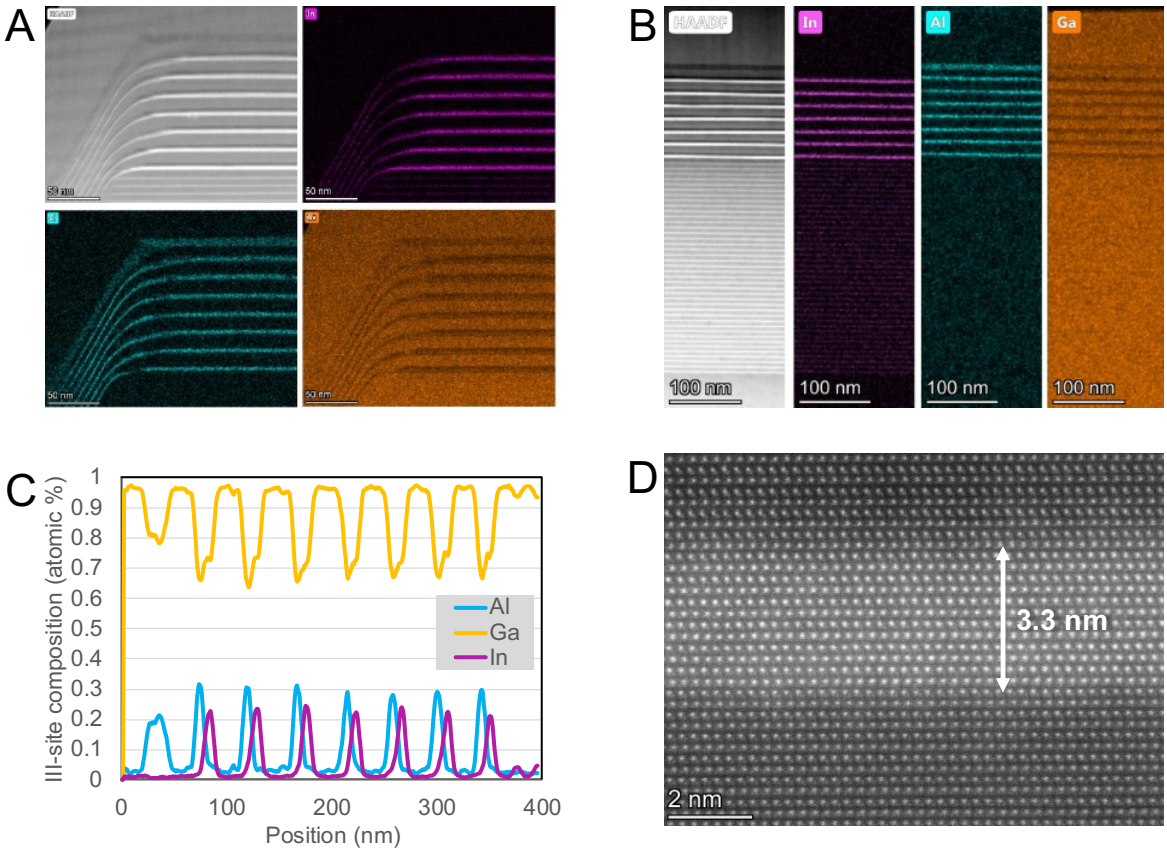

Figure 4.19: HAADF images with energy dispersive x-ray spectroscopy (EDS) analysis showing the relative concentrations of In, Al, and Ga in the LED at the edge of a V-defect (A) and in the c- plane region (B). The c-plane concentrations of Al, GaN, and In measured by EDS. (D) A high definition TEM image of a red/amber InGaN QW with a thickness of 3.3 nm.

Figure 4.19a and 4.19b show the close-up high definition with energy dispersive x-ray spectroscopy (EDS) color maps showing the relative concentrations of In, Al, and Ga at the

edge of the V-defects and in the *c*-plane QWs. Figure 4.19c shows the *c*-plane concentrations of Al, Ga, and In in the active region from EDS. It can be seen that the In concentration at ~23% is relatively uniform throughout the *c*-plane QWs but is significantly less on the semi-polar sidewalls and the QW thickness is much thinner on the sidewalls due to lower Ga uptake and thus slower growth rate. This agrees with previous reports of V-defects. The QW width measured by high-definition TEM was 3.3 nm (Figure 4.19d). Thicker QWs will have a more significant red shift from the QCSE which explain how an LED can emit at 600 nm with only 23% In. However, this comes at the cost of less electron/hole wavefunction overlap which must also be considered in long-wavelength LED design. The Al% in the AlGaN caps (~30%) varies less significantly from *c*-plane to semipolar compared to In as can be seen in the intensity in Fig 4.19a. This is due to Al's incorporation being relatively plane independent compared to Ga and In where uptake is highly plane dependent.

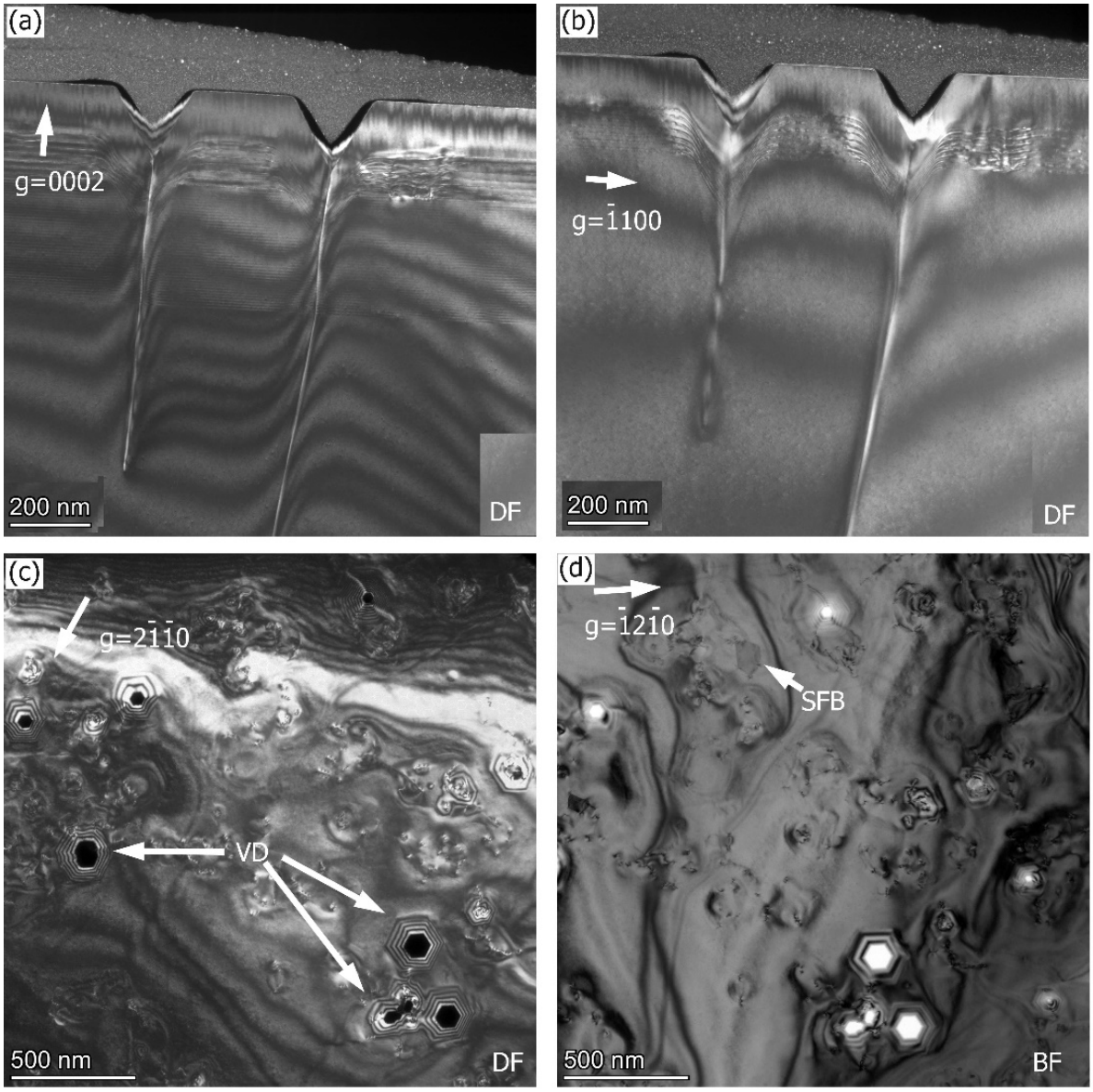

Figure 4.20: Zone axis and b) non-zone axis dark field (DF) scattering contrast TEM images showing large V-defects in a red LED on PSS. The TDs leading to the V-defects show contrast in both diffraction conditions indicating that the TDs are mixed (a+c Burgers vector). c) DF plane-view TEM image shows large V-defects (white arrows) and many smaller defects. d) Bright field (BF) plane-view TEM image also shows large V-defects. A stacking fault box (SFB) is also observed which is very likely to be a significant non-radiative center. Additionally, the smaller defects in both images are likely to be deleterious to performance.

Figures 4.20a and 4.20b show the large V-defects from Figure 4.20 in zone-axis and non-zone axis scattering contrast diffraction conditions. The TDs that lead to the V-defects

show contrast in both images which means that these are mixed (a+c) component TDs. Generally, large V- defects form more readily on mixed component TDs. Reliably forming large V-defects on pure edge TDs is an on-going area of research in our group and important in achieving higher TDs densities on sapphire. Figure 4.20c and 4.20d show dark field (DF) and bright field (BF) plane-view TEM images. In these images we see large V-defects (white arrows in Fig. 4.20c) and a variety of smaller defects. We've argued in previous work that these smaller defects are likely SRH and TAAR centers and are deleterious to device performance[9], [18]. Additionally, Figure 4.20d clearly shows a stacking fault box (SFB). SFBs are significant non-radiative recombination centers and should be eliminated using improved growth techniques. The density of V-defects in these samples from plane-view TEM was ~1 × 10^8 cm^{-2}. This density is much lower than the density achieved on (111) Si by Nanchang university and may be one of the reasons for increased voltage and lower WPE on the PSS LEDs. To achieve complete lateral injection the spacing of V-defects needs to be lateral diffusion length which is ~100 nm. At densities ~1 x 10^8 cm^{-2} the holes can't reach most of the c-plane quantum wells because of the alloy fluctuations which limit the hole diffusion. Optimal V-defect densities have been discussed in previous work through simulations [19]. Therefore, while these LEDs did use V-defects to improve carrier injection and increase WPE, they achieve only partial lateral injection and will likely have non-uniform emission especially at lower voltages. On-going work in our group is investigating ways to increase the TDD on PSS and thus increase the number of V-defects that can form in long-wavelength epitaxy. This will be discussed in Chapter 5.

References:

[1] D. Hwang, A. Mughal, C. D. Pynn, S. Nakamura, and S. P. DenBaars, "Sustained high external quantum efficiency in ultrasmall blue III-nitride micro-LEDs," *Appl. Phys. Express*, vol. 10, no. 3, 2017, doi: 10.7567/APEX.10.032101.

[2] M. S. Wong *et al.*, "Size-independent peak efficiency of III-nitride micro-light-emitting-diodes using chemical treatment and sidewall passivation," *Appl. Phys. Express*, vol. 12, no. 9, 2019, doi: 10.7567/1882-0786/ab3949.

[3] X. Wu *et al.*, "Electroluminescence from the sidewall quantum wells in the V-shaped pits of InGaN light emitting diodes," *Appl. Phys. Lett.*, vol. 104, no. 22, Jun. 2014, doi: 10.1063/1.4880731.

[4] T. Tao *et al.*, "Spatially localised luminescence emission properties induced by formation of ring-shaped quasi-potential trap around V-pits in InGaN epi-layers," *Phys. Status Solidi Appl. Mater. Sci.*, vol. 211, no. 12, pp. 2823–2827, 2014, doi: 10.1002/pssa.201431398.

[5] X. X. Tao *et al.*, "Electroluminescence from the InGaN/GaN Superlattices Interlayer of Yellow LEDs with Large V-Pits Grown on Si (111)," *Chinese Phys. Lett.*, vol. 35, no. 5, May 2018, doi: 10.1088/0256-307X/35/5/057303.

[6] X. Tao *et al.*, "Performance enhancement of yellow InGaN-based multiple-quantum-well light-emitting diodes grown on Si substrates by optimizing the InGaN/GaN superlattice interlayer," *Opt. Mater. Express*, vol. 8, no. 5, p. 1221, May 2018, doi: 10.1364/ome.8.001221.

[7] F. Olivier, S. Tirano, L. Dupré, B. Aventurier, C. Largeron, and F. Templier,

"Influence of size-reduction on the performances of GaN-based micro-LEDs for display application," *J. Lumin.*, vol. 191, pp. 112–116, Nov. 2017, doi: 10.1016/j.jlumin.2016.09.052.

[8] D. J. Myers *et al.*, "Evidence for trap-assisted Auger recombination in MBE grown InGaN quantum wells by electron emission spectroscopy," *Appl. Phys. Lett.*, vol. 116, no. 9, Mar. 2020, doi: 10.1063/1.5125605.

[9] F. Wu *et al.*, "Structure of V-defects in long wavelength GaN-based light emitting diodes," *J. Appl. Phys.*, vol. 035703, no. 133, 2023, doi: 10.1063/5.0135278.

[10] C. Haller *et al.*, "GaN surface as the source of non-radiative defects in InGaN/GaN quantum wells," *Appl. Phys. Lett.*, vol. 113, no. 11, Sep. 2018, doi: 10.1063/1.5048010.

[11] J. Il Hwang, R. Hashimoto, S. Saito, and S. Nunoue, "Development of InGaN-based red LED grown on (0001) polar surface," *Appl. Phys. Express*, vol. 7, no. 7, 2014, doi: 10.7567/APEX.7.071003.

[12] M. S. Wong *et al.*, "High efficiency of III-nitride micro-light-emitting diodes by sidewall passivation using atomic layer deposition," *Opt. Express*, vol. 26, no. 16, p. 21324, 2018, doi: 10.1364/oe.26.021324.

[13] Y. C. Chow *et al.*, "Origins of the high-energy electroluminescence peaks in long-wavelength (~495-685 nm) InGaN light-emitting diodes," *Appl. Phys. Lett.*, vol. 123, no. 9, 2023, doi: 10.1063/5.0167779.

[14] J. M. Smith *et al.*, "Comparison of size-dependent characteristics of blue and green InGaN microLEDs down to 1 μ m in diameter," *Appl. Phys. Lett.*, vol. 116, no. 7,

2020, doi: 10.1063/1.5144819.

[15] R. T. Ley *et al.*, “Revealing the importance of light extraction efficiency in InGaN/GaN microLEDs via chemical treatment and dielectric passivation,” *Appl. Phys. Lett.*, vol. 116, no. 25, 2020, doi: 10.1063/5.0011651.

[16] S. Zhang *et al.*, “Efficient emission of InGaN-based light-emitting diodes: toward orange and red,” *Photonics Res.*, vol. 8, no. 11, p. 1671, 2020, doi: 10.1364/prj.402555.

[17] P. Li *et al.*, “Significant Quantum Efficiency Enhancement of InGaN Red Micro-Light-Emitting Diodes with a Peak External Quantum Efficiency of up to 6%,” *ACS Photonics*, vol. 10, no. 6, pp. 1899–1905, 2023, doi: 10.1021/acsphotonics.3c00322.

[18] J. Ewing *et al.*, “Influence of Superlattice Structure on V-Defect Distribution, External Quantum Efficiency and Electroluminescence for Red InGaN Based μLEDs on Silicon,” *Crystals*, vol. 12, no. 9, Sep. 2022, doi: 10.3390/cryst12091216.

[19] C. H. Ho, J. S. Speck, C. Weisbuch, and Y. R. Wu, “Efficiency and Forward Voltage of Blue and Green Lateral LEDs with v -shaped Defects and Random Alloy Fluctuation in Quantum Wells,” *Phys. Rev. Appl.*, vol. 17, no. 1, Jan. 2022, doi: 10.1103/PhysRevApplied.17.014033.

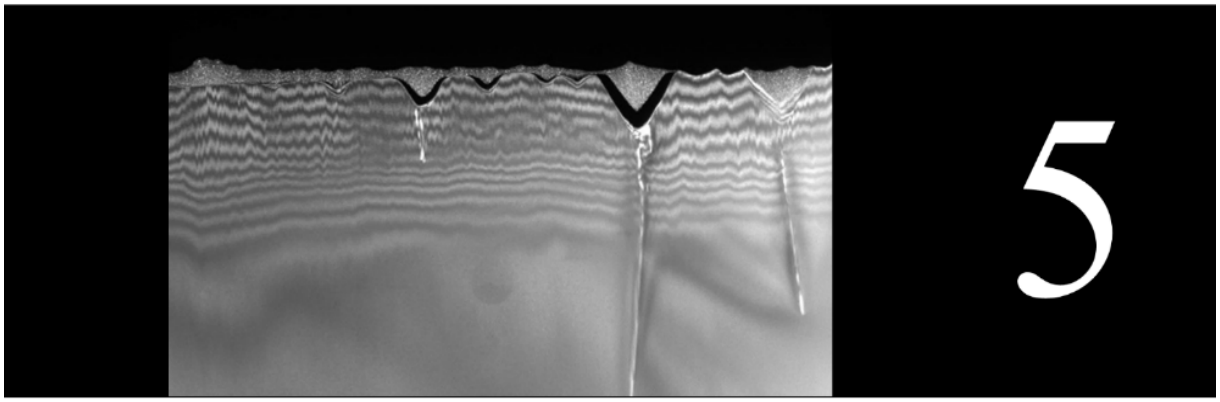

V-defect Engineering for LEDs on Sapphire

5.1 Threading dislocation generation on sapphire

Recent work on III-N light emitting diodes (LEDs) has demonstrated that as the indium composition and wavelength are increased, polarization barriers to carrier injection severely limit the ability of both electrons and holes to populate the quantum wells in *c*-plane LEDs [1]–[3]. This poses a significant challenge for red and green InGaN LEDs due to low current injection leading to high forward voltage and low carrier concentrations in the quantum wells (QWs). These barriers to carrier transport also make it extremely difficult to inject deeper QWs. Laterally injected III-N LEDs are the most promising solution to problem of carrier injection at long wavelengths [4]–[7]. Because a significant portion of the potential barrier arises from the high polarization of *c*-plane, injecting carriers through a semi-polar or non-polar plane in a "3D" device architecture is a promising solution to mitigate some of the forward voltage issues in long-wavelength InGaN [8], [9]. So far, the literature on lateral injection LEDs focuses on the strategic use of naturally occurring V-defects as the pathway for lateral injection of electrons and holes. These naturally occurring defects are inverted hexagonal pyramids with six semi-polar $\{10\bar{1}1\}$ faces. For green and red LEDs, the strain induced polarization by the high In fraction *c*-plane QWs significantly increases the injection barriers. However, In uptake

is dramatically reduced on the semi-polar sidewalls of the V-defects which further enhances the ability of carriers to enter the QWs [10]. Furthermore, Ga uptake is also greatly reduced leading to thinner sidewall QWs which further facilitates carrier transport [11].

Dislocation generation and structural evolution in GaN films grown on sapphire is important to understand and improve the performance of laterally injected InGaN LEDs [12], [13]. GaN growth on sapphire usually starts with a low temperature nucleation layer where small islands of highly defective GaN are initiated. Subsequent high temperature growth results in nearly defect-free 3D islands followed by island coalescence and planarization of the growth surface. The threading dislocations (TDs) form primarily during the 3D island growth and coalescence [14], [15]. TDs form to accommodate the slight misorientation of the high temperature GaN islands [16].

Threading dislocations are of great importance in the formation of V-defects [17]. V-defects readily form on threading dislocations because the surface energy of a dislocation meeting the surface will cause a slight surface depression which becomes the nucleation site for a V-defect under favorable growth conditions [18]. V-defects tend to form more readily on mixed-type TDs (Burgers vector $\boldsymbol{b} = \pm(\boldsymbol{a_i} \pm \boldsymbol{c}) = \frac{1}{3}\langle 11\bar{2}3\rangle$ where $\boldsymbol{a_i}$ and $\boldsymbol{c}$ are the lattice translations for the wurtzite GaN structure) compared to pure edge TDs ($\boldsymbol{b} = \pm\boldsymbol{a_i} = \frac{1}{3}\langle 11\bar{2}0\rangle$) because the surface depression from a mixed-type dislocation is larger [19]. It's also been demonstrated that V-defects affect the way in which a threading dislocation bends. It is at least the case in mixed-type dislocations that the threading dislocation will bend onto one of the six semi-polar faces after the V-defect has formed [11]. Because V-defects form more readily on mixed TDs, early work on V-defect engineered LEDs was primarily from LEDs grown on (111)

Si substrates which have a high fraction of mixed TDs compared to pure edge [20]–[22]. V-defect engineered LEDs grown on sapphire are slightly more difficult because most of the TDs are pure edge and the threading dislocation density (TDD) is low, especially on patterned sapphire substrates (PSS) [23], [24]. PSS is one of the most important substrates for III-N LEDs because of its high light extraction (>90%) [25].

It's been demonstrated that the ammonia flow in the initial island growth and coalescence stage can increase the number of edge type dislocations on flat sapphire [23]. On of the initial experiments was to investigate this effect on patterned sapphire substrates with different pitches and growth conditions to increase the TDD. The aforementioned Nanchang were all done on Si which has a higher TDD compared to GaN on sapphire growth. Achieving effective V-defect engineering on sapphire will require higher dislocations densities to be realized on sapphire. According to theory, the mixed component dislocation density which can be estimated by the on-axis (002) rocking curve full width half max (FWHM) are more favorable for forming V-defects because of the larger surface depression at mixed TDs. Pure edge dislocations (estimated by the off axis rocking curve FWHM) were traditionally thought to be less favorable but also have proved to be easier to generate through growth conditions.

An initial experiment into the differences between coloaded 3 μm pitch and 1 μm pitch PSS. The ammonia flow was varied from 1-6 SLMs while keeping the TMG flow constant at 15 sccm. The on- and off-axis rocking curves were measured and are shown Table 5.1. For the standard 3 μm pitch PSS there isn’t a strong dependence between V/III ratio and defect generation. On the 1 μm pitch PSS there is an increase in off-axis rocking curve width which corresponds to increased pure edge component dislocations but no significant increase in on-axis rocking curve width as a function of V/III ratio. Notably the 1 μm pitch PSS showed higher

on-axis rocking curve widths for all V/III ratios. It's expected that this will lead to higher V-defect densities on 1 µm PSS which is consistent with the proposal where we claimed that reducing the period of the pattern could assist in realizing higher V-defect densities for long-wavelength LEDs. In essence these results showed that small pitch PSS behaves a bit more like flat sapphire in terms of threading dislocation generation.

Ammonia flow	3um Pitch (002) FWHM	1um Pitch (002) FWHM	3um Pitch (201) FWHM	1um Pitch (201) FWHM
1	234.4	261.7	307.1	338.8
2	n/a	252.7	n/a	366.1
4	229.0	269.3	322.6	432.7
6	232.2	275.0	313.6	461.2

Table 3.1: on- and off-axis rocking curves for GaN on PSS templates with varying ammonia flow and pattern pitch, rocking curve widths in arcseconds.

A second set of experiments investigated the use of lower temperature GaN layers as a mechanism for generating defects. The samples had a standard nucleation layer but ~ 1 µm of low temperature GaN was grown followed by high temperature GaN (1220 °C). These experiments showed a more significant increase in both on-axis and off-axis rocking curves.

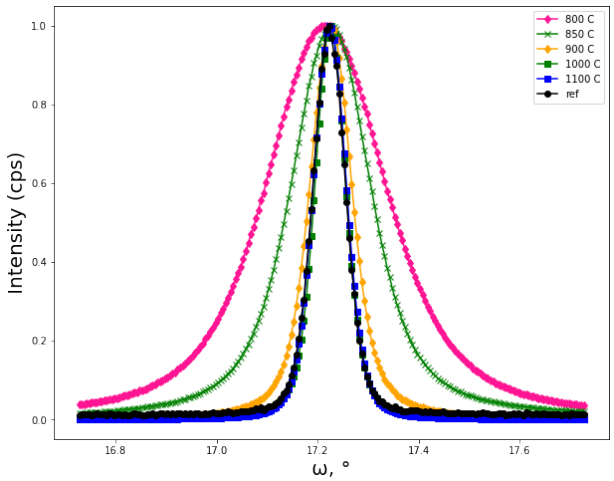

Figure 5.1: On-axis rocking curves for GaN on PSS templates with varying low temp GaN growth

Figure 5.1 shows the on-axis rocking curve widths for various templates with various GaN temperatures for the island growth and coalescence layer. The broadening FWHM indicates an increase in mixed-screw component dislocations which according to theory should be favorable for forming v-defects. Table 5.2 shows the on- and off-axis rocking curves for this experiment. Using low temperature GaN layers increases both on- and off- axis rocking curves which indicates that it increases all types of dislocations.

Intermediate growth temp (C)	1um Pitch (002) FWHM	1um Pitch (201) FWHM
800	1012.7	2923
850	667.9	2696.7
900	350.4	802.4
1000	257.9	466.0
1100	274.8	466.9
ref	269.2	432.8

Table 5.2: On- and off-axis rocking curves for GaN templates with varying growth temperatures for the island growth and coalescence layer. FWHMs are given in arcseconds.

5.2 Low temperature GaN for V-defect nucleation

In V-defect LEDs, the preparation layers grown immediately before QW growth are critical in determining the V-defect structure which facilitates the increased hole injection and lower voltage associated with high performance V-defect LEDs. In the literature, both InGaN/GaN superlattices and low temperature GaN are used as preparation layers. The basic structure of a V-defect LED is shown in Figure 5.2.

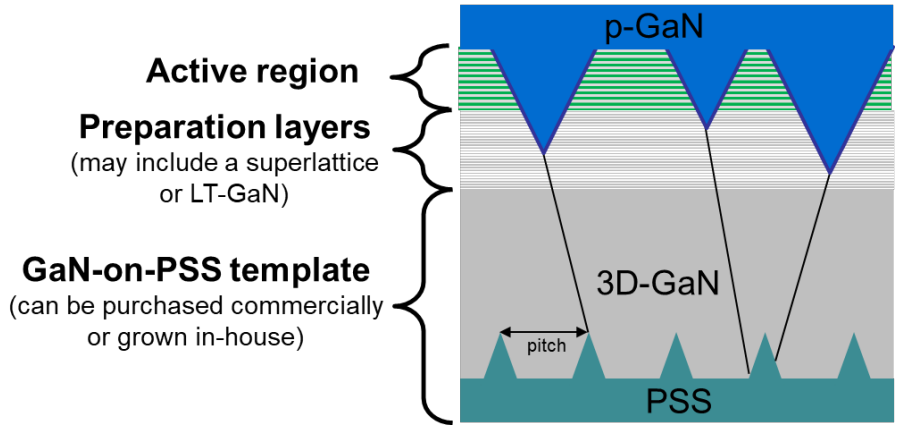

Figure 5.2: Basic structure of a GaN-on-PSS LED with V-defects.

In the V-pit LED literature and in the early work at UCSB, most LEDs used a 30-period InGaN/GaN superlattice to nucleate the V-defects. **Error! Reference source not found.** shows high angle annular dark-field (HAADF) imaging of a green LED grown in Q2 of the project. This LED had a packaged EQE of 22% at 520 nm. These TEM results showed that only ~1/3-1/4 of the threads at the surface were being nucleated into V-defects. This result indicates that improved preparation layers that nucleate V-defects at a higher fraction of the threads is needed for these LEDs to improve lateral carrier injection and decrease the forward voltage.

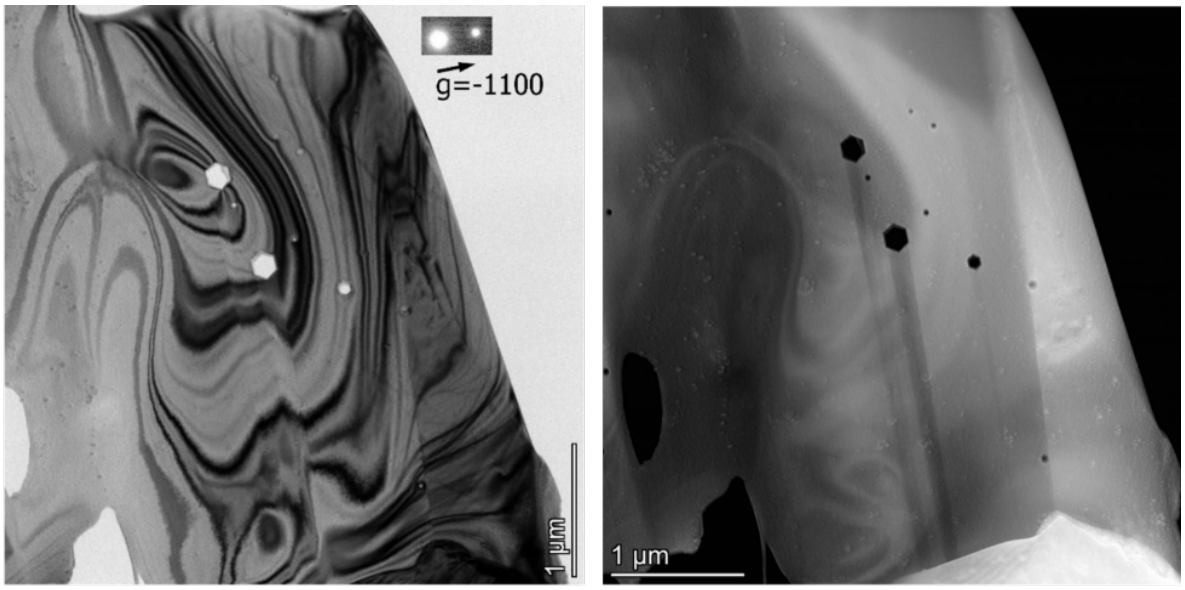

Figure 5.3: Planview TEM images of 22% EQE green LED on patterned sapphire utilizing an InGaN/GaN superlattice to nucleate the V-defects. The V-defect density here is around 25% (2.5×10^7 cm^{-2}) of the expected threading dislocation density (1×10^8 cm^{-2}) indicating that the V-defect nucleation layer isn't very effective.

Low or intermediate temperature GaN is a potential alternative to superlattices for nucleating the V-defects. For an initial experiment we replaced half the superlattice with GaN grown at 850°C. With one sample we grew the GaN with triethylgallium (TEG) which is used to grow the superlattice, active region and *p*-GaN of the LEDs. The other sample grew the LT-GaN using TMG which is used to grow the initial UID and *n*-GaN of the device. Figure 5.4 shows histograms of the V-defect size distribution measured using backscatter scanning electron microscopy (BS-SEM) images and Python-based image processing. The TEG-grown LT-GaN had a V-defect density of 4.4 x 10^7 cm^{-2} and an average V-defect size of 117 nm. The TMG-grown GaN had a V-defect density of 5.5 x 10^7 cm^{-2} and an average V-defect size of 184 nm. This indicates that TMG grown LT-GaN does a better job at nucleating V-defects on existing threading dislocations and nucleates them earlier in the LT-GaN. This result might

also be due to growth rate, since the TMG grown sample had a much faster growth rate. The power of these LEDs was less than half that of LEDs grown with just a superlattice which probably indicates that there's morphological issues associated with the LT-GaN.

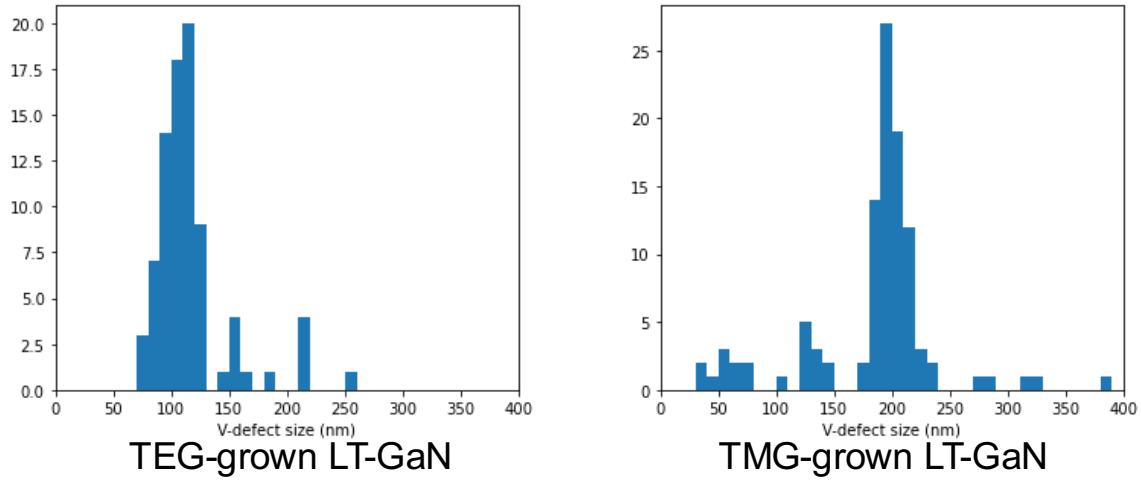

Figure 5.4: Histograms showing the V-defect size-distribution of the LEDs with low temperature (LT) GaN preparation layers.

V-defects nucleate and grow under conditions of kinetically limited growth. This is primarily determined by low growth temperatures (~800-900 °C) but other factors such as V/III ratio, growth rate, Si doping, and carrier gas also play a key role. Under conditions of kinetically limited growth, it's possible to get faster growth in the c-plane [0001] direction compared to the growth rate in the [0001] directions for the semipolar $\{10\bar{1}1\}$ planes of the V-defect sidewalls. When this occurs the V-defects will expand and grow.

An additional study looked at the nucleation of V-defects on commercial n-GaN on 3 µm pitch PSS templates. We used interrupted growths where we grew an initial high temperature GaN layer on the n-GaN template followed by a 50 nm low temperature (LT) GaN layer which designed for V-defect nucleation. The LT-GaN has the potential to degrade the

morphology of the epitaxy prior the superlattice (SL) and quantum well (QW) growth so we added a 7 nm HT-GaN recovery layer at 1000 °C to improve morphology. On top of the LT-GaN and HT-GaN we grew our standard 30-period SL from previous LED structures. It's notable that this SL structure was originally designed and optimized for V-defect nucleation on (111) Si growth but has so far been insufficient at nucleating V-defects on PSS. Here it's used mostly to increase the size of the V-defects and not for nucleation.

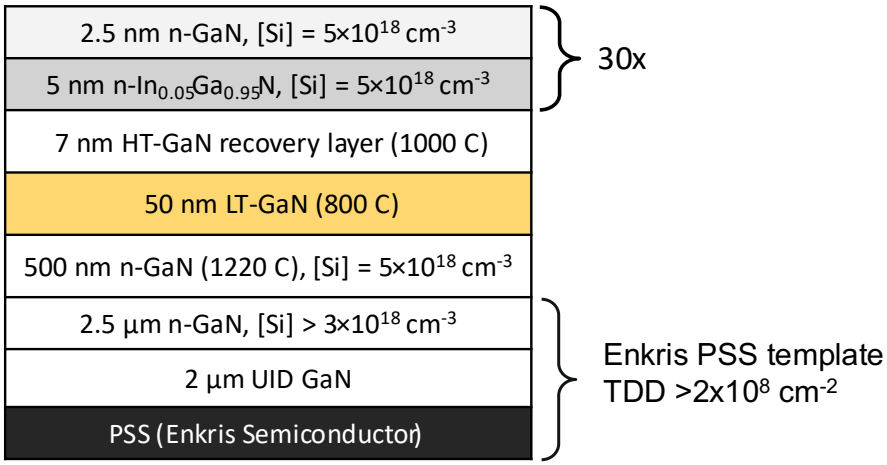

Figure 5.5: Epitaxial structure for initial interrupted growth studies with low-temperature GaN V-defect nucleation layer.

The structure for the LT-GaN interrupted growth studies is shown in Figure 5.5. Initial experiments on LT-GaN used a low Ammonia flow of 1 SLM (compared to 3 SLM typically used). Ammonia flow (V/III ratio) affects the lateral growth rate of GaN. An important factor in opening V-defects is limiting mass transport to the defects which further suppresses growth on the $\{10\bar{1}1\}$ planes. This can be accomplished through use of N_2 instead of H_2 as a carrier gas. N_2, being a larger molecule compared to H_2 will interfere with mass transport of metalorganics (MOs) to the V-defect site and decrease lateral growth rate in the V-defect. In addition, anti-surfactants (such as disilane) may also have the effect of reducing

adatom mobility and favor V-defect nucleation. Both can also have detrimental effects on morphology or generate other types of unwanted defects so that must be balanced when determining conditions for LT-GaN layers.

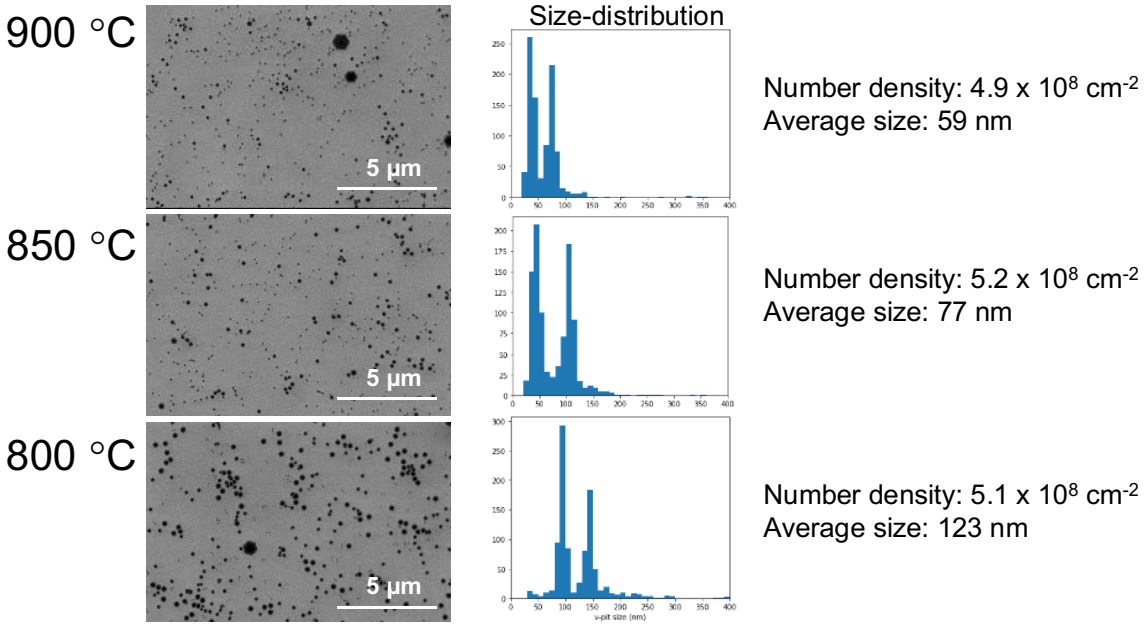

Figure 5.6: Initial LT-GaN experiments on PSS examining the effect of temperature on V-defect nucleation and growth with backscatter SEM images and size distributions.

Figure 5.6 examines the effect of temperature on V-defect distribution in the interrupted growths with backscatter (BS) scanning electron microscope (SEM) images and V-defect distributions calculated from the BS-SEM images. At 900 °C and 850 °C,there is a high density of small V-defects (<50 nm) and relatively few in the (>100 nm) range. The total number density is similar for all three temperatures, but the average size is significantly large for the 800 °C sample. The SL conditions were the same for all three growths. One explanation for this trend is that the V-defects are nucleating on the existing TDs in the GaN template (the TDD for this samples was ~3×10^8 cm^{-2}) but in the case of the higher temperatures many of the threads didn't nucleate V-defects in the LT-GaN so they didn't nucleate until the SL. This accounts for the higher number of smaller V-defects. In the case

of 800 °C, most of the threads were “used up” in the LT-GaN which left fewer nucleation sites during the SL growth. However, there’s still an issue of additional small defect generation in these samples since the pit density on the surface is higher than the TD density. We may want to selectively generate new defects (more on that in a later section) but for now we just want to make a large V-defect on every thread.

Although the backscatter SEM techniques are incredibly useful, they only are able to detect surface features. To better understand the relationship between threading dislocation density and V-defect density cathodoluminescence (CL) was used to better quantify the TDD on various growth templates purchased from industry and on V-pit templates. Figure 5.7 shows an SEM (5.7a) and CL (5.7b) of a GaN on PSS template from Enkris Semiconductor. The long dark streak in the middle is due to SEM damage. In CL a dark spot indicates an area where excitation from an electron beam does not cause any luminescence. In the case of a GaN on PSS template these areas correspond to TDs. Therefore, from Figure 5.7b we can calculate the TDD by simply counting the dark spots and dividing by the area. Based on these calculations we see that the TDD on these PSS templates is ~$2x10^8$ cm^{-2}.

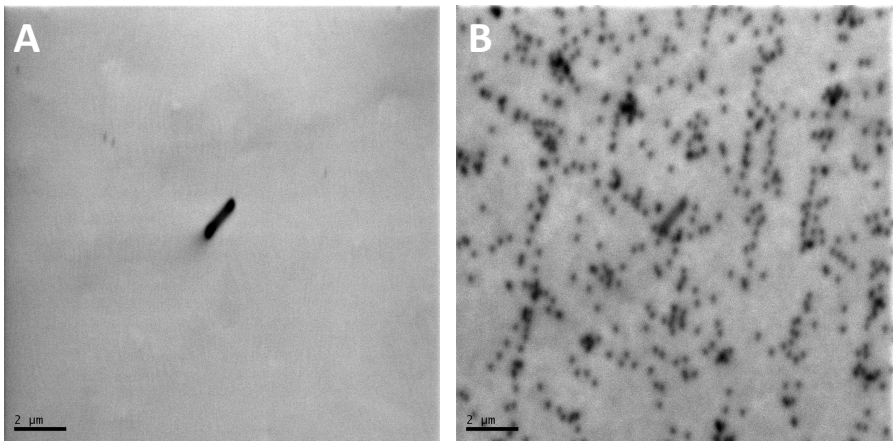

Figure 5.7: (a) SEM and (b) panchromatic CL of an Enkris PSS template. Note that the Long dark line in the center is due to electron beam damage.

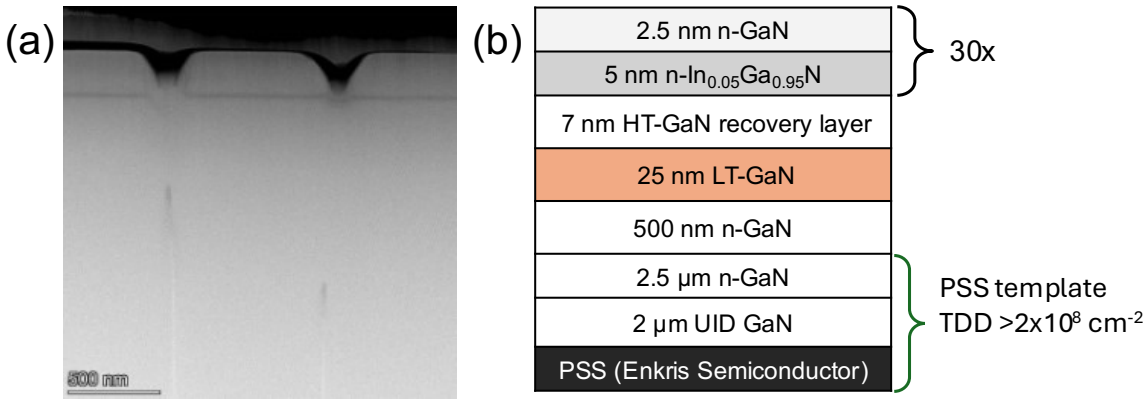

Figure 5.8: (a) HAADF TEM showing V-pit nucleation in a LT-GaN layer. (b) Optimized structure with thinner LT GaN layer.

Optimizing the LT GaN layer required a few iterations of the structure but with feedback from TEM (Figure 5.8a) and SEM an optimized structure (Figure 5.8b) was developed that nucleated all existing threads but didn't generate unwanted defects. This structure used just a 30 s LT GaN layer with a 50 nm/min growth rate (25 nm total thickness). These results are shown in Figure 5.9. The top left is a backscatter SEM image of the template surface. Top right is the thresholded image that was used for image recognition and V-pit detection using python. The python program estimated the size distribution, number density, and average size (shown in the bottom of Figure 5.9. This template structure achieved a monomodal distribution which is ideal for promoting uniform lateral injection. These results are also important because they show evidence of V-pit formation on edge dislocations. Since the V-pit density is similar to the TDD and 80-90% of TDs on PSS are edge TDs, it's certain that many of these V-pits are being formed on pure edge.

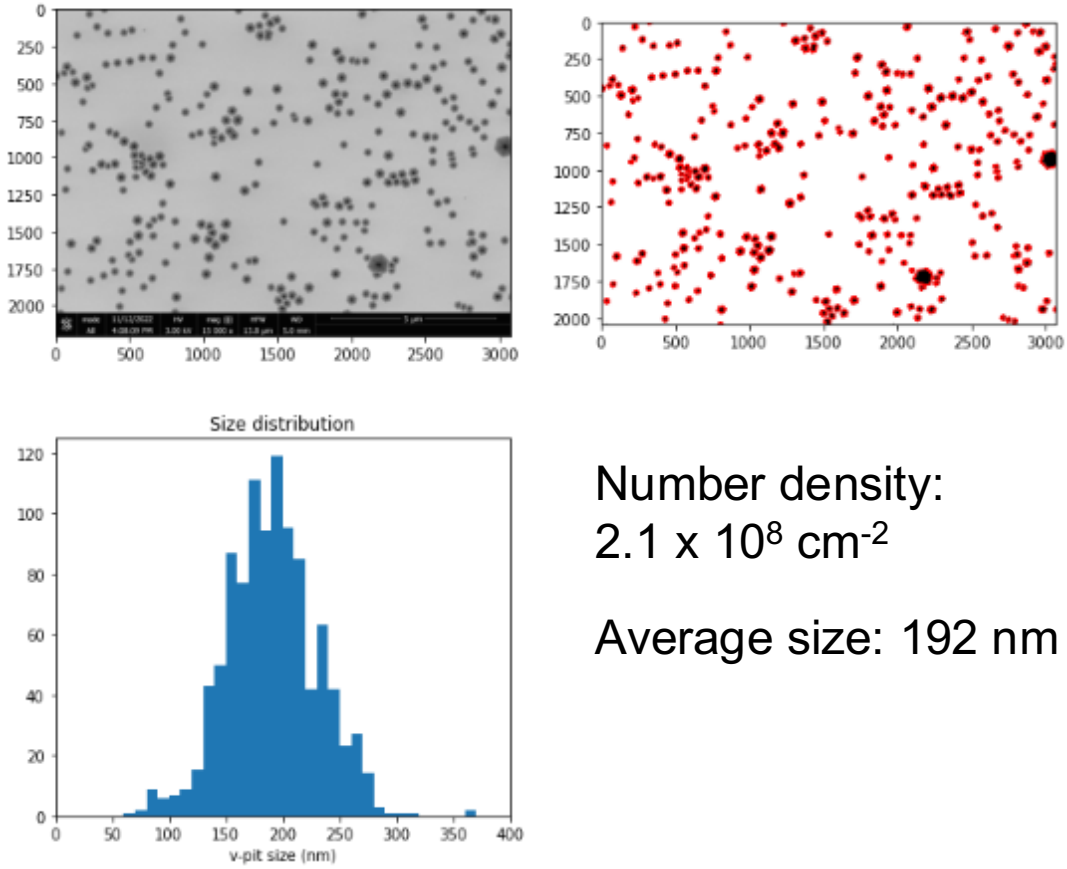

Figure 5.9: (top left) Backscatter SEM image of a V-defect nucleating template growth (top right) thresholded SEM after image processing with python. Red lines have been drawn by the program around the black-white contour lines. The dimensions of these red lines are used to generate size distribution historgrams (bottom left), number density and average size.

The average size of 192 nm is likely too large since this is being measured pre-active region growth. The ideal size in the active region is something around 150 nm at the top of the MQWs but this can be changed simply by changing the SL thickness. More importantly the total V-pit density of 2.1×10^8 cm^{-2} is around 5x lower than simulations suggest for the optimal V-defect density for complete lateral injection. Addressing this issue is the topic of the next two sections of this chapter.

Based on the TDD from Figure 5.7 and the V-pit density in Figure 5.9 it appears that all the existing TDs are becoming sites for V-defect nucleation, but this needed to be confirmed with CL. Figure 5.10a and 5.10b shows SEM and CL micrographs of an interrupted growth (structure shown in Figure 5.8b) using the low temp GaN layer on an Enkris PSS template identical to those imaged in Figure 5.7. The V-defects appear darker in the SEM image and the V-defect with associated TD appear dark in CL for the reasons explained above. With these images we can calculate both the V-defect density (through SEM) and the TDD (through CL). In both images the density was ~$2x10^8$ cm^{-2}. From Figure 5.10, it is clear that the low temperature GaN layer before the pre-well superlattice growth is nucleating all the threads into V-defects.

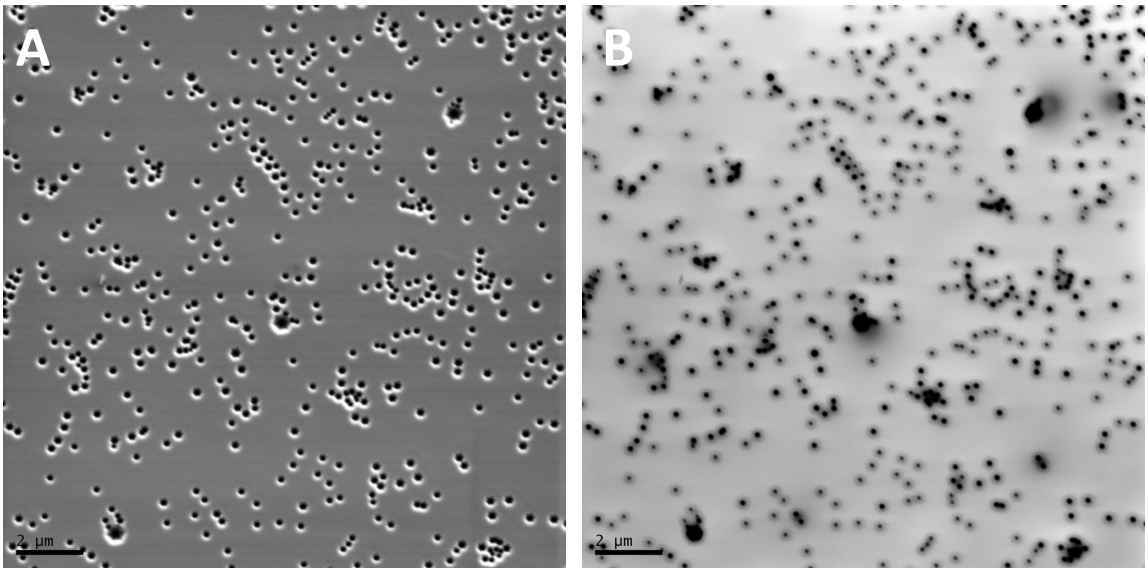

Figure 5.10: (a) SEM and (b) panchromatic CL of an interrupted growth using a low temp GaN pre-superlattice layer grown on an Enrkis PSS template. Because the V-defects are open on the interrupted growths and all TDs have nucleated V-defects, the images look almost identical.

This is a very important result because it indicates both mixed screw component TDs and pure edge TDs are successfully forming V-defects in our LT-GaN layer. These LEDs were

grown on (111) Si which has a higher fraction of mixed component TDs compared to sapphire which tends to have more pure edge TDs. If high V-defect densities are to be achieved in GaN on sapphire, it's critical to nucleate V-defects on pure edge TDs. Figure 3.5 shows direct evidence that our LT-GaN nucleation layer is nucleating V-defects on all of the pure edge TDs.

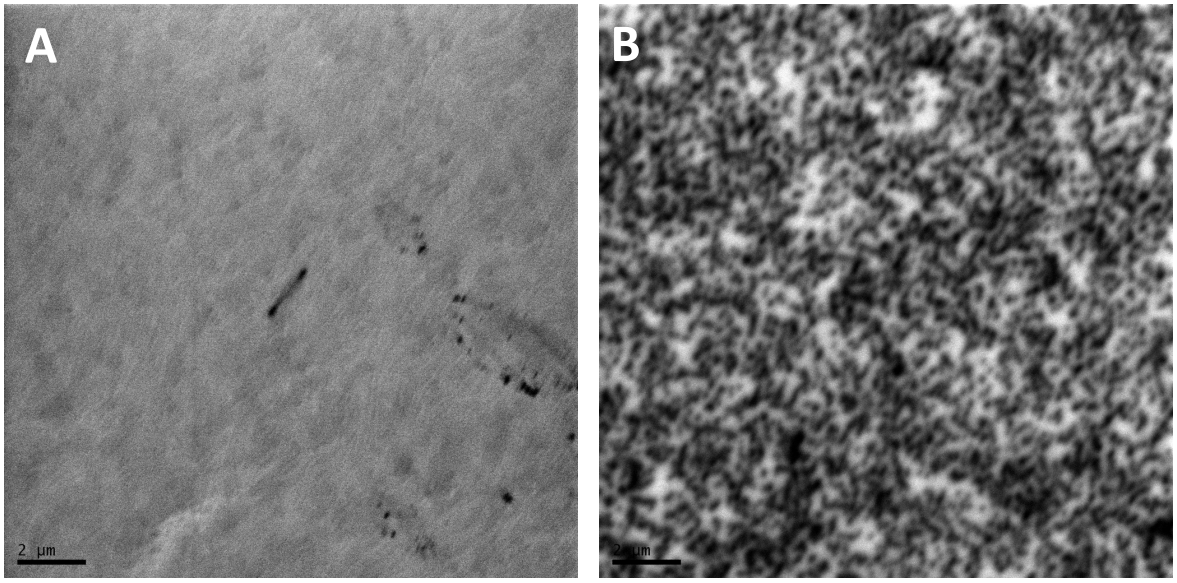

Figure 5.11: (a) SEM and (b) panchromatic CL of an Enkris FSS template.

Despite this result, a V-defect density of 2×10^8 cm^{-2} is most likely too low for uniform lateral injection across a green LED. The reason for this is that the hole diffusion length in GaN is only ~300 nm. At a TDD of 2×10^8 cm^{-2} there will be large areas of epitaxy where there isn't a V-defect within 300 nm. In these areas vertical injection through the *c*-plane barriers is the only viable method for hole injection. To solve this problem, we must either increase the TDD on PSS or grow on FSS which has a much higher TDD. Figure 5.11a and 5.11b show an SEM and CL micrographs, respectively, of an Enkris template grown on (FSS). As with Figure 5.11, the first image has a dark spot associated with electron beam damage. It other dark spots may be particles or small pits in the template. The CL image shows dark spots

on all the TDs which don't luminesce under electron beam excitement. From this we can calculate that the FSS template has a TDD of ~1 × 10^9 cm^{-2}.

We did a few experiments on FSS in an effort to realize higher total V-defect densities. Figure 5.12 shows plane-view SEM images of V-defect templates grown on FSS and PSS. The V-defect density on FSS is ~1.5x10^9 cm^{-2} whereas on PSS it's 2x10^8 cm^{-2}. While PSS has advantages in terms of light extraction, it's difficult to realize high V-defect densities because of the inherently low TDD on PSS. FSS poses other growth issues but it does provide TDDs and thus V-defect densities closer to the ideal value determined by simulations. Although our work focused on V-defect engineering on PSS, FSS is a viable path and is the choice for many LED growers in the industry.

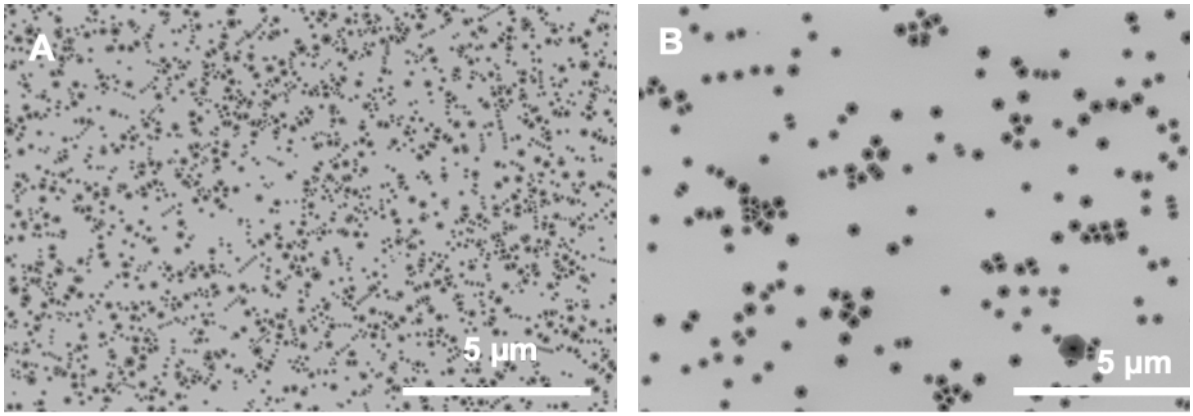

Figure 5.12: V-defect structure from SEM in an interrupted growth with LT-GaN layer and 30 period InGaN/GaN SL on (a) FSS and (b) PSS. The TDDs were ~1.5x10^9 cm^{-2} and 2x10^8 cm^{-2} respectively.

5.3 Pure edge dislocation half-loops for V-defect formation

During epitaxial growth, the corrugation potential is energy needed for species to move between sites on a growth surface. A high corrugation potential means that adatoms tend to get 'trapped' at local minima more easily, whereas a low corrugation potential means that adatoms

can easily move across the surface and have high adatom mobility [26]. In GaN epitaxy, the corrugation potential varies significantly depending on the crystal plane, and whether the growth is on Ga-face (0001) or N-face $(000\bar{1})$. Ga face (0001) GaN has a much lower corrugation potential and thus it's much easier to attain step flow growth. For growth on closed packed planes, such as $\{0001\}$ for wurtzite structures or $\{111\}$ for zinc blende structures, step flow growth is essential to sustain the correct stacking sequence. Under conditions of very large terrace widths or low adatom surface mobility for growth on close packed planes, stacking errors can occur due to 2D island growth away from the step edges on a terrace – this may result in stacking fault (SF) formation where the SFs are bound by partial dislocations. Achieving defect-free, step flow growth is predicated on adatoms ability to reorganize on the surface and move to step edges. Thus, when corrugation potential is high or when adatom have less thermal energy (i.e. low temperature growth), we expect to see more defects (such as stacking faults) forming in the crystal [27], [28]. This is the reason for significantly higher basal stacking fault concentration on N-face GaN and in growth on *a*-plane and *m*-plane [29], [30]. In nearly all epitaxial systems, low temperature growth will see significantly higher formation of stacking faults and other defects, irrespective of stress, due to the lower adatom mobility [31], [32].

The generation of new threading dislocations is rarely observed after the initial 2D to 3D growth and coalescence of islands for *c*-plane growth of GaN under typical LED growth procedures. Some reports suggest that dislocations may form due to stress in alloy layers, grown coherently on underlying GaN layers, but the mechanisms for such dislocation formation are poorly understood [33]. There are few reports of half-loop generation in GaN layers without the presence of stressed InGaN or AlGaN layers [34], [35]. TD half-loop

formation has been observed in previous reports on basal stacking faults [36]. The I_1 stacking fault in GaN, which is most observed, forms due to growth errors which occur when surface mobility is low [37]. I_1 basal stacking fault (BSF) formation is *not* fundamentally a stress driven process. Instead, it's associated with low temperature growth or a species like Al which has relatively low surface mobility compared to In or Ga. There's been some recent work on how the generation of stacked I_1 BSFs can form stacking fault boxes which have been shown to generate between 2 and 6 threading dislocations [38], [39]. This occurs because the overlap of the I1 BSFs will acquire Shockley-like partial dislocations and may lead to the extra threading dislocations out of geometric necessity [40].

In this section, we present evidence for pure edge half-loop generation in low temperature grown nominally unstressed GaN layers. The formation of the half-loops, which are missing planes of atoms in the crystal, is attributed to growth kinetics, low adatom mobility, and "growth errors" in the low temperature grown GaN layer. Additionally, we show clear evidence through scattering contrast transmission electron microscopy (TEM) of the formation of V-defects on pure edge type TDs from the substrate and from half-loops. These results are highly relevant to V-defect engineering for lateral injection on sapphire where most of the TDs are pure edge and where the TDD is often insufficient for complete lateral injection.

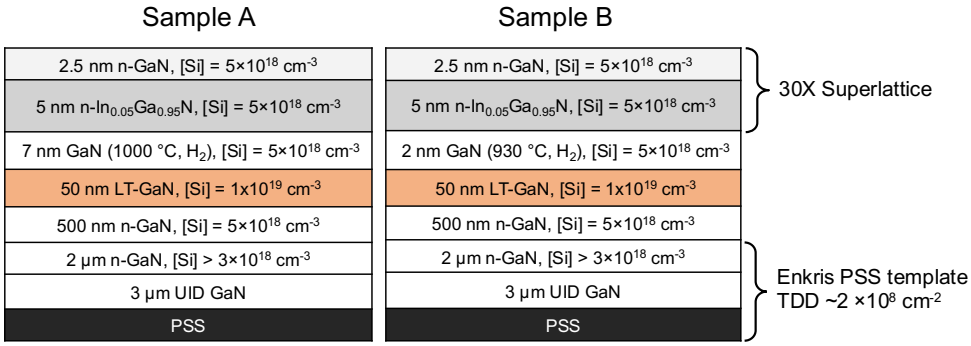

Figure 5.13: Epitaxial structure of LT GaN templates used to generate half-loops and nucleate V-defects.

The GaN samples A and B studied in this paper were grown by atmospheric pressure metalorganic chemical vapor deposition (MOCVD). n-type GaN preparation layers were grown n-GaN on PSS templates from Enkris semiconductor. The templates consisted of 3 μm of unintentionally doped (UID) GaN and 2 μm of n-doped GaN ([Si] > 3 x 10^{18} cm^{-3}). The MOCVD growth at UCSB started with 500 nm of n-doped GaN ([Si] ~ 5 x 10^{18} cm^{-3}) and then 50 nm of low temperature (LT) GaN grown ~800 °C with an N_2 carrier gas at a growth rate of 50 nm/min with a disilane flow of 7 sccm. The high disilane flow acts as an anti-surfacant and the high growth rate, combined with the reduced growth temperature, limits adatom mobility into the surface depression at the top of the threading dislocations which enhances the V-defect formation. Under these conditions of kinetically limited growth the relative growth on different planes can be described by kinetic Wulff plots [41]. It's the varying growth rates between c-plane and $\{10\bar{1}1\}$ that favor V-defect nucleation and growth. After low temperature growth, the temperature was increased to ~1000 °C for sample A and 930 °C for sample B. 7 nm of GaN (Sample A) and 2 nm (Sample B) were grown in H_2 followed by a 30-period 5 nm $In_{0.05}Ga_{0.95}N$/2.5 nm GaN superlattice (SL) with [Si] ~ 5 x 10^{18} cm^{-3} at ~930 °C. The structures are shown in Figure 5.13. No active region was grown on these samples.

Scattering contrast transmission electron microscopy (TEM) and High Angle Annular Dark Field (HAADF) Scanning TEM (STEM) were performed in both cross-section and plane-view configurations with two microscopes, one is a Thermo Fisher Scientific Talos G2 200X TEM/STEM system equipped with energy dispersive x-ray spectroscopy (EDS), another is Thermo Fisher Scientific Spectra 200 S/TEM. Backscatter Scanning Electron Microscopy (SEM) was performed using an FEI Nova Nano 650 FEG SEM. Cathodoluminescence (CL)

measurements were performed using a Gatan MonoCL4 with mono- and pan-chromatic capabilities attached to a field emission scanning electron microscope (Thermo Fisher Apreo C LoVac SEM) operating at 5 kV with a beam current of 0.8 nA.

Figure 5.14**Error! Reference source not found.** shows a plane-view backscatter (BS) SEM image of Sample A. Because the growths were stopped after LT GaN and SL growth, the V-defects remain open and can be easily observed in plane-view SEM. The large V-defects can be seen as dark hexagons in BS SEM image. These large V-defects (100-800 nm in diameter) form on TDs that are generated in the 2D-3D GaN growth. On PSS, TDs cluster around sapphire pyramids which is often reflected in the V-defect distribution. In addition, lines of V-defects are observed which are most likely the result of rows of pure edge TDs that form at coalescence boundaries during the 2D-3D high temperature GaN growth. Furthermore, it's expected that there will be a size difference between mixed (***a***+***c***) and pure edge TDs because the mixed TDs have a higher line tension where the TD meets the crystal surface and will form a larger initial surface depression. It's this larger surface depression that forms larger V-defects more readily. Here we see both pure edge and mixed TDs nucleating V-defects. This is confirmed later in the paper with cathodoluminescence and cross-sectional TEM.

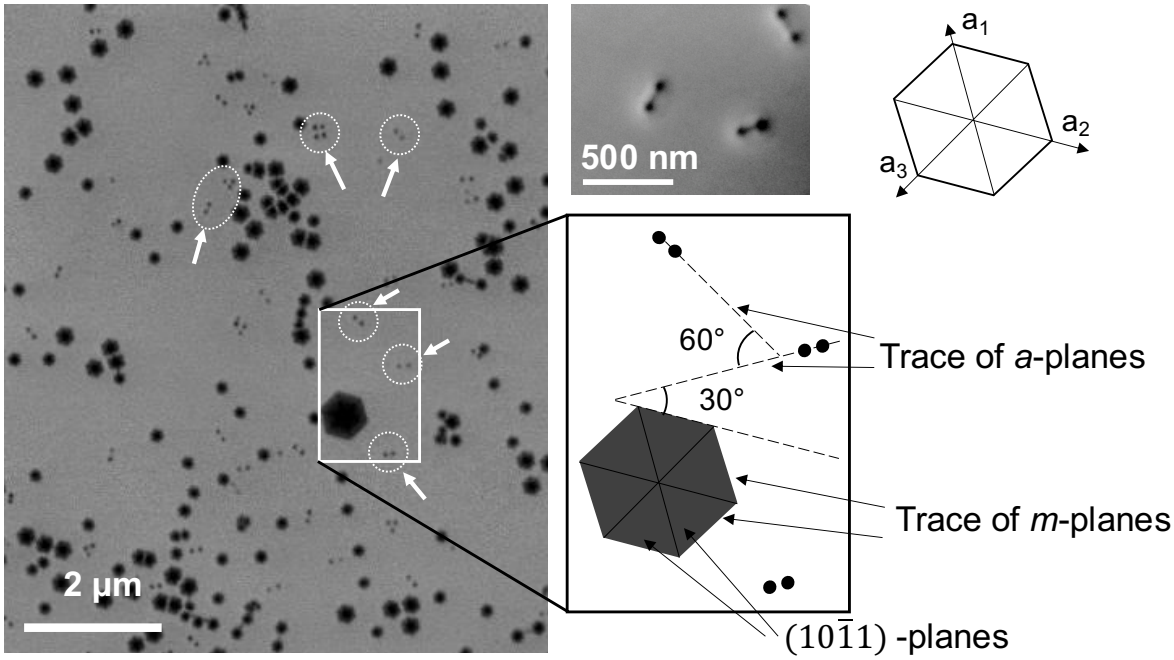

Figure 5.14: Backscatter SEM images (left and higher magnification in top right) of the epitaxial surface of sample A showing the large V-defects generated on mixed and pure-edge TDs. The small pairs of surface depressions correspond to half-loop generation, some of these pairs are indicated with a dashed circle and white arrow. It can be seen from the schematic that the pairs of surface depressions are aligned with the intersection of the *a*-plane and *c*-plane (trace of the *a*-plane) and are rotated 30° from the trace of the *m*-plane and the top of $\{10\bar{1}1\}$-plane sidewalls of the large V-defects (the dashed lines in the schematic correspond to the trace (intersection) of the *m*-planes and *a*-planes with the *c*-plane).

In addition to the large V-defects, we observe pairs of small surface depressions where the direction separating the paired depressions coincides with the trace of the *a*-plane– i.e., $\langle 10\bar{1}0\rangle$ m-directions. V-defects have $\{10\bar{1}1\}$ sidewalls which, viewed from above, are parallel to the trace of the *m*-plane intersection with the *c*-plane – i.e., $\langle 11\bar{2}0\rangle$ a-directions. These small defect pairs, or in some cases triplets and quadruplets, lie 30° from the trace of *m*-plane (which are traces of *a*-planes) as illustrated in Figure 5.14. Triplet formation has not been predicted in the literature on half-loop formation in GaN.

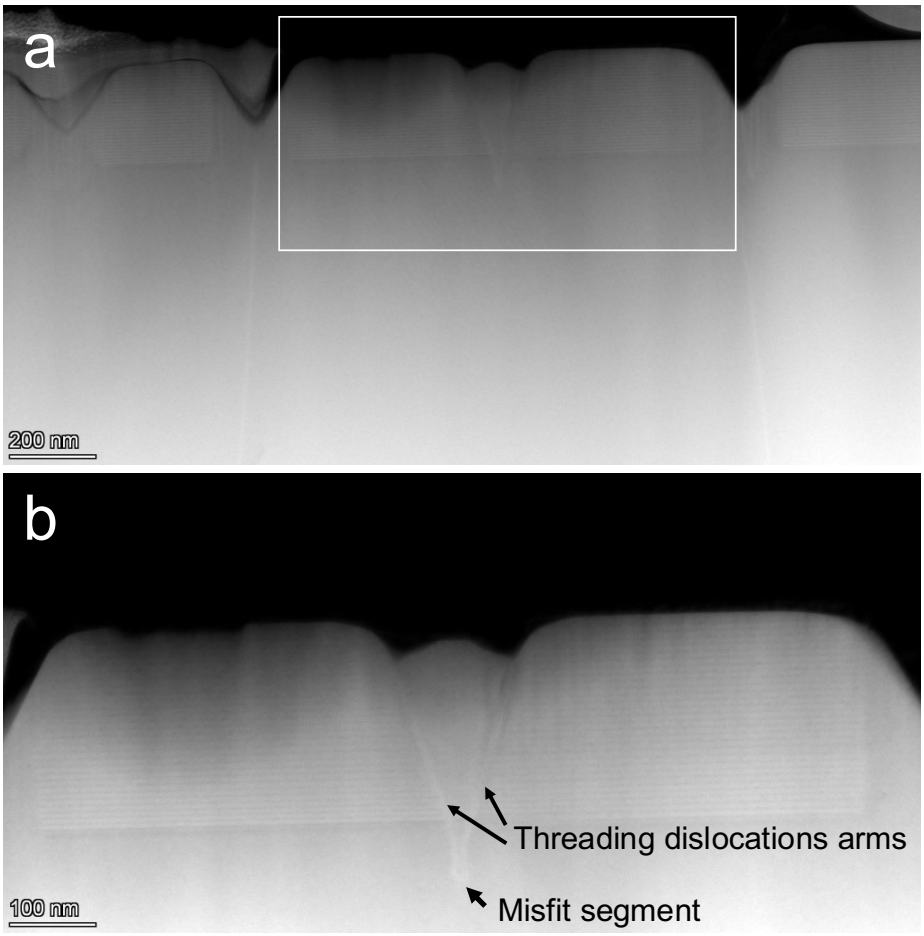

Figure 5.15: (a) and **(b)** are cross-sectional HAADF TEM images showing the half-loop formation the climb-like behavior of the TDs in the m-direction. In (a) several V-defects can be seen forming on TDs from the initial GaN on sapphire growth. (b) is a higher magnification image indicated by the white box in (a).

As discussed in the introduction, recent work has shown the formation of pure edge dislocations from overlapping I_1 BSFs where the new threads are generated from geometry of the stacking fault boxes, bound by partial dislocations [38], [39]. This hypothesis would explain why these form in low temperature GaN with a rapid growth rate since low surface mobility favors I_1 BSF formation. Due to the high disilane flow, there is a possibility of SiN nano-masking at threading dislocations and causing half-loop formation. There are reports of SiN nano-masks forming under high Si doping [42]. While the traditional method for SiN

nano-masking has shown a reduction in TDD via lateral overgrowth through pinholes in the SiN, it's possible that a partial SiN mask could create the type of growth perturbations needed to generated TDs [43]. It's notable however, that SiN nano-masking usually occurs during growth interrupts where only NH_3 and disilane are flown. The half-loops in the samples in this work were generated during continuous flow of TMG. Additionally, there was no Si observed in STEM EDX at the half-loop nucleation site.

Figure 5.15 shows cross-sectional HAADF images of a half-loop forming in a LT GaN layer in Sample A. An edge dislocation loop initiates with a small U-shaped dislocation in the LT GaN layer lying on the *a*-plane. Above the U-shape, two pure edge threading dislocation arms split off and then begin to separate in a climb-like geometry in the GaN before the SL growth. It appears that the climb-like behavior is initiated when the growth temperature was increased from 800 °C to 1000 °C. This would suggest that there is an energetic driving force for climb-like behavior, but it only occurs if there is sufficient adatom mobility during the MOCVD growth. The TDs separate further in the SL and eventually generate a pair of small depressions on the surface. It's notable that the half-loop forms during homoepitaxial growth and not in a stressed InGaN or AlGaN layer.

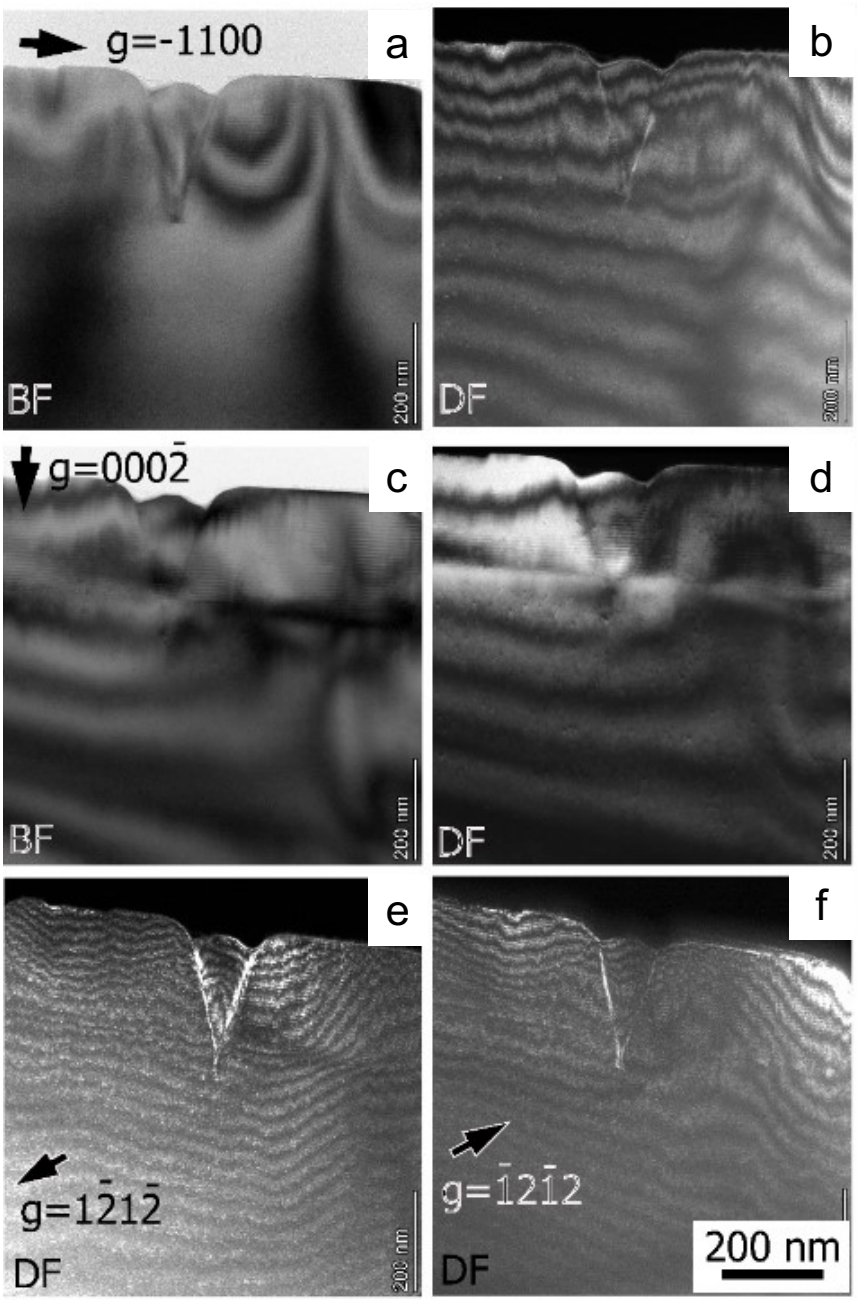

Figure 5.16: (**a**) and (**b**) Shows scattering contrast TEM in bright field (BF) and dark-field (DF) configurations respectively with an in-plane g vector. Only faint contrast is observed in $\boldsymbol{g} = \bar{1}100$ diffraction conditions. **(c)** BF and **(d)** DF show scattering contrast TEM with a zone axis g vector. The dislocation is invisible in $\boldsymbol{g} = 000\bar{2}$ conditions showing only residual contrast. This analysis shows that the Burgers vector has an *a*-component and is pure edge type. The narrow spacing of lower U-shape lines shown in $\boldsymbol{g} = 1\bar{2}1\bar{2}$ weak beam diffraction condition **(e)**, and wider spacing shown in $\boldsymbol{g} = \bar{1}2\bar{1}\bar{2}$ **(f)**, confirm that the dislocation is a *a*-type pure edge half loop.

To examine the nature of the dislocation, scattering contrast TEM was carried out as shown in Figure 5.16. The dislocation shows faint contrast in $\boldsymbol{g} = \bar{1}100$ (Fig. 5.16a and 5.16b), and is nearly invisible in $\boldsymbol{g} = 000\bar{2}$ (Fig. 5.16c and 5.16d), indicating that the Burgers vector is vertical to $\boldsymbol{g} = \bar{1}100$ and $\boldsymbol{g} = 000\bar{2}$, i.e., the Burgers vector is $\frac{1}{3}\langle 11\bar{2}0\rangle$, a pure **a**-type dislocation. The weak beam dark field image (DF) with $\boldsymbol{g} = 1\bar{2}1\bar{2}$ show narrow U-shape as shown in Fig. 5.16e, while taken in the opposite diffraction vector the U-shape show wider as shown in Fig. 5.16f. This is a typical feature of loop dislocation [44]. The images in Fig. 5.16e and 5.16f of loop dislocation are either inside or outside of the real core position depending on the value of $(\boldsymbol{g} \cdot \boldsymbol{b})s$, where s is deviation parameter. In 1g/3g weak beam conditions, s is positive, a change in $\boldsymbol{g}$'s sign will change $(\boldsymbol{g} \cdot \boldsymbol{b})s$; as a result, one image shows a narrow U, while another image show wider U with opposite $\boldsymbol{g}$.

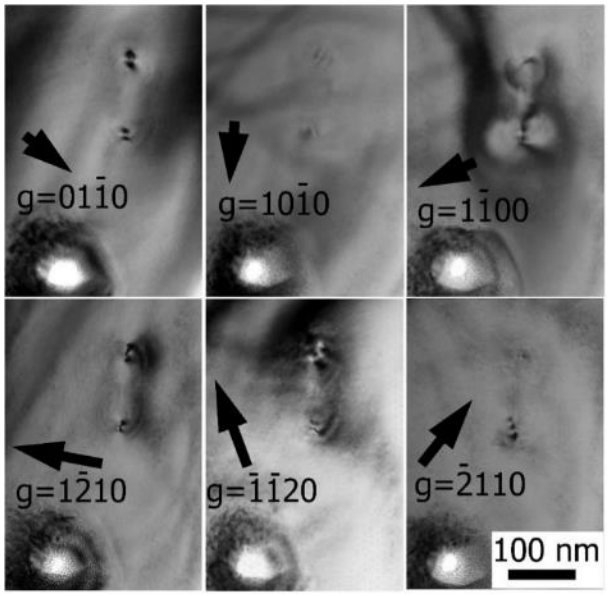

Figure 5.17: From the analysis in Fig. 5.16 we determined that there was no *c*-component to the Burgers vector for the dislocation loops. Here we show plane-view TEM with different diffraction conditions. We see strong contrast in all directions except when $\boldsymbol{g} = 10\bar{1}0$, parallel to the *a*-plane and perpendicular to the *a*-direction. Since no contrast is observed

when $\boldsymbol{g} \cdot \boldsymbol{b} = 0$, we once again confirm that the dislocation has an $\frac{1}{3}\langle 11\bar{2}0\rangle$ *a*-direction Burgers vector $\boldsymbol{b}$.

Figure 5.17 shows planview DF scattering contrast TEM images of a half-loop forming on *a*-plane. Strong dislocation contrast is observed in all directions except for $\boldsymbol{g} = 10\bar{1}0$. Since no contrast is observed when $\mathbf{g} \cdot \mathbf{b} = 0$, this indicates that the Burgers vector $\boldsymbol{b}$ is $\frac{1}{3}\langle 11\bar{2}0\rangle$, oriented in the *a*-direction. The dislocation lies on the *a*-plane and has a climb-like geometry. The sense of climb is in the *m*-direction.

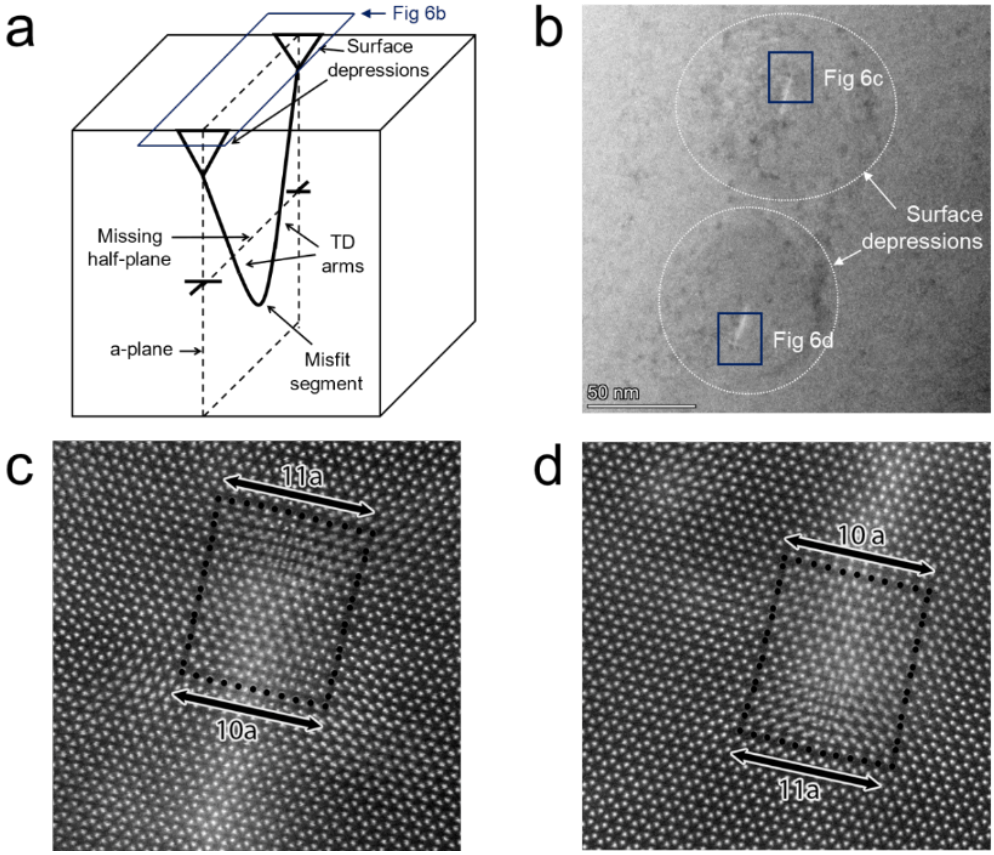

Figure 5.18: (a) Schematic of half-loop formation and missing plane in a GaN film. **(b)** Plane-view HAADF TEM image showing the two TD arms in the foil (bright contrast) and the surface depressions indicated with white circles and the top of the TD arms which appear as white lines in TEM. The orientation of Fig 5.18b with respect to the half-loop is indicated by the blue box the schematic in Fig. 5.18a. **(c)** and **(d)** are high resolution HAADF TEM images of the top and bottom of the half-loop arm respectively as indicated by the boxes in Fig. 5.18b. The orientation of Fig. 5.18c and 5.18d are indicated by the blue boxes in Fig

5.18b. The hexagonal structure of the GaN can be clearly seen. The missing plane of atoms is obvious by counting atomic spacings above and below the half-loop arms which is indicated by the black dots and arrows.

Figure 5.18a shows a schematic in 3D of the half-loop in GaN. The misfit segment is shown at the bottom with two TD arms extending and terminating in small depressions that meet the crystal surface. The missing half plane with *a*-direction Burgers vector $\boldsymbol{b} = \frac{1}{3}[11\bar{2}0]$ as shown. Figure 5.18b is HAADF plane-view image of the surface of the crystal where the half-loop structure meets the crystals surface and forms two small surface depressions. Figures 5.18c and 5.18d show close ups of each side of the half-loop structure. A circuit was drawn around the end of dislocation as indicated by the black dots and arrows in Fig. 5.18c and 5.18d. Here it is obvious that the half loop is the result of a single plane of atoms removed along *a*-plane.

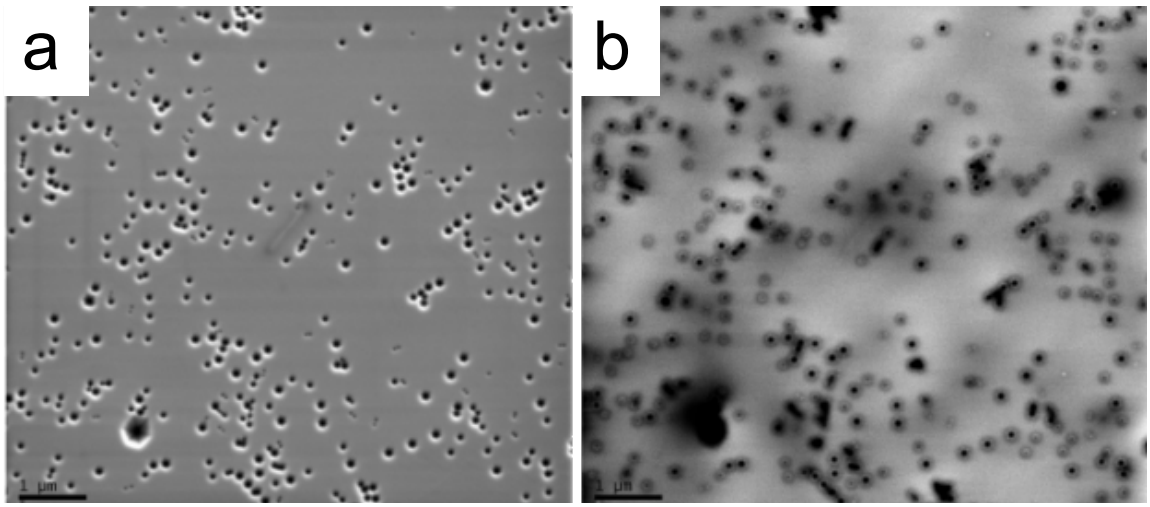

Figure 5.19: (a) SEM and B) panchromatic CL images of sample A showing the large V-defect formation on ~100% of existing threads and the new pure edge half-loops that generate smaller depressions with may turn into V-defects for lateral injection with the right growth conditions.

Figure 5.19 shows the comparison between an SEM image (Fig. 5.19a) and a panchromatic CL image (Fig. 5.19b). The primary conclusion from these images is that all the

dark spots in Fig. 5.19a have corresponding dark spots in the CL image (Fig. 5.19b). This means that all V-defects are nucleated on threads and there are few if any threads without a V-defect. The half-loops can be seen as small dark dots in Fig. 5.19a and pairs of brighter dots in Fig. 5.19b. Since the V-defects, formed both from the substrate and half-loop TDs, remain unfilled, they appear partially brighter in the CL image in Fig. 5.19b due to increased light extraction from the V-defect sidewalls. The V-defect density was ~2×10^8 cm^{-2} and the half-loop density was ~1×10^8 cm^{-2} for sample A. On-going work in our group has shown that the half-loop density can be changed with growth conditions and will be the subject of a future publication.

Figure 5.20 shows a half loop and large V-defect from sample B. Fig. 5.20a shows a lower magnification image where the half loop V-defect can be compared to another large V-defect originating off a TD from the substrate. Figures 5.20b and 5.20c show how the surface depressions on either side of the half-loop turn into a single large V-defect. Figure 5.20c shows clear evidence that semipolar growth is occurring on the sides of this V-defect closely resembling images of semipolar QWs in previous work [11], [24]. Figure 5.20d shows high resolution HAADF STEM images in the region of the half loop formation. From both HAADF STEM imaging and scattering contrast imaging, we were unable to determine the extended defect structure at the initiation site of the half loop – this is a topic of ongoing investigation. Half loop formation has been observed from basal plane stacking faults so it's very possible that Fig. 5.20d shows stacking faults with half-loop formation [36]. Compared to sample A, the climb-like geometry is less pronounced in sample B which likely assisted in opening a single large V-defect rather than two smaller ones as was observed in sample A. It's plausible that there were initially two small pits on each TD arm, but they merged into a single large V-

defect. The only growth difference between sample A and sample B was the thickness and growth temperature of the GaN spacer grown between the LT GaN and the SL, with sample A having a higher temperature and thicker layer.

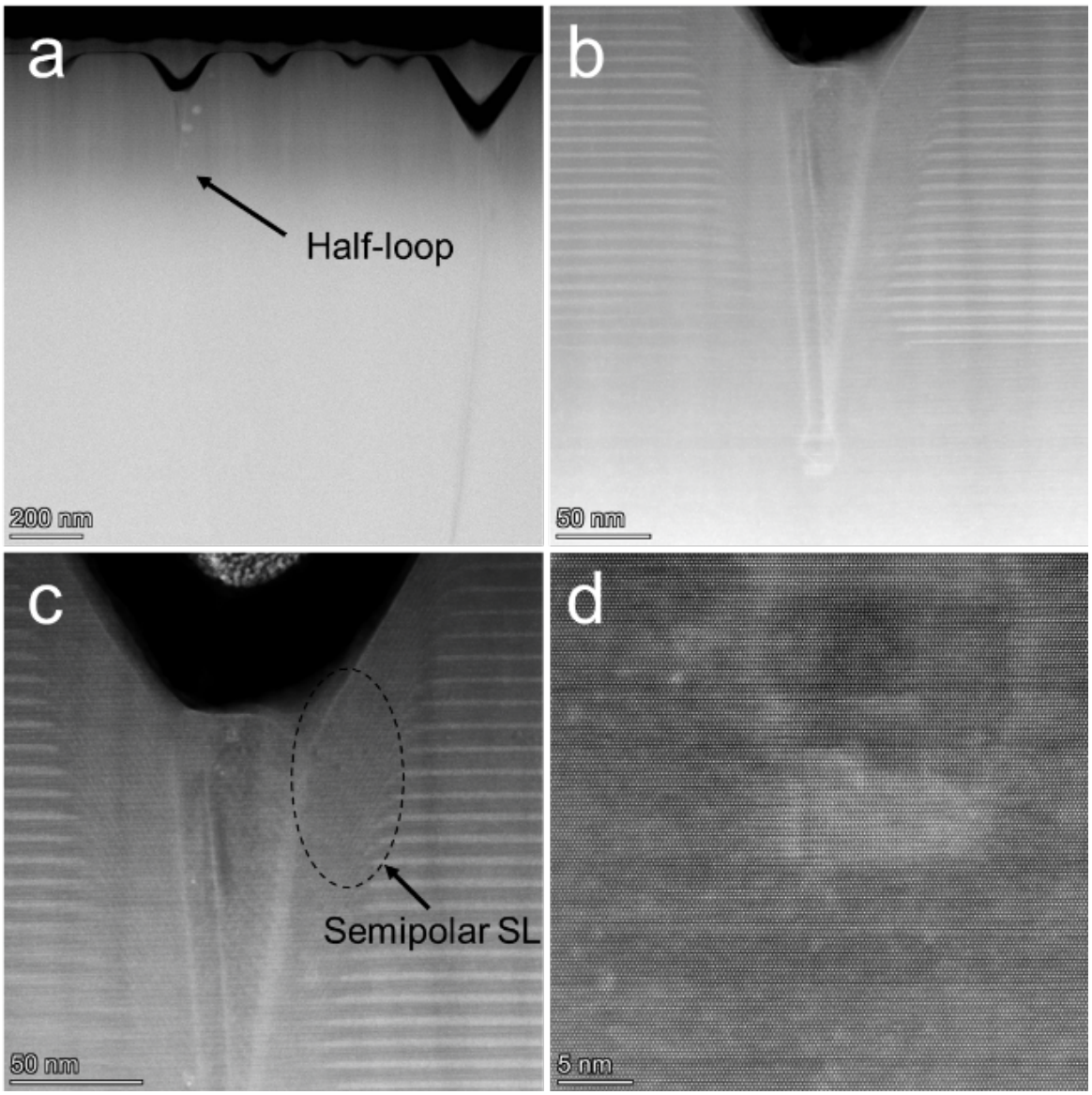

Figure 5.20: (**a**) HAADF cross-sectional TEM image of a half-loop type structure forming in a LT GaN layer in Sample B. **(b)** and **(c)** show close ups of the half loop and V-defect formation from the half loop. It can be seen from these images that rather than opening two V-defects, the surface depressions at each end of the half-loop merge together to form a single large V-defect. From (**c**) we see clear evidence that the semipolar growth is occurring

on the sidewalls of the V-defect. (**d**) shows the extended defect structure of the initiation of the dislocation half loop.

This supports the hypothesis that climb-like behavior of TD arms is dependent on surface kinetics and adatom mobility. Based on previous work in our group [11], forming large V-defects before the active region is beneficial for lateral injection, so while sample A provides a simpler case study for homoepitaxial half loop formation in GaN, sample B produces V-defects that are more likely to be favorable for lateral injection.

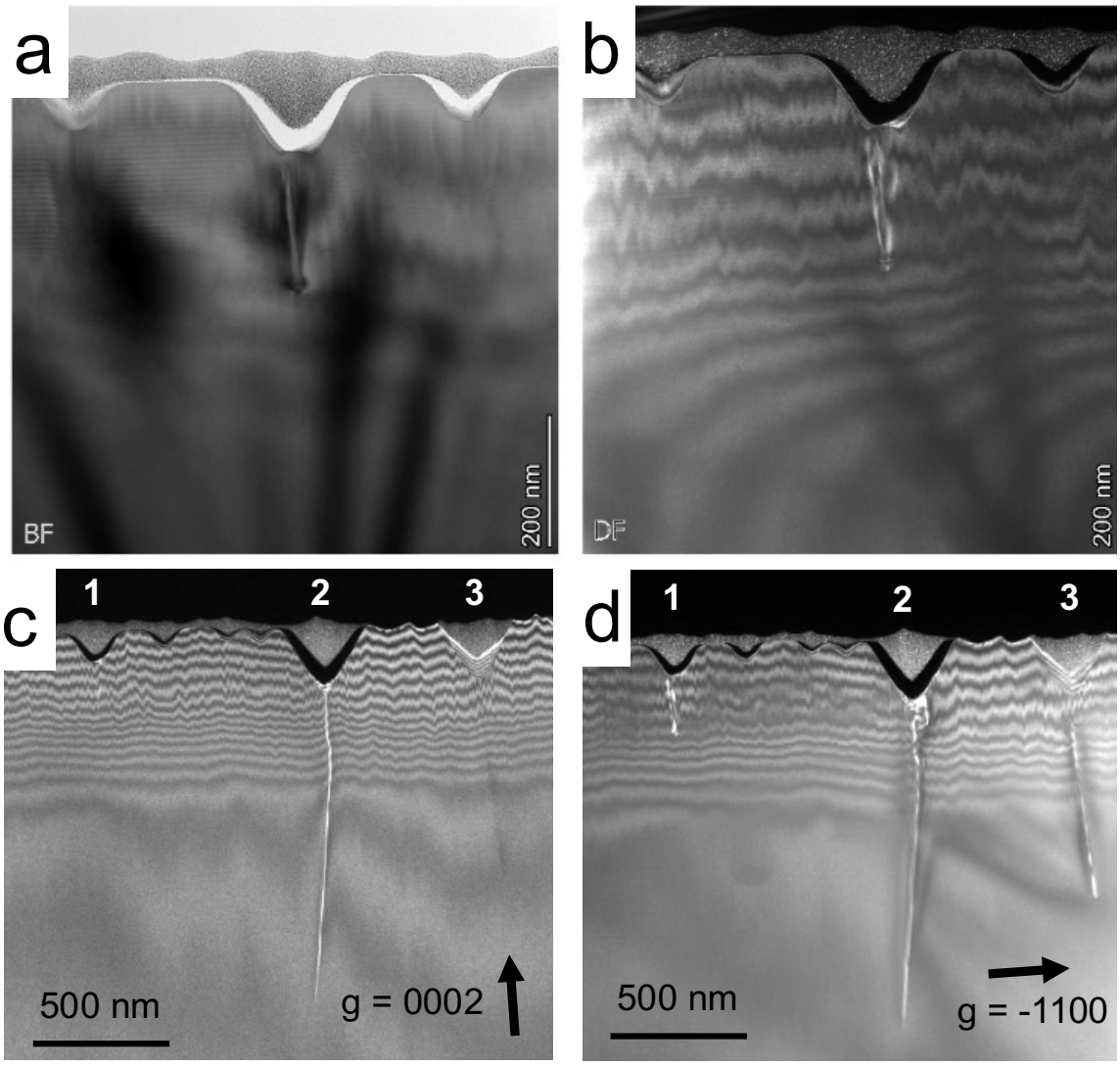

Figure 5.21 BF (**a**) and DF (**b**) scattering contrast TEM images of the large V-defect origination from a half-loop generated in LT-GaN. This V-defect will likely be beneficial for lateral injection in a full LED structure. (**c**) and (**d**) show DF scattering contrast TEM images with 3 distinct types of large V-defects for lateral injection. V-defect 1 is generated from a pure edge half-loop from the LT-GaN. V-defect 2 is generated from a mixed (***a***+***c***) type TD (shows contrast in both diffraction conditions) originating from the substrate, and V-defect 3 is formed on a pure edge type dislocation from the substrate.

Figure 5.21a and 5.21b show BF and DF scattering contrast images of the large V-defect generated half loop in sample B. Figures 9c and 9d show scattering contrast TEM with $\boldsymbol{g} = 0002$ (zone axis) and $\boldsymbol{g} = \bar{1}100$ respectively, showing three large V-defects (labeled 1, 2, and 3) forming in the LT-GaN. What's notable is that each V-defect in Figs. 5.21c and 5.21d forms on a different type of TD. V-defect 1 is the same large V-defect from Figs. 5.21a and 5.21b and forms on the half loop. The residual contrast in the zone axis suggests these TD arms have no c-component to their Burger's vector and are thus pure-edge type. V-defect 2 forms on a mixed component (***a***+***c*** Burgers vector) TD from the underlying GaN layer as can be seen by the strong contrast under both diffraction conditions. V-defect 3 shows only residual contrast in the zone axis which indicates this is a pure edge TD from the substrate. In both V-defect 2 and 3 the TD appears to end but this is due simply to it extending out of the plane of the TEM sample. These TDs are generated in the early 2D to 3D GaN growth. V-defect formation on mixed-type TDs happens most readily and is the mostly widely studied in the literature. V-defects on mixed TDs are generally larger due to the larger surface depression that occurs when a mixed TD meets the GaN surface. Mixed TDs occur in higher frequency in GaN on Si compared to Gan on PSS or flat sapphire, which is one of the reasons for the success of V-defect LEDs in GaN on Si [6], [7]. Few reports in the literature show clear evidence of V-defect formation on pure edge TDs so this is a significant result. For GaN growth on sapphire, usually most of the TDs are pure edge type, so this result is especially important for

V-defect engineering of LED grown on sapphire. The important takeaway from Fig. 5.21 is that we have demonstrated the ability to form large V-defects on any type of TD including those generated in the preparation layers. This provides a versatile toolbox for V-defect LED engineering on any substrates.

Half-loop formation during homoepitaxy has rarely been observed in GaN. There is increasing interest in the strategic use of V-defects for lateral injection of LEDs. Most of the early work on V-defect LEDs was done on Si because of the relatively high threading dislocation density ($>1\times10^9$ cm^{-2}) compared to growth on PSS. Typical PSS has a TDD $< 1 \times 10^8$ cm^{-2} and high TDD PSS rarely exceeds 3×10^8 cm^{-2}. Full device simulations of V-defect LEDs show the importance of achieving a high V-defect density in long-wavelength V-defect engineered LEDs [9]. Because the lateral carrier diffusion length is ~100 nm in GaN with alloy fluctuations, the V-defects need to be, on average, a few hundred nm apart in order to get lateral injection across an entire LED [45]. This requires V-defect densities of $\sim1\times10^9$ cm^{-2} which is achievable on (111) Si and flat sapphire but is difficult to achieve using the existing TDs on PSS. If the separation between V-defects is larger than the carrier diffusion length only partial lateral injection can be achieved. The formation of half-loops and the subsequent nucleation of V-defects provides a promising pathway to realized sufficiently high V-defect densities on PSS. In addition, the demonstration of V-defect formation on pure edge dislocations (both from the substrate and generated in the LT GaN), is critical for V-defect engineering of LEDs grown on sapphire where most of the TDs are pure edge type.

5.4 Optimizing V-defect density and distribution

Note: The results in this section are primarily the work of Alejandro Quevedo, Manuscript: A. Quevedo, F. Wu, T.Y. Tsai, **J. Ewing**, T. Tak, S. Gandrothula, S. Gee, X. Li, S. Nakamura, S.P. DenBaars, J.S. Speck, "Dislocation half-loop control for optimal V-defect density in GaN-based light emitting diodes", *Appl. Phys. Letters*, 125 (4) (2024)

.

To further develop the half-loop TD generation and V-pit nucleation we performed systematic experiments to investigate how growth conditions in the half-loop generation layer impact half-loop density. Seven samples with different half-loop preparation layers were grown on 2" n-GaN-on-PSS substrates from Enkris Semiconductor. The growth parameters used in the half loop generation layer for each sample are summarized in Table 5.3.

Sample	Temperature	Disilane Flow	Thickness
A	800 °C	7 sccm	45 nm
B	800 °C	5 sccm	45 nm
C	800 °C	9 sccm	45 nm
D	775 °C	7 sccm	45 nm
E	788 °C	7 sccm	45 nm
F	800 °C	7 sccm	90 nm
G	800 °C	7 sccm	79 nm

Table 5.3: A summary of the seven half-loop generating structures grown, with growth temperature, disilane flow, and thickness listed for the half-loop generation layer.

The baseline template was almost identical to the parameters used in the half-loops samples in the previous section. The temperature, disilane flow, and layer thickness were varied as shown in Table 5.3. An SEM of the surface of Sample G is shown in Figure 5.22a. The plots in Figure 5.22b-d show the trends of large V-defects and small V-defects (half-loops). The density of large pits was constant for all conditions and equal to the TDD of the n-GaN on PSS template. This is consistent with the result shown earlier in the chapter for V-

defect nucleation on existing TDs using low temperature GaN layers. The half loops form due to growth errors and so the density of half loops is proportional to the number of growth errors that occur in the low temperature layer. Increased disilane flow increases the number of half-loops because disilane has an antisurfactant effect (Figure 5.22b). Generally, growth errors happen more readily at lower growth temperatures thus half loop density will be greater at lower growth temperatures (Figure 5.22c). Finally, the total number of growth errors accumulate the longer the growth time (all other conditions being equal). This explains the significant increase in half loop density with layer thickness shown in Figure 5.22d.

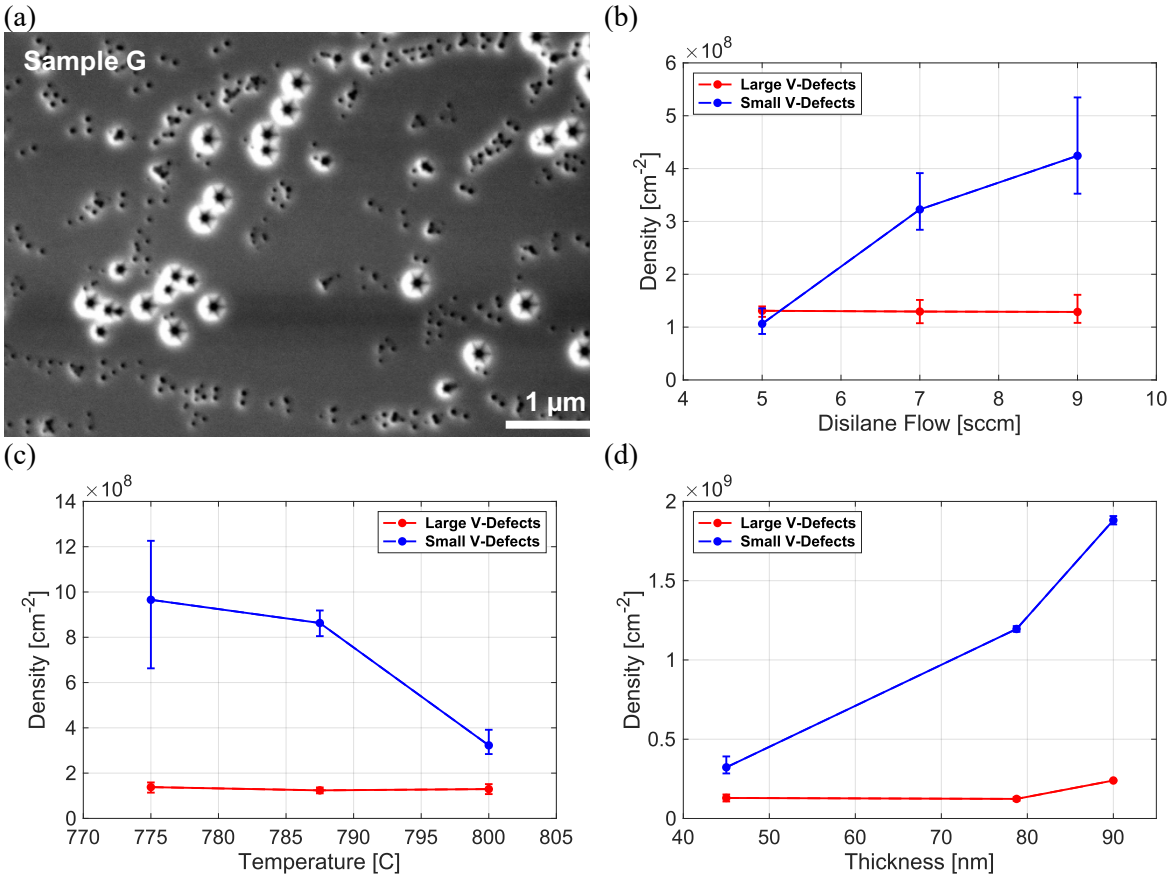

Figure 5.22: (a) Planview SEM image of Sample G showing large V-pits and small pairs of pits which correspond to half loops. The densities of half loops and large V-pits were 1.2×10^{9} cm^{-2} 1.2×10^{8} cm^{-2} respectively. The trends in V-defect density are shown in the plots by varying **(b)** disilane flow, **(c)** growth temperature, and **(d)** LT layer thickness are shown. Large V-defects were identified for counting by their clearly defined, bright hexagonal

sidewalls and were found to have a diameter of 150 – 300 nm between opposite $\{10\bar{1}1\}$ planes. Small V-defects were measured to have a diameter of 40 – 60 nm.

As seen in the previous SEM images of half-loops and discussed in the last section, it's important that the half loops are allowed to nucleate into full V-defects before active region growth. But it would also beneficial if all pits are roughly equal in size. This creates a problem since the half loop generation layer also opens large V-pits on existing threads. One approach that was employed to address this was to add a filling layer followed by the original V-defect opening layer (but with low Si doping so as not to generate more half loops). These results are shown in Figure 5.23.

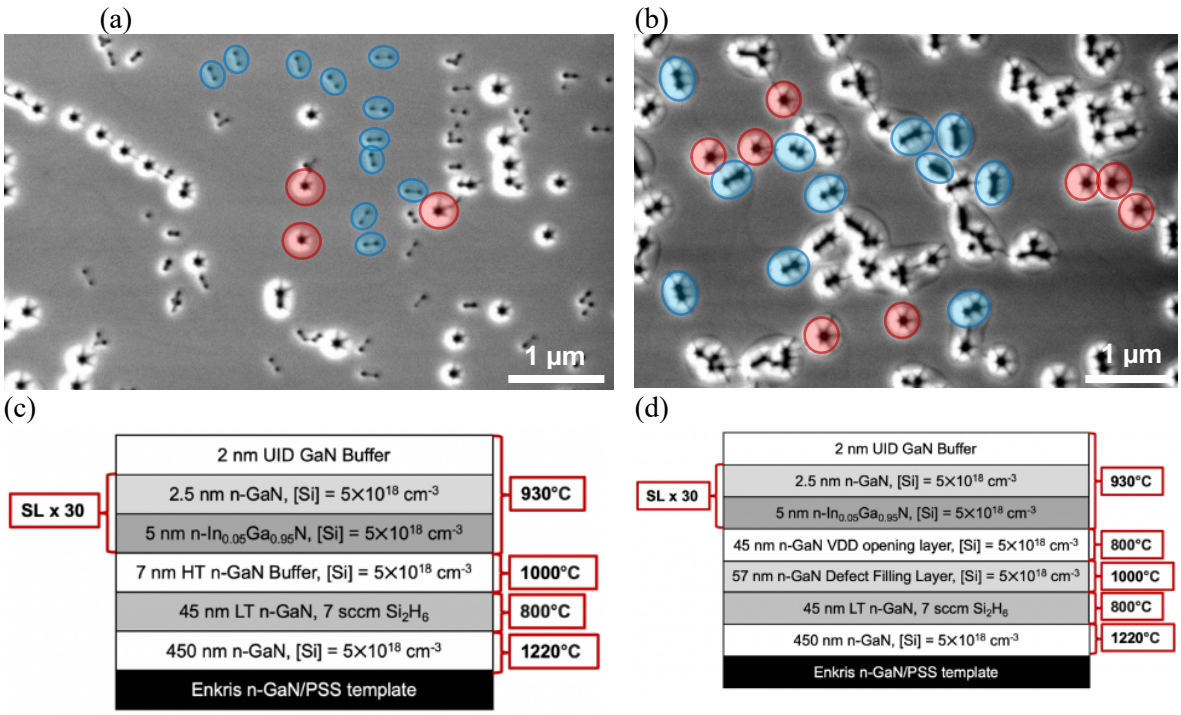

Figure 5.23: A plane view SEM comparison of Sample A **(a)** to the same structure with the additional V-Defect filling and opening layers added **(b)**. In **(a)**, the small V-defects resulting from half-loops are circled in blue and large V-defects from substrate dislocations are circled in red. In **(b)**, pairs of large V-defects resulting from half-loops are circled in blue and lone V-defects resulting from substrate dislocations are circled in red. **(c)** and **(d)** are the epitxial layer structures for the samples shown in **(a)** and **(b)**, respectively.

Figure 5.23a shows an SEM image of the surface of a standard V-pit template with half loop generation (epitaxial structure shown in Fig. 5.23c). Figure 5.23b shows a new template where all pits have been filled with a high temperature planarization layer followed by a second V-defect nucleation layer and a 30 period SL to increase pit size (epitaxial structure shown in Figure 5.23d). Here we see a much more uniform size distribution and higher V-defect density achieving the goal of attaining high V-pit densities on PSS. By using these methods any V-defect density should be achievable on PSS enabling low forward voltage on PSS. There still much more work to be done on optimizing performance, V-defect size, distribution, and reducing voltage barriers for optimal lateral injection. This and much more is the topic of Chapter 6.

References

[1] C. Lynsky *et al.*, “Barriers to carrier transport in multiple quantum well nitride-based c -plane green light emitting diodes,” *Phys. Rev. Mater.*, vol. 4, no. 5, pp. 1–6, 2020, doi: 10.1103/PhysRevMaterials.4.054604.

[2] C. Lynsky *et al.*, “Improved Vertical Carrier Transport for Green III-Nitride LEDs Using (In,Ga) N Alloy Quantum Barriers,” *Phys. Rev. Appl.*, vol. 17, no. 5, May 2022, doi: 10.1103/PhysRevApplied.17.054048.

[3] G. Lheureux, C. Lynsky, Y.-R. Wu, J. S. Speck, and C. Weisbuch, “A 3D simulation comparison of carrier transport in green and blue c-plane multi-quantum well nitride light emitting diodes,” *J. Appl. Phys.*, vol. 128, no. 23, 2020, doi: 10.1063/1.5143276.

[4] Z. Quan, L. Wang, C. Zheng, J. Liu, and F. Jiang, “Roles of V-shaped pits on the improvement of quantum efficiency in InGaN/GaN multiple quantum well light-emitting diodes,” *J. Appl. Phys.*, vol. 116, no. 18, 2014, doi: 10.1063/1.4901828.

[5] X. Wu, J. Liu, and F. Jiang, “Hole injection from the sidewall of V-shaped pits into c -plane multiple quantum wells in InGaN light emitting diodes,” *J. Appl. Phys.*, vol. 118, no. 16, Oct. 2015, doi: 10.1063/1.4934503.

[6] F. Jiang *et al.*, “Efficient InGaN-based yellow-light-emitting diodes,” *Photonics Res.*, vol. 7, no. 2, pp. 144–148, 2019.

[7] S. Zhang *et al.*, “Efficient emission of InGaN-based light-emitting diodes: toward orange and red,” *Photonics Res.*, vol. 8, no. 11, p. 1671, 2020, doi: 10.1364/prj.402555.

[8] C. K. Li *et al.*, “3D numerical modeling of the carrier transport and radiative

efficiency for InGaN/GaN light emitting diodes with V-shaped pits," *AIP Adv.*, vol. 6, no. 5, May 2016, doi: 10.1063/1.4950771.

[9] C. H. Ho, J. S. Speck, C. Weisbuch, and Y. R. Wu, "Efficiency and Forward Voltage of Blue and Green Lateral LEDs with v -shaped Defects and Random Alloy Fluctuation in Quantum Wells," *Phys. Rev. Appl.*, vol. 17, no. 1, Jan. 2022, doi: 10.1103/PhysRevApplied.17.014033.

[10] Y. C. Chow *et al.*, "Origins of the high-energy electroluminescence peaks in long-wavelength (~495-685 nm) InGaN light-emitting diodes," *Appl. Phys. Lett.*, vol. 123, no. 9, 2023, doi: 10.1063/5.0167779.

[11] F. Wu *et al.*, "Structure of V-defects in long wavelength GaN-based light emitting diodes," *J. Appl. Phys.*, vol. 035703, no. 133, 2023, doi: 10.1063/5.0135278.

[12] D. Kapolnek *et al.*, "Structural evolution in epitaxial metalorganic chemical vapor deposition grown GaN films on sapphire," *Appl. Phys. Lett.*, vol. 67, p. 1541, 1995, doi: 10.1063/1.114486.

[13] X. Jiang *et al.*, "Study on the performance of InGaN-based green LED by designing different preparing layers," *Opt. Mater. (Amst).*, vol. 89, pp. 505–511, Mar. 2019, doi: 10.1016/j.optmat.2019.01.068.

[14] J. Elsner *et al.*, "Theory of Threading Edge and Screw Dislocations in GaN," 1997.

[15] M. A. Moram *et al.*, "On the origin of threading dislocations in GaN films," *J. Appl. Phys.*, vol. 106, no. 7, 2009, doi: 10.1063/1.3225920.

[16] P. Vennegues, B. Beaumont, M. Vaille, and P. Gibart, "Microstructure of GaN

epitaxial films at different stages of the growth process on sapphire (0 0 0 1)," 1997.

[17] X. H. Wu *et al.*, "Structural origin of V-defects and correlation with localized excitonic centers in InGaN/GaN multiple quantum wells," *Appl. Phys. Lett.*, vol. 72, no. 6, pp. 692–694, 1998, doi: 10.1063/1.120844.

[18] F. . Frank, "The influence of dislocations on crystal growth," *Discuss. Faraday Soc.*, vol. 5, pp. 48–54, 1949.

[19] I. H. Kim, H. S. Park, Y. J. Park, and T. Kim, "Formation of V-shaped pits in InGaN/GaN multiquantum wells and bulk InGaN films," *Appl. Phys. Lett.*, vol. 73, no. 12, pp. 1634–1636, 1998, doi: 10.1063/1.122229.

[20] J. L. Liu *et al.*, "Status of GaN-based green light-emitting diodes," *Chinese Phys. B*, vol. 24, no. 6, 2015, doi: 10.1088/1674-1056/24/6/067804.

[21] Q. Lv *et al.*, "Realization of Highly Efficient InGaN Green LEDs with Sandwich-like Multiple Quantum Well Structure: Role of Enhanced Interwell Carrier Transport," *ACS Photonics*, vol. 6, no. 1, pp. 130–138, Jan. 2019, doi: 10.1021/acsphotonics.8b01040.

[22] J. Ewing *et al.*, "Influence of Superlattice Structure on V-Defect Distribution, External Quantum Efficiency and Electroluminescence for Red InGaN Based μLEDs on Silicon," *Crystals*, vol. 12, no. 9, Sep. 2022, doi: 10.3390/cryst12091216.

[23] C. Lynsky *et al.*, "Role of V-defect density on the performance of III-nitride green LEDs on sapphire substrates," *J. Cryst. Growth*, vol. 560–561, no. December 2020, 2021, doi: 10.1016/j.jcrysgro.2021.126048.

[24] J. J. Ewing *et al.*, “High External Quantum Efficiency (6.5%) InGaN V-defect LEDs at 600 nm on Patterned Sapphire Substrates,” *Opt. Express (accepted Publ.*, 2023.

[25] L. Y. Kuritzky *et al.*, “High wall-plug efficiency blue III-nitride LEDs designed for low current density operation,” *Opt. Express*, vol. 25, no. 24, p. 30696, Nov. 2017, doi: 10.1364/oe.25.030696.

[26] H. H. Weitering, D. R. Heslinga, and T. Hibma, “Structure and growth of epitaxial Pb on Si(111),” *Phys. Rev. B*, vol. 45, no. 11, pp. 5991–6002, Mar. 1992, doi: 10.1103/PhysRevB.45.5991.

[27] O. P. Karpenko, S. M. Yalisove, and D. J. Eaglesham, “Surface roughening during low temperature Si(100) epitaxy,” *J. Appl. Phys.*, vol. 82, no. 3, pp. 1157–1165, Aug. 1997, doi: 10.1063/1.365883.

[28] J. Schwarzkopf, B. Selle, W. Bohne, J. Röhrich, I. Sieber, and W. Fuhs, “Disorder in silicon films grown epitaxially at low temperature,” *J. Appl. Phys.*, vol. 93, no. 9, pp. 5215–5221, May 2003, doi: 10.1063/1.1563059.

[29] B. N. Bryant, E. C. Young, F. Wu, K. Fujito, S. Nakamura, and J. S. Speck, “Basal plane stacking fault suppression by nitrogen carrier gas in m-plane GaN regrowth by hydride vapor phase epitaxy,” *Appl. Phys. Express*, vol. 6, no. 11, Nov. 2013, doi: 10.7567/APEX.6.115502.

[30] Y. L. Hu, S. Krämer, P. T. Fini, and J. S. Speck, “Atomic structure of prismatic stacking faults in nonpolar a-plane GaN epitaxial layers,” *Appl. Phys. Lett.*, vol. 101, no. 11, Sep. 2012, doi: 10.1063/1.4750238.

[31] Z. Liliental-Weber, W. Swider, K. M. Yu, J. Kortright, F. W. Smith, and A. R. Calawa, “Breakdown of crystallinity in low-temperature-grown GaAs layers,” *Appl. Phys. Lett.*, vol. 58, no. 19, pp. 2153–2155, 1991, doi: 10.1063/1.104990.

[32] B. E. Weir *et al.*, “Low-temperature homoepitaxy on Si(111),” *Appl. Phys. Lett.*, vol. 59, no. 2, pp. 204–206, 1991, doi: 10.1063/1.105966.

[33] A. V. Lobanova, A. L. Kolesnikova, A. E. Romanov, S. Y. Karpov, M. E. Rudinsky, and E. V. Yakovlev, “Mechanism of stress relaxation in (0001) InGaN/GaN via formation of V-shaped dislocation half-loops,” *Appl. Phys. Lett.*, vol. 103, no. 15, Oct. 2013, doi: 10.1063/1.4824835.

[34] S. Fan *et al.*, “Observation of threading dislocations and misfit dislocation half-loops in GaN/AlGaN heterostructures grown on Si using electron channeling contrast imaging,” *J. Appl. Phys.*, vol. 132, no. 10, Sep. 2022, doi: 10.1063/5.0102373.

[35] X. J. Ning, F. R. Chien, P. Pirouz, J. W. Yang, and M. A. Khan, “Growth defects in GaN films on sapphire: The probable origin of threading dislocations,” *J. Mater. Res.*, vol. 11, no. 3, pp. 580–592, Mar. 1996, doi: 10.1557/JMR.1996.0071.

[36] J. Smalc-Koziorowska, C. Bazioti, M. Albrecht, and G. P. Dimitrakopulos, “Stacking fault domains as sources of a-type threading dislocations in III-nitride heterostructures,” *Appl. Phys. Lett.*, vol. 108, no. 5, Feb. 2016, doi: 10.1063/1.4940745.

[37] F. Wu *et al.*, “Stacking fault formation in the long wavelength InGaN/GaN multiple quantum wells grown on m -plane GaN,” *Appl. Phys. Lett.*, vol. 96, no. 23, 2010, doi: 10.1063/1.3447940.

[38] J. Smalc-Koziorowska *et al.*, “The heterogeneous nucleation of threading dislocations on partial dislocations in III-nitride epilayers,” *Sci. Rep.*, vol. 10, no. 1, Dec. 2020, doi: 10.1038/s41598-020-74030-y.

[39] S. Wang, H. Xie, H. Liu, A. M. Fischer, H. McFavilen, and F. A. Ponce, “Dislocation baskets in thick InxGa1-xN epilayers,” *J. Appl. Phys.*, vol. 124, no. 10, Sep. 2018, doi: 10.1063/1.5042079.

[40] I. G. Vasileiadis, I. Belabbas, C. Bazioti, J. Smalc-Koziorowska, P. Komninou, and G. P. Dimitrakopulos, “Stacking Fault Manifolds and Structural Configurations of Partial Dislocations in InGaN Epilayers,” *Phys. Status Solidi Basic Res.*, vol. 258, no. 11, Nov. 2021, doi: 10.1002/pssb.202100190.

[41] Q. Sun, C. D. Yerino, B. Leung, J. Han, and M. E. Coltrin, “Understanding and controlling heteroepitaxy with the kinetic Wulff plot: A case study with GaN,” in *Journal of Applied Physics*, Sep. 2011, vol. 110, no. 5, doi: 10.1063/1.3632073.

[42] R. A. Oliver, M. J. Kappers, J. Sumner, R. Datta, and C. J. Humphreys, “Highlighting threading dislocations in MOVPE-grown GaN using an in situ treatment with SiH4 and NH3,” *J. Cryst. Growth*, vol. 289, no. 2, pp. 506–514, Apr. 2006, doi: 10.1016/j.jcrysgro.2005.12.075.

[43] S. Tanaka, M. Takeuchi, and Y. Aoyagi, “Express Letter Anti-Surfactant in III-Nitride Epitaxy-Quantum Dot Formation and Dislocation Termination,” 2000.

[44] Peter Bernhard Hirsch, *Electron Microscopy of Thin Crystals*, 2nd ed., vol. Chapter 11.5. R. E. Krieger Publishing Company, 1977.

[45] T. Tak *et al.*, “Injection mechanisms in a III-nitride light-emitting diode as seen by self-emissive electron microscopy,” *Phys. Rev. Appl.*, vol. 20, no. 6, p. 064045, Dec. 2023, doi: 10.1103/PhysRevApplied.20.064045.

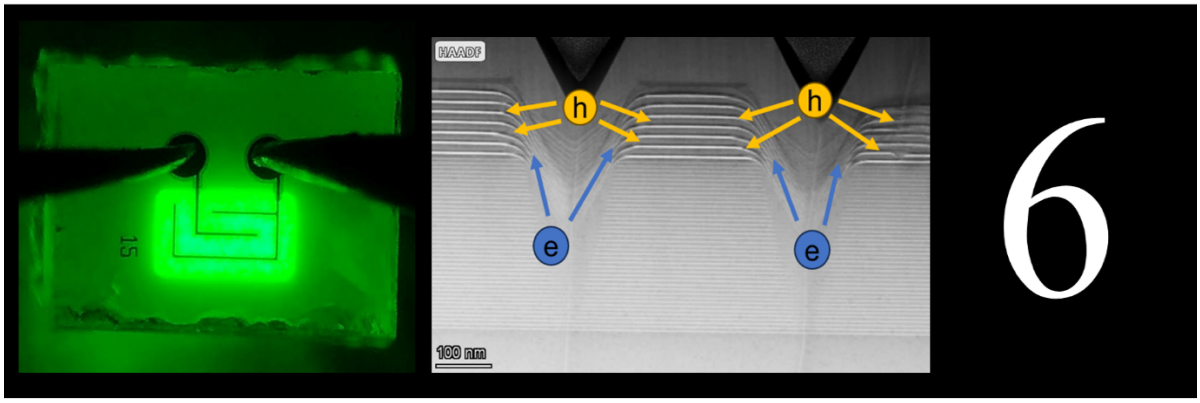

Active Region Design and Lateral Injection

6.1 Active region design for long wavelength III-N LEDs

Chapter 4 touched on some of the principles and methods for growing high quality active regions in red III-N LEDs. In this chapter, we'll take a much closer look at the general methods for growing high efficiency LEDs, but first we'll start with the high-level view. High efficiency means optimizing radiative processes while minimizing non-radiative pathways. Practically speaking, this is achieved by growing the highest quality crystal achievable while minimizing the formation of unwanted defects. Particularly defects that form in the active region, which become centers for Shockley-Read-Hall (SRH) and trap assisted Auger recombination (TAAR).

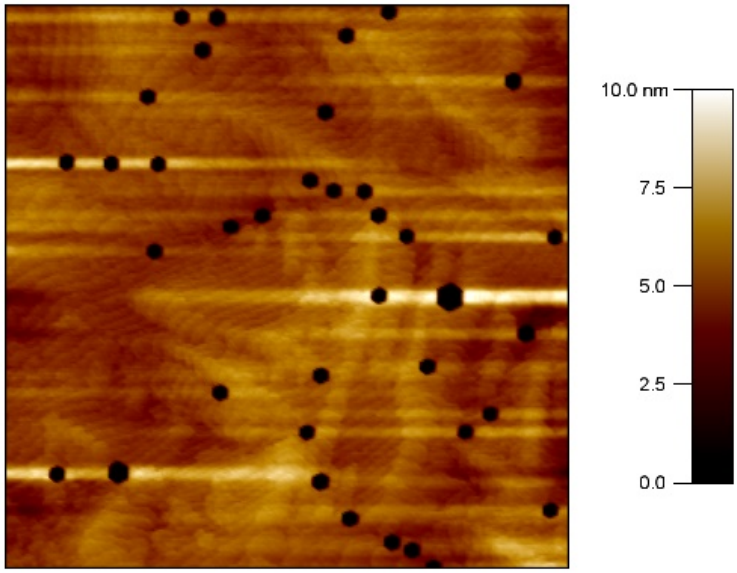

Figure 6.1: Atomic force microscope (AFM) image of the surface of an LED. Note the clearly visible steps that characterize the surface. Maintaining a step terrace structure throughout the entire MOCVD growth via the step-flow growth mode is one of the most important things to growing high efficiency LEDs.

Figure 6.1 shows an atomic force microscope (AFM) image of an LED surface. The step terrace structure can clearly be seen on the surface indicating step-flow growth throughout the process. Maintaining step flow growth is critical for high efficiency LEDs and reducing impurity incorporation and complex defect formation. In fact, some defects, such as stacking faults, can only form during island growth. Step flow growth is enhanced by higher surface mobility and at elevated temperatures. Growing InGaN or AlGaN layers can often disrupt the growth particularly at high In or Al percents and can lead to defect formation. This is partially why longer wavelength III-N LEDs tend to be more defective. Furthermore, growing high In% requires lower growth temperatures which accentuates the problem. It's important to note that just because the overall growth is step-flow, there can still be local regions that see island growth if the step terrace width gets too large. Furthermore, adatoms like Al typically have less desorption and may locally disrupt the step terrace structure causing complex defect formation.

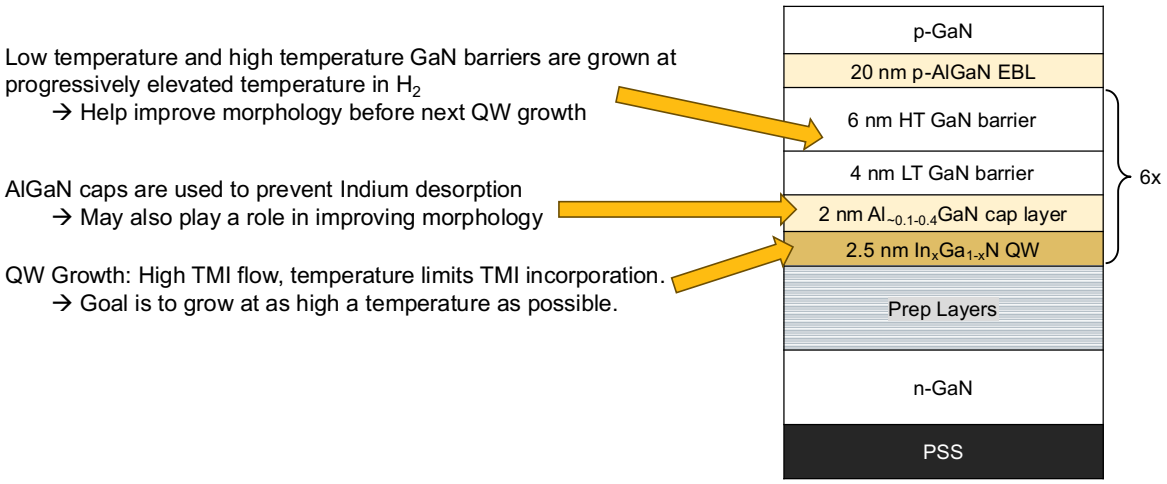

Figure 6.2: Simplified schematic illustration the typical growth approach to long wavelength InGaN LEDs. These growth approaches were demonstrated by Hwang et al. at Toshiba [1]. At UCSB A. Alhassan and C. Lynsky developed the red and green epitaxy. My work was built off their recipies.

Figure 6.2 shows the general approach that we utilize to grow long wavelength LEDs on PSS. The growth always starts with high temperature UID and n-GaN, followed by preparation layers such as a superlattice and/or low temperature GaN for V-pit formation. These have already been discussed in detail in the previous chapters. The QW growth is much colder than other layers so there's always a growth pause and temperature ramp before active region growth starts. The QWs are grown with high TMI flow (often a few times higher than the TEG flow) because In has a very low incorporation rate. The incorporation of In is highly temperature dependent so the quantum well emission wavelength is controlled by changing the temperature of that layer. In also desorbs very easily so the capping layer (can be GaN or AlGaN) is grown immediately after the QW at the same temperature and an increased growth rate. After the cap the low temperature and high temperature GaN quantum barriers (QBs) are grown immediately at successively elevated temperatures ~75 °C and 150 °C higher than the QW. The QBs are also grown in H2 which helps limit impurity uptake and improve morphology. The QBs structure was optimized by A. Alhassan and is described in this PhD

dissertation. Figure 6.3 shows a cross sectional STEM image of a 7 QW active region in one of our LEDs. The lighter lines are the InGaN QWs. In STEM they appear whiter because In has a higher Z compared to Ga. The light gray are the GaN layers and the dark gray is the AlGaN caps. AlGaN appears darker due to the lower Z compared to Ga.

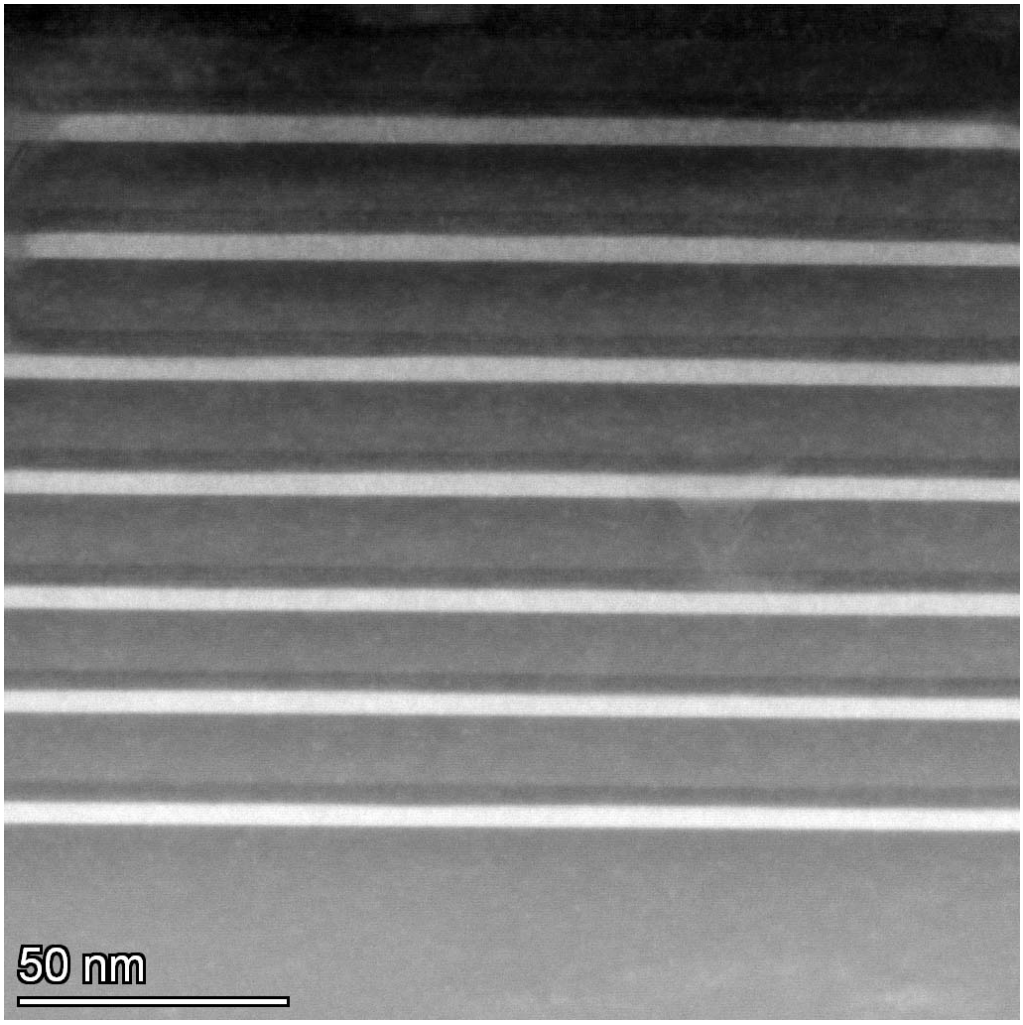

Figure 6.3: STEM image of a 7 QW active region for a green LED. The lighter regions are InGaN, grey is GaN and the dark grey are the AlGaN caps.

During my PhD a key improvement to the active region was the addition of a pre-QW layer which is grown immediately before the QW. Because the QBs are grown at a higher temperature compared to the QW, a temperature ramp (and growth pause) are required between each MQW. This growth pause can cause etching or surface damage and the 0.5 nm

pre-QW layer, which is grown at the same temperature as the InGaN QW, can help repair this damage and increase the quality of the active region. This was motivated by the work of Nanchang in ref [2]. The epitaxial structure of a green LED on PSS with the pre-QW GaN layer is shown in **Error! Reference source not found.** 6.4. We grew a set of LEDs with the pre-QW layer (Figure 6.4) and one without (same epitxial structure but no pre-QW layer) to determine its effect on performance.

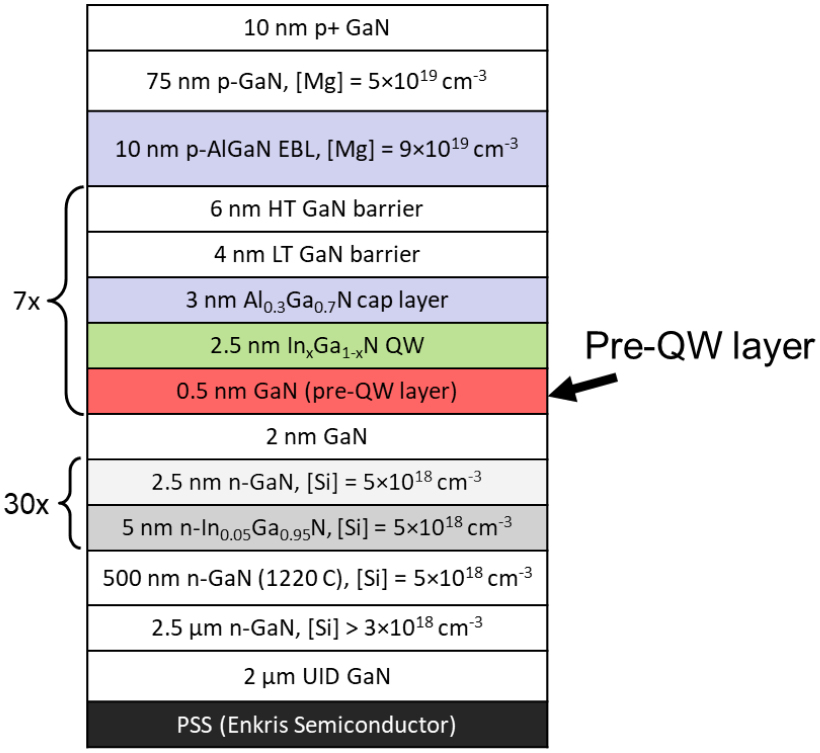

Figure 6.4: Epitaxial structure of a green LED with addition of pre-QW layer.

These LEDs were processed using our 'quickfab' structure which provides ohmic contacts and backside on-chip emission. We measured relative EQE and wavelength dependence using the integrating sphere setup for on-chip measurements that was described in chapter 4 (with a modification for backside collection). The results of this experiment are shown in Figure 6.5.

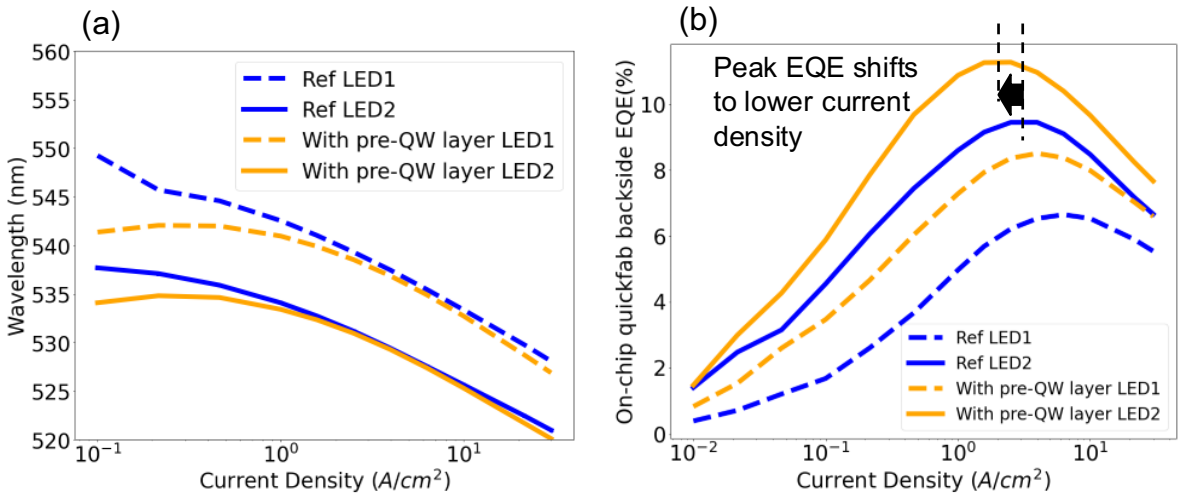

Figure 6.5: (a) Wavelength vs. current density for 4 LEDs. The blue lines are the reference withouth the pre-QW layer. The yellow lines show the LEDs with the pre-QW layer. Because LED performance is higher dependent on wavelength, it's very imporant to compare the LEDs of equivatly wavelengths. The dashed lines (LED1) are around 540 nm at peak EQE and the solide lines are approximately 530 nm at peak EQE. (b) the EQE plots comparing the two dashed lines and the two solid lines. It's very obvious tha the pre-QW layer has a dramtic effect on effcieny across multiple LEDs. Around 30% increase in EQE was observed. Furthermore the peak EQE shifts to a lower current density indicating reduced SRH.

When comparing EQE trends between LEDs it's important to compare LEDs at equivalent wavelengths because there is always an EQE trend associated with wavelengths (shorter wavelength LEDs are always more efficient, all other things being equal). Figure 6.5a shows the wavelength comparison for two LEDs from each sample. Blue lines are the LEDs with no pre-QW layer, and the yellow lines have the pre-QW layer. One LED from each sample reaches peak EQE ~530 nm (solid lines) and one around ~540 nm (dashed lines). Then we can be sure that EQE differences between samples are due to growth changes and not just wavelength variation. Figure 6.5b shows the on-chip relative EQEs. In both cases we see that the sample with the pre-QW GaN layer shows significantly higher EQE (20%-30% higher).

Furthermore, the peak EQE shifts to a lower current density for the solid lines compared to the dashed lines. This indicates that the A coefficient (SRH) is reduced with the pre-QW layer, supporting the hypothesis that the pre-QW layer is reducing defect formation or impurity uptake in the QWs.

6.2 V-defect LED performance with half-loops

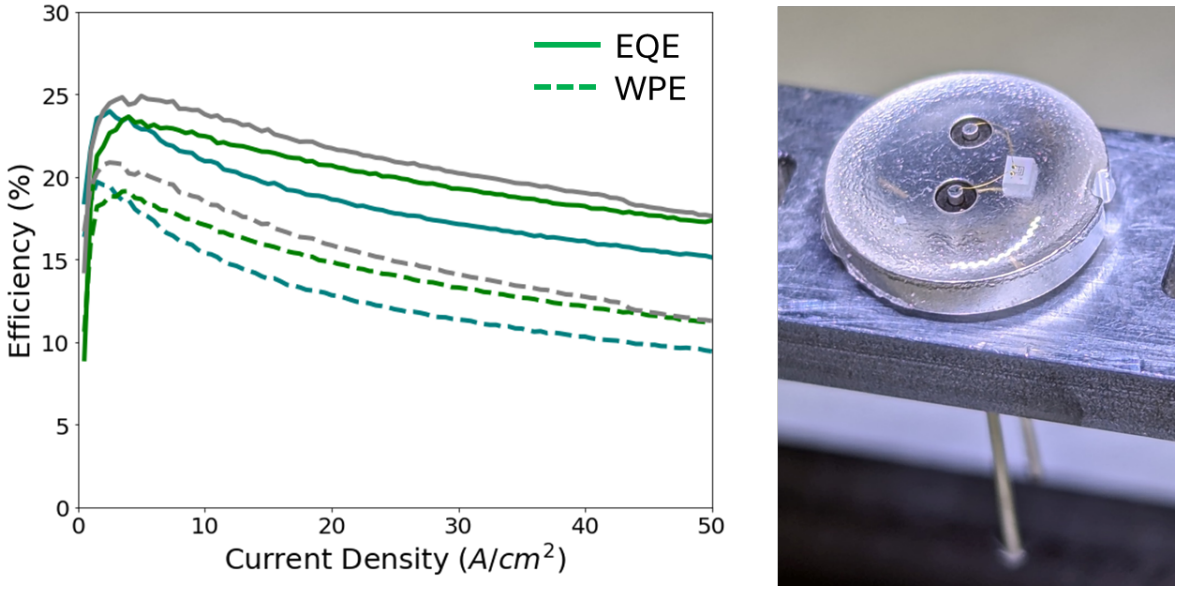

Figure 6.6: Left: EQE and WPE for 3 green LEDs from the same chip with the half loop and V-pit generation layers described at the end of chapter 5. Right: A packaged green LED.

Figure 6.6 shows the efficiencies of a green LED with the growth methods described above, combined with the half-loop and V-defect generation layers that were described in chapter 5. These LEDs show peak EQEs around 25% and WPEs as high as 21%. While the absolute EQE is not nearly as good as other reports in the literature, these are relatively good LEDs as indicated by the droop behavior and peak EQE occurring at 1 or 2 A/cm^2. While UCSB still leads the field in many areas of LED research, the reactors are decades old, and the

process control is far from state-of-the-art. This means that our absolute numbers simply don't compete with industry reactors anymore. However, these LEDs demonstrate the high WPE is achievable with half-loop generated V-pits.

Figure 6.7 shows the JV curves for these same LEDs compared to an older generation of green epi grown with the same growth methods but no half-loops. This illustrates very clearly the impact of V-pit density and the effectiveness of half-loops in generation V-pits and reducing forward voltage. The half-loop V-pit LEDs were co-processed with state-of-the-art industry LEDs and while the total voltage was still 0.4 V higher, the series resistance was almost identical indicating a sharper turn-on.

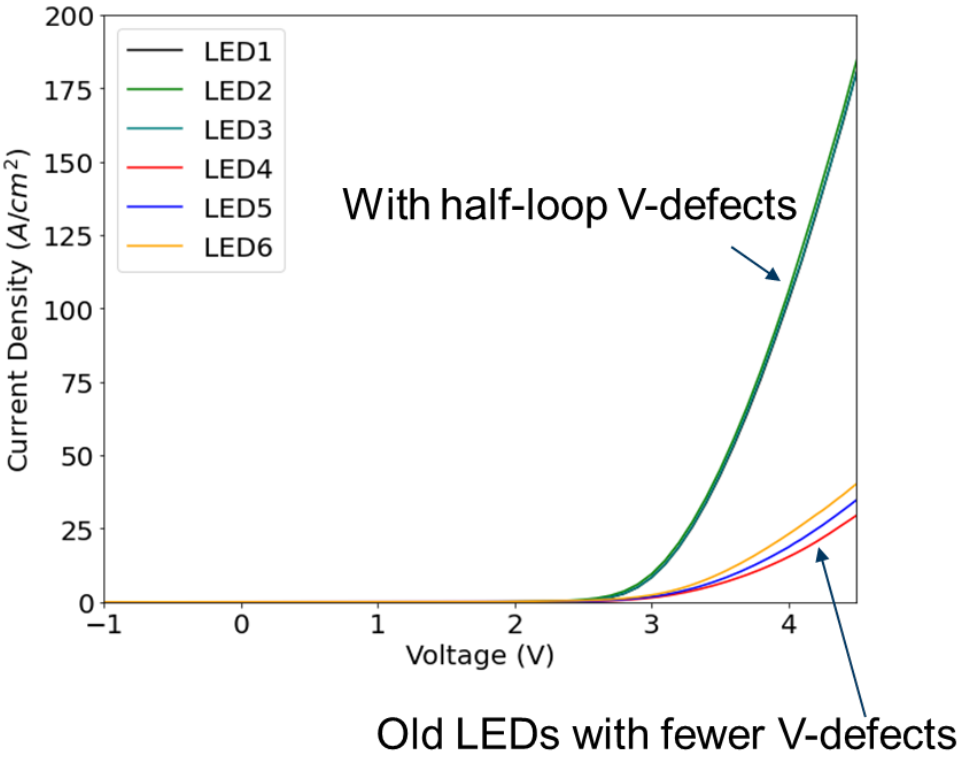

Figure 6.7: Comparison in JVs with V-defects from half-loops and older LED from UCSB which had similar growth parameters but no intentional half-loop formation and thus a much lower V-pit density.

6.3 Extended defects in the MQW region

As we've discussed already, reducing non-radiative recombination is central to developing efficient long wavelength LEDs. Practically this often comes down to reducing the formation of extended defects in the active region. Previous research at UCSB, particularly the work of Abdullah Alhassan, focused extensively on this through interrupted growth studies. The slow growth rate and use of hydrogen in the GaN QBs for these LEDs are some of the methods that were developed to reduce extended defect formation and are used in all the long wavelength LEDs grown throughout this dissertation. However, extended defect formation still occurs and is still a topic of study. In chapters 3 and 4 we discussed the issue of V-pit formation in the active region and how that effects radiative efficiency. One of the key improvements which was demonstrated in chapter 5 was to nucleate V-pits on all existing threading dislocations prior to active region growth. In general, extended defects need a nucleation point and threading dislocations can often become that nucleation point. However, the V-pits themselves can also be the source of extended defect formation, particularly the thread which inclines on the sidewall which we demonstrated in chapter 3. Figure 6.8 shows stacking fault box (SFB) formation on inclined threading dislocations in V-defects.

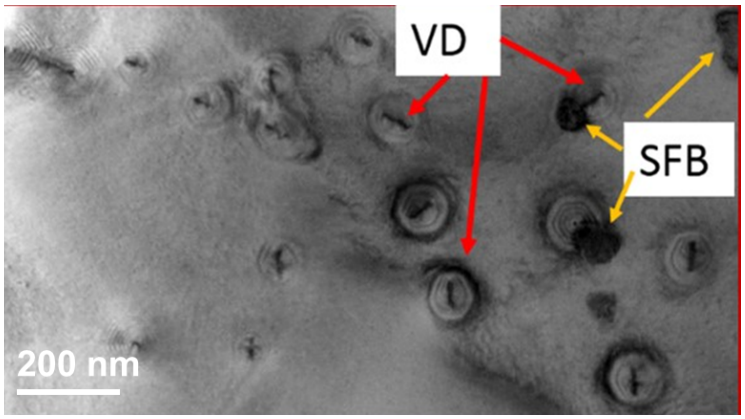

Figure 6.8: Stacking fault box (SFB) formation as a result of inclinded threading dislocations on V-defects (VD). This is a significant challenge for maximizing radiative efficiency in V-defect LEDs. From Ref [3].

One of the potential culprits of SFB formation is the AlGaN layers (both the QW cap and the EBL). As mentioned in chapter 5, stacking fault formation can only occur during island growth. Practically, in an LED, this usually means that the terrace width becomes large in places and local adatom mobility is low enough that atoms stop diffusing to the terrace step. This can be accentuated in an AlGaN layer because Al is 'sticky' with low desorption and low adatom mobility. This means that in a low temperature AlGaN layer (especially if the Al% is high), stacking fault formation is expected and this is what we observe in TEM image shown in Figure 6.9.

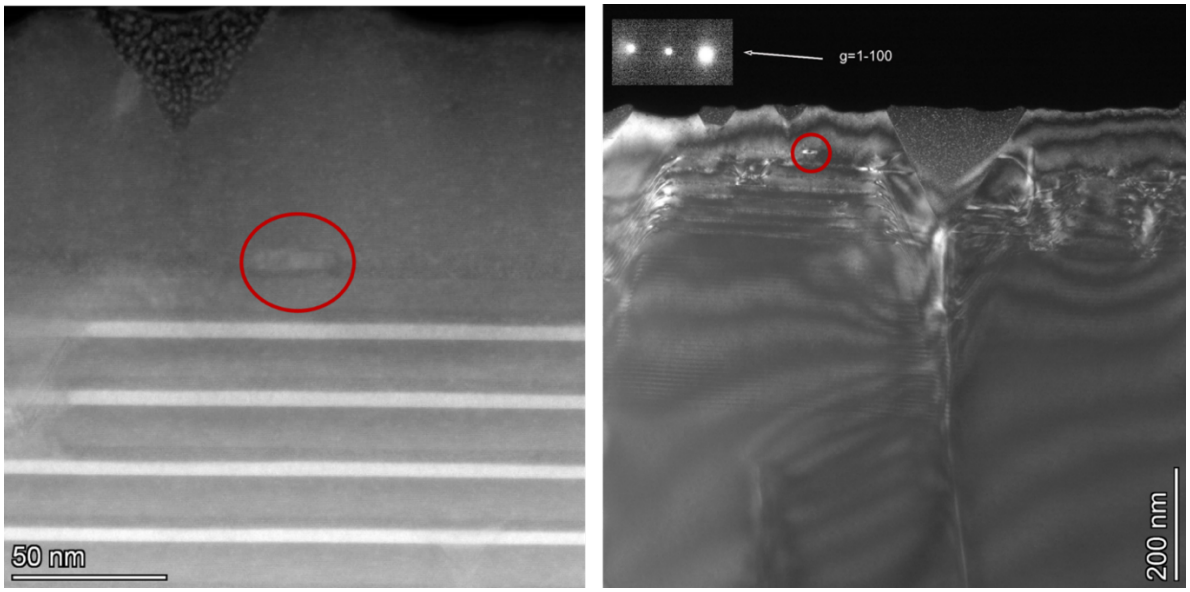

Figure 6.9: HAADF (left) and electron diffraction contrast images (right), showing a SFB generated in the AlGaN EBL layer as shown in red circle. It is buried in the structure and is likely a source of SRH and TAAR. In this case it does not induce a V-defect although we've seen small V-pit nucleation off SFBs in other samples during active region growth.

Figure 6.10 shows a close-up image of a SFB forming using high resolution HAADF imaging in TEM. A stacking fault box is the result of an I_1 stacking fault capped with a second stacking fault and bounded by partial dislocations. It's the partial dislocations at the edge of

the stacking fault that are most likely to serve as non-radiative centers. On-going work with Feng Wu and Jim Speck is aimed at fully understanding the structural details and mathematics of the formation of stacking fault boxes which will likely result in a future publication.

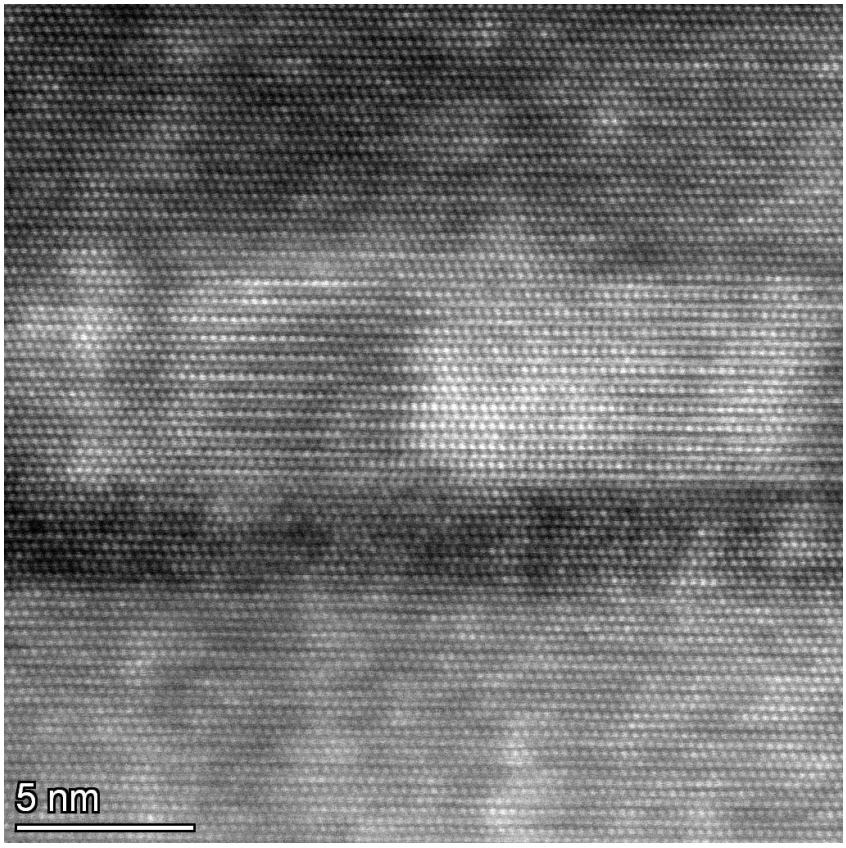

Figure 6.10: Close up HAADF image of SFB forming in AlGaN on sapphire

Other types of extended defects are observed in V-defect LED active regions. Figure 6.11 shows an interrupted growth that stopped immediately after the active region. This image reveals the formation of unwanted point and ring defects, shown in white circles. Ring defects have been observed by other groups and are understood to non-radiative centers and may see high In inside the ring [4], [5].

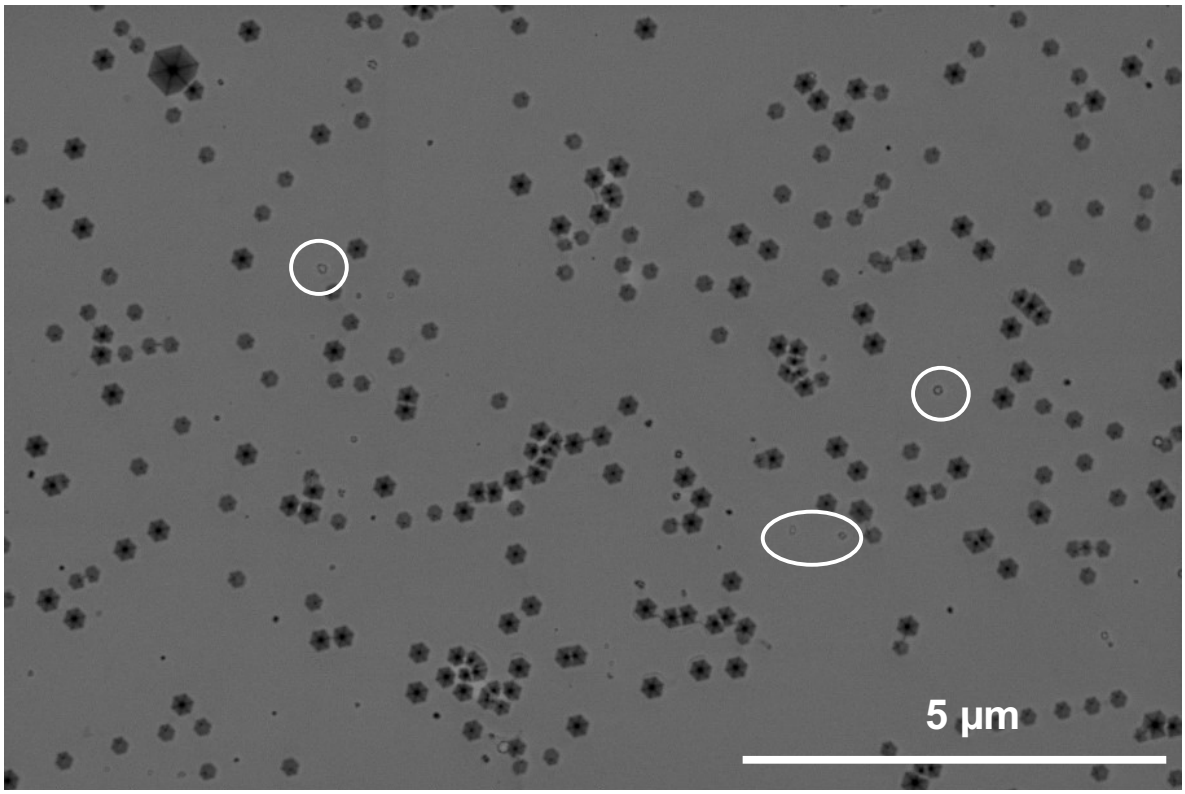

Figure 6.11: Planview SEM showing a growth that was stopped immediately above the quantum wells. We see that the V-defects successfully propagate through the active region without filling, and we observe new defects being formed (shown in white circles). Thes ring-shaped defects are similar to what's been described as 'trench' defects by other groups [4].

6.4 Experimental evidence of lateral injection through V-defects

This section was a collaboration with Saulius Marcinkevičius at KTH in Sweden. V-pit samples were grown at UCSB with the methods described in the last two chapters. The characterization was performed at KTH. The figures in this section were created by S. Marcinkevičious. The text has been rephrased.
Article: S. Marcinkevičious, J. Ewing, R. Yapporov, F. Wu, S. Nakamura, J.S. Speck, *Appl. Phys. Lett.* 123, 201102 (2023). [6]

Previous work from our group has shown that at long wavelengths it can be very difficult for holes to inject into more than the top few QWs [7]. One of the primary claims of V-defect engineering is that V-defects provide a pathway for carriers to inject laterally into the active region through the 3D geometry of the pits and to bypass the c-plane barriers to carrier transport. This should result in a deeper injection into the QWs. In collaboration with S. Marcinkevičius at KTH, Sweden we aimed to test this experimentally. At UCSB we grow a 3 QW active region where the QW closest to the n-side of the structure had a larger In content and width which red shifted it's emission compared to the two other QWs which emitted green. Figure 6.12 shows as band energy schematic of the MQW structure (a) and a detailed epitaxial stack (b) grown at UCSB. Since the deeper QW (DQW) is on the n-side, it should be populated with electrons but if it emits that indicates that it's also being populated with holes. Therefore, the hole transport path from the p-side to the DQW can be evaluated with time-resolved photoluminescence (PL) using the technique of marker QWs (QWs which have a different emission profile than the rest). This can be used to evaluate interwell carrier transport dynamics [8]–[11].

The sample was grown on double side polished (DSP) sapphire. Although the substrate chosen is suboptimal for far-field measurements due to the modulation of optical spectra by Fabry–Pérot oscillations, it was selected with future near-field spectroscopy in mind. Structural parameters were determined through cross-sectional high-angle annular dark-field scanning

transmission electron microscopy (HAADF-STEM) and energy-dispersive X-ray spectroscopy (EDS). Electroluminescence (EL) of the LED was analyzed on the wafer using needle contact probes.

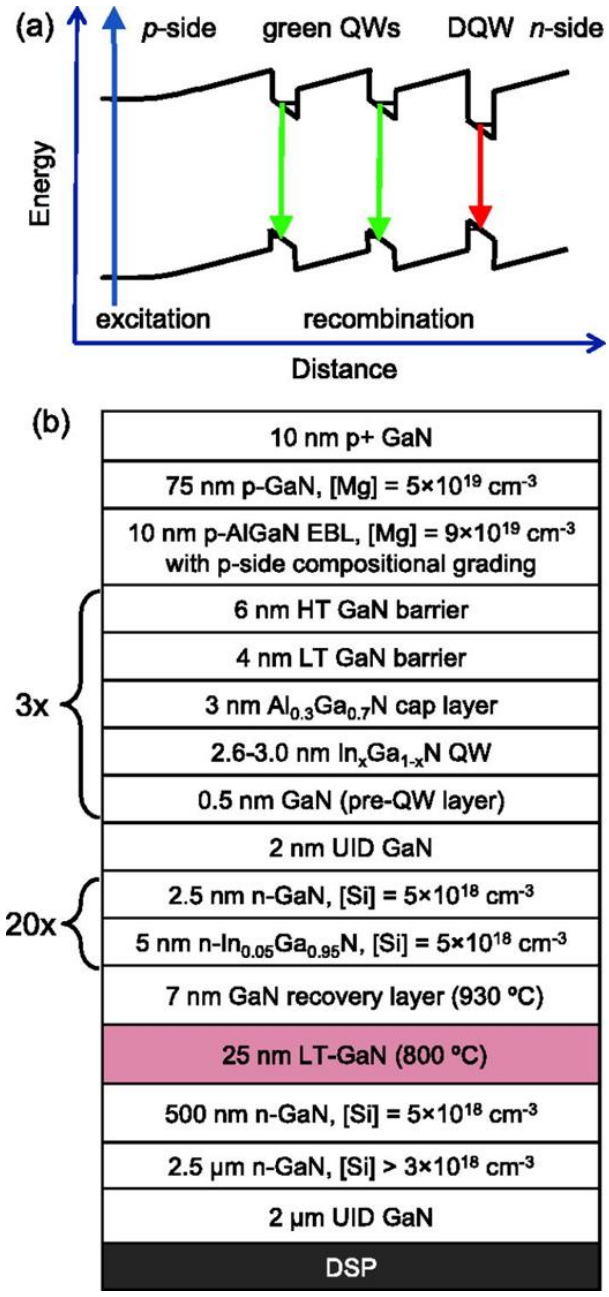

Figure 6.12: Schematics of the LED active region. The blue arrow indicates optical excitation, green and red arrows—recombination in the green and detector QWs, respectively (a). LED structure (b). Abbreviations: DSP—double side polished (sapphire), UID—unintentionally (*n*-) doped, HT—high temperature, LT—low temperature, and EBL—electron blocking layer. From ref [6].

To confirm hole transport across the green quantum wells (QWs) to the deep quantum well (DQW), two types of experiments were conducted. One involved measuring EL spectra, while the other involved measuring time-resolved photoluminescence (PL) at the peak energy of the DQW. Both experiments utilized a 0.5 m spectrometer with a liquid nitrogen-cooled CCD detector. For time-resolved PL, carriers were excited by 200 fs pulses at a central wavelength of 260 nm generated by a self-mode-locking Ti:sapphire laser and third harmonic generator. To accommodate the long PL decay times, the original laser pulse repetition rate of 80 MHz was reduced to 4 MHz using an acousto-optic pulse picker. PL dynamics were measured using a time-correlated single photon counter with a temporal response of 50 ps after selecting emission from specific QWs (green or red) using bandpass filters. Most carriers were excited in the p-side layers, as the absorption length for the 260 nm excitation is approximately 50 nm. The pulse energy density was 15 μJ/cm−2, corresponding to a photoexcited carrier density in the GaN layers of approximately 2 × 1018 cm−3. Lateral atomic force microscopy (AFM) scans were conducted in Quantitative Imaging mode using a JPK NanoWizard 3. Cross-sectional HAADF-STEM images and EDS chemical element maps were acquired using a Talos G2 200× TEM/STEM system equipped with ChemiSTEM EDS, operating at 200 kV.

Figure 6.13a shows an AFM image of the sample surface. Both V-pits are clearly visible at a range of sizes. The large ones form in the low temperature GaN or superlattice and are believed to serve as hole injectors; the small ones originate in the active region and have an enhanced rate of the nonradiative recombination [3], [12], [13]. The density and diameter of the V-defects can, to some extent, be controlled by the growth conditions and structure parameters. Generally, higher growth rates and kinetically limited growth conditions favor the formation of the V-defects.

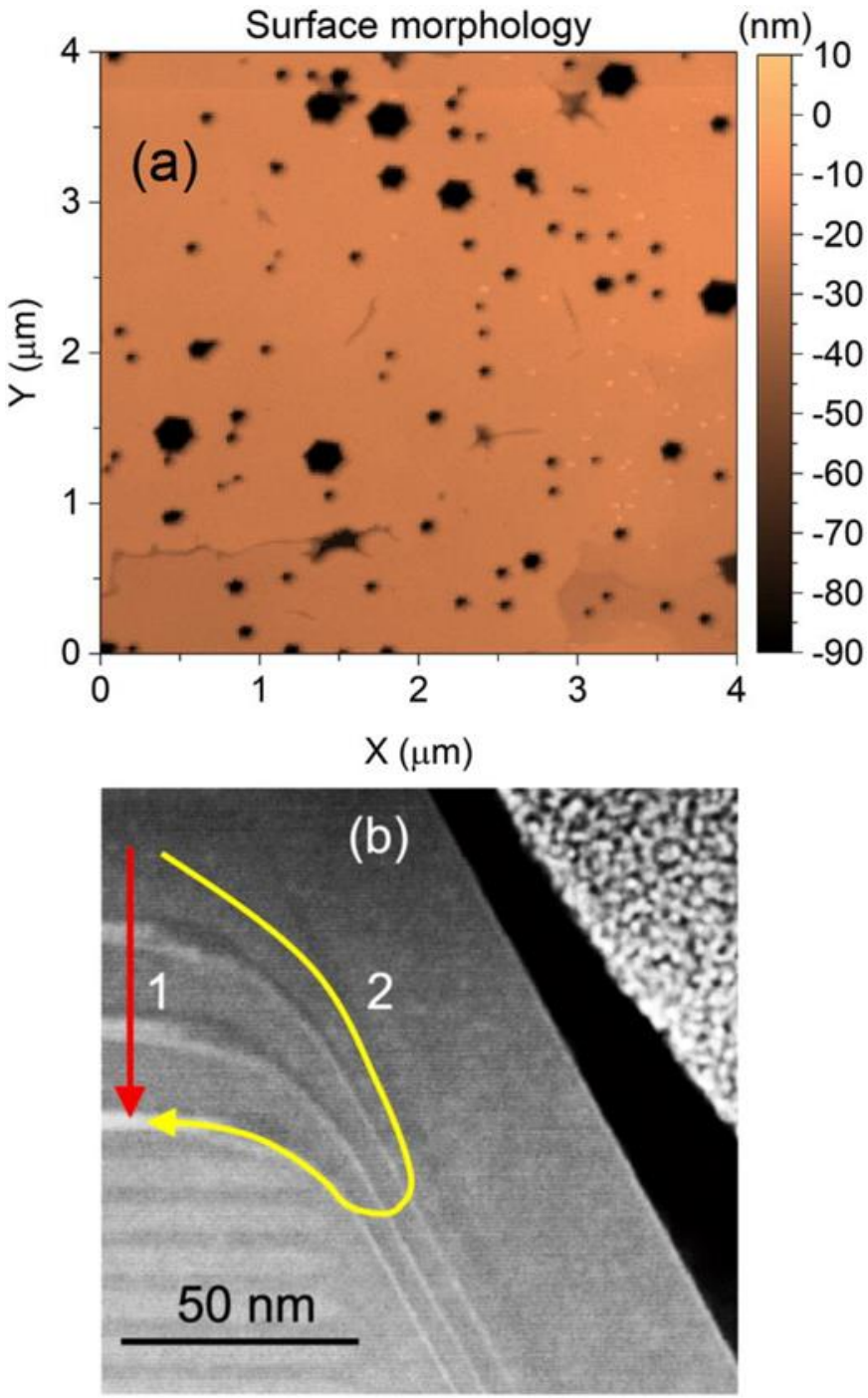

Figure 6.13: AFM image of the LED structure displaying small and large hexagonal V-defects (a). Cross-sectional HAADF-STEM image of the structure in the vicinity of a large V-defect with schematically illustrated paths of the hole transport toward the DQW directly across the green QWs (1) and via semipolar QWs at the V-defect facets (2) (b). From ref [6].

Figure 6.13b shows a cross-section HAADF-STEM image of the epitaxial structure near the sidewall of a V-pit in this sample. The red line (1) shows the hypothetical *c*-plane pathway for carriers which at these wavelengths is very unlikely to see much carrier transport. The yellow line (2) shows the transport pathway via the semipolar sidewall. This is lateral injection and is the proposed mechanism for hole transport in a V-pit LED. Because the bottom QW is longer wavelength the EL spectra will shed light on wither the lateral pathway is being used since vertical transport would barely populate under c-plane injection, especially at low bias.

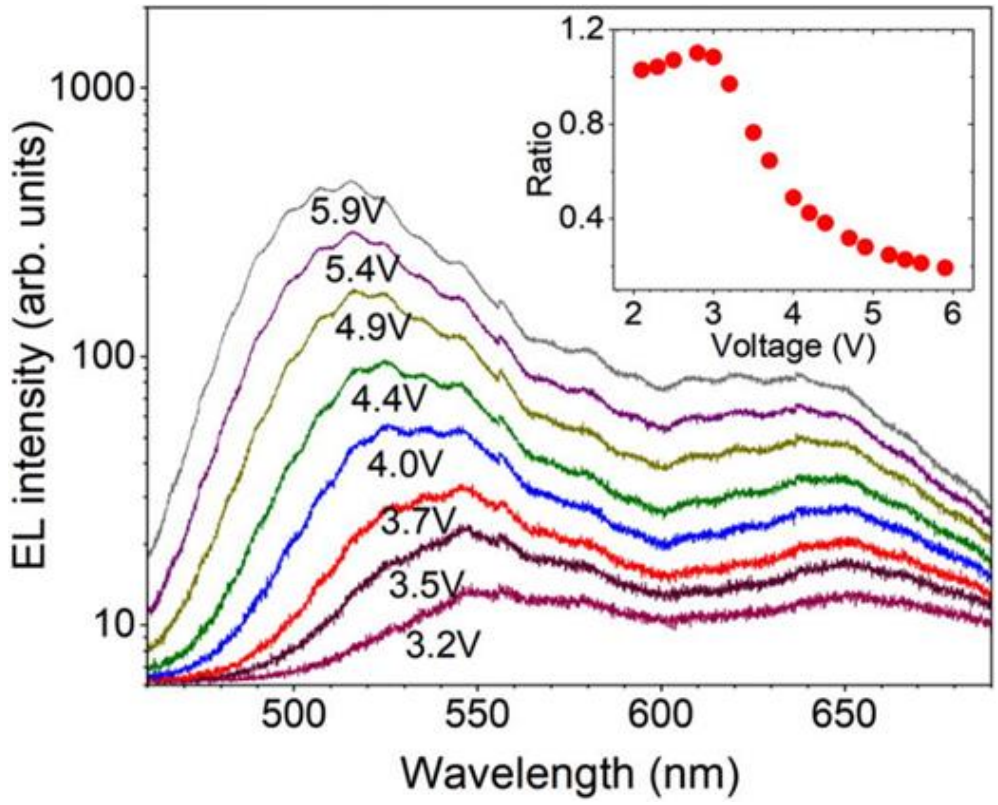

Figure 6.14: EL spectra at different bias voltages. The inset shows the spectrally integrated EL intensity ratio for the red and green peaks as a function of the applied bias. Votlages are relatively high here because of the contact resistance of the In contacts that were used.

Figure 6.14 shows the EL spectra at different applied biases. These samples had In contacts which have significant contact resistance thus the absolute voltages are high and not

reflective of actual diode voltages. Nevertheless, the relative EL spectra at low to high bias are informative of the hole transport pathway. Hole transport can either move directly across the green QWs via c-plane, this would take place via subsequent capture to thermionic emission until the DQW is reached [8], [12]. The other option is lateral injection via the V-defect sidewalls. Alternative transport mechanisms, like ballistic hole transport across the quantum wells (QWs) and tunneling through the barriers, can be discounted. Ballistic transport is not feasible due to the significantly shorter hole mean free path at room temperature compared to the barrier width. Similarly, tunneling is improbable because the barriers, measuring 13 nm in thickness, are too thick for effective tunneling. Additionally, the thermionic hole transport time, already prolonged for relatively shallow $In_{0.12}Ga_{0.88}N$/GaN QWs (1–10 ns), is exponentially dependent on the barrier height. Hence, for the deep $In_{0.20}Ga_{0.80}N$/GaN QWs in our device, thermionic transport is deemed unlikely. Nonetheless, to obtain clear experimental evidence, we conducted tests by measuring the photoluminescence (PL) dynamics.

Figure 6.15 shows the time-integrated photoluminescence (PL) and electroluminescence (EL) spectra measured at a bias of 3.5 V, a point where the device is approaching flat-band conditions but has not yet exhibited strong EL emission. In the PL spectrum, the intensity of the green quantum well (QW) emission notably surpasses that of the DQW. This contrasts with the EL spectrum, where the intensities of the green QW and DQW peaks appear similar. This discrepancy is linked to differing hole transport mechanisms, as elaborated below. Additionally, a faint PL peak around ~440 nm, attributable to recombination in the sidewall semipolar QWs has been detected. We studied the sidewall QW peak in a related article by Y. C. Chow and T. Tak [14].

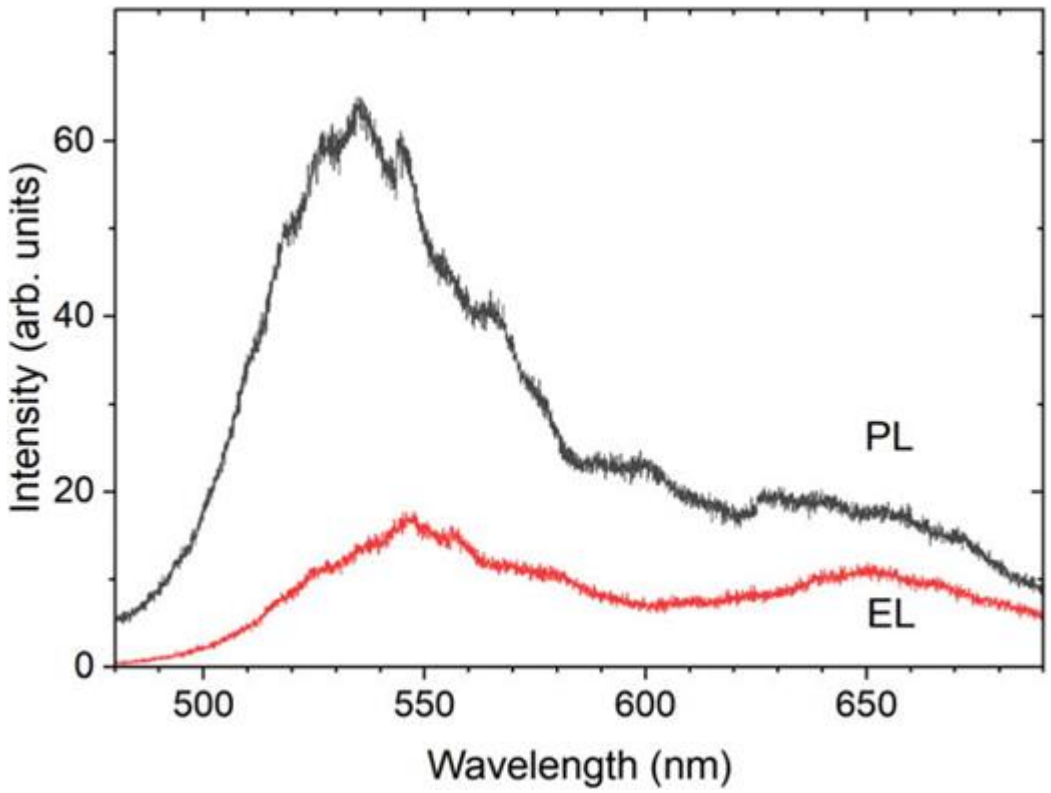

Figure 6.15: EL (red curve) and PL (black curve) spectra measured at 3.5 V forward bias.

QW PL transients exhibit a sharp ascent followed by a gradual decay, with decline times of 3.2 and 6.5–7.0 ns for the green and detector QWs, respectively. The transients for the DQW are illustrated in Figure 6.16. In the optical marker method, insights into carrier transport are gleaned from the dynamics of the DQW PL rise, wherein two distinct contributions emerge—a fast and slow one.

The fast component signifies direct carrier excitation in the DQW and neighboring barriers. Despite the presence of thick cap layers, some level of direct photoexcitation is inevitable due to the exponential decrease in excitation intensity with distance in a material. The rapid rise time primarily stems from carrier relaxation within the DQW and capture from the barriers. These processes, occurring in less than or equal to 1 ps [15], are well below our temporal resolution and appear instantaneous in Fig. 6.16.

The slow component, when it exists, arises from the radiative recombination of carriers arriving at the DQW post-excitation outside the DQW, typically in the cap layer. The slow rise time reflects the duration of carrier transport to the DQW. For shallow GaAs- or InP-based QWs, the slow rise time ranges from tens to hundreds of ps; however, for significantly deeper nitride QWs, it extends to several to tens of ns.

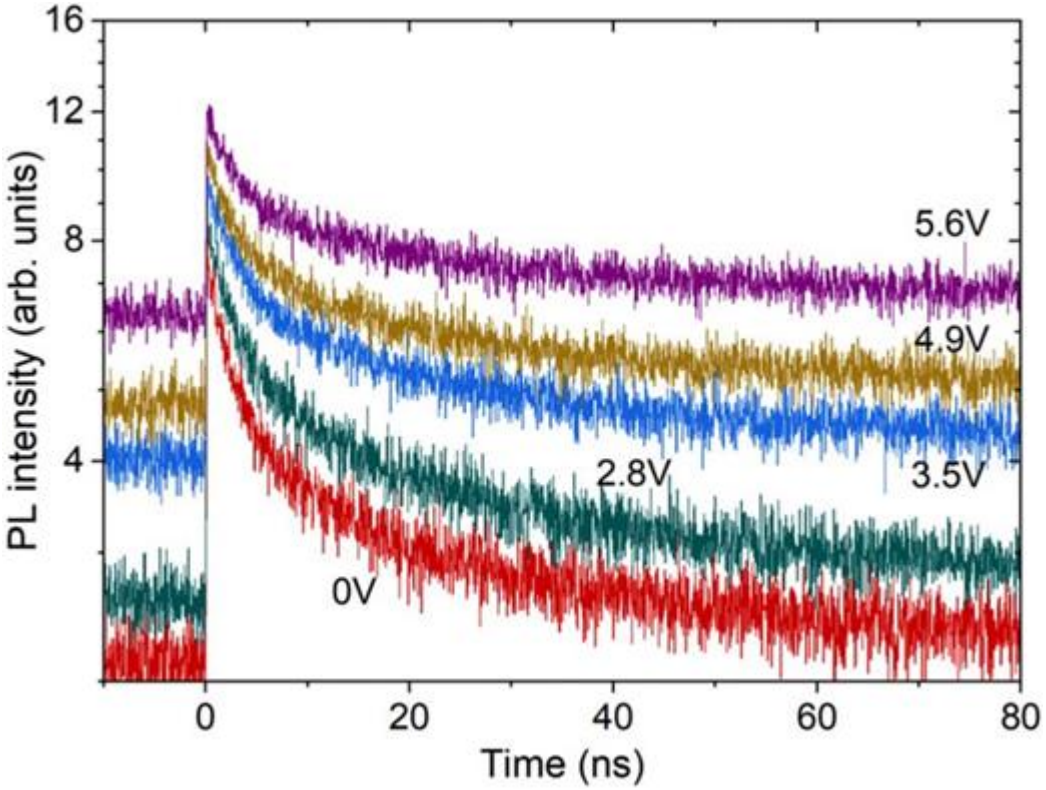

Figure 6.16: Detector QW PL transients at different bias values.

As evident from Fig. 6.16, the DQW photoluminescence (PL) transient exhibits solely the fast rise component. The absence of the slow rise component serves as confirmation that vertical thermionic interwell transport (depicted as path 1 in Fig. 6.13) is not occurring. Conversely, the presence of both DQW electroluminescence (EL) and PL peaks (as seen in Figs. 6.14 and 6.15) provides evidence of hole migration from the p-side of the structure to the DQW. Since thermionic interwell transport is not facilitating hole transfer to the DQW, the

only viable transport mechanism is via the semipolar sidewall quantum wells (illustrated as path 2 in Fig. 6.13).

Comparing the EL and PL spectra of the green QW and DQW peaks (Fig. 6.15) reveals that hole transfer into the DQW is more efficient during electrical carrier injection. The distinction between these injection mechanisms lies in the following: in the EL scenario, only holes are transported from the p-side to the DQW, while in PL, ambipolar diffusion serves as the transport mechanism, owing to the higher density of photoexcited carriers compared to doped holes. The less efficient transfer of photoexcited electron–hole pairs is likely attributed to the short electron lifetime in p-GaN. Recent time-resolved PL measurements have indicated that photoexcited electron–hole pairs in p-GaN recombine within 150 ps [16], with a significant fraction of electrons being trapped by nitrogen vacancies within 20 ps. Utilizing these trapping and recombination times along with an ambipolar diffusion coefficient of 1.6 cm^2/s [17], the corresponding lateral carrier diffusion distances are estimated to be 60 and 150 nm, respectively. Even considering the larger value of 150 nm as the distance from which carriers are captured by large V-defects, only a small region, approximately 10% of the total sample area, is where carriers would be collected into the V-defects, explaining the poor collection of photoexcited electron–hole pairs into the DQW. Conversely, photoexcited carrier capture into the first green QW occurs after vertical transport of several tens of nm, resulting in more carriers being captured by the first green QW than by the semipolar V-defect QWs.

Regarding the dependence of EL spectra on bias (Fig. 6.14), two observations are notable: (i) a blue shift of the QW peaks, particularly pronounced for the green QWs, and (ii) a nonlinear dependence of the green and detector QW EL intensity ratio (inset to Fig. 6.14).

The shift can be attributed to the screening of the QW electric field and band filling of localized states [18], which are more pronounced for the green QWs with a higher carrier concentration. The faster increase in green QW EL intensity with bias likely occurs due to a more rapid direct hole transfer from the p-side to the first green QW at large forward biases, thereby limiting the number of holes available for transport to the DQW via the V-defects. Furthermore, a red QW will in theory operate a slightly lower bias compared to green, all else being equal. Therefore, we expect the red QW to turn on at a lower bias compared to green.

In summary, through EL and time-resolved PL measurements on long-wavelength InGaN multiple QW LEDs with a detector QW, we have experimentally confirmed the existence of a hole injection mechanism via semipolar QWs situated on the sides of the V-defects. Unlike direct interwell transport facilitated by thermionic emission, this transport mechanism allows for the population of all QWs within a multiple QW structure, despite the high potential barriers in the long-wavelength InGaN/GaN quantum wells. This is an important experimental confirmation of the V-defect LED results that have been presented throughout this dissertation which is why it's been included in this section. Again, this section was primarily the work of S. Marcinkevičious with samples I grew at UCSB using the growth methods that have been described earlier in this dissertation. In the final section, I'll zoom out a bit, try to put the V-defect project in a broader context and look towards the future of laterally injected LEDs.

6.5 Novel Methods of Lateral Injection: Beyond V-defects

This dissertation has described V-defects in detail, studying their formation, structure, and how they influence LED performance. In short V-defects are a way of utilizing some of the beneficial aspects of semipolar planes in III-Ns (namely the beneficial carrier transport), while taking advantage of the cheap and effective epitaxial growth on *c*-plane GaN. In this chapter we've discussed some of the details of lateral injection as well in order to understand the carrier transport aspects of V-defects. But why the V-defect? And is there anything inherently special about the *V-defect* as the mechanism for lateral injection? Based on our current understanding of lateral injection it seems like there isn't. There should be many possible planes and architectures that allow for lateral injection, it's just that the V-pit is the most convenient and already exists in so many epitaxial structures.

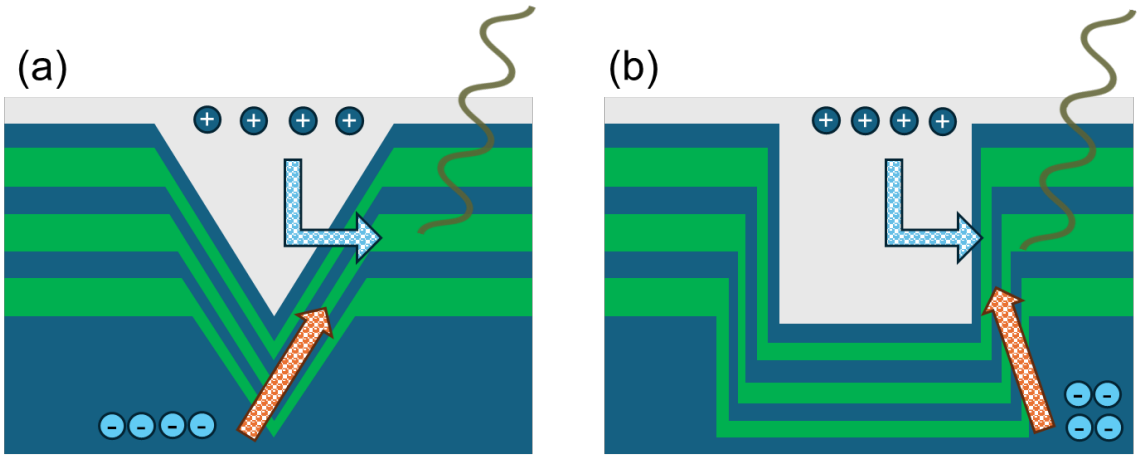

Figure 6.17: (a) schematic lateral injection on along a semipolar plane such as the sidewalls of the V-defect (b) schematic of lateral injection on a non-polar plane such as *m*-plane.

Figure 6.17 illustrates how lateral injection may be able to occur on planes other than $\{10\bar{1}1\}$. There was project at UCSB where we tried to etch hexagons in an LED then regrow p-GaN. These devices came out rather leaky but did show a lower voltage. It's unclear if there

was actually light being generated at a lower voltage or just leakage current. In any case, it was interesting as an initial proof of concept for etching and regrowth methods of lateral injection.

A second approach which we were investigating towards the end of my PhD (and wasn't covered extensively in this dissertation) was lithographic patterning of V-pits. While this dissertation focused on using threading dislocations has the nucleation mechanism for V-pits, in principle they can form on any surface perturbation. With the help of Alejandro Quevedo, I demonstrated V-pit nucleation an array of SiN dots.

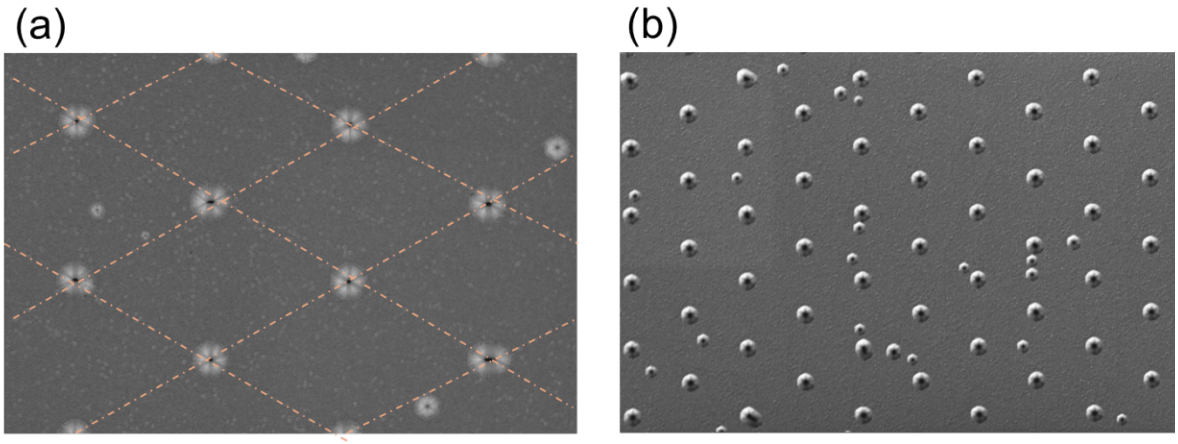

Figure 6.18: (a) and (b) are topside SEM images of V-pit arrays that were grown ontop of SiN dot arrays. These arrays were patterned lithographically. Their spacing is limited by the lithographic method used.

Figure 6.18 shows topside SEM images of V-pit arrays that are space a couple microns apart. While the initial demonstration didn't come close to realizing the optimal density of V-pits, this clearly shows that arrays are possible. In this case, the spacing was simply limited by the lithographic method that was used (in this case a maskless aligner). Other lithographic methods such as holographic lithography could produce much smaller pits with tighter spacing and that project is underway at UCSB as of this writing.

As can be seen from these examples, V-pits nucleated on threading dislocations are just one of many ways to realize laterally injected LEDs. We also aren't limited to pits. One could imagine, lithographically patterning "V-trenches" or simply etching vias and wet etching to expose *m*- or *a*-planes. Lithographic approaches could also open up other applications for lateral injection such as ultra-small μLEDs and lasers. The important point here is that V-defect engineered LEDs as described in this thesis are a case study in a much more significant transformation in the way LEDs are designed. Namely, V-defects are the first 3D LEDs where multiple crystal planes are utilized strategically to create devices that beneficially combine electrical and optical properties of two different planes in the device operation. But I would postulate that in the following years, LED researchers will find many other innovative ways of utilizing the anisotropic properties of Wurzite III-N epitaxy and that this will be vital in achieving better performance in long-wavelength III-N LEDs.

References:

[1] J. Hwang, R. Hashimoto, S. Saito, and S. Nunoue, "Development of InGaN-based red LED grown on (0001) polar surface," *Appl. Phys. Express*, vol. 7, no. 7, 2014, doi: 10.7567/APEX.7.071003.

[2] F. Jiang *et al.*, "Efficient InGaN-based yellow-light-emitting diodes," *Photonics Res.*, vol. 7, no. 2, pp. 144–148, 2019.

[3] F. Wu *et al.*, "Structure of V-defects in long wavelength GaN-based light emitting diodes," *J. Appl. Phys.*, vol. 035703, no. 133, 2023, doi: 10.1063/5.0135278.

[4] F. C. P. Massabuau *et al.*, "Morphological, structural, and emission characterization of trench defects in InGaN/GaN quantum well structures," *Appl. Phys. Lett.*, vol. 101, no. 21, 2012, doi: 10.1063/1.4768291.

[5] F. C. P. Massabuau *et al.*, "Towards a better understanding of trench defects in InGaN/GaN quantum wells," *J. Phys. Conf. Ser.*, vol. 471, no. 1, 2013, doi: 10.1088/1742-6596/471/1/012042.

[6] S. Marcinkevičius, J. Ewing, R. Yapparov, F. Wu, S. Nakamura, and J. S. Speck, "Experimental evidence of hole injection through V-defects in long wavelength GaN-based LEDs," *Appl. Phys. Lett.*, vol. 123, no. 20, 2023, doi: 10.1063/5.0179513.

[7] C. Lynsky *et al.*, "Barriers to carrier transport in multiple quantum well nitride-based c -plane green light emitting diodes," *Phys. Rev. Mater.*, vol. 4, no. 5, pp. 1–6, 2020, doi: 10.1103/PhysRevMaterials.4.054604.

[8] S. Marcinkevičius *et al.*, "Interwell carrier transport in InGaN/(In)GaN multiple

quantum wells," *Appl. Phys. Lett.*, vol. 114, no. 15, 2019, doi: 10.1063/1.5092585.

[9] B. Lambert, B. Deveaud, A. Chomette, A. Regreny, and B. Sermage, "Density-dependent transition from electron to ambipolar vertical transport in short-period GaAs-AlGaAs superlattices," *Semicond. Sci. Technol.*, vol. 4, no. 7, pp. 513–517, Jul. 1989, doi: 10.1088/0268-1242/4/7/002.

[10] H. Hillmer, A. Forchel, T. Kuhn, G. Mahler, and H. P. Meier, "Optical vertical transport interface heterostructures," *Phys. Rev. B*, vol. 43, no. 17, pp. 13992–14000, 1991.

[11] S. Marcinkevicius, K. Frojdh, U. Olin, C. Silfvenius, B. Stalnacke, and G. Landgren, "Interwell carrier transport in InGaAsP/InP quantum well laser structures," *Conf. Lasers Electro-Optics Eur. - Tech. Dig.*, vol. 3697, p. 263, 1996, doi: 10.1364/cleo_europe.1996.cthi24.

[12] R. Yapparov *et al.*, "Variations of light emission and carrier dynamics around V-defects in InGaN quantum wells," *J. Appl. Phys.*, vol. 128, no. 22, 2020, doi: 10.1063/5.0031863.

[13] J. Ewing *et al.*, "Influence of Superlattice Structure on V-Defect Distribution, External Quantum Efficiency and Electroluminescence for Red InGaN Based μLEDs on Silicon," *Crystals*, vol. 12, no. 9, Sep. 2022, doi: 10.3390/cryst12091216.

[14] Y. C. Chow *et al.*, "Origins of the high-energy electroluminescence peaks in long-wavelength (~495-685 nm) InGaN light-emitting diodes," *Appl. Phys. Lett.*, vol. 123, no. 9, 2023, doi: 10.1063/5.0167779.

[15] Ü. Özgür *et al.*, “Ultrafast optical characterization of carrier capture times in InxGa1-xN multiple quantum wells,” *Appl. Phys. Lett.*, vol. 77, no. 1, pp. 109–111, 2000, doi: 10.1063/1.126893.

[16] S. Marcinkevičius, Y. C. Chow, S. Nakamura, and J. S. Speck, “Effect of Mg doping on carrier recombination in GaN,” *J. Appl. Phys.*, vol. 134, no. 8, 2023, doi: 10.1063/5.0157378.

[17] P. Ščajev, K. Jarašiunas, S. Okur, Ü. Özgür, and H. Morkoç, “Carrier dynamics in bulk GaN,” *J. Appl. Phys.*, vol. 111, no. 2, 2012, doi: 10.1063/1.3673851.

[18] D. F. Feezell, J. S. Speck, S. P. Denbaars, and S. Nakamura, “Semipolar 2021 InGaN / GaN Light-Emitting Diodes for High-Ef fi ciency Solid-State Lighting,” vol. 9, no. 4, pp. 190–198, 2021.